

AN ABSTRACT FOR THE THESIS OF

Marlene Mainland Burr for the degree of Doctor of Philosophy in Mechanical Engineering presented on March 16, 1998. Title: Investigation of Instantaneous Hydrodynamics and Heat Transfer to a Horizontal Tube Immersed in a High-Temperature Gas-Solid Fluidized Bed of Large Particles.

Redacted for privacy

Abstract approved: _____

(James R. Welty)

Experimental results are presented related to the hydrodynamic and heat transfer behavior between a high-temperature, bubbling, gas-solid fluidized bed of large particles and an immersed horizontal tube.

A methodology has been developed to interpret signals from optical probes inserted in a bed which was validated by comparing experimental results to video-tape of a two-dimensional bed (2D). The optical probe signals (voltages) were filtered to calculate bubble (or emulsion) frequency, bubble velocity, pierced length, characteristic bubble size, bubble (or emulsion) residence time, and bubble (or emulsion) residence time fraction.

A fast-response heat flux sensor suitable for the high-temperature, abrasive bed environment was built and mounted on the outside of a 51 mm outside diameter tube. Experiments were performed with the optical probes and instantaneous heat flux sensor in

a three-dimensional (3D) bed at temperatures ranging from 600 K to 1000 K, over a range of fluidization velocities, with 2.0 mm and 2.9 mm refractory particles. Instantaneous heat transfer information was collected at circumferential intervals on the tube of 45°. Bubble phase and emulsion phase properties and heat transfer coefficients were determined and their dependence on bed temperature, fluidization velocity and particle size were established. Existing correlations for the prediction of time- and space-averaged heat transfer coefficients were evaluated. From these, new relations are presented to correlate local emulsion and bubble phase heat transfer coefficients. These expressions are

$$\text{Nu}_{p,e} = 8.95 (1 - \varepsilon(\theta))^{2/3} + 0.16 \text{Ar}^{0.3} \text{Re}_{p,mf}^{0.5} \text{Pr}^{1/3} \frac{(1 - \varepsilon(\theta))^{0.133}}{\varepsilon(\theta)^{0.8}}$$

for the emulsion phase, and

$$\text{Nu}_{p,b} = \frac{\text{Re}_{p,mf}^{0.73}}{\text{Re}_p^{0.3}}$$

for the bubble phase. These correlations each predicted heat transfer coefficients for the conditions in the present work within $\pm 15\%$. They apply to the range of conditions investigated in the present work: $44,000 < \text{Ar} < 136,000$; $27 < \text{Re}_{mf} < 57$; $39 < \text{Re} < 72$; and $6.8 < \text{Pr} < 7.0$.

Investigation of Instantaneous Hydrodynamics and Heat Transfer to a Horizontal Tube
Immersed in a High-Temperature Gas-Solid Fluidized Bed of Large Particles

by

Marlene Mainland Burr

A THESIS

submitted to

Oregon State University

in partial fulfillment of
the requirements for the
degree of

Doctor of Philosophy

Completed March 16, 1998
Commencement June 1998

Doctor of Philosophy thesis of Marlene Mainland Burr presented on March 16, 1998

APPROVED:

Redacted for privacy

Major Professor, representing Mechanical Engineering

Redacted for privacy

Head of Department of Mechanical Engineering

Redacted for privacy

Dean of Graduate School

I understand that my thesis will become part of the permanent collection of Oregon State University libraries. My signature below authorizes release of my thesis to any reader upon request.

Redacted for privacy

Marlene Mainland Burr, Author

ACKNOWLEDGEMENTS

I would like to thank Dr. James R. Welty for his helpful, kind and intuitive discussions through the course of this research. His support and guidance throughout the entire duration of these studies is greatly appreciated.

I would also like to thank Dr. Robert Wilson, Dr. Dwight Bushnell, Dr. Jose Reyes, and Dr. Rakesh Gupta for serving on my doctoral committee.

My appreciation goes to Dr. Alan George of Montana State University for his work developing the optical probe and heat flux transducer hardware and his for input.

I am appreciative of the assistance of Dr. David Pidwerbecki for his help discussing and demonstrating the fluidized bed laboratory apparatus. I am also grateful for the mechanical and instrument support provided by Orrie Page and Ken McCracken, and the assistance provide by DyAnn McVicker, as well as the entire department.

The financial support in the form of graduate fellowships from the Department of Defense (National Defense Science and Engineering Graduate Fellowship Program), the Oregon Space Grant Fellowship Program, and the Department of Energy (Integrated Manufacturing Predoctoral Fellowship Program) is greatly appreciated.

Finally, and most importantly, I would like to thank my family for their patience, confidence and inspiration. I would like to thank my Mom for her never-ending encouragement and faith in me as well as for her friendship. This work is completed in honor of the memory of my Dad, who believed in and understood me; my Grandmothers; and my mother-in-law, Rita. My greatest appreciation and gratefulness go to my dear husband, Ron, for sharing, understanding and sticking with me through this journey. I look forward to our new life with our baby on the way.

TABLE OF CONTENTS

1. INTRODUCTION	1
1.1 Background	1
1.2 The Phenomena of Gas-Solid Fluidization	3
1.3 Previous Research	6
1.3.1 Particle Classification	7
1.3.2 Flow Regime Delineation	8
1.3.3 Bed Hydrodynamics and Bubble Modeling	11
1.3.4 Experimental Techniques for Bubble Detection	15
1.3.5 Heat transfer Models	18
1.3.6 Particle Convection	21
1.3.7 Gas Convection	22
1.3.8 Radiation	25
1.3.9 Heat Transfer Correlations and Data	27
1.3.10 Instantaneous Heat Transfer	30
1.3.11 Interaction of Hydrodynamics and Instantaneous Heat Transfer	33
1.4 Present Work	35
2. SENSORS AND EXPERIMENTAL APPARATUS	37
2.1 Optical Probe	37
2.1.1 Optical Probe Design	37
2.1.2 Probe Signal Processing Methodology	40
2.2 2D Bed Experiments	41
2.3 Optical Probe Signal Processing	43
2.4 Calculation of Bubble Properties	51
2.4.1 Bubble Frequency	51
2.4.2 Local Bubble Residence Time and Local Bubble Time Fraction	51
2.4.3 Bubble Velocity	53
2.4.4 Pierced Length	53
2.4.5 Characteristic Bubble Diameter	55
2.4.6 Visible Bubble Flow	59
2.4.7 Local Bubble Space Fraction	60

TABLE OF CONTENTS (Continued)

2.5 Instantaneous Heat Flux Sensor	60
2.5.1 Design and Principle of Operation of Heat Flux Transducer	63
2.5.2 Analog Signal Conditioning Unit	67
2.5.3 Calibration of β	71
2.5.4 Calibration of k/L	73
2.6 OSU High-Temperature Fluidized Bed Facility	76
2.6.1 Apparatus	76
2.6.2 Data Acquisition System	80
2.7 Experiments and Test Procedure	80
3. RESULTS AND DISCUSSION	85
3.1 Bubble Properties	85
3.1.1 Bubble Frequency	85
3.1.2 Bubble Velocity	87
3.1.3 Local Bubble Time Fraction	90
3.1.4 Local Bubble and Emulsion Residence Time	90
3.1.5 Bubble Diameter	92
3.1.6 Visible Bubble Flow	97
3.1.7 Bubble Property Correlations	97
3.2 Time-Average Heat Transfer Coefficients	100
3.2.1 Time- and Space-Average Heat Transfer Coefficients	100
3.2.2 Radiative Heat Transfer Coefficient	104
3.3 Time-Average Local Heat Transfer Coefficients	106
3.4 Instantaneous Local Heat Transfer Coefficients	108
3.4.1 Instantaneous Heat Transfer Coefficient Standard Deviation	164
3.4.2 Maximum and Minimum Heat Transfer Coefficients	170
3.4.3 Bubble and Emulsion Phase Frequency on the Tube	176
3.4.4 Average Bubble Residence Time on the Tube	180
3.4.5 Bubble Time Fraction on the Tube	183
3.5 Hydrodynamic and Heat Transfer Interaction	183
3.6 Heat Transfer Correlations	187
3.6.1 Emulsion Phase (Average Maximum Heat Transfer Coefficient)	191
3.6.2 Bubble Phase (Average Minimum Heat Transfer Coefficient)	195

TABLE OF CONTENTS (Continued)

4. CONCLUSIONS AND RECOMMENDATIONS	203
4.1 Conclusions	203
4.2 Recommendations	210
BIBLIOGRAPHY	213
APPENDIX	232

LIST OF FIGURES

<u>Figure</u>		<u>Page</u>
1.1	Flow regimes in fluidized beds.	4
1.2	Voidage distribution at a cylinder wall.	16
2.1	Schematic of optical probe.	38
2.2	OSU 2D fluidized bed facility.	42
2.3	Raw probe signal in 2D bed ($d_p=2.0$ mm, $U/U_{mf}=1.4$).	44
2.4	FFT of signal shown in Figure 2.3 ($d_p=2.0$ mm, $U/U_{mf}=1.4$).	45
2.5	Ideal and Second-order Butterworth filter.	47
2.6	Effect of first-stage filter on signal shown in Figure 2.3($d_p=2.0$ mm, $U/U_{mf}=1.4$).	48
2.7	Effect of first- and second- stage filter on signal shown in Figure 2.3 ($d_p=2.0$ mm, $U/U_{mf}=1.4$).	50
2.8	Comparison of observed and calculated local bubble residence time.	52
2.9	Comparison of observed and calculated average bubble velocity ($d_p=2$ mm, $U/U_{mf}=1.4$).	54
2.10	Comparison of observed and calculated pierced length ($d_p=2$ mm, $U/U_{mf}=1.4$).	56
2.11	Comparison of observed and calculated bubble diameter ($d_p=2$ mm, $U/U_{mf}=1.4$).	58
2.12	Eroding thermocouple, heat flux transducer, and instrumented cylinder.	64
2.13	Time response of heat flux transducer.	70
2.14	Equipment lay-out for calibration of β .	72

LIST OF FIGURES (Continued)

<u>Figure</u>		<u>Page</u>
2.15	Calibration results for β .	74
2.16	OSU High-temperature fluidized bed facility.	77
2.17	Schematic of test bed.	81
3.1	Bubble frequencies versus fluidization velocity ($d_p=2$ mm, optical probes 1 and 2 (op1 and op2)).	86
3.2	Bubble frequencies versus fluidization velocity ($d_p=2$ mm and 2.9 mm, optical probe 1 (op1)).	86
3.3	Comparison of measured bubble frequencies to other data.	88
3.4	Bubble velocities versus fluidization velocity ($d_p=2$ mm and 2.9 mm).	89
3.5	Bubble velocities versus dimensionless velocity ($d_p=2$ mm and 2.9 mm).	89
3.6	Local bubble time fraction versus fluidization velocity ($d_p=2$, optical probes 1 and 2 (op1 and op2)).	91
3.7	Local bubble time fraction versus excess velocity ($d_p=2$ mm and 2.9 mm, optical probe 1 (op1)).	91
3.8	Local bubble residence time versus excess velocity ($d_p=2$ mm and 2.9 mm, optical probe 1 (op1)).	93
3.9	Local emulsion residence time versus excess velocity ($d_p=2$ mm and 2.9 mm, optical probe 1 (op1)).	93
3.10	Pierced length distribution ($d_p=2$ mm, $U/U_{mf}=1.4$, $T_{bed}=600K$).	95
3.11	Bubble diameters versus fluidization velocity ($d_p=2$ mm and 2.9 mm).	95

LIST OF FIGURES (Continued)

<u>Figure</u>		<u>Page</u>
3.12	Bubble diameters versus excess velocity ($d_p = 2$ mm and 2.9 mm).	96
3.13	Visible bubble flow versus fluidization velocity ($d_p = 2$ mm and 2.9 mm).	96
3.14	Bubble velocity versus bubble diameter correlations ($d_p = 2$ mm and 2.9 mm).	99
3.15	Time- and space- averaged heat transfer coefficients ($d_p = 2$ mm and 2.9 mm).	101
3.16	Time- and space- averaged heat transfer coefficients compared to other experimental data (a) $T_{bed} = 700$ K, 900 K; (b) $T_{bed} = 800$ K, 1000 K.	102
3.17	Radiative contribution to the heat transfer coefficient from Pidwerbecki (1994).	105
3.18	Time-averaged local heat transfer coefficients versus circumferential location (a) 600 K, (b) 700K, (c) 800 K, (d) 900 K and (e) 1000 K.	107
3.19	Instantaneous local heat transfer coefficients ($T_{bed} = 600$ K, $d_p = 2$ mm, $U = 1.69$ m/s).	111
3.20	Instantaneous local heat transfer coefficients ($T_{bed} = 600$ K, $d_p = 2$ mm, $U = 1.77$ m/s).	112
3.21	Instantaneous local heat transfer coefficients ($T_{bed} = 600$ K, $d_p = 2$ mm, $U = 1.85$ m/s).	113
3.22	Instantaneous local heat transfer coefficients ($T_{bed} = 700$ K, $d_p = 2$ mm, $U = 1.80$ m/s).	114
3.23	Instantaneous local heat transfer coefficients ($T_{bed} = 700$ K, $d_p = 2$ mm, $U = 2.00$ m/s).	115
3.24	Instantaneous local heat transfer coefficients ($T_{bed} = 700$ K, $d_p = 2$ mm, $U = 2.16$ m/s).	116

LIST OF FIGURES (Continued)

<u>Figure</u>		<u>Page</u>
3.25	Instantaneous local heat transfer coefficients ($T_{\text{bed}} = 800 \text{ K}$, $d_p = 2 \text{ mm}$, $U = 1.71 \text{ m/s}$).	117
3.26	Instantaneous local heat transfer coefficients ($T_{\text{bed}} = 800 \text{ K}$, $d_p = 2 \text{ mm}$, $U = 2.11 \text{ m/s}$).	118
3.27	Instantaneous local heat transfer coefficients ($T_{\text{bed}} = 800 \text{ K}$, $d_p = 2 \text{ mm}$, $U = 2.48 \text{ m/s}$).	119
3.28	Instantaneous local heat transfer coefficients ($T_{\text{bed}} = 900 \text{ K}$, $d_p = 2 \text{ mm}$, $U = 1.91 \text{ m/s}$).	120
3.29	Instantaneous local heat transfer coefficients ($T_{\text{bed}} = 900 \text{ K}$, $d_p = 2 \text{ mm}$, $U = 2.21 \text{ m/s}$).	121
3.30	Instantaneous local heat transfer coefficients ($T_{\text{bed}} = 900 \text{ K}$, $d_p = 2 \text{ mm}$, $U = 2.52 \text{ m/s}$).	122
3.31	Instantaneous local heat transfer coefficients ($T_{\text{bed}} = 900 \text{ K}$, $d_p = 2 \text{ mm}$, $U = 2.74 \text{ m/s}$).	123
3.32	Instantaneous local heat transfer coefficients ($T_{\text{bed}} = 1000 \text{ K}$, $d_p = 2 \text{ mm}$, $U = 2.26 \text{ m/s}$).	124
3.33	Instantaneous local heat transfer coefficients ($T_{\text{bed}} = 1000 \text{ K}$, $d_p = 2 \text{ mm}$, $U = 2.50 \text{ m/s}$).	125
3.34	Instantaneous local heat transfer coefficients ($T_{\text{bed}} = 1000 \text{ K}$, $d_p = 2 \text{ mm}$, $U = 2.82 \text{ m/s}$).	126
3.35	Instantaneous local heat transfer coefficients ($T_{\text{bed}} = 1000 \text{ K}$, $d_p = 2 \text{ mm}$, $U = 3.03 \text{ m/s}$).	127
3.36	Instantaneous local heat transfer coefficients ($T_{\text{bed}} = 600 \text{ K}$, $d_p = 2 \text{ mm}$, $\theta = 180^\circ$).	128
3.37	Instantaneous local heat transfer coefficients ($T_{\text{bed}} = 600 \text{ K}$, $d_p = 2 \text{ mm}$, $\theta = 135^\circ$).	129

LIST OF FIGURES (Continued)

<u>Figure</u>		<u>Page</u>
3.38	Instantaneous local heat transfer coefficients ($T_{\text{bed}} = 600 \text{ K}$, $d_p = 2 \text{ mm}$, $\theta = 90^\circ$).	130
3.39	Instantaneous local heat transfer coefficients ($T_{\text{bed}} = 600 \text{ K}$, $d_p = 2 \text{ mm}$, $\theta = 45^\circ$).	131
3.40	Instantaneous local heat transfer coefficients ($T_{\text{bed}} = 600 \text{ K}$, $d_p = 2 \text{ mm}$, $\theta = 0^\circ$).	132
3.41	Instantaneous local heat transfer coefficients ($T_{\text{bed}} = 700 \text{ K}$, $d_p = 2 \text{ mm}$, $\theta = 180^\circ$).	133
3.42	Instantaneous local heat transfer coefficients ($T_{\text{bed}} = 700 \text{ K}$, $d_p = 2 \text{ mm}$, $\theta = 135^\circ$).	134
3.43	Instantaneous local heat transfer coefficients ($T_{\text{bed}} = 700 \text{ K}$, $d_p = 2 \text{ mm}$, $\theta = 90^\circ$).	135
3.44	Instantaneous local heat transfer coefficients ($T_{\text{bed}} = 700 \text{ K}$, $d_p = 2 \text{ mm}$, $\theta = 45^\circ$).	136
3.45	Instantaneous local heat transfer coefficients ($T_{\text{bed}} = 700 \text{ K}$, $d_p = 2 \text{ mm}$, $\theta = 0^\circ$).	137
3.46	Instantaneous local heat transfer coefficients ($T_{\text{bed}} = 800 \text{ K}$, $d_p = 2 \text{ mm}$, $\theta = 180^\circ$).	138
3.47	Instantaneous local heat transfer coefficients ($T_{\text{bed}} = 800 \text{ K}$, $d_p = 2 \text{ mm}$, $\theta = 135^\circ$).	139
3.48	Instantaneous local heat transfer coefficients ($T_{\text{bed}} = 800 \text{ K}$, $d_p = 2 \text{ mm}$, $\theta = 90^\circ$).	140
3.49	Instantaneous local heat transfer coefficients ($T_{\text{bed}} = 800 \text{ K}$, $d_p = 2 \text{ mm}$, $\theta = 45^\circ$).	141
3.50	Instantaneous local heat transfer coefficients ($T_{\text{bed}} = 800 \text{ K}$, $d_p = 2 \text{ mm}$, $\theta = 0^\circ$).	142

LIST OF FIGURES (Continued)

<u>Figure</u>		<u>Page</u>
3.51	Instantaneous local heat transfer coefficients ($T_{\text{bed}} = 900 \text{ K}$, $d_p = 2 \text{ mm}$, $\theta = 180^\circ$).	143
3.52	Instantaneous local heat transfer coefficients ($T_{\text{bed}} = 900 \text{ K}$, $d_p = 2 \text{ mm}$, $\theta = 135^\circ$).	144
3.53	Instantaneous local heat transfer coefficients ($T_{\text{bed}} = 900 \text{ K}$, $d_p = 2 \text{ mm}$, $\theta = 90^\circ$).	145
3.54	Instantaneous local heat transfer coefficients ($T_{\text{bed}} = 900 \text{ K}$, $d_p = 2 \text{ mm}$, $\theta = 45^\circ$).	146
3.55	Instantaneous local heat transfer coefficients ($T_{\text{bed}} = 900 \text{ K}$, $d_p = 2 \text{ mm}$, $\theta = 0^\circ$).	147
3.56	Instantaneous local heat transfer coefficients ($T_{\text{bed}} = 1000 \text{ K}$, $d_p = 2 \text{ mm}$, $\theta = 180^\circ$).	148
3.57	Instantaneous local heat transfer coefficients ($T_{\text{bed}} = 1000 \text{ K}$, $d_p = 2 \text{ mm}$, $\theta = 135^\circ$).	149
3.58	Instantaneous local heat transfer coefficients ($T_{\text{bed}} = 1000 \text{ K}$, $d_p = 2 \text{ mm}$, $\theta = 90^\circ$).	150
3.59	Instantaneous local heat transfer coefficients ($T_{\text{bed}} = 1000 \text{ K}$, $d_p = 2 \text{ mm}$, $\theta = 45^\circ$).	151
3.60	Instantaneous local heat transfer coefficients ($T_{\text{bed}} = 1000 \text{ K}$, $d_p = 2 \text{ mm}$, $\theta = 0^\circ$).	152
3.61	Instantaneous local heat transfer coefficient, Shape 1 ($T_{\text{bed}} = 1000 \text{ K}$, $d_p = 2 \text{ mm}$, $\theta = 0^\circ$, $U = 2.82 \text{ m/s}$).	156
3.62	Instantaneous local heat transfer coefficient, Shape 2 ($T_{\text{bed}} = 800 \text{ K}$, $d_p = 2 \text{ mm}$, $\theta = 180^\circ$, $U = 2.11 \text{ m/s}$).	156
3.63	Instantaneous local heat transfer coefficient, Shape 3 ($T_{\text{bed}} = 900 \text{ K}$, $d_p = 2 \text{ mm}$, $\theta = 0^\circ$, $U = 2.52 \text{ m/s}$).	158

LIST OF FIGURES (Continued)

<u>Figure</u>		<u>Page</u>
3.64	Instantaneous local heat transfer coefficient, Shape 4 ($T_{bed}=900K$, $d_p=2$ mm, $\theta = 45^\circ$, $U=1.91$ m/s).	158
3.65	Instantaneous local heat transfer coefficient, Shape 5 ($T_{bed}=600K$, $d_p=2$ mm, $\theta = 135^\circ$, $U=1.85$ m/s).	160
3.66	Instantaneous local heat transfer coefficient, Shape 6 ($T_{bed}=700K$, $d_p=2$ mm, $\theta = 90^\circ$, $U=1.81$ m/s).	160
3.67	Instantaneous local heat transfer coefficient, Shape 7 (a) ($T_{bed}=800K$, $d_p=2$ mm, $\theta = 180^\circ$, $U=2.11$ m/s); (b) ($T_{bed}=900K$, $d_p=2$ mm, $\theta = 90^\circ$, $U=2.74$ m/s).	162
3.68	Instantaneous local heat transfer coefficient, Shape 8 (a) ($T_{bed}=800K$, $d_p=2$ mm, $\theta = 180^\circ$, $U=1.71$ m/s); (b) ($T_{bed}=900K$, $d_p=2$ mm, $\theta = 0^\circ$, $U=1.71$ m/s).	163
3.69	Standard deviation of instantaneous heat transfer coefficient versus θ ($T_{bed}=600K$, $d_p=2$ mm).	165
3.70	Standard deviation of instantaneous heat transfer coefficient versus θ ($T_{bed}=700K$, $d_p=2$ mm).	165
3.71	Standard deviation of instantaneous heat transfer coefficient versus θ ($T_{bed}=800K$, $d_p=2$ mm).	166
3.72	Standard deviation of instantaneous heat transfer coefficient versus θ ($T_{bed}=900K$, $d_p=2$ mm).	166
3.73	Standard deviation of instantaneous heat transfer coefficient versus θ ($T_{bed}=1000K$, $d_p=2$ mm).	167
3.74	Standard deviation of instantaneous heat transfer coefficient versus U/U_{mf} ($\theta = 0^\circ$, $d_p=2$ mm).	167
3.75	Standard deviation of instantaneous heat transfer coefficient versus U/U_{mf} ($\theta = 45^\circ$, $d_p=2$ mm).	168

LIST OF FIGURES (Continued)

<u>Figure</u>		<u>Page</u>
3.76	Standard deviation of instantaneous heat transfer coefficient versus U/U_{mf} ($\theta = 90^\circ$, $d_p=2$ mm).	168
3.77	Standard deviation of instantaneous heat transfer coefficient versus U/U_{mf} ($\theta = 135^\circ$, $d_p=2$ mm).	169
3.78	Standard deviation of instantaneous heat transfer coefficient versus U/U_{mf} ($\theta = 180^\circ$, $d_p=2$ mm).	169
3.79	Average maximum, average, and average minimum heat transfer coefficient versus θ ($T_{bed}=600K$, $d_p=2$ mm).	171
3.80	Average maximum, average, and average minimum heat transfer coefficient versus θ ($T_{bed}=700K$, $d_p=2$ mm).	171
3.81	Average maximum, average, and average minimum heat transfer coefficient versus θ ($T_{bed}=800K$, $d_p=2$ mm).	172
3.82	Average maximum, average, and average minimum heat transfer coefficient versus θ ($T_{bed}=900K$, $d_p=2$ mm).	172
3.83	Average maximum, average, and average minimum heat transfer coefficient versus θ ($T_{bed}=1000K$, $d_p=2$ mm).	173
3.84	Δh_{max} and Δh_{min} versus U ($\theta = 0^\circ$ $d_p=2$ mm).	173
3.85	Δh_{max} and Δh_{min} versus U ($\theta = 45^\circ$ $d_p=2$ mm).	174
3.86	Δh_{max} and Δh_{min} versus U ($\theta = 90^\circ$ $d_p=2$ mm).	174
3.87	Δh_{max} and Δh_{min} versus U ($\theta = 135^\circ$ $d_p=2$ mm).	175
3.88	Δh_{max} and Δh_{min} versus U ($\theta = 180^\circ$ $d_p=2$ mm).	175
3.89	Bubble frequency on tube versus U/U_{mf} ($\theta = 0^\circ$, $d_p=2$ mm).	177
3.90	Bubble frequency on tube versus U/U_{mf} ($\theta = 45^\circ$, $d_p=2$ mm).	177
3.91	Bubble frequency on tube versus U/U_{mf} ($\theta = 90^\circ$, $d_p=2$ mm).	178

LIST OF FIGURES (Continued)

<u>Figure</u>		<u>Page</u>
3.92	Bubble frequency on tube versus U/U_{mf} ($\theta = 135^\circ$, $d_p=2$ mm).	178
3.93	Bubble frequency on tube versus U/U_{mf} ($\theta = 180^\circ$, $d_p=2$ mm).	179
3.94	Average bubble residence time on tube versus U/U_{mf} ($\theta = 0^\circ$, $d_p=2$ mm).	179
3.95	Average bubble residence time on tube versus U/U_{mf} ($\theta = 45^\circ$, $d_p=2$ mm).	181
3.96	Average bubble residence time on tube versus U/U_{mf} ($\theta = 90^\circ$, $d_p=2$ mm).	181
3.97	Average bubble residence time on tube versus U/U_{mf} ($\theta = 135^\circ$, $d_p=2$ mm).	182
3.98	Average bubble residence time on tube versus U/U_{mf} ($\theta = 180^\circ$, $d_p=2$ mm).	182
3.99	Bubble time fraction on tube versus U/U_{mf} ($\theta = 0^\circ$ $d_p=2$ mm).	184
3.100	Bubble time fraction on tube versus U/U_{mf} ($\theta = 45^\circ$ $d_p=2$ mm).	184
3.101	Bubble time fraction on tube versus U/U_{mf} ($\theta = 90^\circ$ $d_p=2$ mm).	185
3.102	Bubble time fraction on tube versus U/U_{mf} ($\theta = 135^\circ$ $d_p=2$ mm).	185
3.103	Bubble time fraction on tube versus U/U_{mf} ($\theta = 180^\circ$ $d_p=2$ mm).	186
3.104	Relationship between bubble arrival and magnitude of heat transfer coefficient on tube.	186
3.105	Comparison of measured emulsion phase (average maximum) heat transfer coefficients to values predicted by various correlations.	192
3.106	Void fraction dependence on θ .	194

LIST OF FIGURES (Continued)

<u>Figure</u>		<u>Page</u>
3.107	Comparison of measured emulsion phase (average maximum) heat transfer coefficients to correlation developed in the present work ($\theta = 0^\circ$).	196
3.108	Comparison of measured emulsion phase (average maximum) heat transfer coefficients to correlation developed in the present work ($\theta = 45^\circ$).	196
3.109	Comparison of measured emulsion phase (average maximum) heat transfer coefficients to correlation developed in the present work ($\theta = 90^\circ$).	197
3.110	Comparison of measured emulsion phase (average maximum) heat transfer coefficients to correlation developed in the present work ($\theta = 135^\circ$).	197
3.111	Comparison of measured emulsion phase (average maximum) heat transfer coefficients to correlation developed in the present work ($\theta = 180^\circ$).	198
3.112	Comparison of measured bubble phase (average minimum) heat transfer coefficients to correlation developed in the present work.	199
3.113	Comparison of measured bubble phase (average minimum) heat transfer coefficients to correlation developed in the present work.	201

LIST OF APPENDIX FIGURES

<u>Figure</u>		<u>Page</u>
A.1	Analog conditioning circuit representing transfer function.	233
A.2	Signal conditioning circuit associated with heat flux sensor (Smalley, 1990).	234

NOTATION

a	variable defined by Equation 3.19
a_1	constant used in Equation 2.15
A	variable defined by Equation 3.20
A_{bed}	cross-sectional area of bed
A_{bub}	area of observed bubble
Ar	Archimedes number = $\frac{gd_p^3(\rho_s - \rho_g)}{\rho_g v_g^2}$
$c_{p,g}, c_{p,p}, c_{p,s}$	specific heat of gas, specific heat of particle, specific heat of solid
d	bubble diameter
d_{char}	characteristic bubble diameter (calculated)
d_{eq}	equivalent bubble diameter of observed bubble
d_p	diameter of particle
D_T	diameter of tube
$\bar{e}(s), e(j\omega)$	Laplace transfer functions used in Equations 2.12 and 2.13
f, f_b, f_e	frequency, bubble phase frequency, emulsion phase frequency
$f(d)$	bubble diameter probability density function
g	gravitational constant
$h, h(t)$	heat transfer coefficient
h_b	bubble phase heat transfer coefficient
h_{bgc}	bubble phase gas convective heat transfer coefficient

h_{br}	bubble phase radiative heat transfer coefficient
h_e	emulsion phase heat transfer coefficient
h_{egc}	emulsion phase gas convective heat transfer coefficient
h_{er}	emulsion phase radiative heat transfer coefficient
h_{pc}	emulsion phase particle convective heat transfer coefficient
h_r	radiative heat transfer coefficient
$H(s), H(\omega)$	transfer function for low-pass filter
k_g, k_s, k_s	thermal conductivity of gas, thermal conductivity of solid, thermal conductivity of gas
L	distance between two points of temperature measurement; also average bubble length
L_m, L_{mf}, L_f	height of fixed bed, bed at minimum fluidization, and bubbling fluidized bed, respectively.
Nu, Nu_p	Nusselt number, $= \frac{hd}{k_g}$
$Nu_{p,b}$	Nusselt number for bubble phase
$Nu_{p,e}$	Nusselt number for emulsion phase
$Nu_{p,e,gc}, Nu_{p,e,pc}$	Nusselt number for emulsion phase particle convection, emulsion phase particle convection
Pr	Prandtl number, $= \frac{c_{p,g} \mu_g}{k_g}$
$q_s(t)$	heat flux at surface of tube
Q_b	visible bubble volumetric flow

Re_p	particle Reynolds number, $= \frac{\rho_g U d_p}{\mu_g}$
$Re_{p,mf}$	Reynolds number at minimum fluidization, $\frac{\rho_g U_{mf} d_p}{\mu_g}$
R_n	radius of curvature of nose of a bubble
s	$j\omega/\omega_{cut}$
S	constant defined in Equation 2.7
t_{cc}	time lag between upper and lower probe signals
t_{ccho}	time lag between heat transfer and optical probe signals
t_{path}	calculated time lag for bubble travel from optical probe to heat transfer surface
T_{bed}	bed temperature
T_i	temperature at interior of tube
T_s	tube surface temperature
T	bed thickness; also, temperature
u, U	fluidization velocity
u_b, U_b	rise velocity of bubble
u_{mf}, U_{mf}	minimum fluidization velocity
$\bar{v}(s), v(j\omega)$	Laplace transfer functions used in Equations 2.14 and 2.15
$v_2(t), \langle v_2 \rangle$	heat flux analog signal conditioning unit output signal, average of output signal
V	average bubble velocity
V_{cut}	cut-off voltage for second stage filter

V_{\max}	maximum value of first-stage-filtered data
V_{\min}	minimum value of first-stage-filtered data
W	bed width
y	pierced length variable for ϕ
\bar{y}	average pierced length for a randomly pierced circular bubble

Greek Letters

α	constant used in Equation 3.5
β	calibration constant for instantaneous heat transfer coefficient; also time fraction that the tube is in contact with bubbles
β_1	constant used in equation 2.15
δ	bubble phase space fraction; (emulsion phase space fraction = 1- δ)
$\bar{\epsilon}, \epsilon, \epsilon_w$	void fraction, void fraction in the bulk of the bed, void fraction at tube wall
$\epsilon_e, \epsilon_f, \epsilon_m, \epsilon_{mf}$	void fraction in the emulsion phase, void fraction in a fluidized bed as a whole, void fraction in a fixed bed, void fraction in a bed at minimum fluidization velocity
$\epsilon_b, \epsilon_{bs}, \epsilon_p, \epsilon_s$	emissivity of bed, effective bed and surface, particle, and tube surface
$\phi(y)$	pierced length probability density function
$\phi'(y)$	derivative of $\phi(y)$ with respect to y
μ_g	absolute viscosity of gas
ρ_g, ρ_p, ρ_s	density of gas, density of particle, density of solid
$\tau_b, \bar{\tau}_b$	bubble residence time, average bubble residence time
$\tau_e, \bar{\tau}_e$	emulsion residence time, average emulsion residence time
ν_g	kinematic viscosity of gas

ω

frequency

ω_{cut}

cut-off frequency for first-stage (low-pass) filter

AN INVESTIGATION OF INSTANTANEOUS HYDRODYNAMICS AND HEAT TRANSFER TO A HORIZONTAL TUBE IMMERSED IN A HIGH-TEMPERATURE GAS-SOLID FLUIDIZED BED OF LARGE PARTICLES

1. INTRODUCTION

1.1 Background

Fluidization is described as the process in which particles behave in a fluid-like manner due to their suspension in a gas or liquid. Gas-solid fluidized beds are useful for operations involving solid-fluid contact whenever high rates of heat and mass transfer between solid and fluid are required. Industrial applications of fluidized beds are widespread. Among the first uses of fluidized beds were a coal gasifier, which first went into operation in 1926 (Kunii and Levenspiel, 1991), and catalytic cracking for the production of high-octane aviation gasoline during World War II. Further developments in fluidized bed technology resulted in the use of fluidized beds for catalytic cracking, production of gasoline from natural and synthesis gases, synthesis reactions, and metallurgical processes such as the roasting of sulfide ores. From these beginnings, fluidized beds have found many applications. Modern applications include the production of polymers, the production of ultrapure silicon for the semiconductor industry, and a variety of uses in the food and pharmaceutical industries (coffee bean roasters and pill-making, for example), and for treatment of radioactive waste. Among

the physical mechanisms in these applications are the solidification of a melt to make granules, the coating of objects, drying of solids, particle growth, adsorption, synthesis gas production, catalytic cracking, fluid coking, thermal cracking, and heat exchange.

One heat exchange application of interest to the present work is fluidized bed combustion. Low-grade (high-sulfur content) coal can be used for power production in an environmentally acceptable way by burning the coal in a bed of limestone or dolomite particles which adsorb sulfur oxides, which are the primary constituents of acid rain. Thus, the operation can comply with air-quality standards without expensive and potentially unreliable stack-gas cleaning equipment. Additionally, the dynamic character of fluidization results in relatively high heat transfer rates, thereby achieving significant energy transfer between a combusting bed and an internal water-carrying tube at lower temperature differences than would otherwise be necessary. This low temperature operation (~ 850 °C) also inhibits the formation of nitrogen oxides which play a major role in smog formation. Also, the higher heat transfer rate reduces the necessary size of the heat exchanger which results in reduced cost. Disadvantages of fluidized bed coal combustion include processing the sulfur-laden particles and the abrasive effects of the particles. Fluidized bed coal combustion generally involves large particles (>1 mm) and it is this application that is considered in the present work. Considerable research has been reported on pilot-scale fluidized bed combustors (Skinner, 1971; Leon et al., 1979; Goblirsch et al., 1980; Golan and Cherrington, 1981; Doss et al., 1984; Carson et al., 1991). The current work focuses on the fundamental mechanisms of hydrodynamics and

heat transfer to an immersed horizontal tube in a high-temperature fluidized bed which simulates these fluidized bed combustors.

1.2 The Phenomena of Gas-Solid Fluidization

When fluid is passed through a bed of particles at low velocities, the bed is fixed and the fluid passes through the spaces or voids between the particles. As the gas velocity increases, a point is reached where the drag force on each particle equals the weight of the particle, and the particle is then fluidized and the bed is said to be at minimum fluidization. As the fluidizing velocity in the bed is increased above the minimum fluidization velocity, voids or "bubbles" form and pass upward through the bed and the bed is called a bubbling fluidized bed. As the fluidizing velocity is further increased, the bed passes through stages of slugging, then turbulent fluidization and finally pneumatic transport where the particles are actually carried out of the bed. A schematic of these flow regimes is shown in Figure 1.1. Non-circulating fluidized bed coal combustors generally operate in the bubbling and slugging regimes.

When in the fluidized state, a bed has many interesting and useful properties. The gas-solid mixture behaves as a liquid, which allows easy handling and transport and close contact between fluid and gas. The rapid mixing of solids allows for near isothermal conditions in the bed, and the rates of heat and mass transfer between gas and particles or to an immersed surface are high. Some of the disadvantages of fluidized beds include the fact that the stochastic nature of the bed makes extensive modeling of bed characteristics based on first principles unrealizable at this time. The abrasive nature

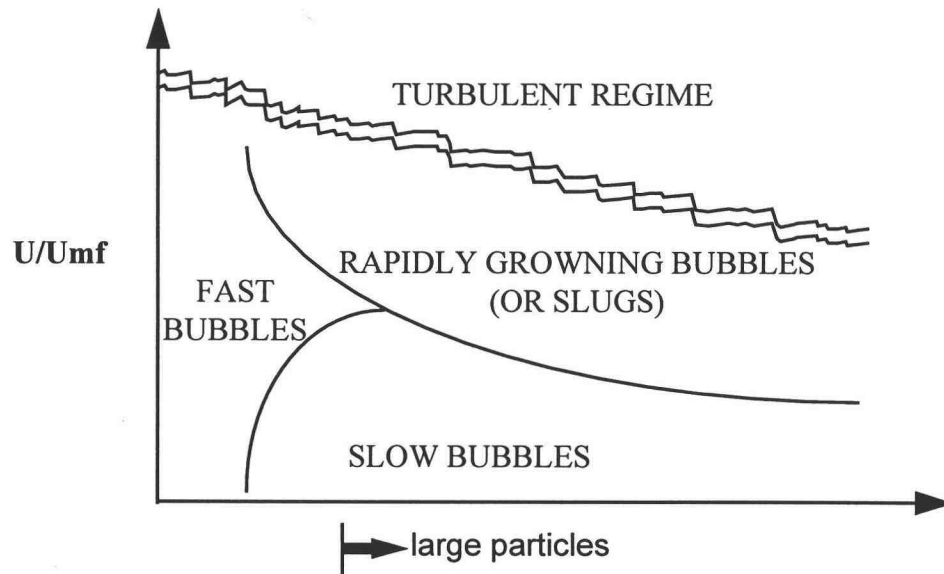
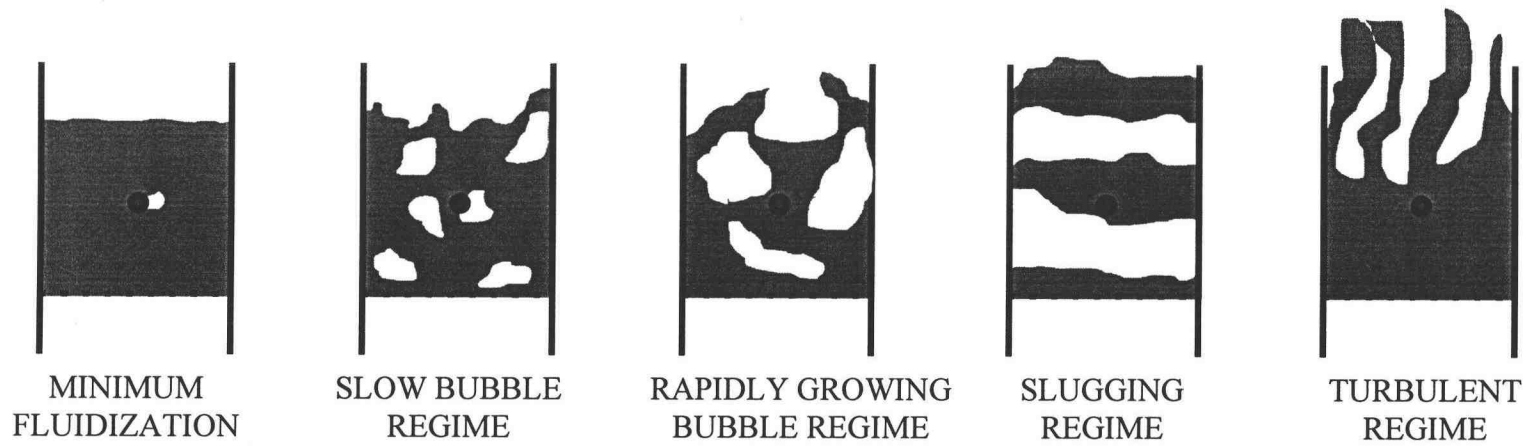


Figure 1.1 Flow regimes in fluidized beds.

of the bed leads to pipe and vessel erosion. Levy and Stallings (1991) conducted an experimental and theoretical investigation on tube erosion of horizontal tubes in a bubbling bed and found that erosion is caused by the impact of bubble wakes on the tube. Erosion rates increased with particle size due to increased bubble wake velocity. Erosion rates in a fluidized bed boiler were found to be as high as 0.001 mm/hr during a limited 1210 hour study by Leckner and Hogberg (1984). Also, bubbling and slugging can represent inefficient and unpredictable contact.

For the case of fluidized bed coal combustion, enhanced heat transfer results from the ability of fluidized beds to provide overall temperature uniformity, good particle mixing and good particle contact with an immersed surface. Bubbles cause rapid exchange of bed material between the region adjacent to the immersed surface and the bulk of the bed, allowing for continuous renewal of hot particles near the immersed surface. Bubbles are also responsible for inducing large-scale particle circulation and mixing which is advantageous for heat transfer (Botterill, 1975). Efficient heat transfer is obtained by uniform bubble distribution throughout the bed. In the case of removing solvents from air, however, bubbles create a path of least resistance by which air can bypass the dense phase, thereby reducing contact time with adsorbing particles. The detection and characterization of bubble behavior is therefore important in understanding fluidized bed performance. The heat transfer to an immersed surface such as a tube carrying water or steam is intimately related to bed hydrodynamics. Both average and instantaneous heat transfer information are necessary to understand, model and optimize fluidized bed operation. Fluctuations in the local, instantaneous value of the heat

transfer coefficient, caused by passage of bubbles or the formation of a stack of particles on the top of a horizontal tube, may give rise to thermal cycling, stresses, fatigue and even corrosion of the tube material (Glicksman et al., 1978).

1.3 Previous Research

Analytical, numerical, and experimental methods have been used to study fluidized bed characteristics. Extensive reviews of literature in the field of fluidization are available, including those given by Saxena (1989), Saxena et al. (1978), Gutfinger and Abuaf (1974), and Gelperin and Ainstein (1971). Most applications of fluidized bed technology, such as catalytic reactions, use relatively small particles (<1 mm). As a result of this, research has traditionally focused on small particles. Large particles, however, are used in many processes such as coal combustion and waste incineration. Of particular relevance to the present work is research conducted in large-particle, high-temperature fluidized beds which has concentrated on bed hydrodynamics and time-average and instantaneous, space-average and local heat transfer to horizontal tubes immersed in the bed. Many experiments have been conducted in two-dimensional (2D) fluidized beds to either validate tools and techniques or contribute to the general understanding of bed operation. Two-dimensional beds are generally constructed such that the height and width of the bed are large compared to the depth and are often constructed of materials such as Plexiglas so that phenomena such as bubbles can be directly observed. The term '2D' is somewhat of a misnomer since these '2D' beds are not two-dimensional representations of three-dimensional (3D) beds.

1.3.1 Particle Classification

Geldart (1973) observed particles of various composition and size and came up with four kinds of particle behavior which he classified as follows:

Group A: aeratable particles having a relatively low particle density. These particles fluidize easily with considerable bed expansion.

Group B: sand-like particles. Beds bubble vigorously and the majority of fluidized bed applications use particles in this group. These are the particles generally called 'small particles'.

Group C: very fine powders. Interparticle forces are greater than those resulting from the action of gas making normal fluidization extremely difficult.

Group D: large and/or dense particles. Fluidized beds of these particles tend to behave erratically. They have some undesirable properties such as being spoutable and requiring enormous amounts of gas to fluidize. In many applications, however, this particle size cannot be avoided. These are the particles generally called 'large particles'.

Jovanovic and Catipovic (1983) developed a new criterion for classifying solids in bubbling gas-fluidized beds. Particles were distinguished as small (fine) or large (coarse) based on their heat transfer and fluid dynamic characteristics. A different powder classification scheme for fluidized beds based on the Archimedes number, a dimensionless group which is based on the ratio of the weight of a particle to the drag force on a particle ($Ar = gd^3(\rho_s - \rho_g)/\rho_g v_g^2$). This was proposed by Saxena and Ganzha

(1984) and also considers, simultaneously, the hydrodynamic and thermal properties. This classification is primarily based on whether the boundary layer around the particles is laminar or turbulent. For a bed of small particles when the fluid flow is laminar (Group I), the criterion is

$$Ar \leq 1600 \quad (1.1)$$

while for a bed of large particles when fully developed turbulent flow exists (Group III), the condition is

$$Ar \geq 1.6 \times 10^6 \quad (1.2)$$

A third transitional group is proposed for $1600 \leq Ar \leq 1.6 \times 10^6$ which is divided into two parts. An extended laminar flow regime (Group IIA) is defined such that

$$1600 \leq Ar \leq 21700 \quad (1.3)$$

and the modified transitional group (Group IIB) is specified by

$$21700 \leq Ar \leq 1.6 \times 10^6 \quad (1.4)$$

For the conditions investigated in the current work, the particles are classified as Group D in the Geldart scheme and Groups IIA and IIB in the Saxena and Ganzha scheme.

1.3.2 Flow Regime Delineation

Catipovic et al. (1978) developed criteria for distinguishing between gas-solid fluidized bed flow regimes. They described the following regimes: a fast bubble regime where $u < u_b$ (typical of small particle bubbling beds); a slow bubble regime where $u > u_b$ (typical of large particle bubbling beds); a rapidly growing bubble regime where the

bubble growth rate is the same magnitude as the bubble rise velocity (found in large particle shallow beds at higher u); and the turbulent regime which occurs at relatively higher u . Mei et al. (1991) studied flow regime transition for large particles using void fraction and pressure fluctuation data. They were able to detect transition from slugging to pneumatic transport regimes. Saxena and Rao (1993) used pressure and temperature time series to determine void phase renewal frequencies for flow regime delineation. Ni and Moslemian (1993) studied statistical properties of a pressure fluctuation time series and studied the relation of these parameters to bed operating conditions. Qian et al (1993) measured instantaneous heat transfer coefficients to a horizontal tube immersed in a bed of 2.19 mm particles at 1013 °C. They present some representative results and discuss their use for identification of flow regimes.

In recent years, it has been shown that the dynamic behavior of fluidized beds can be characterized using quantitative measures from deterministic chaos theory. Possible applications of chaos are regime delineation, dimensionless scaling of fluidized beds, and the development of more effective mathematical models and control strategies. The approach is basically a non-linear time series analysis and can be used as an alternative to Fourier-type analyses, which can be limited by the inherent assumptions in the technique. For example, from the power spectra, peak frequencies can be determined, but their interpretation can be limited due to the fact that characteristic bed time-series are broad-band in nature. Flow regime classification is expressed in qualitative terms as “broad-banded” or “sharp” spectra, and “higher” and “lower” frequencies.

Deterministic chaos, however, can provide some quantitative information. Any characteristic time series such as pressure, voidage, heat flux or temperature can be used (Stringer, 1989). The time series is first remapped into a new coordinate system, a process known as 'embedding' and is based on Takens embedding theorem (Takens, 1980). The result is a 'state trajectory' or 'phase portrait'. The eigenvectors of this system define the embedding dimension. Detailed discussion of this technique is available in Broomhead and King (1986), Grassberger and Procaccia (1983), Daw et al. (1990), Daw and Halow (1991) and Tam and Devine (1992). The trajectory remains confined to a subregion of the embedding space over time if it is ergodic and is then said to be following an 'attractor'. Any ergodic dynamic system will have an attractor, but only chaotic systems will have 'strange' attractors. If the attractor is indeed strange, it will have distinctive characteristics that can be used to confirm the presence of chaos and quantify its features. Two commonly used measurements used to detect strange attractors are the correlation dimension and the Kolmogorov entropy. The correlation dimension is a measure for the number of degrees of freedom of the system and will be nonintegral (fractal) for strange attractors. The Kolmogorov entropy represents the rate of memory loss in the system due to chaos and is therefore a measure of the predictability of a system. The values of these numbers change at transitions between flow regimes (Stappen et al., 1992). The shape and size of the trajectory plots can also be used to distinguish between flow regimes, as demonstrated by Daw and Halow (1991). Fuller et al. (1993) continued the work of Daw and Halow and applied chaotic time series analysis to a pilot-scale fluidized bed combustor and developed a new index as

well as standards for acquiring time series. Stappen et al. (1993) applied deterministic chaos theory to both measured time series of pressure fluctuations and simulated ones of overall voidage from their particle array model. The model was able to reproduce the chaotic characteristics calculated from the measured time series accurately. Skrzycke et al. (1993) demonstrated that chaotic time series analysis can be used to distinguish between the behavior of fluidizing particles belonging to different Geldart groups.

Research conducted by Schouten and Bleek (1991 and 1992) and Bleek and Schouten (1993) has shown progress in using deterministic chaos for scaling of fluidized beds. They found, for instance, that a non-dimensional Kolmogorov entropy should be used to assess the dynamic similarity of scaled fluidized-bed reactors. Daw and Halow (1993) further investigated the use of chaotic features in determining the type of fluidization and suggest how this information can be used for implementing closed-loop control of bed hydrodynamics. Deterministic chaos time series analysis continues to be an area of active research with promising applications in the areas of flow regime determination, scale-up and control.

1.3.3 Bed Hydrodynamics and Bubble Modeling

Due to the stochastic nature of a bubbling bed, it is difficult to achieve meaningful information based on first principles, and most of the reliable information about bubbles is empirical in nature. Progress in the area of hydrodynamic equations for fluidized beds have been accomplished by several researchers (O'Brien et al., 1993; Jackson, 1963). The earliest view of the bubbling bed was given by the 'two-phase'

theory of fluidization proposed by Toomey and Johnstone (1952). In this theory, all gas flow in excess of the minimum fluidization velocity, u_{mf} , thus $u - u_{mf}$, passed through the bed as bubbles. Thus the visible bubble flow, which is defined as the rate at which bubble volume crosses any level in the bed, was equal to the excess gas flow. Additionally, the theory states that the emulsion phase (the particulate phase) remained at minimum fluidization conditions, except when moving aside to let bubbles through. In practice, numerous experimental investigations have shown that the situation is more complex than as viewed by this model. The visible bubble flow, for example, has been reported to be on the order of 50 percent smaller than the theory suggests for Geldart D particles (Geldart, 1973). Other models have been suggested, but there is still much controversy concerning flow models for bubbling beds. For large particle beds, bubble behavior is significantly different than for small particle beds, except when the bubbles are in the fast bubble regime. Because of this, bubble models developed for small particle beds are not applicable to large particle beds.

In large particle fluidized beds, bubbles generally begin as horizontal, elongated lenticular voids at the bottom of the bed, although, on occasion, their initial appearance is spherical. As these voids rise, the voids move to form bubbles which take on a mushroom cap shape (or a lima bean shape in a 2D bed). Bubbles tend to travel toward the center of the bed as they rise. These characteristics in 2D have been observed in the present work as well as reported by Loew et al (1979) and Cranfield and Geldart (1974). Glicksman et al. (1981) found that correlations and models for small particle beds gave erroneous results when applied to large particle beds. They proposed a new bubble

growth theory to calculate average bubble size and frequency versus height, which needs the initial condition of bubble size above the distributor. Glicksman and Yule (1986) numerically investigated gas flow through a bubble near a bed surface and found agreement with the model for large-particle bed data. They found that when a bubble approaches the surface, the maximum gas velocity is substantially greater than the velocity through an identical void deep within the bed. They also found that emulsion phase gas flow is substantially greater than the flow found by the two-phase model.

Cranfield and Geldart (1974) studied bubble frequencies, concentration, visible bubble flow rate, and bubble velocity in a 3D bed of large particles. They found that bubbles in large particle beds expand rapidly and can become quite large and do not achieve a maximum stable bubble diameter. They found that the Geldart correlation for bubble diameter in small particle beds was unsatisfactory for large particle beds, so they derived their own correlation. Glicksman and McAndrews (1985) studied the effect of bed width on bubble behavior for large particle fluidized beds and found that, for an open bed width equal to or larger than five times the mean bubble diameter, bubble behavior was independent of bed width. Also, a maximum upper limit to bubble size was not observed. They also observed that for a given bubble diameter, 2D bubbles rise slower than 3D bubbles for beds of the same height fluidized at the same fluidization velocity. Geldart and Cranfield (1972) studied bubble fluidization properties of large-particles at ambient and medium-temperature for 2D and 3D beds. Minimum fluidization velocities were described by an expression based on Ergun's equation (1952). Also, they found that the distribution of gas between emulsion and bubble

phases was significantly different than predictions based on the two-phase theory of fluidization. Saxena and Vadivel (1989) found a dependence of bubble velocity on frontal area in 2D beds of large and small particles. Glicksman et al. (1987) experimentally studied bubble properties in a 2D bed of 1 mm particles at ambient temperature. They found that the bubble velocity depended on the proximity of bubbles above it and that the average velocity was closely approximated by the Davidson and Harrison expression (Davidson and Harrison, 1963). Glicksman et al. did not find a maximum bubble size unless the bubble size approached the bed width. They also developed a bubble growth model.

Bubble studies for small-particle fluidized beds are vast (Rowe, 1976; Allahwala et al., 1981; Hager and Thomson, 1973; Jin et al, 1982; Godard and Richardson, 1969; Zhang et al., 1987; Horio and Nonaka, 1987; Werther and Molerus, 1973(a) and 1973(b); Werther, 1974(a) and 1974(b); Chiba et al., 1975 and 1974; Ho et al., 1983; Tsutsui and Miyauchi, 1980; Grace and Harrison, 1969; Peeler and Whitehead, 1982; Sellakumar and Zakkay, 1988; Clough and Weimer, 1985; Sitnai et al, 1982; Horio and Koike, 1993; Sitnai, 1981; Cai et al, 1993; Geldart, 1972). Although most of these are not applicable to large-particle beds, several investigators found some interesting results with implications for large-particle beds. Geldart (1970) presented a straightforward approach for relating bubble properties and investigated bubble properties in 2D and 3D beds of small particles. Matsen (1973) found evidence of a maximum stable bubble size in a fluidized bed, but suggested that this was not the case for larger particles. Godard and Richardson (1968) observed that bubble velocities in

freely-bubbling small-particle beds were influenced more markedly by surrounding bubbles than by the size of the individual bubble itself. Bubble behavior in beds of small-particles is not of particular interest here, and the focus will be on large-particle systems.

When an obstacle such as a tube is immersed in the bed, three characteristics are known to occur: (1) a relatively defluidized cap of particles (often called the lee-stack) is present on the top face of the obstacle, (2) a thin film or gas cushion attaches to the bottom surface of the obstacle, and (3) bubbles appear at the sides of the obstacle due to local gas acceleration. Figure 1.2 shows a typical bubble and particle distribution around a horizontal tube in a bubbling bed. These effects are generally more pronounced for 2D beds than for 3D beds (Rooney and Harrison, 1976). The size and replacement time of the cap generally decrease with an increase in fluidization velocity.

1.3.4 Experimental Techniques for Bubble Detection

A general review of experimental methods for studying bubble and particle behavior in a fluidized bed is provided by Cheremisinoff (1986). X-Ray photography (Hager and Thomson, 1973; Rowe and Partridge, 1965) provides some information on bubbles, but is limited to beds containing a low concentration of bubbles. Cine photography and video-tape (Kunii et al., 1967; Weihong et al., 1987) are useful but are limited by the need for visual access to the bed and the requirement for an abundance of

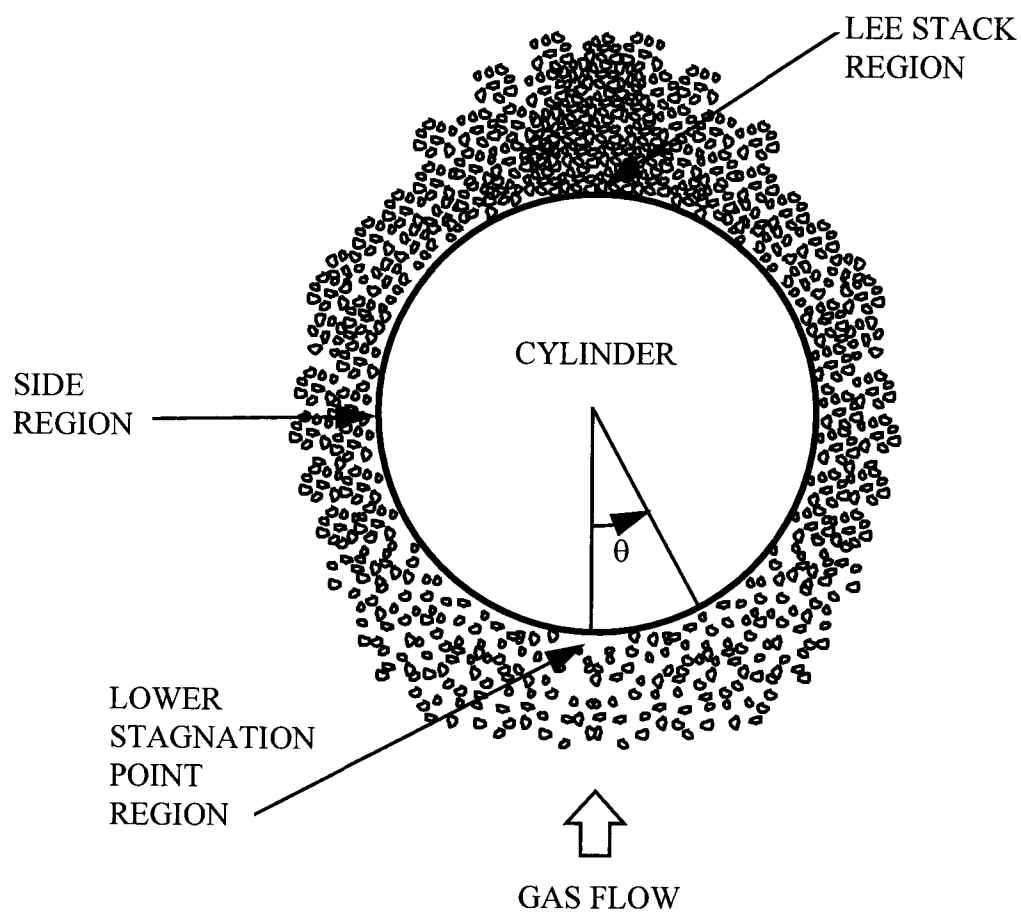


Figure 1.2 Voidage distribution at a cylinder wall.

pictures to be taken and analyzed. Mudde et al (1994) used image processing techniques to quantify local void fraction as well as bubble properties.

Several types of intrusive probes have been discussed in the literature which measure bubble properties. Their operations are based on a variety of physical effects such as temperature, resistivity, capacitance, inductance, and pressure changes between dense phase and bubble phase. Several probe concepts possess certain operational limitations. Intrusive probes, in general, have been shown by Rowe and Masson (1981) to interact with the bed dynamics and results must be interpreted with this fact in mind. Hot-wire probes (Tsutsui and Miyauchi, 1980) might not be sturdy enough for placement in a bed composed of large particles. Electrical resistivity probes (Matsuura and Fan, 1984; Yoshida et al., 1982; Park et al., 1969) can only be used with liquids and conductive solids. Inductance probes (Cranfield, 1972) use a magnetic field and consequently bed materials must have magnetic properties. Capacitance probes have been used in fluidized bed applications with some success (Geldart and Kelsey, 1991; Werther and Molerus, 1973; Gunn and Al-Doori, 1985). A serious shortcoming of capacitance probes is that they must be calibrated for every fluid-solid system and operating condition (in particular temperature and pressure) (Dutta and Wen, 1979). Probes based on sensing local electrical properties of the fluidized bed would be cumbersome to use in beds that operate over a range of temperatures and particle compositions such as is the case in fluidized bed combustion. Fiber optic (Lord et al., 1982) and optical probes (Rowe and Masson, 1981; Yasui and Johanson, 1958; Dutta and Wen, 1979; Masson and Jottrand, 1978; Katoh et al., 1991) have also been

introduced but have shortcomings such as excessive intrusion in the flow pattern, unsuitability for high-temperature use and incomplete signal interpretation methodology. Pressure differential probes have been shown to be useful for determining bubble properties (Sitnai, 1982) but the interpretation of the pressure records needs more extensive experimental validation. Differential pressure fluctuations from a probe were used by Ramayya et al. (1993) to determine local bubble properties in a large particle fluidized beds. Their work validated the technique, and they proposed a correlation for bubble size in large-particle beds.

1.3.5 Heat transfer Models

The mechanism of heat transfer between a fluidized bed and an immersed horizontal tube is closely tied to bed hydrodynamics. In general, the heat transfer rate is influenced by a large number of variables such as particle size, particle size distribution, particle shape, particle and gas thermal properties, bed geometry, type of gas distributor, fluidization conditions, radiative properties of the bed material, heat transfer surface and fluidizing gas, and tube design. Referring to Figure 1.2, the maximum local heat transfer coefficient is expected generally to occur at the sides or top of the horizontal tubes in the 'surflines'. At low velocities, the point of maximum heat transfer occurs near 90° and at higher velocities, the location moves upward to approximately the 135° to 180° position. Porosity close to the tube surface in this zone increases with velocity, resulting in a decrease in heat transfer rate. The minimum coefficients are found at the top and bottom regions of the tube, which leads to high local temperatures and possible corrosion

(Stringer, 1978). An increase in fluidization velocity removes the stagnant cap at the top of the tube and dramatically increases heat transfer with fluidization velocity. Heat transfer at the bottom of the tube where there is a gas shroud is less sensitive to changes in gas velocities. These phenomena are generally agreed on, but more insight can be gained by looking at local instantaneous heat transfer coefficients.

The bed can be divided approximately into emulsion and bubble phases. When the emulsion phase is in contact with the surface, the heat transfer is generally greater than when the bubble phase is in contact. As bubbles approach and depart the tube, they bring fresh particles to the heat transfer surface. The fraction of the total time a bubble contacts the surface, the local bubble time fraction, is designated f_b , and the emulsion phase local time fraction is then $1 - f_b$. To a first approximation, the overall heat transfer coefficient can be represented in terms of the emulsion phase coefficient, h_e , and the bubble phase coefficient, h_b :

$$h = (1 - f_b)h_e + f_b h_b \quad (1.5)$$

where

$$h_e = h_{pc} + h_{egc} + h_{er} \quad (1.6)$$

and

$$h_b = h_{bgc} + h_{br} \quad (1.7)$$

These components are described as follows:

h_{pc} = particle convective component accounting for the heat transfer to aggregates of particles by unsteady conduction through the thin gas layer

between solid particles and the surface, and then the convective heat transfer between these particles and the bulk of the bed.

h_{egc} = emulsion phase gas convective component accounting for heat transfer due to gas flow between particles

h_{er} = emulsion phase radiative component

h_{bgc} = bubble phase gas convective component accounting for heat transfer due to gas flow in the bubble

h_{br} = bubble phase radiative component

These relations can be considered as either local or space-average.

As mentioned above, large particles tend to remain relatively isothermal near a heat transfer surface while small particles tend to experience a temperature decrease near a lower temperature surface. In beds of small particles, particle residence time and packing density affect the heat transfer rate. Unsteady conduction exists between the emulsion phase and the tube while the emulsion phase is in contact with the tube. Bubbles have two opposing effects: they raise the heat transfer coefficient by bringing new hot particles to the tube, but then when the bubble is in contact with the heat transfer surface, the coefficient is generally lower. For small particle systems, then, the particle convective component is predominant for non-pressurized systems at temperatures such that radiation can be neglected (<900K). In large particle bubbling beds, the thermal time constant of a particle is usually greater than the residence time. Thus, the heat transfer between emulsion phase and the tube is approximately steady state. The gas convective components of heat transfer are predominant for denser and larger particles

and at high operating pressures. The radiative contribution acts in parallel with the other heat transfer components for large particle systems because the particles stay approximately isothermal. For small particles, however, there is a significant reduction in particle temperature while it is near the surface and thus radiation cannot be simply added to the other modes of heat transfer. Because of these fundamental differences between the mechanisms of heat transfer for large and small particle beds, different modeling approaches have been taken. A number of theoretical models have been proposed for the different modes of heat transfer, namely particle convection, gas convection and radiation.

1.3.6 Particle Convection

Models for particle convection are generally developed to predict heat transfer for small particle systems since this is the dominant mode. Small particle models generally need as input the bubble time fraction at the heat transfer surface as well as the bubble frequency. Since the emphasis is on large particles, these will only briefly be mentioned. Basically, there are three different approaches taken:

1. Levenspiel and Walton (1952) developed the film concept. In this model, the principal resistance to heat transfer to an immersed surface is due to a fluid film, and the film resistance is decreased due to a reduction in film thickness caused by a scouring action by the particles. Many others have developed similar models but this concept has been found inadequate.

2. The 'packet' theory based on the work of Mickley and Fairbanks (1955) is widely used for small particle systems. In this model, 'packets' of particles are considered homogenous with effective thermal properties. While in contact with an immersed surface, the packet exchanges energy, thereby reducing the packet temperature, and is then convected away from the surface and is replaced by a fresh packet. The Mickley-Fairbanks model has been modified by several investigators (Baskakov, 1964; Baskakov et al., 1973; Chung et al., 1972; Kubie and Broughton, 1975) by the introduction of a contact resistance.
3. Another approach is to model heat transfer to distinct particles rather than treating the particle packet as a homogenous medium. Botterill (1975) and Decker and Glicksman, (1981) modeled heat transfer by unsteady conduction from a single row of particles. Some of these models have been extended to depths of two particles and a particle chain of unlimited length.

1.3.7 Gas Convection

O'Brien et al. (1985) conducted experiments on gas convective and total heat transfer for a horizontal tube submerged in an ambient-temperature fluidized bed of particles ranging from 125 μm to 3.4 mm. They found that the relative contribution of gas convection to total heat transfer ranged from 6.8 percent, for the smallest particles at optimum fluidization for heat transfer, to 100 percent for the largest particles. At

minimum fluidization the gas convective contribution was found to be 40 and 100 percent for the smallest and largest particles, respectively. Based on this, models for large-particle beds need only account for gas convection and, for high-temperature operation, radiation. These models can also sometimes account for the following small-particle systems: high operating pressure, very high velocities, gas velocities near minimum fluidization conditions, and surface geometry which result in regions of either high voidage or stagnant particles.

Gabor (1970) proposed a model to predict gas convective heat transfer between an immersed vertical surface and a bed for gas flows less than or equal to that required for minimum fluidization. Xavier and Davidson (1981) modified this model to account for gas velocities greater than minimum fluidization velocity. Botterill and Denloye (1978) developed a model for heat transfer between a vertical immersed surface and packed and incipiently fluidized beds. The model considers that the bed consists of two regions: (1) a high-voidage region near the heat transfer surface and (2) the region comprising the rest of the bed. Their solution at minimum fluidization was taken as equal to the convective component of the heat transfer coefficient.

Adams and Welty (1979) developed a model for gas convective heat transfer, which is expected to be the dominant mode in large particle beds. The model also includes radiation heat transfer. The model is limited by the fact that it requires as input the specification of the interstitial turbulence level, the voidage distribution and the particle spacing near the heat transfer surface. These results were correlated by Adams, (1981a) to obtain an approximate formula for the Nusselt number and the results

compared well with experimental data for operation near minimum fluidizing conditions. The model was then used with an approximate hydrodynamic model to analytically determine local and space-average heat transfer to a tube with an adjacent bubble in a 2D bed (Adams and Welty, 1982). An approximate model of the bubble contribution to heat transfer to a tube was then developed to calculate the average bubble convective heat transfer in a 2D bed (Adams, 1982a). Adams (1982b) extended the Adams-Welty model to account for unsteady conduction effects in the particle. Adams (1981b) also extended the Adams-Welty model near minimum fluidization to the large-particle packed-bed case. Catipovic et al. (1982) validated the Adams-Welty model including all components of the model except the thermal radiation portion since their experiments were not at high temperature. The Adams-Welty model discussed above treats separately the contributions of emulsion and bubble phase heat transfer. These models were consolidated to predict local and overall time-average heat transfer to immersed surfaces (Adams, 1984). This requires information regarding emulsion-phase residence time and bubble-phase contact fraction. The model was validated by Catipovic et al. (1982) in a 2D ambient pressure and temperature bed. The Adams-Welty model, like most mechanistic models, can be used to predict average maximum and minimum local instantaneous heat transfer coefficients, corresponding to the emulsion phase and bubble phase contact, respectively.

Ganzha et al. (1982) developed a mechanistic theory for heat transfer between fluidized beds of large particles and immersed surfaces. The model accounts for conductive and convective components of heat transfer. Decker and Glicksman (1983)

developed a physically based model for heat transfer to large-particle fluidized beds. The model needs, as input, the bubble voidage. Good agreement was found with data from several sources. They found that the gas convective component in fluidized bed heat transfer is not simply related to overall gas convection in a packed or quiescently fluidized bed. Catipovic (1979) studied heat transfer to a horizontal tube and tube array in a room temperature bed of particles ranging from 0.37 to 6.6 mm. Simultaneous measurements were made of instantaneous, as well as time-averaged, local heat transfer coefficients, voidage, and surface pressure variations at several positions around the circumference of an instrumented tube. A model was developed to predict heat transfer coefficients over a wide range of operating conditions, including large-particle and small-particle limits. This model is actually semi-empirical and accounts for all modes of heat transfer.

1.3.8 Radiation

While the importance of the radiative component of heat transfer is argued among investigators, it is generally agreed that the radiative contribution increases with particle size and temperature. The alternate slab model was used to predict radiative heat transfer for small particle systems by Kolar et al (1979). Ozkaynak et al. (1983) found that radiation heat transfer contributed as much as 30 percent of the total heat transfer to an immersed surface for an 800 °C bed of 1.03 mm particles. Yoshida et al. (1974) found that the contribution due to radiant heat transfer was insignificant at temperature levels up to 1000 °C in small particle beds. Basu (1978) found the radiation contribution to be

5-10 percent for small particle beds. Radiation heat transfer for beds of small particles have been studied by several other investigators (Szekely and Fisher, 1969; Borodulya and Kovenskii, 1981; Chen and Chen, 1981; and Brewster and Tien, 1982).

All models mentioned above are basically applicable to fluidized beds of small particles. Fewer models are available for predicting the radiative component in large-particle beds. Fatani (1983) used the alternate slab model mentioned above to predict combined radiative and convective components. Mahbod (1984) used the Adams-Welty model to predict the radiation contribution to the total heat transfer between a large-particle fluidized bed and an immersed horizontal tube. These models are difficult to use in practice, however, because they require knowing some parameters which are not readily available. An approximate method which gives an upper limit for radiation was given by Glicksman and Decker (1980 and 1982) and Glicksman (1984). In addition to the large-particle heat transfer models discussed above, some of which include the radiative contribution, other research has been done to examine the importance of radiation in large-particle beds. Adams et al. (1984) and Alavizadeh et al. (1990) studied the radiative contribution to heat transfer in a high-temperature large particle fluidized bed and found, for 2.14 mm particle bed, radiation contributions of about 8 and 13 percent for bed temperatures of 810 and at 1050 K, respectively. The radiative contribution for a black tube was found to increase from 6 to 14 percent with particle diameters from 0.52 mm to 3.23 mm in a bed at 812 K, and to increase from 14 to 22 percent with bed temperatures from 812 K to 1050 K for 3.23 mm particles. Chung and Welty (1991) studied total and radiative local and spatial-average heat transfer

coefficients in large-particle fluidized beds at high-temperatures and found that radiation contributed at most 12 percent to total heat transfer at 810K. They also found that there was some indication that the values of total heat transfer coefficients for an array of tubes were slightly higher than those for a single tube, but by no more than 5 percent over the conditions examined (Chung and Welty, 1989). Ozkaynak et al. (1983) studied radiative heat transfer in a fluidized bed of 1.03 mm particles at temperatures up to 1073 K and found the radiative contribution approached 30 percent of the total heat flux.

1.3.9 Heat Transfer Correlations and Data

Many researchers have conducted experiments to establish a data base, to test and modify available correlations and models, or to propose new correlations. The available literature for small particle systems is vast. For space-average heat transfer coefficients in small particle beds these include the following: Gabor, 1972; Grewal, 1981; Chen, J.C., 76; Shah et al., 1981; Vreedenberg, 1958; Canada et al., 1977; Baskakov et al., 1973; Grewal and Saxena, 1980; Ozkaynak and Chen, 1980; Andeen and Glicksman, 1978; Gloski et al., 1984; Kurosaki et al., 1991; and Gel'perin et al. 1964. Local and spatial-average coefficients for small particle systems have been investigated by the following researchers: Samson, 1973; Chandran et al., 1980; Berg and Baskakov 1974; and Richardson and Shakiri, 1979. Heat transfer coefficients for small particles and tube bundles have been examined by the following: Gel'perin et al, 1969; Saxena, 1979; Borodulya et al., 1980; Grewal, 1981; and Grewal and Saxena,

1983. In general, Borodulya et al. (1980) found that the correlation by Grewal and Saxena (1983) was best for small particle beds.

Several correlations have also been proposed for large-particle systems. The correlations are generally useful for time- and space- average coefficients but do not give insight into local and instantaneous coefficients. Some of the mechanistic models described above can be used to examine local, instantaneous coefficients, although information such as local bubble time fraction or space fraction is necessary to determine time- or space-average coefficients. The thrust of the present work is to investigate instantaneous heat transfer and hydrodynamics. Since the time- and space-average correlations for the heat transfer coefficient can be dissected to assist in this investigation, they will be briefly discussed here. More complete summaries of available correlations are given by Grewal (1981) and Grewal and Saxena (1980, 1981).

Botterill and Denloye (1978(a) and 1978(b)) and Denloye and Botterill (1978) proposed a dimensional correlation appropriate for small and large-particle beds at incipient fluidization. Baskakov and Suprun (1972) developed a correlation for the gas convective heat transfer coefficient based on the analogy between heat and mass transfer. Correlations are given for gas velocities below and above that necessary to give a maximum heat transfer coefficient. Glicksman and Decker (1980) developed a model for the gas convective component. Zabrodsky (1966) developed a simple correlation for the gas convective component. Several others have also developed or tested correlations appropriate for small- or large-particle beds (Chandran. and Chen, 1981; Wright et al., 1970; Botterill and Williams, 1963; Syromyatnikov, 1974; and Xavier

and Davidson, 1978), for just large-particle beds (Tang and Howe, 1981; McGaw, 1977; Maskaev and Baskakov, 1974; Mathur and Saxena 1986; and Borodulya et al., 1991), and for large particles and tube bundles (Zabrodsky et al., 1981; Borodulya et al., 1980; Borodulya, et al., 1983; Borodulya et al., 1984; Ku et al., 1981; and Tamarin et al. 1976). Grewal (1981) found that the correlations by Catipovic, Glicksman and Decker, and Zabrodsky are in good agreement with most existing data.

Many aspects of heat transfer in beds of large particles have been researched. Vadivel and Vedamurthy (1980) investigated the influence of bed parameters on the local, time-average radiative and total heat transfer coefficients to an immersed horizontal tube in a bed of large particles at high temperature. George (1981) studied local and spatial-average heat transfer coefficients to high-temperature large-particle beds containing a horizontal tube. Goshayeshi et al. (1985, 1986) and Goshayeshi (1989) investigated local and spatial-average heat transfer coefficient for horizontal tube arrays in high-temperature large-particle beds and found that single tube studies are representative of heat transfer behavior of tube arrays. Alavizadeh (1985) studied local total and radiative heat transfer coefficient in high-temperature large-particle fluidized beds containing single horizontal tubes and tube bundles. Pidwerbecki (1994) studied local and spatial-average total and radiative heat transfer coefficients in the splash zone of a fluidized bed and included some in-bed results. Local time-average coefficients for large-particle beds have also been experimentally investigated by Cherrington (1977), and Chandran et al. (1980) at ambient temperature and George (1981) and Vadivel and Vedamurthy (1980) at high-temperature. The investigators who conducted experiments

to measure local instantaneous heat transfer coefficients are mentioned below (see Section 1.3.10) and some of these have also reported local and spatial-average time-average coefficients.

Botterill et al. (1981) experimentally investigated several correlations for small and large particles and found that the Zabrodsky (1966) correlation works best for Geldart B particles and the Denloye and Botterill (1978) correlation works best for Geldart D particles.

1.3.10 Instantaneous Heat Transfer

In order to test the accuracy of a mechanistic model or correlation, instantaneous and local heat transfer coefficients are needed. Sensors used to measure instantaneous heat transfer coefficients must be fast-responding (on the order of 100 Hz, George, 1993), must be able to withstand the abrasive atmosphere of the bed, and, for high-temperature applications, must be able to withstand combustion-level temperatures. Mickley et al. (1961) were the first to obtain instantaneous data using a thin platinum foil on a vertical tube. Other investigations followed which typically used thin foils and films such as Tuot and Clift (1973); Baskakov et al. (1973); Bernis et al. (1977); Syromyatnikov et al., 1976; and Crescitelli et al. (1981). These measurements had some limitations including error due to variation in probe surface temperatures and significant temperature difference between sensor and the object on which it was placed. Additionally, these types of sensors are usually not suitable for high-temperature applications since they work by maintaining a slightly higher temperature than the bed,

which could destroy the sensors. Catipovic (1979), as discussed above, used platinum resistance heaters and held the surface temperature constant by an electronic control circuit. This type of sensor is also not suitable for high-temperature usage. Figliola et al. (1984) measured instantaneous heat transfer coefficients for a horizontal tube in a fluidized bed of small particles at ambient temperature. Their results validated small particle models for particle convective and overall coefficients, but showed that predictions were inaccurate for binary particle mixtures. Mueller et al. (1995) measured instantaneous heat transfer coefficients on a horizontal immersed tube in an ambient temperature bed of 450 μm to 1200 μm spheroidal glass particles. The heat flux sensor used was a platinum-film probe which is unsuitable for high-temperature operation. In the work of Pence et al. (1994), the contact behavior was divided into three groups: bubble phase contact, stationary emulsion phase (identified by transient decaying heat transfer coefficient) and mixing emulsion phase contact (identified by the heat transfer coefficient fluctuating about a constant value). They developed a signal processing technique to calculate average contact times and contact time distributions for each type of contact. McKain et al. (1993) measured instantaneous temperature and pressure information on a horizontal tube immersed in an ambient-temperature fluidized bed of small particles. They numerically calculated heat transfer coefficient based on 1-D conduction and determined bubble frequencies from pressure signal autocorrelation.

George (1987) developed a transducer to measure instantaneous local heat flux and heat transfer coefficients to a surface immersed in a high-temperature fluidized bed. The sensor measured temperatures which were converted to heat flux by electric analog

solution to the 1-D transient heat conduction problem. The sensor was proven functional in a small-particle fluidized bed operated at 282 °C. George and Smalley (1991) built a cylinder instrumented with the sensor developed by George. They obtained instantaneous heat transfer coefficients for a horizontal tube immersed in a bed of 0.9 and 2.1 mm particles at temperatures of approximately 550 °C and 743 °C. They were unable to compare their instantaneous heat transfer coefficient results since there are no other published data. Good agreement was found, however, for spatial-average heat transfer coefficients and time-average local heat transfer coefficients. George (1993) measured instantaneous heat transfer coefficients in a 562°C fluidized bed of 1 mm particles. Use of instantaneous data allowed various components of the Adams-Welty model to be compared and validated with experiment. Average coefficients agreed well with established correlations. It was also found that bubble phase heat transfer was much greater (by a factor of 2 or 3) if the bubble was simultaneously erupting at the bed surface compared to the case of fully immersed bubbles.

Khan and Turton (1992) built a probe based on the concept developed by George to measure instantaneous local heat transfer coefficients on a tube immersed in a fluidized bed of 0.73 mm and 1.2 mm particles at 900K. To find the heat transfer coefficient, the 1-D heat conduction equation was solved numerically. It appears that the probe was calibrated for temperature, but that the numerical results for heat flux were not calibrated. This could lead to large error due to contact resistance which is not accounted for in the 1-D model, and uncertainties in material properties. The qualitative

results compared favorably with limited available data (George, 1989 and Catipovic, 1979).

Instantaneous heat transfer data provide a good means to evaluate the accuracy of a proposed mechanistic model since the data allow individual terms in the model to be checked for accuracy. For instance, the bubble phase convective (together with radiative for high-temperature operation) term can be compared to the low values of the heat transfer coefficient found when a bubble is in contact with the surface. The maximum and minimum values of the instantaneous heat transfer coefficient at one location of the surface will correspond to conditions in which the surface is covered by a group of particles and a bubble, respectively.

Other uses of instantaneous data have been proposed. Saxena et al. (1993) pursued the possibility of characterizing the quality of fluidization by statistically analyzing instantaneous pressure and temperature fluctuations in a large-particle ambient-temperature bed which could prove to be a practical use of instantaneous data.

1.3.11 Interaction of Hydrodynamics and Instantaneous Heat Transfer

Tuot and Clift (1973) studied instantaneous local wall-bed heat transfer coefficients in the vicinity of a rising bubble in a 2D small-particle fluidized bed. They found that as a bubble approached the heat flux sensor, the heat transfer coefficient increased. When a bubble encompassed the sensor, the heat transfer coefficient decreases. Finally, there was a sharp rise in the heat transfer coefficient after the bubble departed. The heat transfer coefficient passed through a maximum some time after the

bubble departs. When a bubble passed near the sensor but did not engulf it, there was also a rise in the heat transfer coefficient as the bubble approached and a decrease in the heat transfer coefficient when the bubble departed the horizontal plane of the sensor. Henwood (1969) and Mickely et al. (1961) found the same results for 2D and 3D beds, respectively. Bock and Molerus (1980) studied simultaneous measurements of local bubble behavior and time-averaged local heat transfer coefficients on a vertical tube in beds of small particles and they concluded that bubble activity was the controlling mechanism of heat transfer. Kubie (1976) studied bubble-induced heat transfer in gas fluidized beds of small particles at ambient temperature. A platinum wire was used as an instantaneous heat transfer probe and bubbles were injected into an incipiently fluidized bed. They found that bubble wakes were primarily responsible for renewal of the emulsion on the wire surface (and hence the increase in instantaneous heat transfer coefficient). The "noses" were shown to be responsible for some of the surface renewal (and hence increased heat transfer coefficient), but that the main effect on the time-average heat transfer coefficient was due to the contribution of the bubble wake. Crescitelli et al. (1981) simultaneously measured instantaneous heat transfer coefficients and observed local particle-renewal using film and confirmed the relationship between particle-renewal and heat transfer coefficient. Ishiguro et al. (1991) experimentally studied instantaneous heat transfer coefficients, wall pressure, and discrimination between emulsion and bubble phases at a horizontal tube wall for a bed of small particles. Their results were used to develop a model of local heat transfer coefficients for small particle beds.

1.4 Present Work

The purpose of this research is to study fluidized bed hydrodynamics and their relationship to heat transfer. First, two optical probes were used in a 2D bed to validate the interpretation of the probe signals. The probe signals (voltages) were compared to video tape of the bed to determine information contained in the probe signals. Bubble properties such as bubble (or emulsion) frequency, bubble velocity, pierced length, characteristic bubble size, bubble (or emulsion) residence time, and bubble (or emulsion) time fraction were calculated by filtering and processing the probe signals. Calculated bubble properties were compared to and validated by the values obtained with the video-tape. The next step was to use the probes in a high-temperature 3D bed where the bubbles could not be observed directly.

In order to simultaneously study the heat transfer, a tube instrumented with an instantaneous heat flux sensor was built so that instantaneous heat transfer coefficients could be measured. The sensor was based on surface temperature measurements of the tube. To convert these data to heat transfer coefficients, the signals were processed using an analog signal conditioning unit. This required calibration to relate voltages to instantaneous heat transfer coefficients.

Experiments were performed in a high-temperature fluidized bed over a range of temperatures and fluidization velocities. Bubble properties were measured for two different particle sizes and heat transfer coefficients were taken at circumferential intervals on the tube of 45° . Bubble phase and emulsion phase properties that were obtained in the 2D bed were also obtained in the 3D bed. Local, instantaneous heat

transfer coefficients were measured. Time- and space-averaged heat transfer coefficients, time-averaged local heat transfer coefficients, instantaneous heat transfer coefficient standard deviation, average maximum and minimum local heat transfer coefficients were calculated using these instantaneous results. By filtering the instantaneous heat transfer coefficient, bubble (and emulsion phase) frequency on the tube, bubble (and emulsion phase) residence time on the tube, bubble (and emulsion phase) time fraction on the tube were also calculated. Finally, available time- and space-averaged correlations were compared to the average maximum and minimum local heat transfer coefficients. The best correlations were identified and then modified and extended to account for local variation around the circumference of the tube.

2. SENSORS AND EXPERIMENTAL APPARATUS

2.1 Optical Probe

2.1.1 Optical Probe Design

A schematic of the optical probe unit is shown in Figure 2.1. Infrared light (880 nm spectral peak) is produced by a high-intensity LED. The light travels down a fused quartz rod, is reflected across a gap, then is reflected down a second rod, and is subsequently incident on a silicon infrared phototransistor which is matched to the LED. The excitation current to the LED is provided as a square wave at approximately 10 kHz with a constant nominal current large enough that the current supplied is never negative. A periodic signal is used so that radiant emission from a high-temperature bed and other noise can be removed. The phototransistor output is processed using amplitude modulation (Doebelin, 1991). The amplitude-modulated signal contains the useful bubble information at the corresponding side frequencies of the 10 kHz carrier signal. This signal is high-pass filtered to remove 50 or 60 Hz noise pick-up due to AC power lines as well as the constant or slowly fluctuating component of the phototransistor output due to radiant emission from a high-temperature bed. The signal conditioning unit also filters out the extremely high frequency emission from bed thermal radiation (approximately 10^{11} - 10^{15} Hz, including infrared frequencies). The remaining square wave signal is amplified, full-wave rectified and filtered to yield a voltage which can be recorded by an oscilloscope or a digital data acquisition system. Essentially all of the

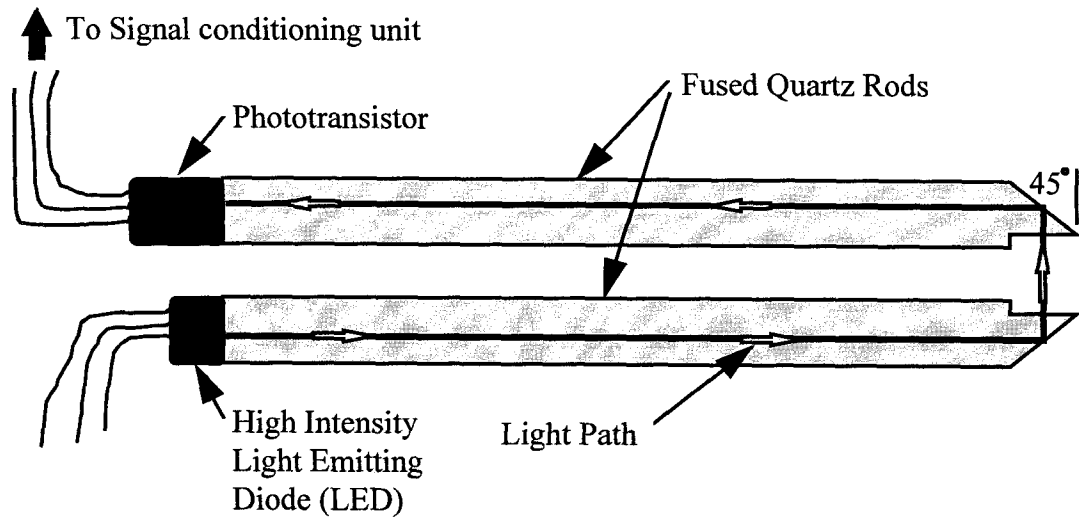
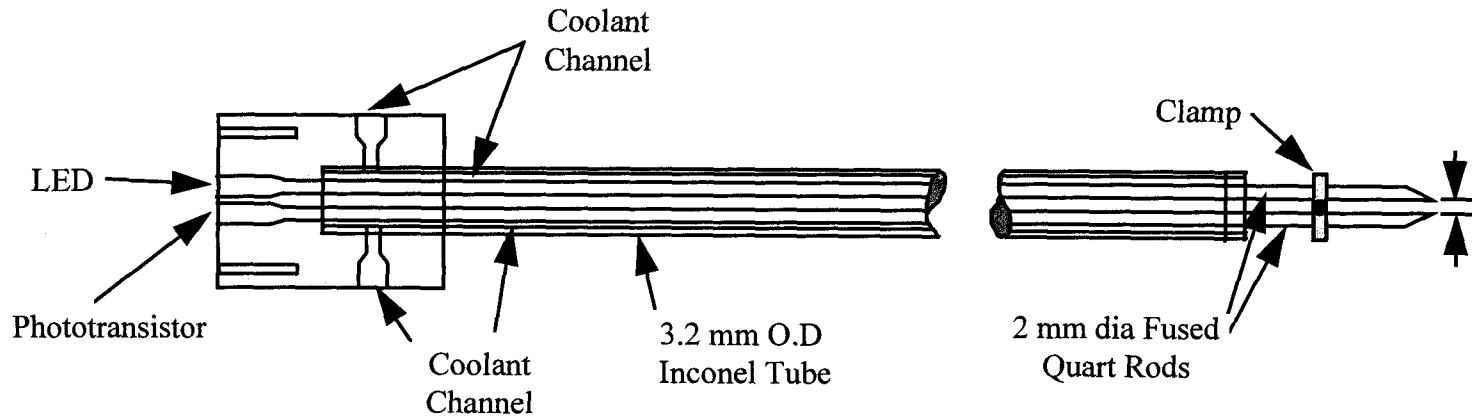


Figure 2.1 Schematic of optical probe

signal retained after the conditioning has its source at the LED and is not due to radiant emission from a high-temperature bed as transmitted to the phototransistor through the quartz rods because of the amplitude modulation signal conditioning method employed.

For common gas fluidized systems, the bubble phase is essentially optically clear, and light is transmitted across the gap to the photodetector when a bubble occupies the gap. Assuming opaque particles (or at least particles which sufficiently scatter light), essentially no transmission of light occurs across the gap when the dense (emulsion) phase fills the gap. In this work the signal was amplified such that the voltage range was approximately 0-3.0 volts. The frequency response of the optical probe and signal conditioning unit was experimentally found to be approximately 125 Hz.

The rods, LED and phototransistor were encased in stainless steel coolant channels suitable for high-temperature operation. All joints exposed directly to the high-temperature bed were silver brazed and the quartz rods, which were exposed beyond the coolant channel, were held stationary in Inconel tubing. The Inconel tubes were fixed relative to each other by a clamp and the quartz rods were held fixed inside each of the Inconel tubes by a set pin located at the base of the probes. One optical probe was supplied by Dr. Alan George of Montana State University. A second probe was built for the current research. The coolant channels were re-designed to allow a simpler cooling path and easier manifold connections to the coolant system at the high-temperature fluidized bed facility. Some of the dimensions on the second probe are slightly different to accommodate alternative materials purchased for the probes. The length of this second probe was the shortest length allowed in order to fit the probe into the high-

temperature fluidized bed. The shorter path provided reduced material cost and allowed for shorter quartz rods to be used. The quartz rods are commercially available. The rods with 2.1-mm-diameter were used for the first probe, and 1.9-mm-diameter rods were used in the second probe. These sizes were the largest that would fit into the Inconel tubes. The quartz rods were shaped by grinding the top and bottom surfaces as shown in Figure 2.1 using a circular sander. These surfaces were then fire polished using an acetylene torch to produce maximum reflectance and transmittance. The fused quartz rods could operate at combustion level temperatures without softening or undergoing a significant loss of transmittance at infrared wavelengths. To demonstrate their suitability for use at combustion-level temperatures, the probes were tested in a high-temperature furnace with coolant water supplied to the probes. For temperatures ranging from 290 K to 1200 K, the open gap voltage remained essentially constant - within approximately $\pm 10\%$ of the room temperature value. Additionally, the sensitivity of the phototransistor was found to be essentially unaffected by the radiant emission from the high-temperature environment. After dozens of hours of operation in a fluidized bed at 660 K, during which the quartz tips of the probe were subject to abrasion by the bed particles, the calibration of the probe remained essentially constant.

2.1.2 Probe Signal Processing Methodology

While in principle the probe delivers an "on-off" signal corresponding to bubble phase and emulsion phase, respectively, the real analog signal varies from this for two reasons. First, the bubbles contain particles which block the light and reduce the voltage

below its maximum "on" value. The particle occurrence inside bubbles is more pronounced in a 2D bed than a 3D bed because of the wall effect. Second, the voidage in the dense phase adjacent to a bubble can be large (Lockett et al., 1967) which could allow some light to travel across the probe gap. As bubble properties were of interest in the present work, it was necessary to remove particle effects from the signal. This was accomplished by two-stage filtering the raw signal such that the relatively low frequency bubble information was retained and the higher frequency particle effect was removed. The filtering technique was verified by comparing the optical probe signal to video-tape of the exact same events in a 2D bed.

2.2 2D Bed Experiments

The 2D bed facility consisted of a gas supply system, orifice flow meter, and test section. A schematic of the fluidized bed apparatus is shown in Figure 2.2. Ambient air is pumped by a positive displacement blower through an orifice flow meter, followed by a plenum and finally into the test section. Experiments were run in the 2D bed at approximately 313 K and atmospheric pressure in a 2D fluidized bed. The test section was rectangular in shape with a width of 68.6 cm, a height of 45.7 cm and a thickness of 3.2 cm. The distributor plate was a 3.2 mm-thick aluminum sheet with 3 rows of 55 holes, 2.38 mm in diameter, spaced 1.27 cm between centers. The front of the test section was 3.1-mm thick scratch-resistant Plexiglas to allow visual observation. The bed material consisted of silica-alumina particles having a density of 2700 kg/m^3 and a nominal diameter of 2.0 mm. The packed bed was 30.5 cm deep and the minimum

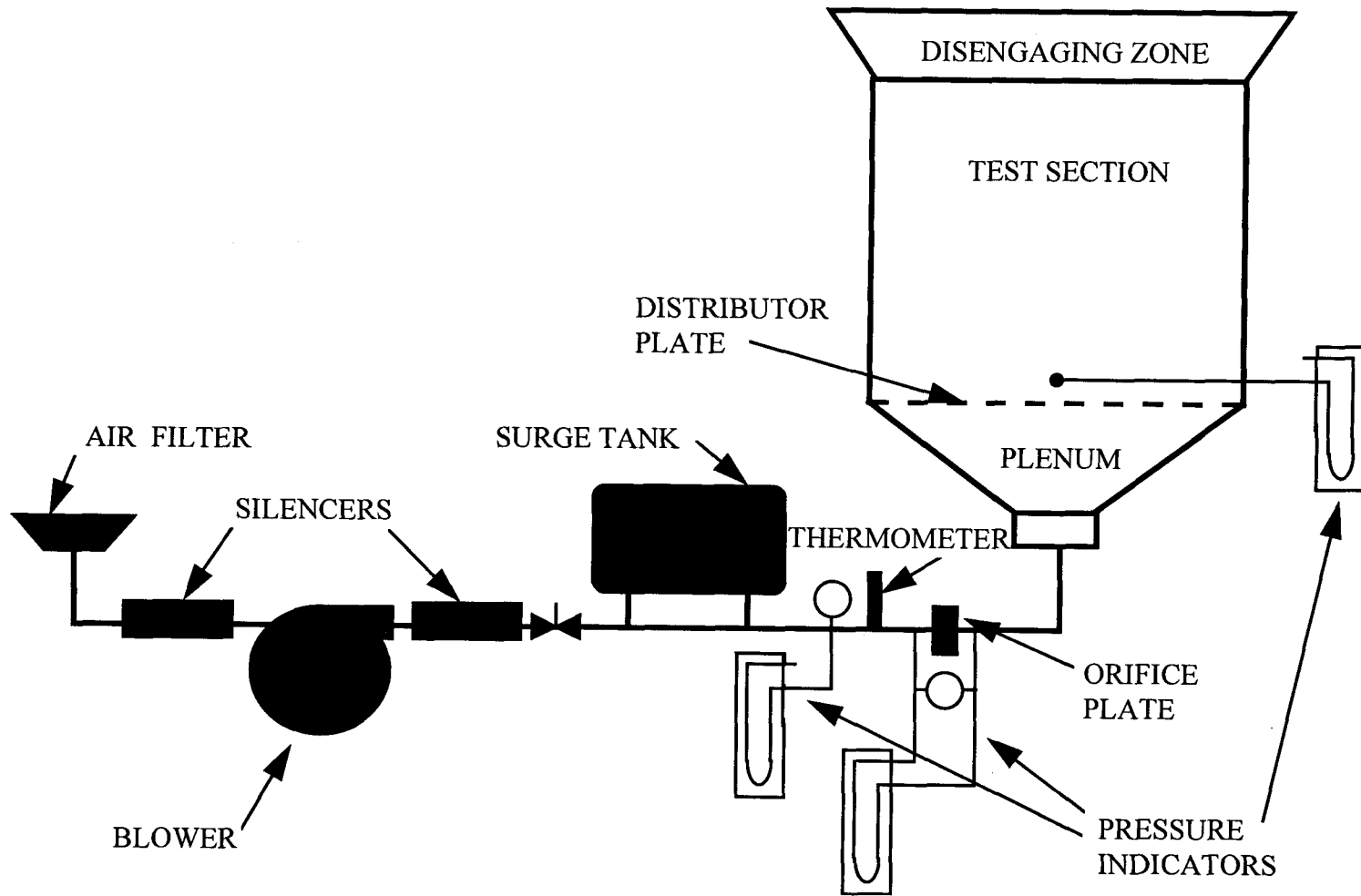


Figure 2.2 OSU 2D fluidized bed facility.

fluidization velocity was found to be $U_{mf} = 115$ cm/s. Two optical probes were mounted horizontally through the back of the test section. The lower probe was located 15.2 cm above the distributor plate and the second probe was located 5.1 cm above the lower probe. Data were taken over a range of fluidization velocities from minimum fluidization velocity (U_{mf}) to $1.6 U_{mf}$ with increments of $0.1 U_{mf}$. Five data sets were taken at each fluidization velocity for a period of 163 seconds each. The sampling rate was 200 Hz. The data taking and signal processing were performed on a digital computer.

2.3 Optical Probe Signal Processing

Typical raw probe signals are shown in Figure 2.3 for $U/U_{mf} = 1.4$. Results obtained for $U/U_{mf} = 1.4$ are representative of the other fluidization velocities employed.

The two-stage filter consisted of a digital low-pass filter followed by a digital amplitude-cut-off filter. The first-stage, low-pass filtering was done in the frequency domain following the procedure discussed in Press et al. (1989).

To illustrate the methodology, consider the data set from which the data in Figure 2.3 were taken. The Fourier transform of the data, which was calculated using the Fast Fourier Transform (FFT), is shown in Figure 2.4. The time domain data are denoted $v(t)$ while the frequency domain data are $V(\omega)$. The bubble information is contained in the relatively low-frequency portion of the signal while the particle information is contained in the higher frequencies. Therefore, $V(\omega)$ was multiplied by a

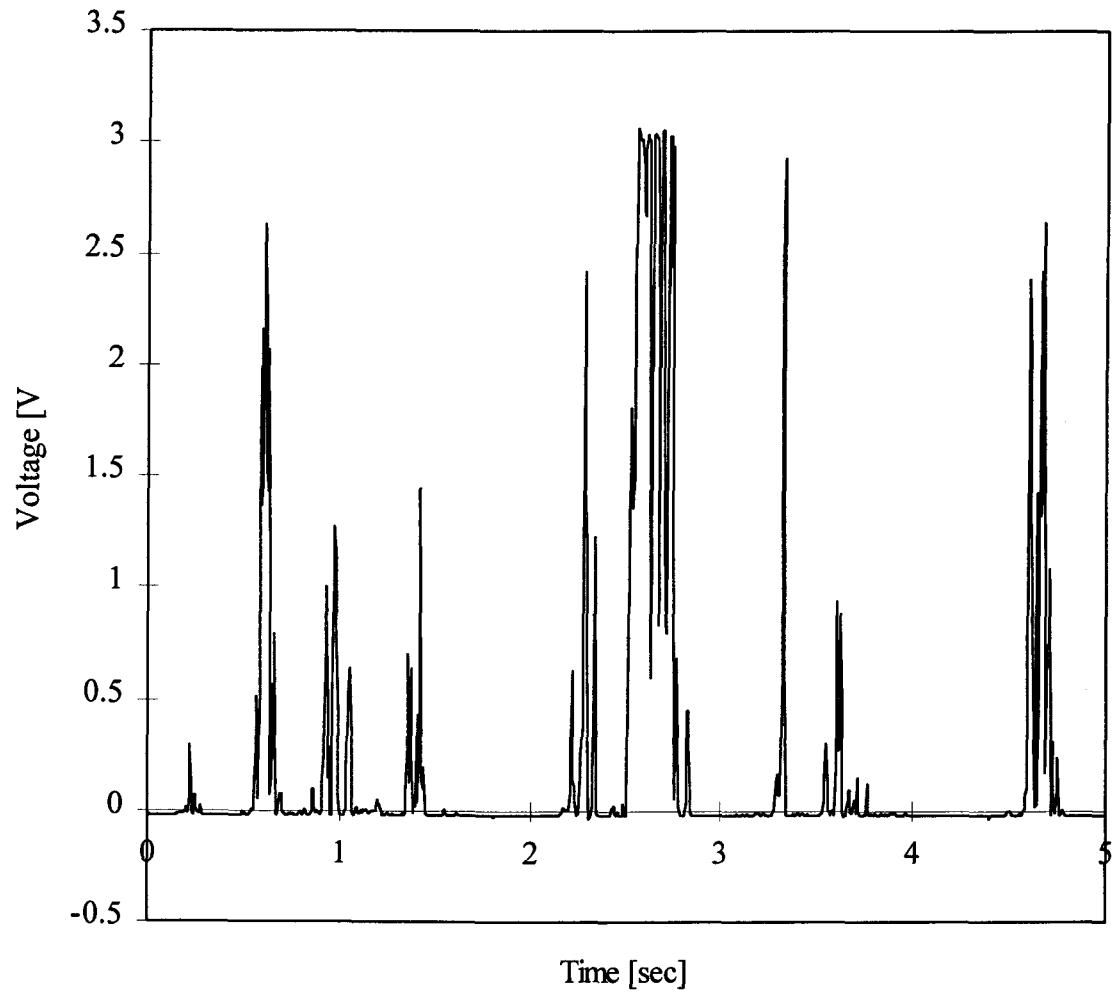


Figure 2.3 Raw probe signal in 2D bed ($d_p=2.0$ mm, $U/U_{mf}=1.4$).

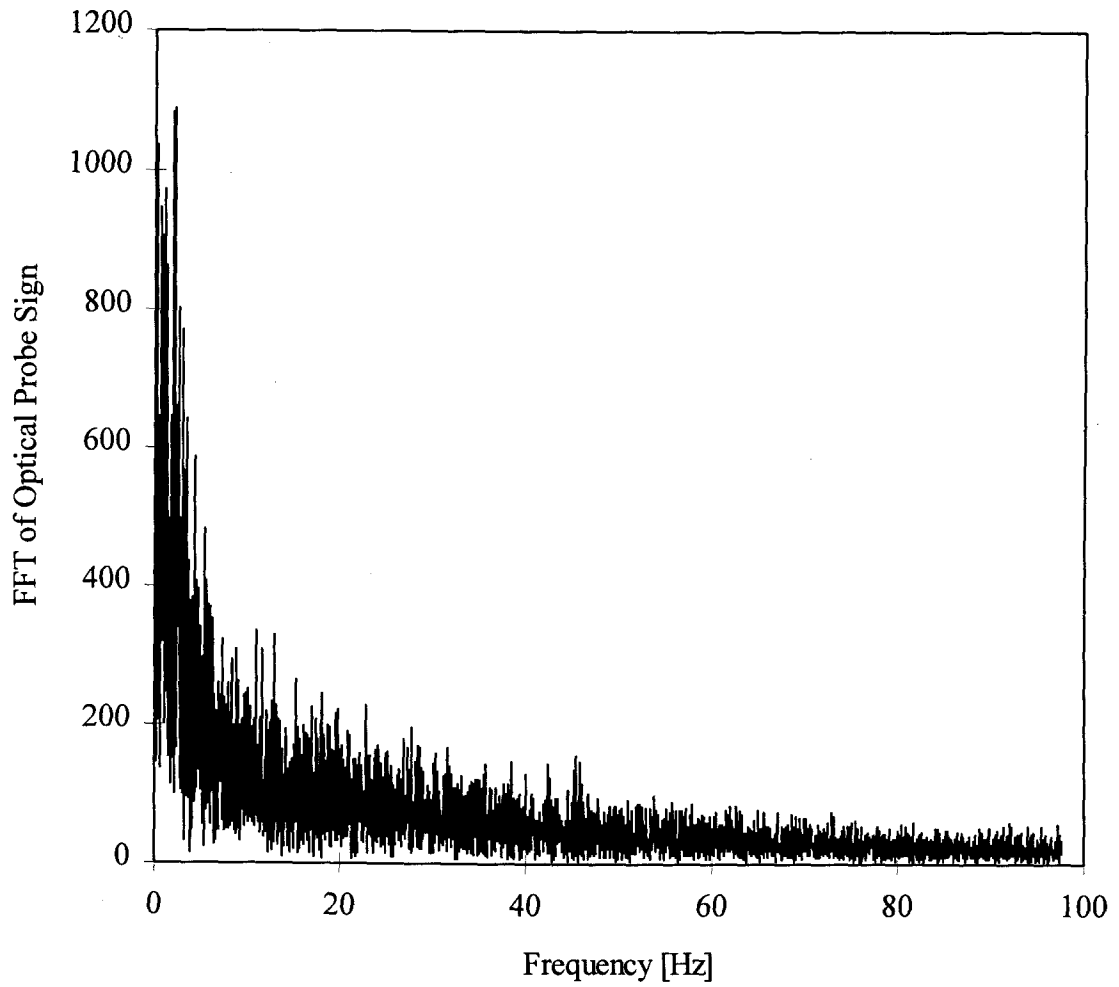


Figure 2.4 FFT of signal shown in Figure 2.3 ($d_p=2.0$ mm, $U/U_{mf}=1.4$).

function which passes values of $V(\omega)$ for small ω and eliminates values of $V(\omega)$ for large ω . Such a function might be the following ideal low-pass filter:

$$H(\omega) = \begin{cases} 1 & \omega \leq \omega_{\text{cut}} \\ 0 & \omega > \omega_{\text{cut}} \end{cases} \quad (2.1)$$

where ω is the cut-off frequency. Using a filter with such sharp transition in amplitude can cause Gibbs phenomena (Walker, 1991) which results in signal distortion when the inverse transform is performed. To avoid this problem, a filter with a more gradual change from 1 to 0 was used.

The filter selected was a second-order magnitude-squared Butterworth (Johnson, 1976) filter having the following transfer function:

$$H(s) = \left| \frac{1}{s^2 + \sqrt{2}s + 1} \right|^2 \quad (2.2)$$

where $s=j\omega/\omega_{\text{cut}}$ and $j= \sqrt{-1}$. The cut-off frequency selected was $\omega_{\text{cut}}=7$ Hz. This filter is shown in Figure 2.5. To use this filter, the FFT of the probe signal, $V(\omega)$ was multiplied by the filter transfer function $H(\omega)$ and then the product was transformed back to the time domain. The effect of this filter on the raw signal in Figure 2.3 is shown in Figure 2.6.

The second-stage filter was an "on-off" amplitude cut-off filter and was used in the time domain. A cut-off voltage, v_{cut} , was calculated and then values of the first-stage-filtered signal above v_{cut} were assigned a value of 1 (on) while those below v_{cut} were assigned a value of 0 (off). The value of v_{cut} was determined using the following relation:

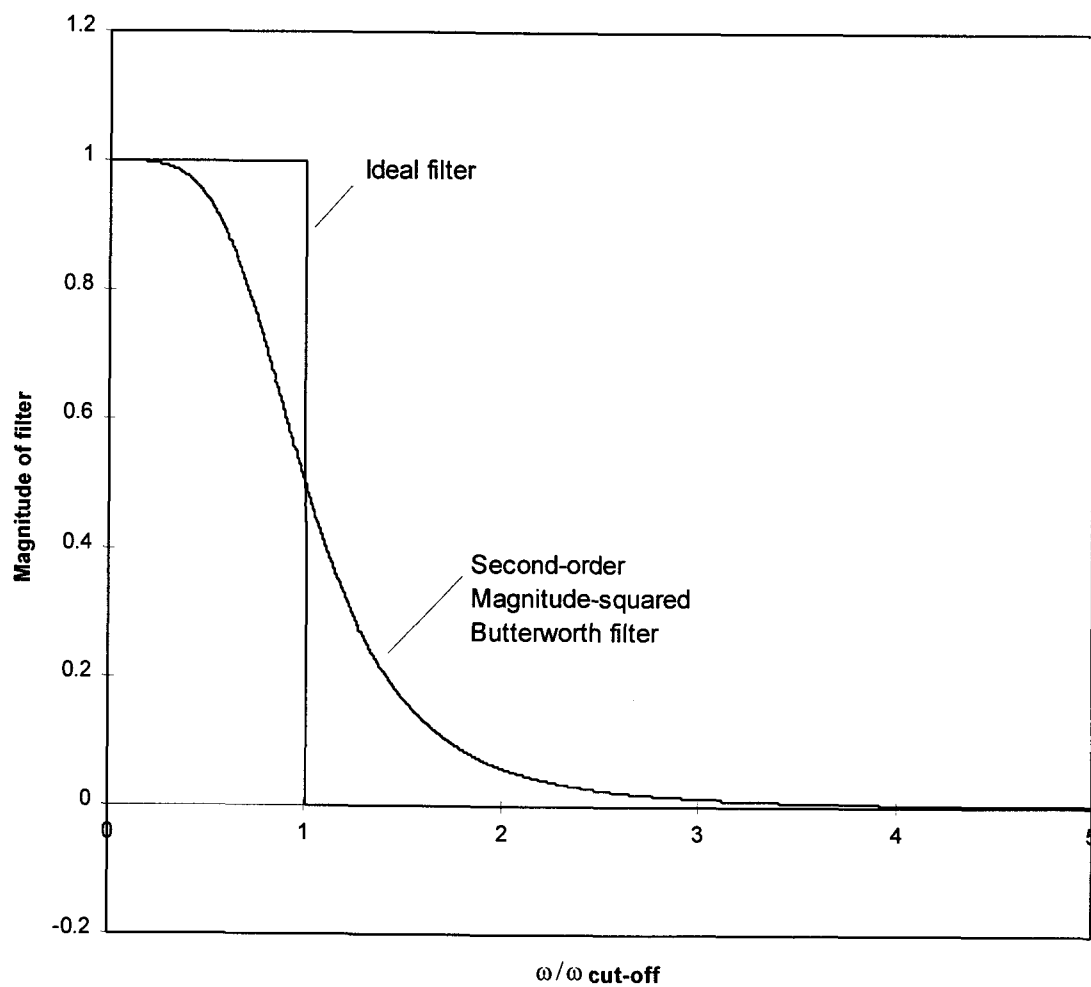


Figure 2.5 Ideal and Second-order Butterworth filter.

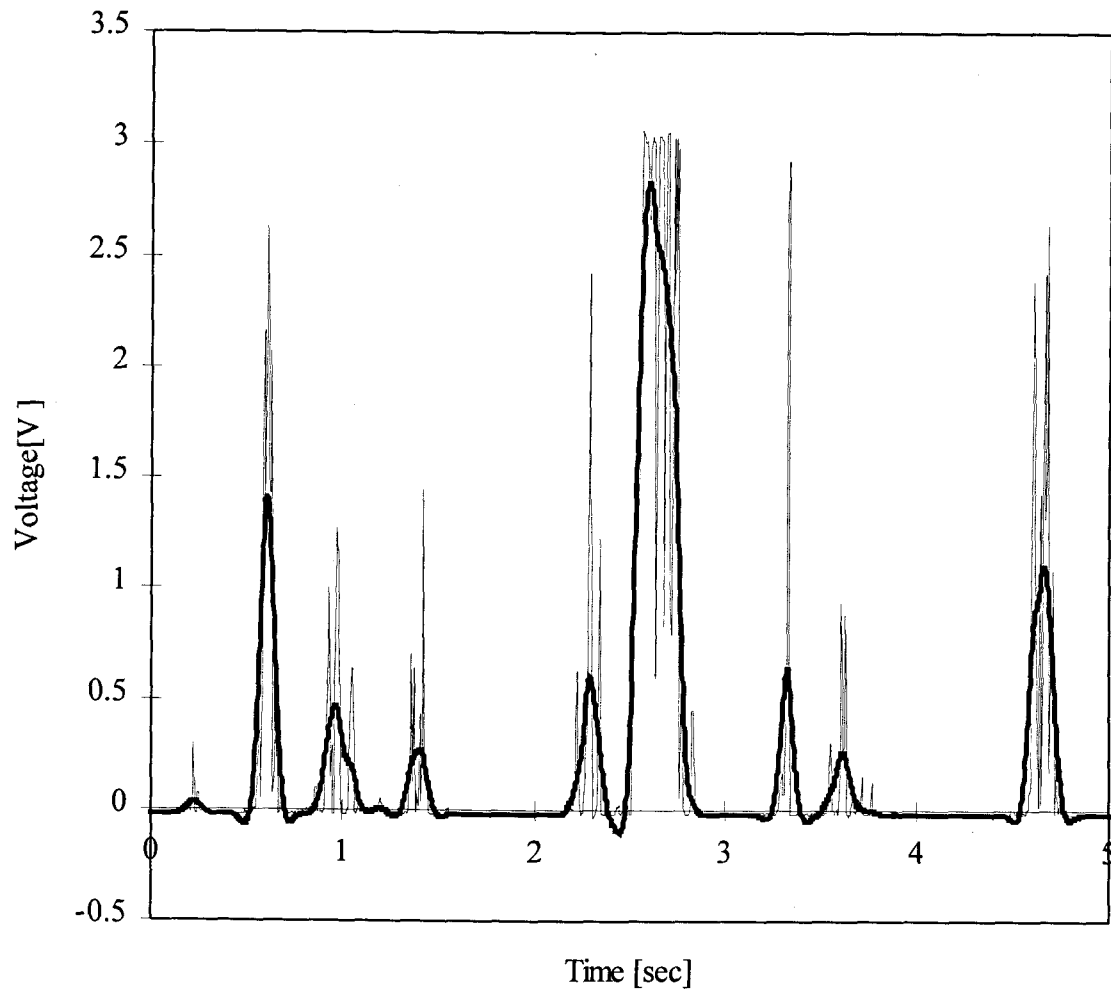


Figure 2.6 Effect of first-stage filter on signal shown in Figure 2.3
($d_p=2.0$ mm, $U/U_{mf}=1.4$).

$$v_{\text{cut}} = 0.05(v_{\text{max}} - v_{\text{min}}) \quad (2.3)$$

where v_{max} and v_{min} were the maximum and minimum values of the first-stage-filtered data, respectively. The resulting signal has a value of 1 when the probe is immersed in a bubble and a value of 0 when the probe is immersed in the dense phase. The three stages of the probe signal, overlaid, are shown in Figure 2.7.

A satisfactory filter is one that eliminates extraneous particle effects yet retains the bubble information. Whenever there is a positive voltage, there is a void (either a bubble or a high-void-fraction region) and whenever the voltage is zero, particles occupy the gap. When two bubbles are very close, it is subjective whether to consider them as one or two bubbles. The assignment of the bubble boundary location is also subjective due to the high void fraction region at the boundary and the large particle content in the bubbles. This is the nature of two-phase flow; the goal is to quantify bubble behavior with the greatest accuracy possible so that their properties can be related to a heat and/or mass transfer process of interest. A filter which appeared to capture as much information as possible was therefore selected. As long as the filtered signal appears to capture the desired information (by comparing the raw signal to the filtered signal and considering the comments above), then the resultant bubble properties are not overly sensitive to the value of the filter parameters. Note that the uncertainty associated with observed bubble properties arises primarily from these inherent bubble characteristics. This filtered signal was compared extensively to the 2D bed video tape to ensure that the raw signal was being interpreted and processed appropriately.

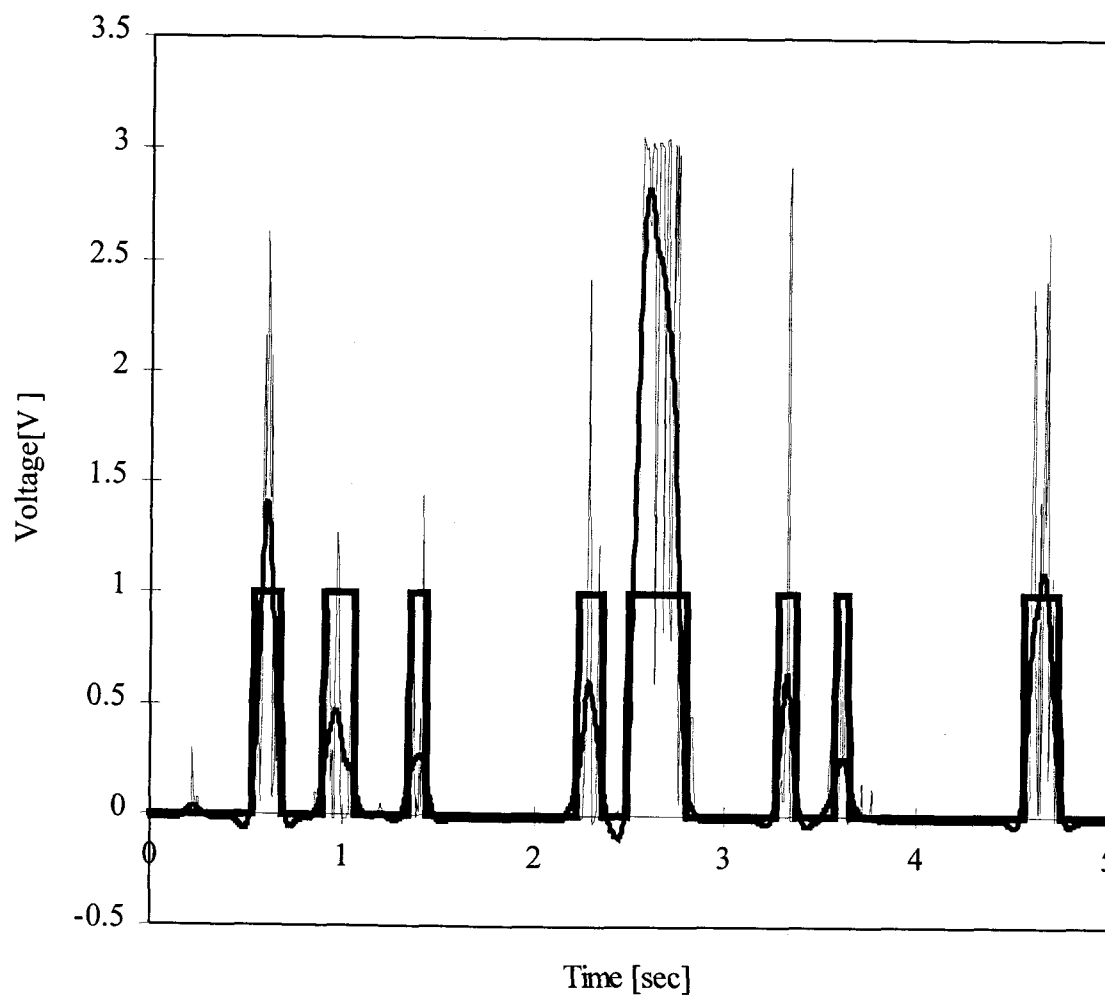


Figure 2.7 Effect of first- and second- stage filter on signal shown in Figure 2.3
($d_p=2.0$ mm, $U/U_{mf}=1.4$).

2.4 Calculation of Bubble Properties

The filtered probe signal yields information about the following bubble properties: bubble frequency, local bubble residence time, local bubble time fraction, bubble velocity, pierced length, bubble diameter, and visible bubble flow.

2.4.1 Bubble Frequency

The bubble frequency was found simply by dividing the number of bubble occurrences by the experiment time duration. Frequency calculations using the probe signal agreed closely with the visually-observed frequency. The probe information was more accurate because the probe will respond to any void through which light can pass. It was sometimes difficult, however, to determine if the probe was intercepting a bubble by observing the video-tape since the probe was located 1.6 cm from the Plexiglas and because of the inherent uncertainty in observations discussed above.

2.4.2 Local Bubble Residence Time and Local Bubble Time Fraction

The local bubble residence time is the time that the probe is immersed in a bubble during the passage of that bubble (emulsion phase residence time can be calculated similarly). It is calculated simply by determining how long the signal stays 'on'. A comparison of values obtained using the probe and those observed is shown in Figure 2.8. The observed value contains uncertainty due to inexact assignment of the bubble boundary and the time resolution of the video tape which is between one field

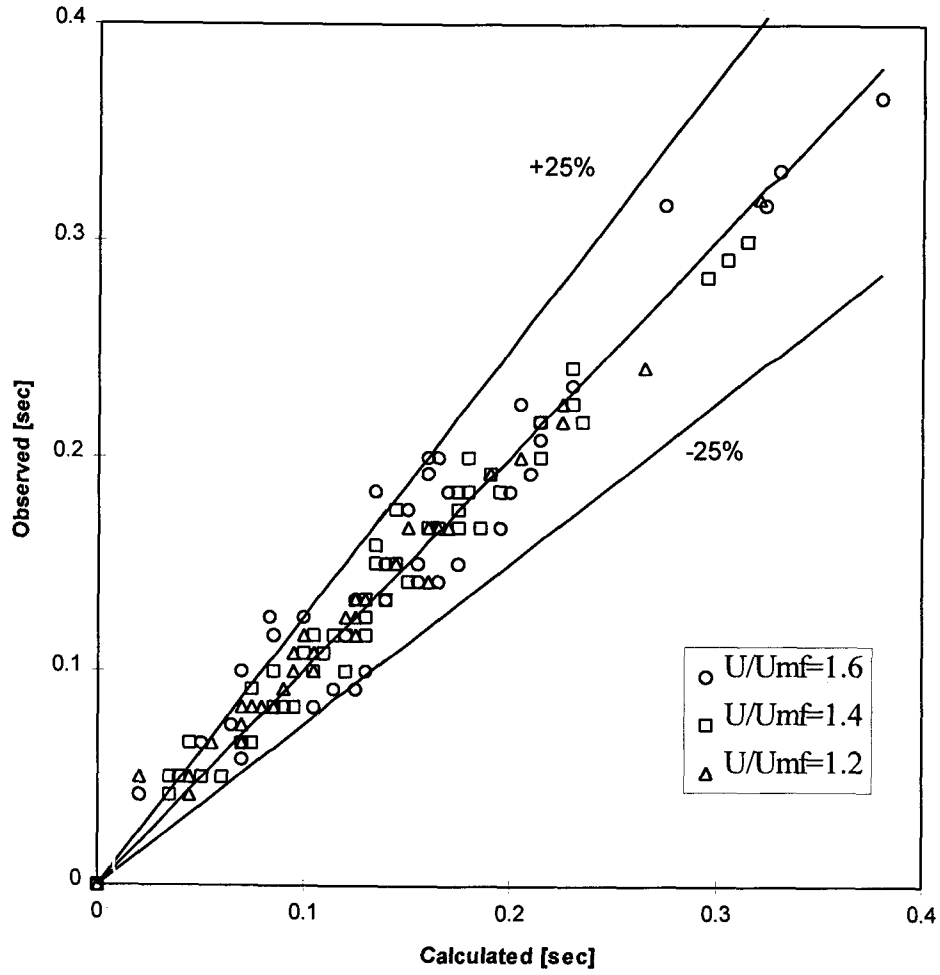


Figure 2.8 Comparison of observed and calculated local bubble residence time.

and one frame (16.7 - 33.3 msec). The fraction of total time the probe is immersed in the bubble (emulsion phase), which is called the local bubble time fraction (local emulsion time fraction), can also be calculated in a straightforward manner.

2.4.3 Bubble Velocity

The bubble velocity is a difficult parameter to specify since bubbles collapse, coalesce, have horizontal components of velocity, and have inexact boundaries. Werther (1974) showed that the instantaneous rise velocity of a bubble is a stochastic quantity and that the measurement of individual rise velocities is pointless. Instead of calculating individual rise velocities, a mean bubble velocity was found by cross-correlating the two filtered probe signals. When the upper probe signal is a close copy of the lower probe signal but lags by a time difference, t_{cc} , then the cross-correlation function will be a maximum at t_{cc} (Press et al., 1989). The distance between the two probes divided by t_{cc} is the mean bubble velocity. The bubble velocity, calculated using the cross-correlation, is compared to the relative frequency polygon of observed bubble velocities in Figure 2.9. Agreement relative to the uncertainty in the observed values as discussed above is considered good.

2.4.4 Pierced Length

The pierced length was found by multiplying the bubble velocity by the local bubble residence time. The relative frequency polygon for the pierced lengths calculated using

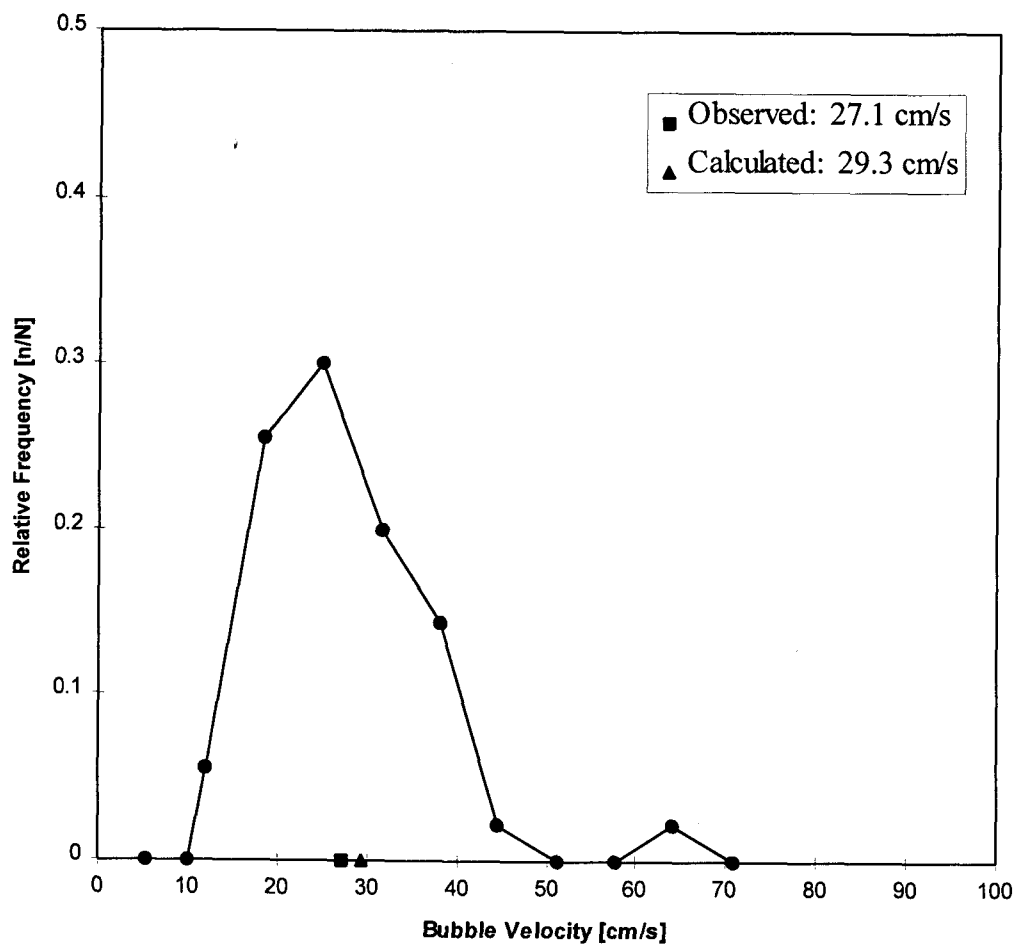


Figure 2.9 Comparison of observed and calculated average bubble velocity ($d_p=2$ mm, $U/U_{mf}=1.4$).

the probe information is compared to that of the observed pierced lengths in Figure 2.10 for one $U/U_{mf}=1.4$ run. The agreement is excellent considering the uncertainty inherent in the observed values.

2.4.5 Characteristic Bubble Diameter

The pierced length distribution can be used to calculate a characteristic bubble diameter. Bubbles of varying sizes traverse the probe and the probe detects a pierced length less than or equal to the bubble diameter. For the case of a 2D bed, the bubbles have an approximately circular cross-section and this shape will be assumed here, although a semi-circular shape could just as easily be used. The relationship between $\phi(y)$, the pierced length probability density function, and $f(d)$, the circle diameter probability density function, is as follows (Reid, 1955):

$$f(d) = \frac{1}{\pi d} \int_{\infty}^d y (y^2 - d^2)^{-\frac{1}{2}} \phi'(y) dy \quad (2.4)$$

Replacing the lower bound with d_{max} , the maximum pierced length measured, results in an equivalent integral. The value of d corresponding to the maximum value of $f(d)$ is the most probable (characteristic) circle diameter, d_{char} . Because f is calculated using the pierced length data, its values are discrete and the integration in Equation 2.4 is done numerically. Because the integration contains a non-integratable singularity at the upper limit, the Second Euler-Maclaurin summation formula (Press et al., 199), an open formula not requiring the integrand to be evaluated at the endpoints, was used. The probability density function, ϕ , and its derivative, ϕ' , were calculated numerically by

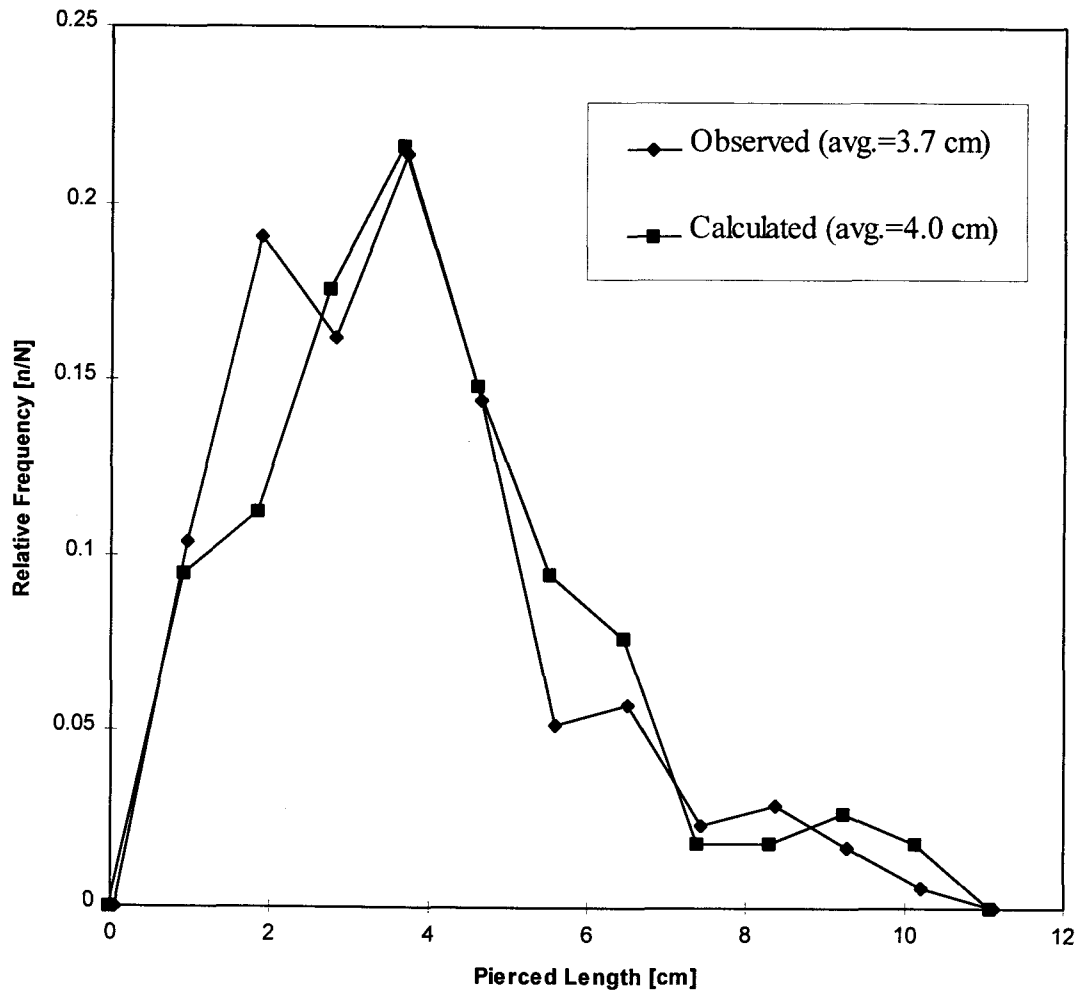


Figure 2.10 Comparison of observed and calculated pierced length ($d_p=2$ mm, $U/U_{mf}=1.4$).

putting the measured pierced lengths into bins. Choosing the number of bins equal to the square root of the number of measured pierced lengths available was found to be satisfactory. Since f depends on the derivative of the discrete function ϕ , ϕ was first smoothed using a low-pass filter. Because a large number of pierced lengths were required to accurately determine f , the pierced lengths from the five different runs at each fluidization velocity ratio were lumped together to calculate f . Observed bubble diameters, d_{eq} , were calculated using the following relation:

$$d_{eq} = \sqrt{\frac{\pi}{4} A_{bub}} \quad (2.5)$$

where A_{bub} is the observed bubble area. The calculated characteristic bubble diameter is shown in comparison to the relative frequency polygon of observed values for $U/U_{mf}=1.4$ in Figure 2.11. Note that the characteristic bubble diameter overpredicts the average observed bubble diameter. This is due not only to the uncertainty inherent in the observations, but also because the assumed bubble shape is not always accurate. As noted by Geldart and Cranfield (1972), long, thin, horizontal bubbles exist close to the distributor plate which grow into circles further up in the bed. For $U/U_{mf}=1.4$ in this 2D bed, the lower probe is located in the transition region between the long, thin bubbles and the circular bubbles. When the probe is intercepting long, thin horizontal bubbles, the average d_{eq} will be greater than d_{char} .

For 3D beds, appropriate bubble shapes can be assumed such as the spheroid family suggested by Tsutsui and Miyauchi (1980). Considering observations made by other researchers about the mushroom-cap shape of bubbles in 3D beds, a hemisphere shape was chosen. For this case, the probability distribution function of bubble

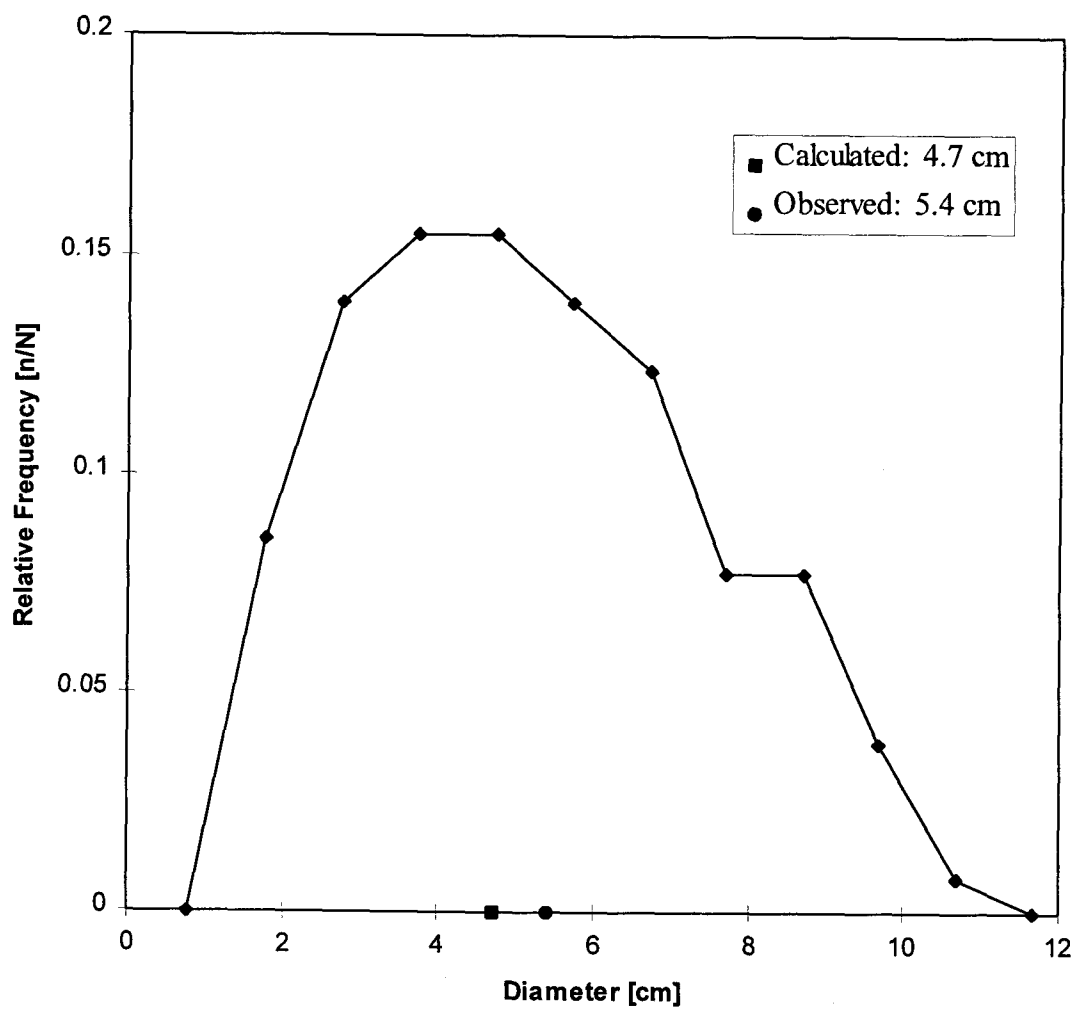


Figure 2.11 Comparison of observed and calculated bubble diameter ($d_p=2$ mm, $U/U_{mf}=1.4$).

diameters for bubbles ascending through a horizontal plane including the measurement plane is given by $F(d)$:

$$F(d) = -S \frac{d}{dy} \left(\frac{\phi(y)}{y} \right) \quad (2.6)$$

where

$$S = \int_0^{\infty} -\frac{d}{dy} \left\{ \frac{\phi(y)}{y} \right\} dy \quad (2.7)$$

and S is a constant.

2.4.6 Visible Bubble Flow

The visible bubble flow, Q_b , is the volume of gas that is carried by the rising bubbles across a horizontal plane per unit time in the bed assuming no gas flows through the bubble. In order to calculate the visible bubble flow based on measured bubble frequency and pierced length, the simplifying assumption is made that the bed is bubbling uniformly at a certain height. Assuming uniform bubble distribution across the width of the bed, the visible bubble flow across a horizontal plane including the probe is

$$Q_b = f_b \bar{y} TW \quad (2.8)$$

where f_b is the bubble frequency measured at a point by the probe, T is the bed thickness and W is the bed width.

2.4.7 Local Bubble Space Fraction

The local bubble (emulsion) time fraction is the fraction of time that a point is immersed in the bubble (emulsion) phase. It is determined by dividing the measured time the probe is in a bubble (emulsion) by the total sample period.

The instantaneous space fraction, δ , is the fraction of the bed that is occupied by the bubble phase at any given time. Like the visible bubble flow, the calculation of the instantaneous space fraction is based on the assumption that the bed is bubbling uniformly. This assumption is necessary since the bubble properties were measured at only one point in the bed cross-section. The instantaneous space fraction can be calculated as follows:

$$\delta = \frac{Q_b}{A_{bed} U_b} = \frac{f_b \bar{y}}{U_b} = f_b \bar{\tau}_b \quad (2.9)$$

The instantaneous emulsion phase fraction could be calculated similarly. Note that the instantaneous space fraction is equal to the local bubble time fraction when the assumption is made that the bed is bubbling uniformly.

2.5 Instantaneous Heat Flux Sensor

In order to measure instantaneous heat transfer coefficients on a horizontal tube submerged in a high-temperature fluidized bed, several constraints first had to be met. First, the instantaneous heat flux sensor had to be able to survive the abrasive environment caused by the solid particles in the fluidized bed. Second, the sensor had to

be able to withstand the high-temperatures (up to 1100 K) encountered in the fluidized bed. By cooling the tube on which the sensor was mounted, however, the transducer temperature was in practice expected to not exceed 500 K. This temperature of 500 K was therefore the design temperature. Third, the sensor had to fit onto a 5.08 cm diameter stainless steel tube with a wall thickness of 0.95 cm. Finally, the sensor and its associated instrumentation must have a frequency response fast enough to capture bubble and particle events. For the operating conditions considered in the present work, bubble frequency was on the order of 1-5 Hz. The response of the sensor to particle activity depends somewhat on its size. A sensor with a small active area which might cover only a couple of particle contact points would require a higher frequency response than a sensor with a larger active area. A larger sensor would not be able to measure the high frequency fluctuations which occur during moving emulsion phase contact. A frequency response of at least 100 Hz was recommended by George (1993) for similar operating conditions and this is considered more than sufficient.

Several researchers have measured instantaneous local heat transfer rates (or, equivalently, instantaneous local heat transfer coefficients) as mentioned above. Most of these studies utilized electrically heated foils or thin metal films of low heat capacity as heat flux traducers. The operating principle of these devices and the signal conditioning methods used require that the transducer surface be at a higher temperature than the fluidized bed. This fact, combined with limited abrasion resistance, means that these sensors are not capable of surviving in a high-temperature fluidized bed. Thermopile type gages, which use arrays of thermocouple junctions or resistance temperature

detectors to obtain the temperature difference across thin wafers of insulating material, are not abrasion resistant. Thus, they must be covered with a protective film such as shim stock such as those used by George (1981) and Goshayeshi (1989). The resultant frequency response is much too slow to accurately measure instantaneous local heat flux. The thermopile-type transducer used by George and others, which was covered by stainless steel shim stock, had a frequency response (defined as the frequency corresponding to the time interval after application of a step change in surface heat flux for the output voltage to remain within 2% of the final value) of 1.042 Hz (960 ms). Without the shim stock, the frequency response was 12.5 Hz (80 ms). The circular foil heat flux gage, also known as a Gardon gage (Gardon (1960)) has been found by Gosameyer (1979) and George (1987) to be unsatisfactory for use in high-temperature fluidized beds. These researchers determined that the Gardon gage did not accurately translate the heat flux to an output voltage unless the heat flux was uniform over the gage surface.

George (1987) found that a device based on surface temperature measurement and use of the heat conduction solution for the semi-infinite wall is suitable for determination of instantaneous local instantaneous heat transfer coefficients. A few researchers (Khan and Turton, 1992; Pence et al., 1994; Figliola, 1984) have since used his design to measure instantaneous local heat transfer coefficients, although not under the conditions in the present study. The sensor selected for the present work was that based on the design of George (1987), Smalley (1990) and George and Smalley (1991).

2.5.1 Design and Principle of Operation of Heat Flux Transducer

The principle of operation of the transducer is as follows. The (fluctuating) surface temperature of the tube and the in-wall temperature are measured and used as boundary conditions in the solution to the one-dimensional unsteady heat transfer in a semi-infinite medium which is assumed to occur. The in-wall temperature is measured at a location sufficiently far into the tube wall so that temperature fluctuations are dampened and the in-wall temperature is essentially constant.

The fluctuating surface temperature is measured using an eroding-type thermocouple. Although eroding-type thermocouples are manufactured by Nanmac Corporation of Framingham, Massachusetts, they are too small for the present use. A schematic of the type of thermocouple used in this work is shown in Figure 2.12. Thin thermocouple sheets are separated by mica sheets. The thermocouple junction is formed by small burrs at the surface which bridge over the thin mica sheets. Thus a thermocouple of extremely small thermal mass is formed at the surface which is continually renewed by the abrasive bed. George and Smalley formed these thin metal sheets by hammering and annealing thermocouple wire until the desired thickness was obtained. In the present work, thin sheets of thermocouple metal, which were commercially available, were welded to thermocouple wire. The heat flux transducer and the instrumented cylinder are shown in Figure 2.12. The cylinder is explained in detail by Smalley (1990). The heat flux transducer slips into the cylinder such that points A and B match-up. The seal at B is created by a light press fit and the seal at A is made using a small amount of high-temperature silicone gasket seal. The transducer surface is

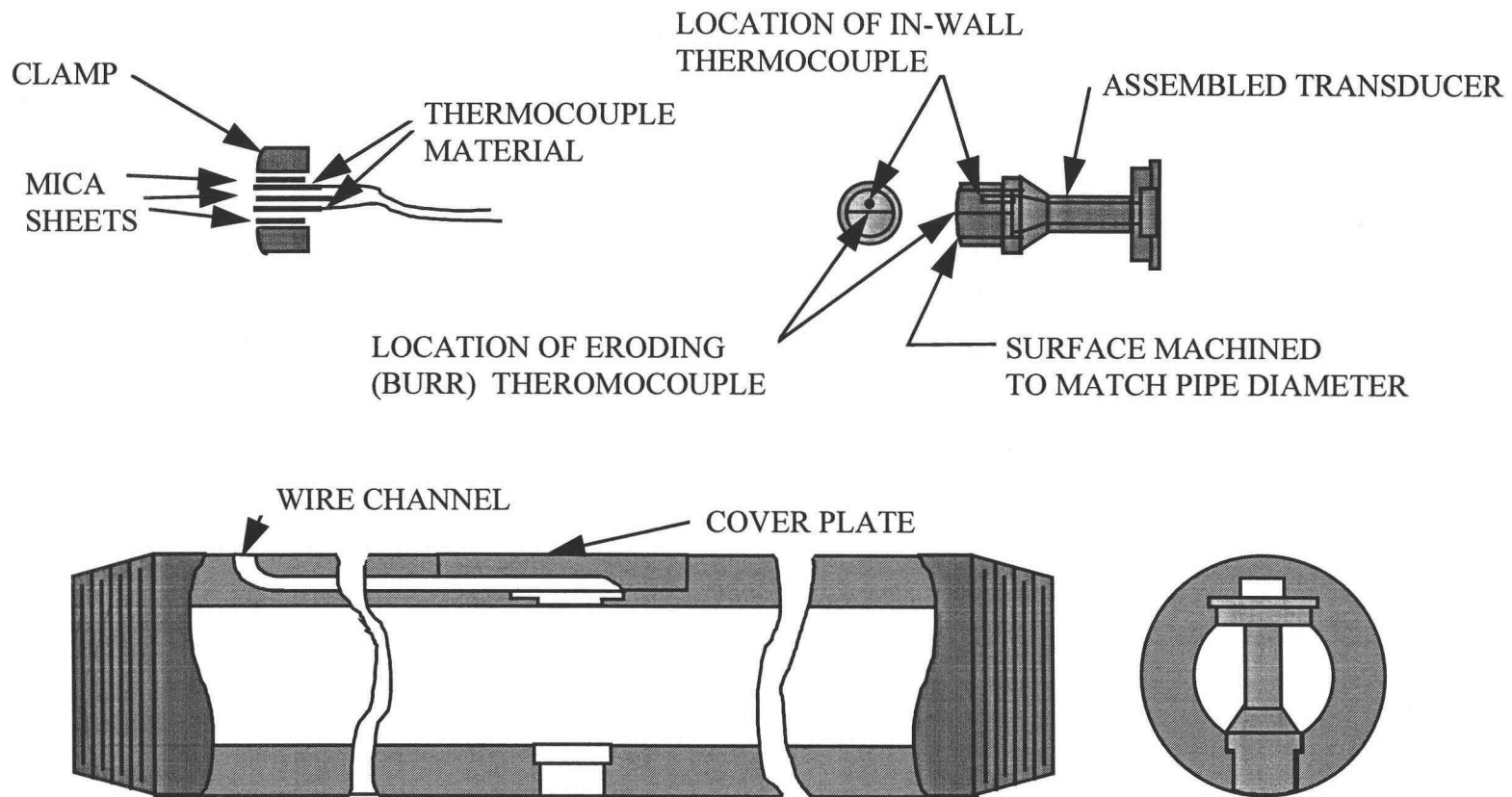


Figure 2.12 Eroding thermocouple, heat flux transducer, and instrumented cylinder.

machined to match the cylinder. A cover plate was fitted over the non-active end of the transducer. The thermocouple wires were located along the tube in the wire channel. The wire channel cover plate was retained by stainless steel screws. There was a 0.25 mm wide air gap between the cylinder and the transducer clamping ring to help ensure one-dimensional heat transfer within the transducer.

Both thermocouples were constructed of ANSI type E thermocouple wire which can operate in the range $-100\text{ }^{\circ}\text{C}$ to $1000\text{ }^{\circ}\text{C}$ and has the highest Seebeck coefficient of the common thermocouple pairs. The thermocouple foils sheets were approximately 0.025 mm thick. The mica sheets, which were used to electrically insulate the thermocouple transducer body were approximately 0.025 mm thick, and the mica sheets which were used to insulate the thermocouple sheets from each other was approximately 0.0125 thick. The mica sheets were split from samples provided by Perfection Mica Company. The effective width of the eroding thermocouple junctions was approximately 4 mm. The in-wall thermocouple was formed by welding and then was silver-soldered into a drilled hole in the thermocouple clamp. The in-wall thermocouple was located approximately 6 mm from the cylinder surface.

The measured values of the surface temperature, $T_s(t)$, and the in-wall temperature, T_i , were used as boundary conditions to solve the unsteady conduction problem. This solution could be used to calculate the surface heat flux, $q_s(t)$ using either numerical or analog methods. An electric analog circuit was provided by Dr. Alan George and was used in the present work. The analog circuit has the advantage of providing real time solution and the ease of processing several signals.

The solution to the unsteady conduction problem for large values of time is independent of initial conditions and is given by (George, 1987):

$$q_s(t) = \frac{k_s}{L} \left[\langle T_s \rangle - T_i \right] + \sqrt{\frac{k_s \rho_s c_{p,s}}{\pi}} \int_{\eta=0}^t \frac{1}{\sqrt{t-\eta}} \left(\frac{dT_s}{d\eta} \right) d\eta \quad (2.10)$$

It should be noted that this solution for large time is independent of the initial temperature distribution within the transducer which greatly simplifies the problem. The first term in Equation 2.10 represents the time-average heat flux. The second term is the solution to the semi-infinite medium conduction problem with a step change in surface temperature (Holman, 1976) and applying Duhamel's superposition integral. This second term is a function of time and represents the fluctuations in heat flux, $\delta q_s(t)$, due to surface temperature fluctuations δT_s . To use this equation, the transducer must have been at the desired steady state bed operating conditions for at least 5 seconds as calculated for the present application (George, 1987). This was easily achieved in the present work since, as a minimum, several minutes are required to establish steady state in the fluidized bed facility. Some researchers who have used this type of formulation for a numerical solution have erred by not discarding the first approximately 5 seconds of calculated heat flux, so it is advised to use this solution only where appropriate. Calculations from the second term in Equation 2.10 also reveal that a minimum distance from the tube surface of 6.4 mm is required for the in-wall temperature measurement, T_i , to remain approximately constant. Since these conditions were met in the present application, knowledge of the initial condition was not necessary.

2.5.2 Analog Signal Conditioning Unit

The analog solution to Equation 2.10 provides a DC voltage which is linearly related to the heat flux fluctuations, $\delta q_s(t)$. The design of this circuit has been described in detail by George (1987) and Smalley (1990) and will be briefly outlined here. The first term in Equation 2.10, representing the time-average heat flux, is straightforward and does not need any signal conditioning techniques. Using the Laplace transformation and the heat conduction formulation for the semi-infinite medium, the following transfer function is obtained:

$$\frac{\overline{\delta q}(s)}{\overline{\delta T}_s(s)} = \sqrt{k\rho c} \sqrt{s} \quad (2.11)$$

where s is the Laplace transform parameter. Let

$$\overline{v}(s) = \beta_1 \overline{\delta q}(s) \quad (2.12)$$

$$\overline{e}(s) = a_1 \overline{\delta T}_s(s) \quad (2.13)$$

where β_1 and a_1 are constants. The transfer function for the signal conditioning unit is therefore

$$\frac{\overline{v}(s)}{\overline{e}(s)} = \frac{\beta_1 \sqrt{k\rho c}}{a_1} \sqrt{s}. \quad (2.14)$$

It follows that the frequency response of the signal conditioning unit must be

$$\frac{v(j\omega)}{e(j\omega)} = \frac{\beta_1 \sqrt{k\rho c}}{a_1} \sqrt{\omega} \angle 45^\circ \quad (2.15)$$

This means that the circuit must provide an amplitude ratio proportional to the square root of the frequency and a constant phase angle of 45°. An equivalent form of this relationship was first given by Skinner (1960). A circuit was built to represent this transfer function. A circuit which incorporates this analog signal conditioning circuit was built to amplify the thermocouple signals and filter noise. The output voltage of the circuit is used to calculate the heat flux using the following relation:

$$q_s(t) = \frac{k}{L} \left[\langle T_s \rangle - T_i \right] + \frac{1}{\beta} \left[v_2(t) - \langle v_2 \rangle \right] \quad (2.16)$$

where β is the calibration constant discussed below and $\langle v_2 \rangle$ is the time-average value of the output voltage, $v_2(t)$. The instantaneous heat transfer coefficient is then given by

$$h(t) = \frac{q_s(t)}{T_{bed} - \langle T_s \rangle} \quad (2.17)$$

George and Smalley (1991) checked the input-output relationship for the analog signal conditioning circuit above by subjecting the transducer to a step change in surface heat flux and checking that a near step change in output voltage, v_2 , was produced. They found, instead, that the circuit produced an output voltage with overshoot of approximately 30%. They showed that contact resistance between the thermocouple and the tube could account for this overshoot. In order to correct for the effects of contact resistance, they experimentally adjusted the circuit until the overshoot was no longer present.

Using Equations 2.16 and 2.17, the instantaneous heat transfer coefficient can be calculated for measured $T_s(t)$, T_i , T_{bed} and $v_2(t)$ if k/L and β are known. George and

Smalley (1987) first computed these analytically based on the transducer and thermocouple wire physical properties. They found, however, that this method contained too much uncertainty and instead calibrated k/L and β . This was the technique followed in the present work. The input-output relationship of the transducer and circuit were tested by applying a step change in surface heat flux and recording the output voltage, v_2 . The data acquisition equipment consisted of an IBM AT computer, a Data Translation Hybrid board and LabTech Notebook software. The voltage was recorded at 200 Hz which is the frequency to be used in the fluidized bed experiments. The radiation source was a Barnes 11-210 Radiation Reference Source. The step change was produced by moving a shutter in front of the heat source. The circuit was adjusted until the overshoot was eliminated and the time response of the transducer and circuit were greater than 100 Hz. A plot of the time response of the transducer and circuit are shown in Figure 2.13. The time response is less than 9 ms which corresponds to a frequency response greater than 111 Hz. The exact frequency response is not known, since it is uncertain whether the limiting factor in determining the frequency response was the transducer and circuit or the ability to move the shutter quickly enough. In any case, this frequency response is more than adequate for the present application. It was also found that the signal remains constant for at least 5 seconds. Events in the bed are expected to fluctuate more rapidly than this, so this response is more than adequate.

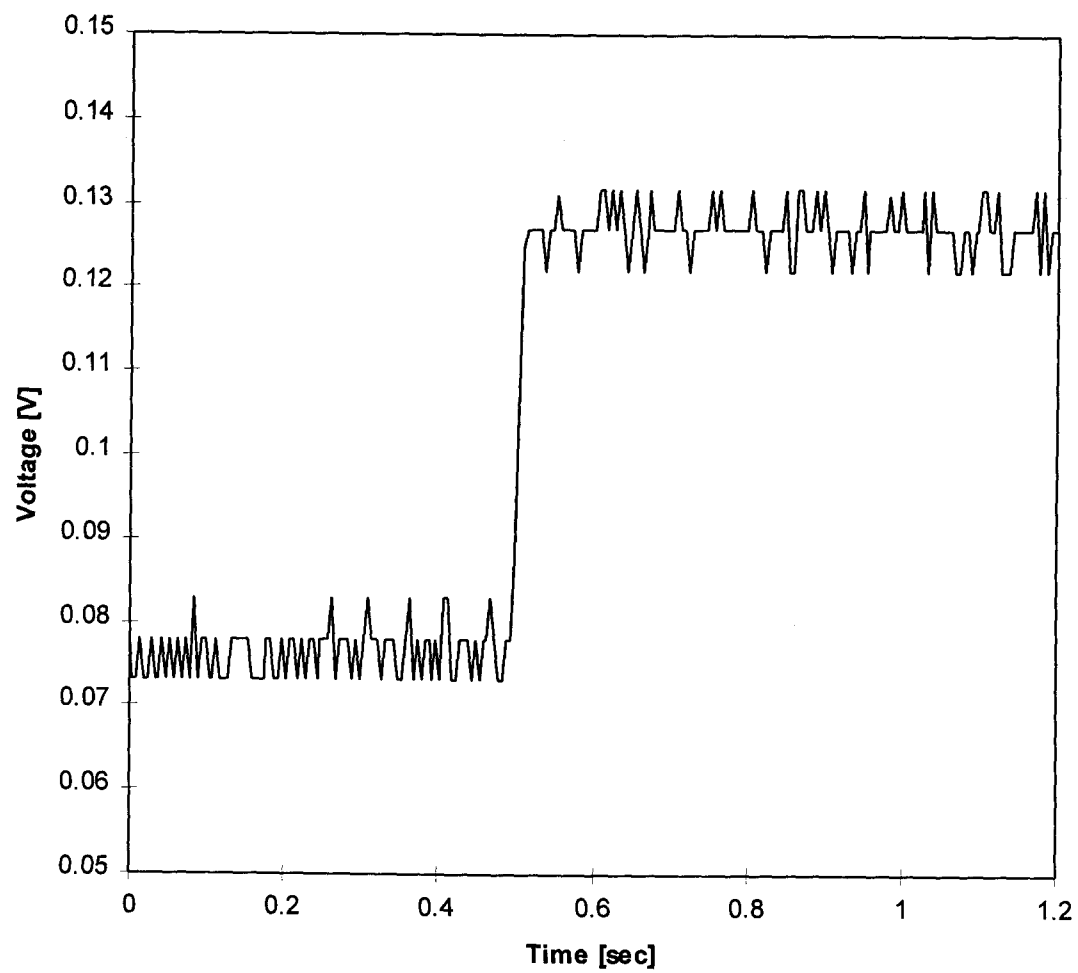


Figure 2.13 Time response of heat flux transducer.

2.5.3 Calibration of β

Calibration of the heat flux transducer and associated signal conditioning unit to determine β was conducted using a Barnes radiant heat flux source to produce a step change in the surface heat flux. The calibration constant, β , was then found from the following relation

$$\beta = \frac{\Delta v_2}{\Delta q_s} \quad (2.18)$$

where β is a function of tube surface temperature.

A commercial heat flux transducer with known calibration characteristics was used to determine the step change in heat flux at the surface of the tube. The commercial transducer used was a Micro-Foil heat flow sensor model 20455-1 made by RdF Corporation, Hudson, New Hampshire. The Micro-Foil transducer was attached to a tube using OmegaTherm 201 High Temperature Thermally Conductive Paste made by Omega Engineering, Inc., Stamford, CT. Both transducers were coated with soot from an acetylene torch, with the oxygen turned off, so that the surface emissivity would be the same for each transducer. A schematic of the calibration set up is shown in Figure 2.14. The magnitude of the heat flux was measured by carefully locating the tube with the Micro-Foil transducer in front of radiation source and measuring the heat flux for a given heat source temperature and tube surface temperature (approximately room temperature). This was done for several heat source temperatures. The maximum heat flux obtained was 40,000 W/m². The next step was to repeat the process using the experimental transducer for the same surface

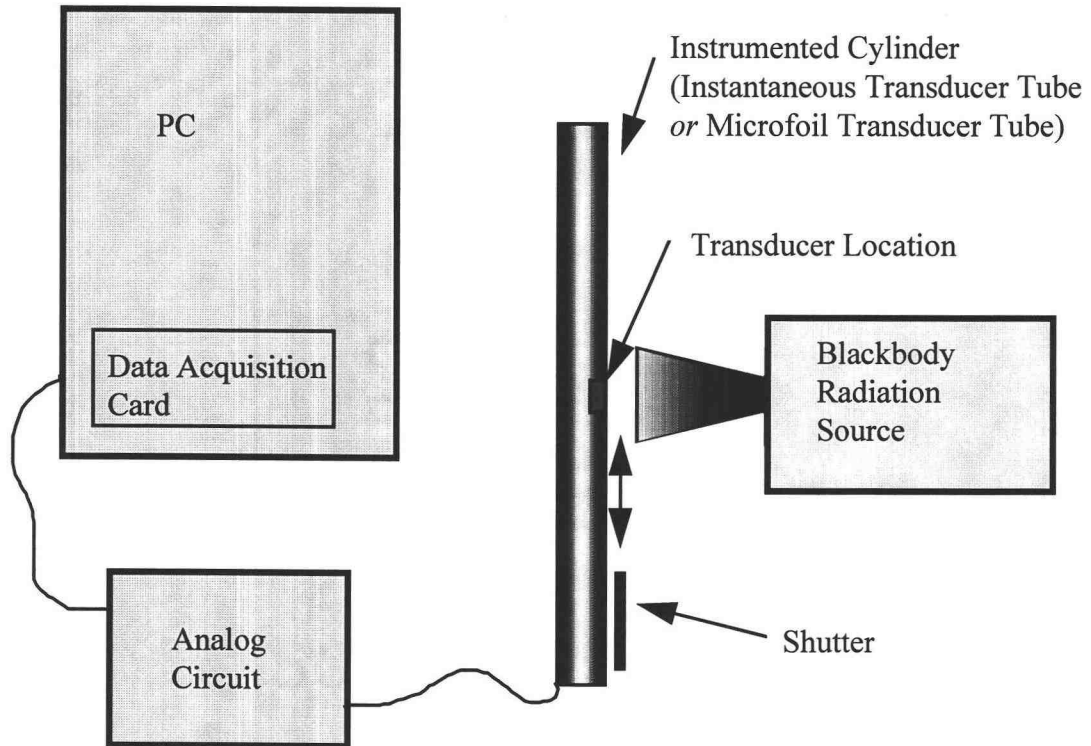


Figure 2.14 Equipment lay-out for calibration of β .

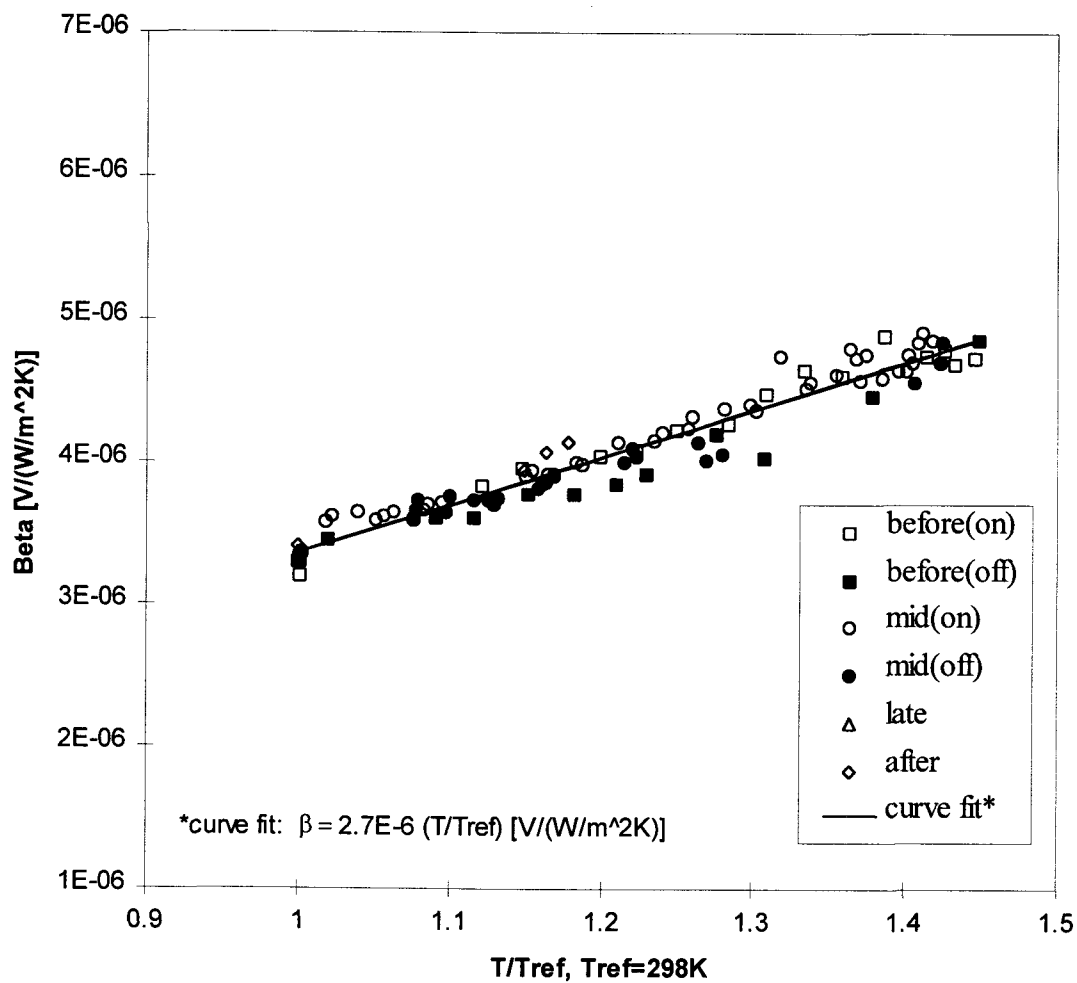
temperature. As expected, β was found to be independent of heat flux. The calibration process was then extended to determine β for surface temperatures higher than 298 K. Four band heaters, rated at each 200 W, were fastened to the tube and used to control its temperature. The tube was heated to a temperature of 460 K. Measurements of β were taken at approximately 2 K intervals while the tube was slowly heating up and cooling down. The results of these measurements are shown in Figure 2.15. Also shown on this Figure are repeated calibrations halfway through the fluidized bed experiments and at the completion of the experiments. The data show that the calibration of β was repeatable and did not change significantly during the experiments. Linear regression was performed on the calibration data for β and the following relationship was determined:

$$\beta = 2.7 \left(\frac{T}{T_{\text{ref}}} \right) \left[\frac{\mu\text{V}}{\text{W}/(\text{m}^2\text{K})} \right]; \quad T_{\text{ref}} = 298 \text{ K.} \quad (2.19)$$

The circuit provided a noise output of 10 mV peak-to-peak which, for the conditions of operation in the present work, corresponds to a fluctuation in the measured instantaneous local heat transfer coefficient of approximately 11 W/(m²K).

2.5.4 Calibration of k/L

The calibration for the value of k/L was attempted in the OSU high-temperature fluidized bed facility (described later). The method tried was placing both cylinders in the bed at the same height with the transducers located facing down. The heat transfer coefficient at this angular position is the least effected by changes in



superficial gas velocity. It was assumed that the heat transfer coefficient would be the same for both transducers since the bed condition was the same. With equal heat transfer coefficients, the measured values of the Micro-Foil heat flux and surface temperature, bed temperature, T_s , and T_i , the value of k/L can be calculated. It was found, however, that the tube surface temperature, T_s , and the in-wall temperature, T_i , were too close to each other to be used accurately to determine the heat flux.

It was decided instead to measure the average heat flux using the tube with the Micro-Foil transducer. Two approaches were investigated. First, both tubes were placed in the bed at the same elevation and separated by 0.2 m. The transducers on each tube were located at the same angular positions. The Micro-Foil transducer was used to measure the average heat flux (and average heat transfer coefficient) and the experimental transducer was used to measure the fluctuating heat flux (and fluctuating heat transfer coefficient). The fluctuating component has zero mean value, as shown in Equation 2.16. The instantaneous heat transfer coefficient was then found by adding together the average and fluctuating values. The second approach taken was to place each tube alone in the bed and take measurements at each of the bed operating condition and transducer angular position for each tube. The instantaneous heat flux and heat transfer coefficient were then found in the same manner as the first approach. It was found that placing both tubes in the bed did produce interference and thus the second approach was taken. The advantage of using this approach over actually calibrating k/L as explained above is that this approach is effectively calibrating k/L at every operating condition.

2.6 OSU High-Temperature Fluidized Bed Facility

2.6.1 Apparatus

A schematic of the Oregon State University high-temperature fluidized bed test facility is shown in Figure 2.16. Detailed discussion of different components of the facility as well as recommended operating procedures are given by Junge (1978) and Alavizadeh (1989). A brief discussion of the principal components of the facility will be outlined here. Referring to Figure 2.16, combustion and fluidization air is compressed by a roots style positive displacement blower. The compressed air flow is then metered through an ASME standard venturi meter and directed into an industrial propane burner. The pressure difference between the venturi meter throat and upstream section is monitored using a manometer. Downstream air pressure and temperature are also measured. The air flow rate and superficial gas velocity in the bed are calculated based on the calibration by Gosmeyer (1979). Propane flow is regulated to the burner and is burned in a refractory lined combustion chamber. A proportional type controller is used to regulate the propane flow rate and provide the desired gas temperature at the combustion chamber exit. The fuel flow rate can also be manually controlled by a bypass valve. The air flow rate and its inlet pressure to the propane burner are controlled by adjusting the air inlet and bypass valves. The hot combustion gases are directed by a plenum into a 0.3 m by 0.6 m (1 ft by 2 ft) test section through a nickel based alloy distributor plate designed by Pidwerbecki (1994). The distributor plate consists of two flat alloy plates with a 9 x 17 square hole array.

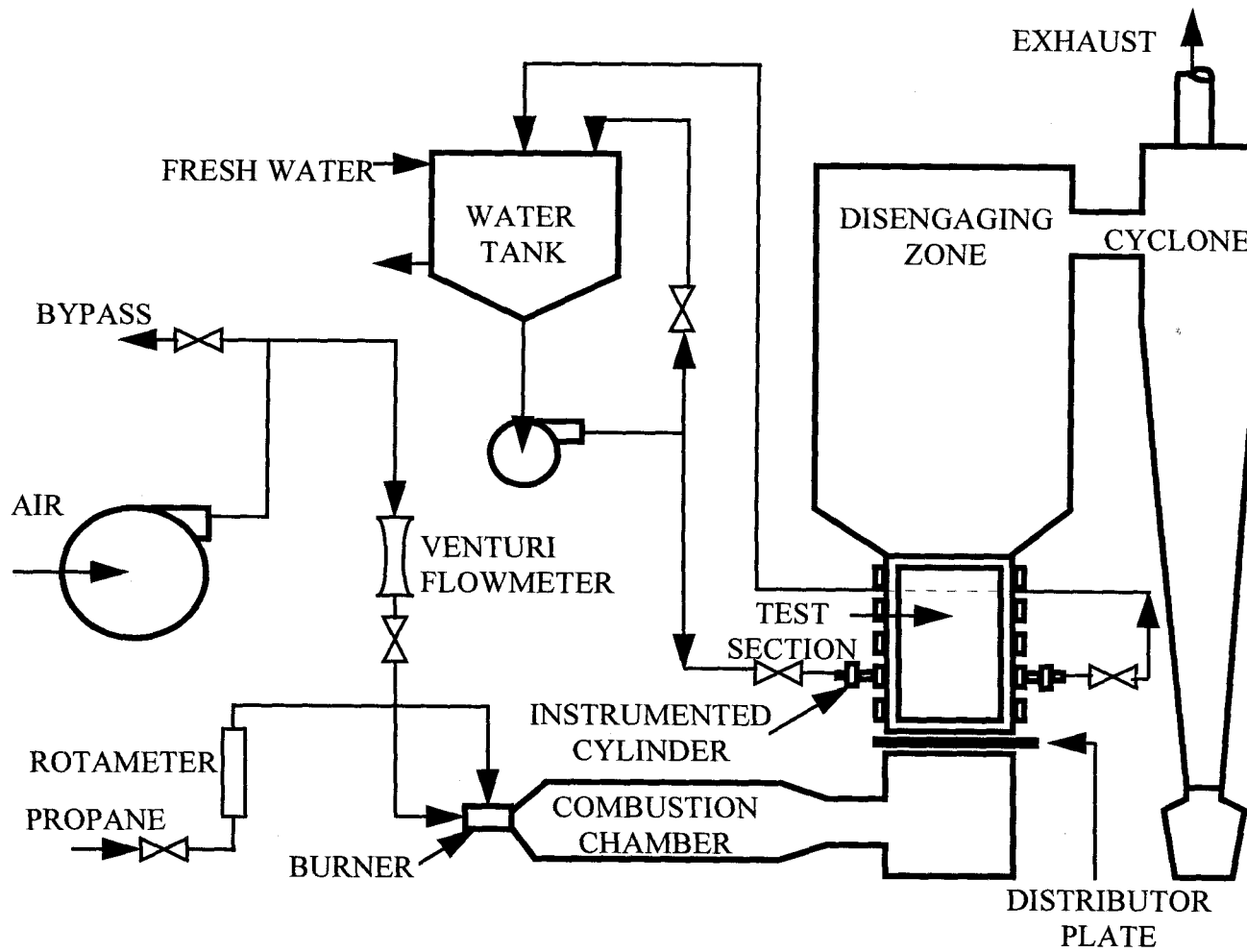


Figure 2.16 OSU High-temperature fluidized bed facility.

The hole diameters are 7.9 mm and the centerline-to-centerline hole pitch is 25.4 mm. Sandwiched between the plates is a 40 mesh Inconel 800 screen to keep the particles from falling through the distributor plate. After the distributor plate, the hot gases flow through the fluidized bed test section and then through a disengaging zone and finally out through an exhaust pipe. The disengaging zone serves to prevent particles from escaping. Any particles that escape are collected by the cyclone separator in a bucket. A glass viewport is provided at the top of the disengaging zone allowing visual observation of the top of the bed and also serves as a place to add particles into the test section. A plug is located just above the distributor plate to allow particle drainage from the bed. A large door mounted on a trolley system permitted access to the test section and instruments for maintenance and inspection purposes.

The test section was constructed to accommodate horizontal mounting for both single tubes and tube arrays with different tube configurations. Fifteen mounting ports were provided on each side of the test section with an equilateral triangular configuration and 15.2 cm (6-inch) spacing between centers. The ports were set in 3 columns and 5 rows. The centerline of the bottom row was 30.48 cm (1 ft) above the distributor plate. For the current research, the instrumented tube was located 43.7 cm above the distributor plate and 34 cm from one of the 0.30 m side walls of the test section. The tube was located so that the transducers were positioned as near as possible to the center of the test section. The tubes (and transducers) were cooled by circulating water. The coolant system was modified for the current work to provide maximum cooling capability. This was accomplished by eliminating a heat exchanger

and directly cooling the heat transfer tubes and optical probes. A rotary union allowed adjustment of the instrumented tube to the desired angular positions. This mounting arrangement allowed the rotation of the cylinder to different angular positions without disconnecting any piping. A single heat flux transducer was used to take data at all angular positions considered. The test section walls were instrumented with five type-K thermocouples, three located in the fluidizing region, one on the wall of the disengaging zone, and one on the ceiling of the disengaging zone. Pressure taps were located at the bottom and top of the bed and hooked up to a manometer to detect the pressure drop across the bed.

Two mounting ports were drilled into the test section in order to insert the optical probes in the bed. The holes were drilled such that the probes protruded into the bed at an 8° angle of declination to ensure that vapor or air would not get trapped at the end of the cooled portion of the probes. The probes were located directly below the lower stagnation point (0°) on the tube and in-line with the center of the tube. The upper optical probe was located 5.08 cm (2 inches) below the lower stagnation point of the tube and the lower optical probe was located 5.08 cm (2 inches) below the upper probe. The upper probe location was selected to be as close as possible to the tube yet not be in the surf which occurs at the bottom of the tube since it was desired to measure rising bubble properties only. The lower probe location was selected so that the distance from the upper probe was large enough to give adequate accuracy for the bubble velocity calculation yet close enough to ensure that both probes were detecting

the same bubble. A schematic of the optical probe and tube locations is shown in Figure 2.19.

2.6.2 Data Acquisition System

An HP3852A with HP44705A and HP 44708A cards, controlled by a personal computer, was used to record the Micro-Foil heat flux voltages and surface temperatures. This system was also used to record the bed temperatures and the surface temperatures of the experimental transducer. The data acquisition program was written in HT BASIC and it was used to collect the voltage data, convert these into local heat fluxes and temperatures and then calculate the local heat transfer coefficients at each position on the instrumented tube. A personal computer computer with a Hybrid Data Translation board and Labtech Notebook software was used to record the higher speed voltage samples of the optical probes and the heat flux transducer at 200 Hz. These signals and data were reduced later in a FORTRAN program into bubble properties, heat transfer coefficients and other related parameters.

2.7 Experiments and Test Procedure

Experiments were conducted in the high-temperature fluidized bed to acquire data for the instantaneous optical probes and the instantaneous, local heat transfer coefficients on an immersed horizontal tube. The purpose of the experiments was to examine the relationship between the information provided by the optical probes and

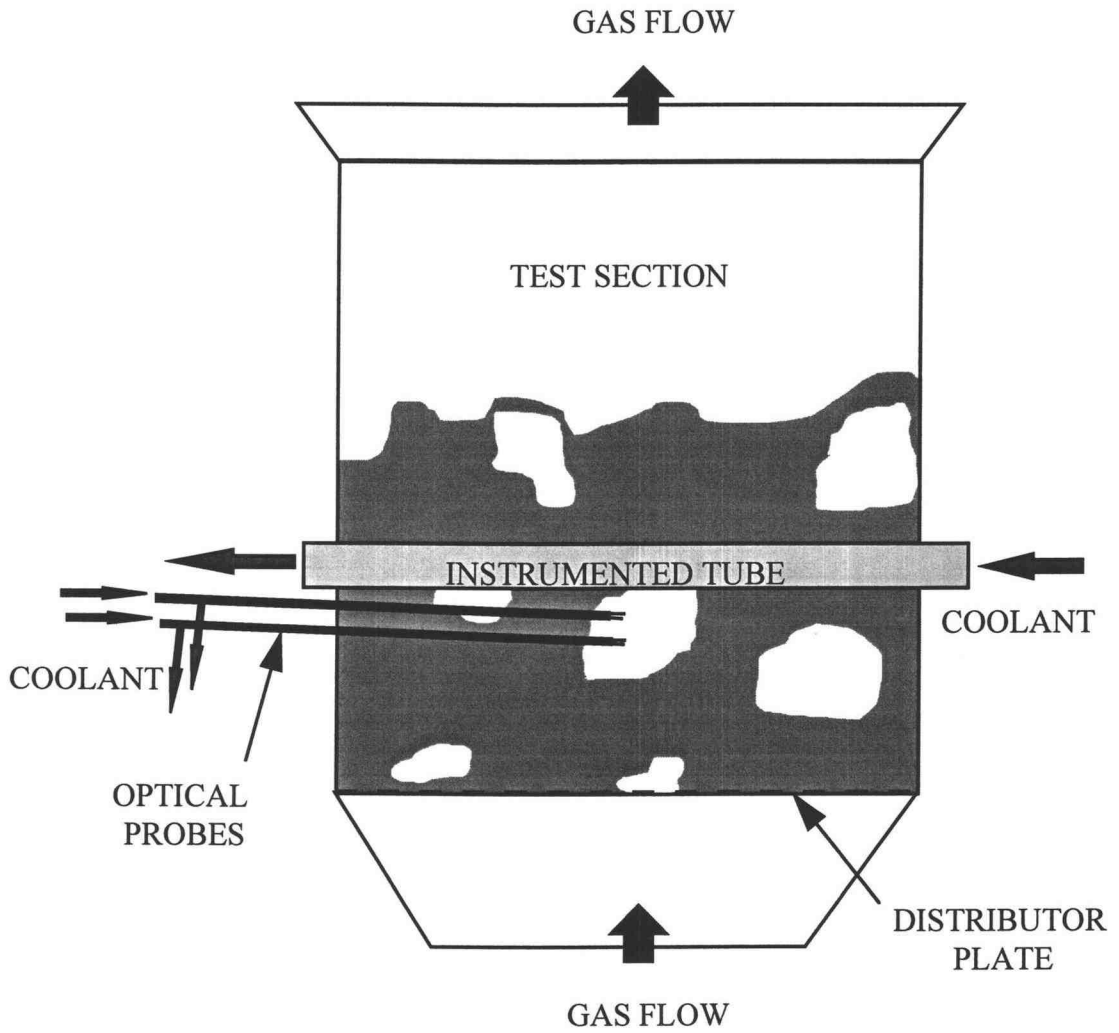


Figure 2.17 Schematic of test bed.

heat flux sensors and their dependence on the following four variables: particle size, superficial velocity, temperature, and tube circumferential location.

A refractory material with commercial designation, Ione Grain, with density 2700 kg/m^3 was used as the bed material (particles). The chemical composition of the particles is 53.5% silica, 43.8% alumina, 2.3% titania and 0.4% other substances. The particle thermal properties are similar to those commonly used as bed material in fluidized-bed combustors and are listed in detail by Chung and Welty (1989). Two particle sizes were used with nominal diameters of 2.0 mm and 2.9 mm. The particle sizes were determined by mechanical sifting performed by Pidwerbecki (1994) and using the cut between a Number 8 and Number 10 standard Tyler Screen for the 2.0 mm diameter and a Number 4 and Number 5 standard Tyler Screen for the 2.9 mm diameter.

Five bed temperatures, 600 K, 700 K, 800 K, 900 K and 1000 K, were used with the 2.0 mm particles and three bed temperatures, 700 K, 800 K and 900 K, were used with the 2.9 mm particles. Since the bubbling bed fluidization was of interest, the fluidization velocity was varied from just above minimum fluidization (U_{mf}) to over $1.6 U_{mf}$. The maximum fluidization velocity used was determined by the blower capacity. Data were taken with the heat flux gages positioned at 0° , 45° , 90° , 135° and 180° relative to the lower stagnation point.

The fluidized bed was allowed to reach steady state operating conditions at the selected temperature and superficial gas velocity. Because of the large mass of the test facility, it took several hours to heat up the facility to the experimental test

temperatures. Temperature readings from the two thermocouples that were immersed in the bubbling bed, one located in the lower portion of the bed and the other located in the upper portion of the bed along with the tube surface temperature readings were used to determine steady state. The requirements for steady state were that the two bed temperature readings matched each other and that none of the (average) temperature readings were changing with time. For a bubbling bed of large particles, the temperature is nearly constant throughout the bed. Near or less than minimum fluidization, however, temperature gradients can exist and data taken at those conditions should be considered unreliable.

The bed temperature was maintained within ± 5 K of the specified value for all cases considered. After steady state was reached, data were recorded for approximately 82 seconds with the optical probe and experimental transducer data being taken at 200 Hz and the other signals being recorded at approximately 3 Hz. The tube was then rotated to locate the heat flux sensor at the next desired angular location and the procedure was repeated. The temperature level was selected randomly and then the fluidization velocities were selected randomly at the specified temperature level to randomize the experiments. Most of the experiments were repeated with several experiments being repeated on separate days to test for repeatability and for the analysis of variance which will be covered later. Experiments were completed first for the 2.0 mm particles and then for the 2.9 mm particles. Separate runs were made for the tube with the Micro-Foil transducer and the experimental transducer. The minimum fluidization velocity for each particle size and

bed temperature was determined using three approaches. First, pressure taps located on the test section walls were used to measure the pressure drop across the bed. Pressure drop is known to increase with fluidization velocity until the minimum fluidization velocity is reached at which point it stays approximately constant as the fluidization velocity is increased. Second, the optical probe signals were observed to detect the passage of a void (bubble). For large particle fluidized beds, minimum fluidization velocity is very close to minimum bubbling velocity and therefore the smallest fluidization velocity at which a bubble is detected corresponds approximately to U_{mf} . Third, the bed was visually observed from the sight glass located on the ceiling of the test section.

3. RESULTS AND DISCUSSION

3.1 Bubble Properties

While investigating the bubble properties, analysis of variance (ANOVA) was used to determine relationships between the bubble properties and the variables. In general, a significance level of 90% was used as the criterion to determine whether to reject the null hypothesis being investigated.

3.1.1 Bubble Frequency

Bubble frequency was measured for beds of 2 mm and 2.9 mm particles at the temperatures and velocities described earlier. Since bed conditions were maintained as the tube was rotated to each of the five circumferential locations, bubble frequency measurements were repeated at least five times (in addition to the number of runs that were repeated). Bubble frequencies were measured by both the lower and upper optical probe. Figure 3.1 shows bubble frequency results for a bed of 2 mm particles over the range of temperatures and fluidization velocities studied for both the lower and the upper probe. It is clear that while the results for the lower and upper probe are similar, the upper probe (optical probe 2) has slightly higher frequencies. This is to be expected since the upper probe is closer to the fluctuating wake at the bottom of the tube and the lower might split a rising bubble. The results from the lower probe are used for presentation and analysis since this is considered the most accurate

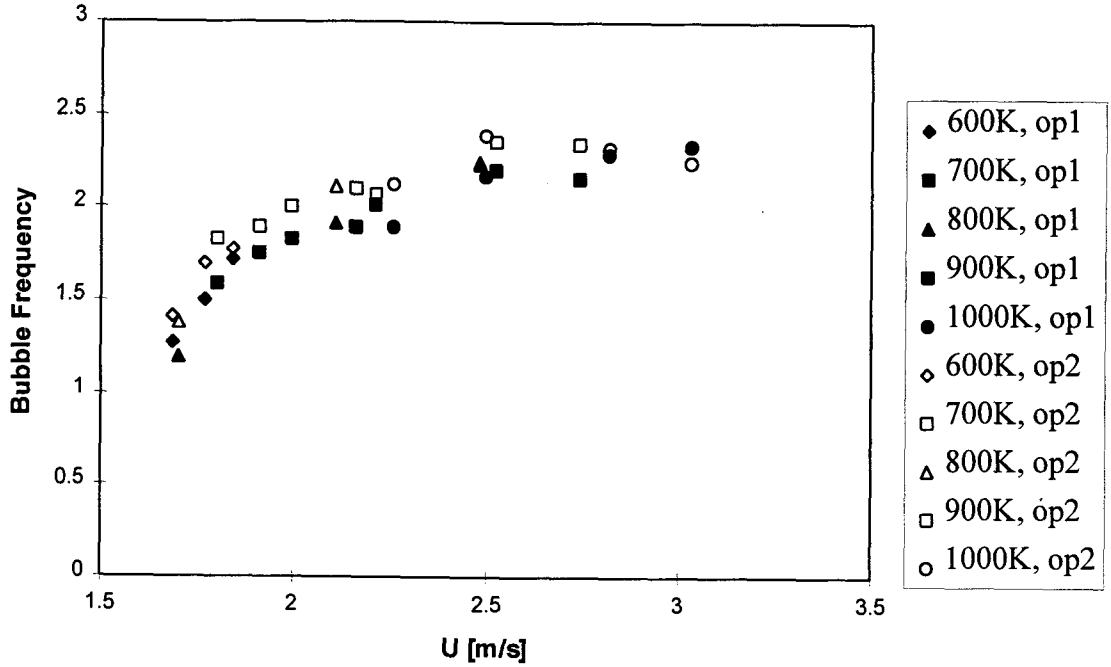


Figure 3.1 Bubble frequencies versus fluidization velocity ($d_p=2$ mm, optical probes 1 and 2 (op1 and op2)).

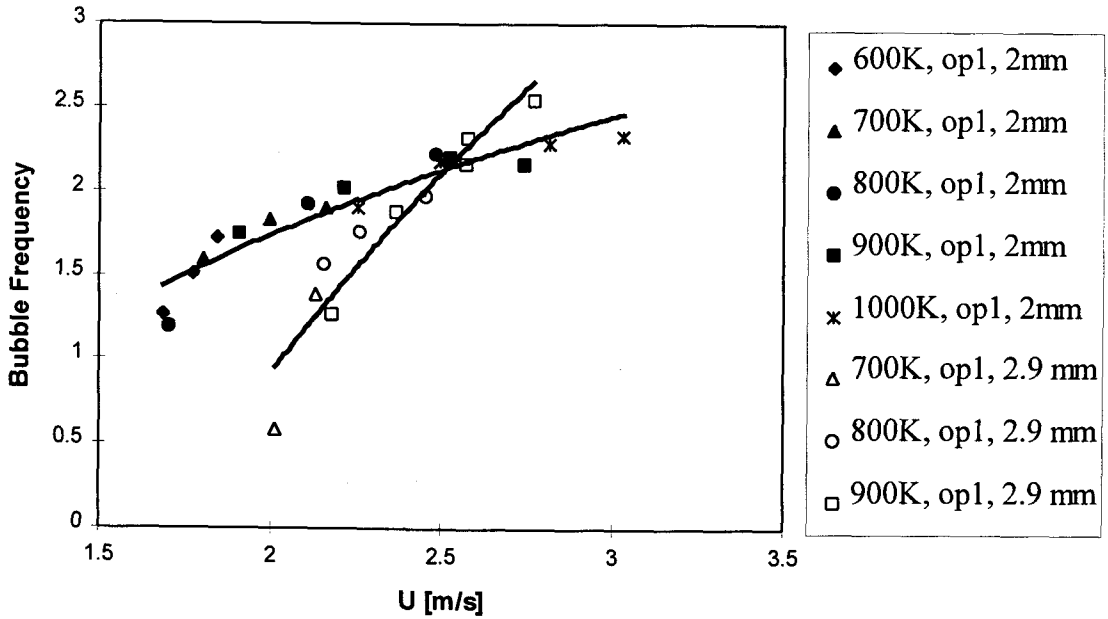


Figure 3.2 Bubble frequencies versus fluidization velocity ($d_p=2$ mm and 2.9 mm, optical probe 1 (op1)).

representation of approaching bubbles. Figure 3.2 shows bubble frequency versus fluidization velocity for beds of 2 mm and 2.9 mm over the temperatures investigated. Using ANOVA, it was determined that the bubble frequency was not likely a function of temperature. It was also determined that the experiments were repeatable and that the bubble frequency was a function of particle diameter and fluidization velocity (U , U/U_{mf} , and $U-U_{mf}$). The bubble frequencies measured are compared to the closest available data in the literature in Figure 3.3. The results suggest that bubble frequency increases for a given excess velocity, $U-U_{mf}$, for large particles.

3.1.2 Bubble Velocity

Bubble velocities were calculated at each fluidization velocity, temperature and particle size in the experimental matrix. As with bubble frequency, these calculations were repeated five times (as the tube was rotated to each of five circumferential locations) in addition to repetitions from repeated matrix points. The resulting average bubble frequencies are plotted versus fluidization velocity in Figure 3.4. An ANOVA was performed with a confidence level of 90% and it was determined that the bubble velocity was, at most, a slight function of temperature. ANOVA was also performed on the variables U and d_p and it was found that these factors and their interaction were significant. Further ANOVA was performed to study the various forms of presenting the fluidization velocity, namely, U , U/U_{mf} , and $U-U_{mf}$. It was found that if $U-U_{mf}$ were used as a variable instead of U , the dependence on d_p fell out. This implies that scaling the bubble velocity with $U-U_{mf}$ correctly accounts for particle size and is thus

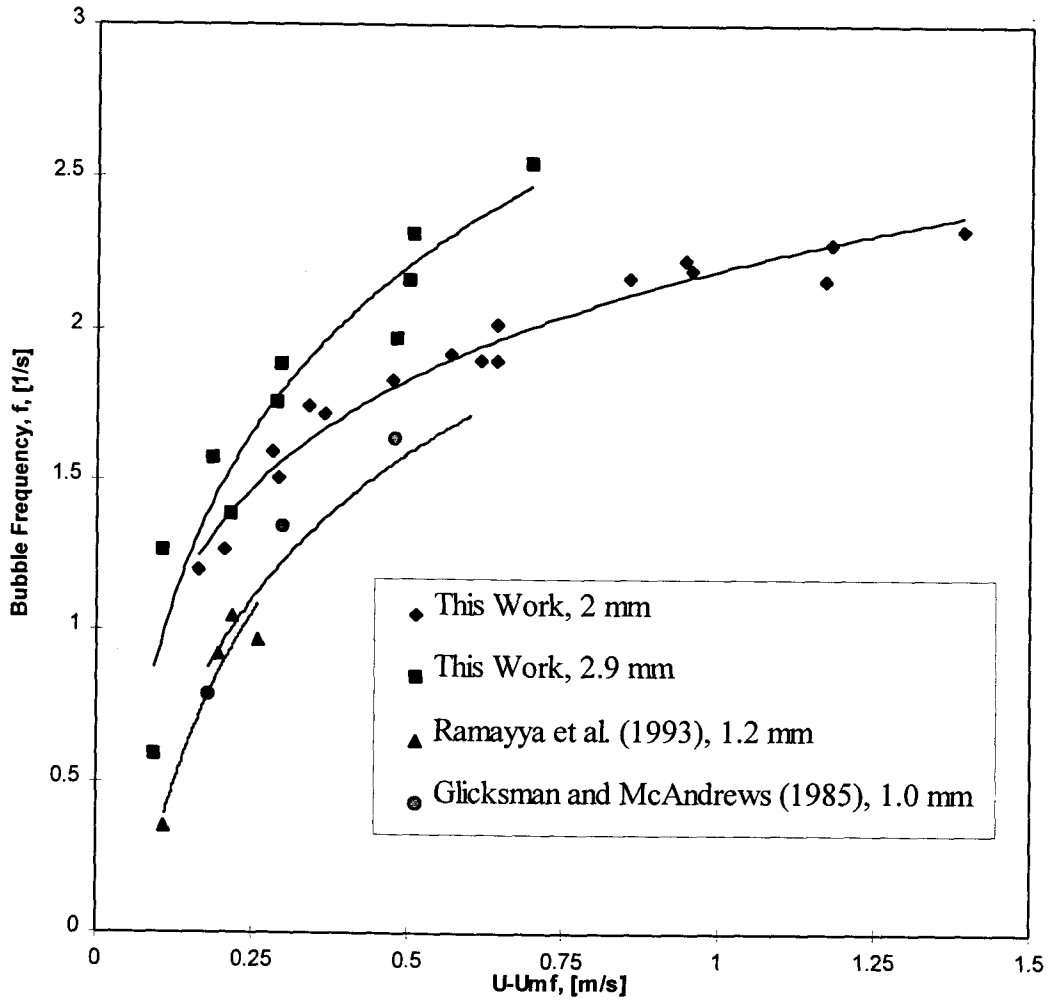


Figure 3.3 Comparison of measured bubble frequencies to other data.

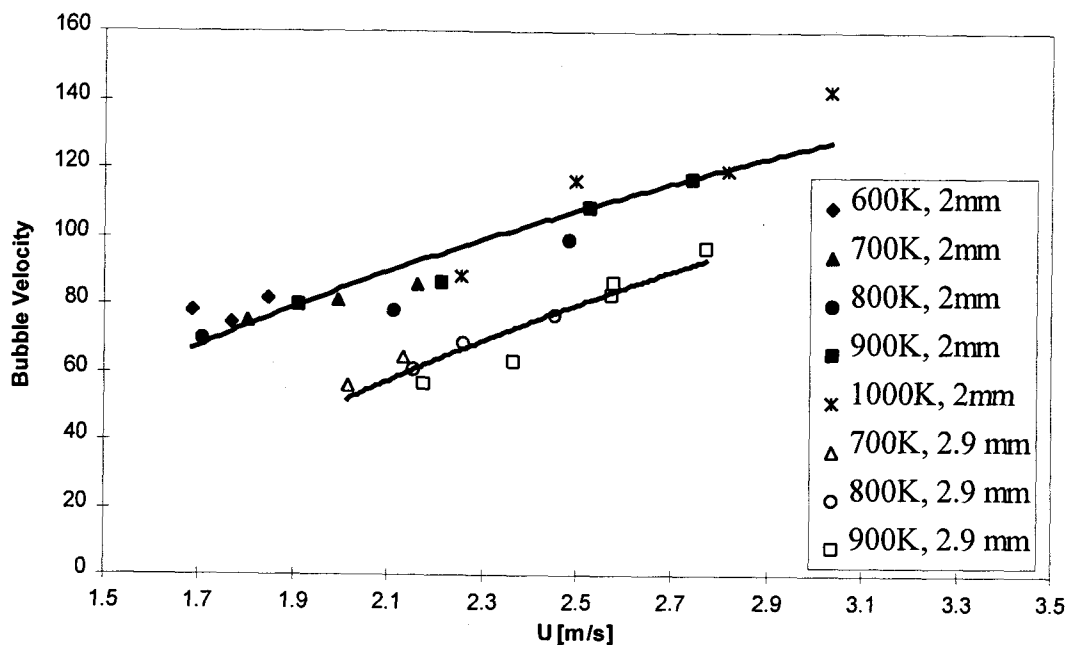


Figure 3.4 Bubble velocities versus fluidization velocity ($d_p=2$ mm and 2.9 mm).

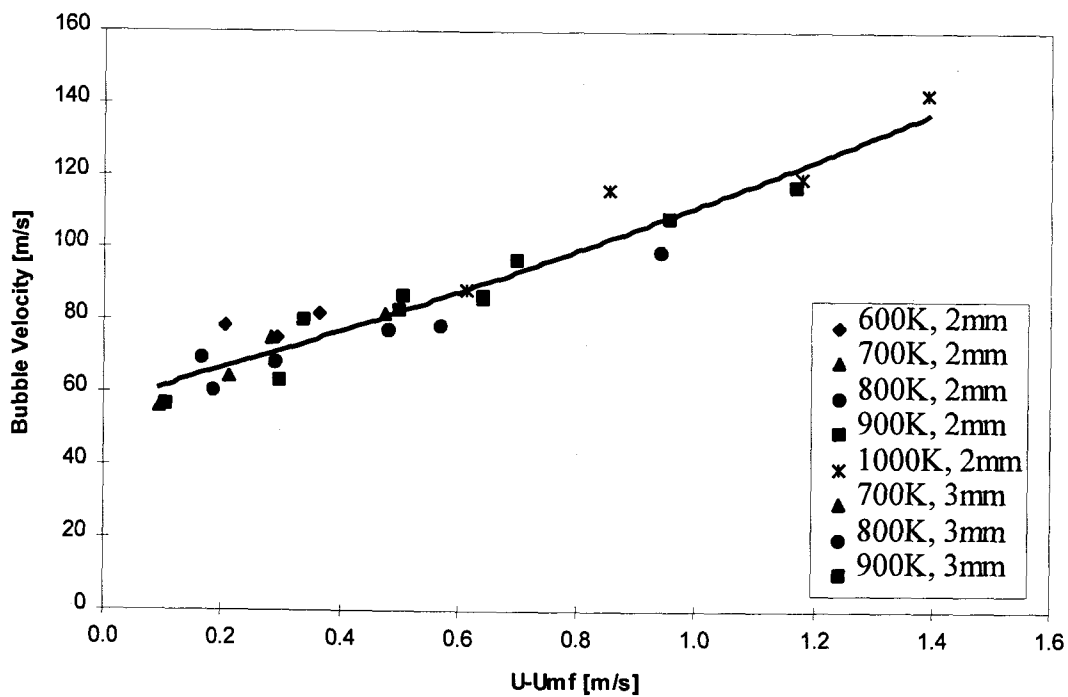


Figure 3.5 Bubble velocities versus excess velocity ($d_p=2$ mm and 2.9 mm).

the only important variable for predicting bubble velocity. These results are displayed in Figure 3.5. This relationship was established with a smaller degree of probability when replacing U with U/U_{mf} .

3.1.3 Local Bubble Time Fraction

Local bubble time fractions were calculated for all experimental runs. As was the case for bubble frequency, the local bubble time fraction was measured at both upper and lower optical probes. Results for a bed of 2 mm particles are shown in Figure 3.6 for both upper and lower probe. The local bubble time fraction is higher at the upper probe, which can be explained using the same arguments as in the bubble frequency calculation. The lower probe results are considered to be the most representative of the conditions in the bed before the bubble arrives at the tube and will thus be used for presentation and analysis purposes. Results for beds of 2 mm and 3 mm particles are shown plotted versus excess velocity, $U - U_{mf}$, in Figure 3.7. ANOVA was performed and it was determined that the local bubble time fraction is not a function of temperature but it is a function of particle diameter and fluidization velocity (in each of the forms: U , U/U_{mf} , and $U - U_{mf}$).

3.1.4 Local Bubble and Emulsion Residence Time

Similar to other bubble properties, the local bubble residence time was measured (with the optical probes) for each experimental run. As was the case with

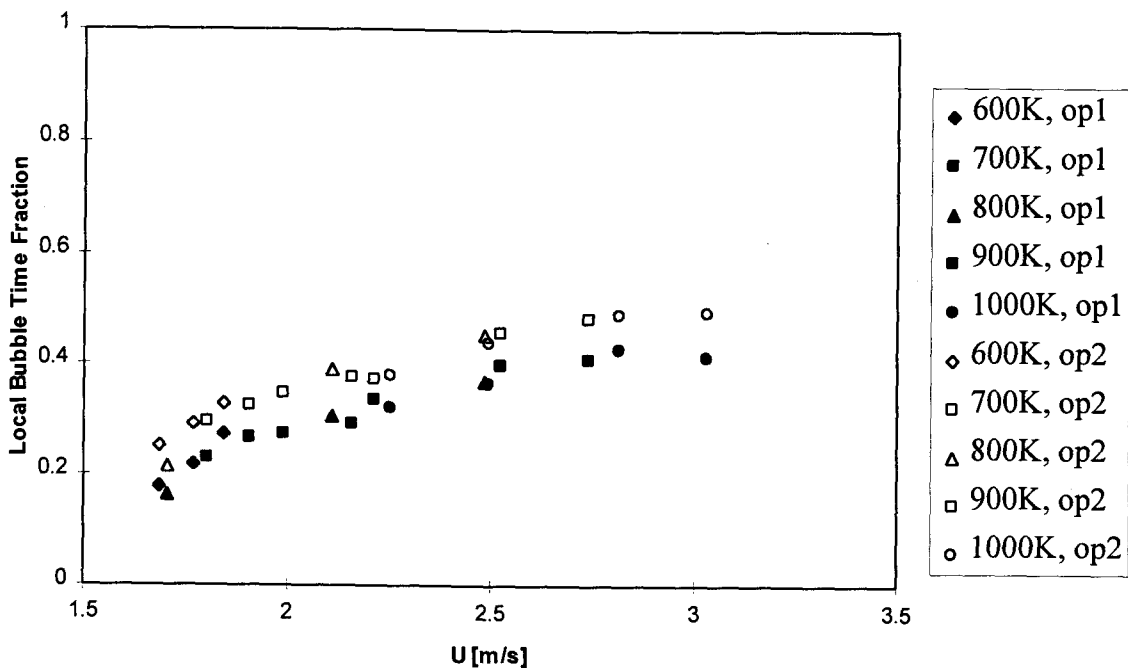


Figure 3.6 Local bubble time fraction versus fluidization velocity ($d_p=2$, optical probes 1 and 2 (op1 and op2)).

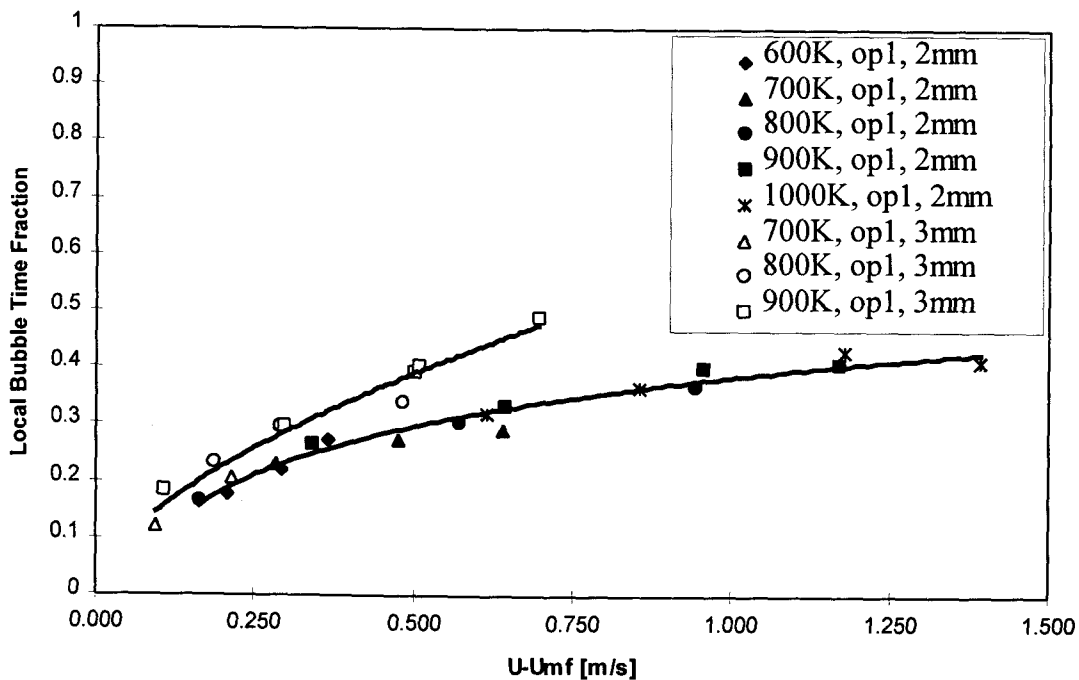


Figure 3.7 Local bubble time fraction versus excess velocity ($d_p=2$ mm and 2.9 mm, optical probe 1 (op1)).

other bubble properties, the lower probe was used for calculations. A plot of the local bubble residence time versus excess velocity is shown in Figure 3.8. ANOVA was performed and local bubble residence time was found to be independent of bed temperature, but dependent on fluidization velocity (U , U/U_{mf} , $U-U_{mf}$) and particle diameter. The local emulsion residence time can be calculated based on values already presented and is shown in Figure 3.9. Like the bubble residence time, it is independent of bed temperature, but dependent on fluidization velocity (U , U/U_{mf} , $U-U_{mf}$) and particle diameter.

It should be noted that the six properties of bubble and emulsion phase frequency, average residence time, and local time fraction are interrelated. Knowledge of any two of these values allows calculation of the other four values using the following relationships (these relationships apply for either in the bed or on the tube):

$$(f_b)(\tau_b) = \delta \quad (3.1)$$

$$(f_e)(\tau_e) = (1 - \delta) \quad (3.2)$$

3.1.5 Bubble Diameter

The characteristic bubble diameter is calculated using the probabilistic and statistic methods described in Chapter 2. This method uses the measured pierced lengths for a given set of experimental conditions, T_{bed} , U and d_p , and forms a probability distribution. This distribution is then used to calculate the most probable (characteristic) bubble diameter. The method takes into account the fact that a larger

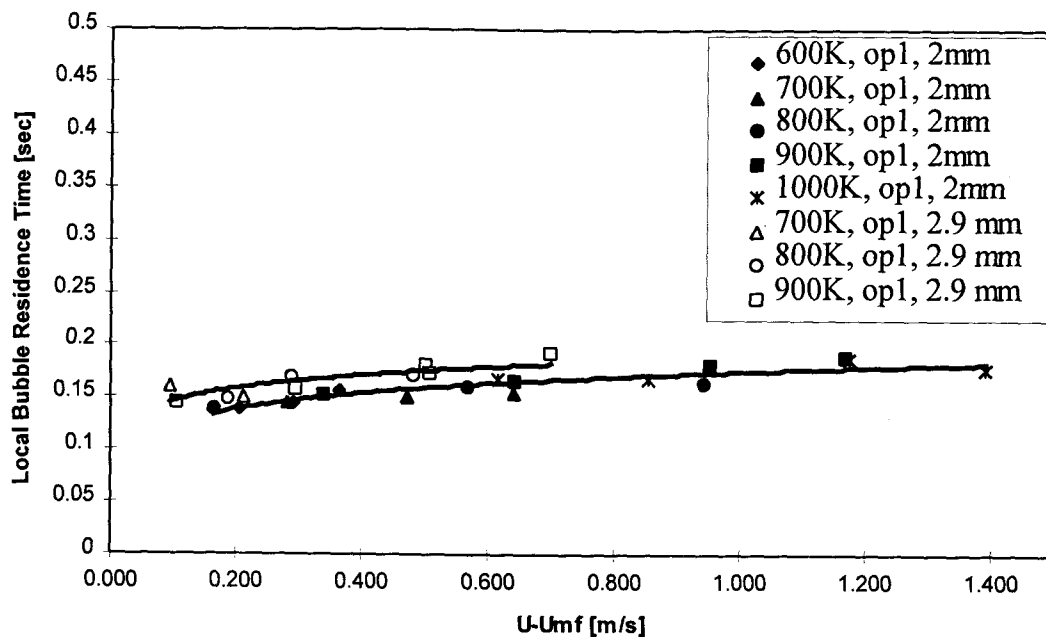


Figure 3.8 Local bubble residence time versus excess velocity ($d_p=2$ mm and 2.9 mm, optical probe 1 (op1)).

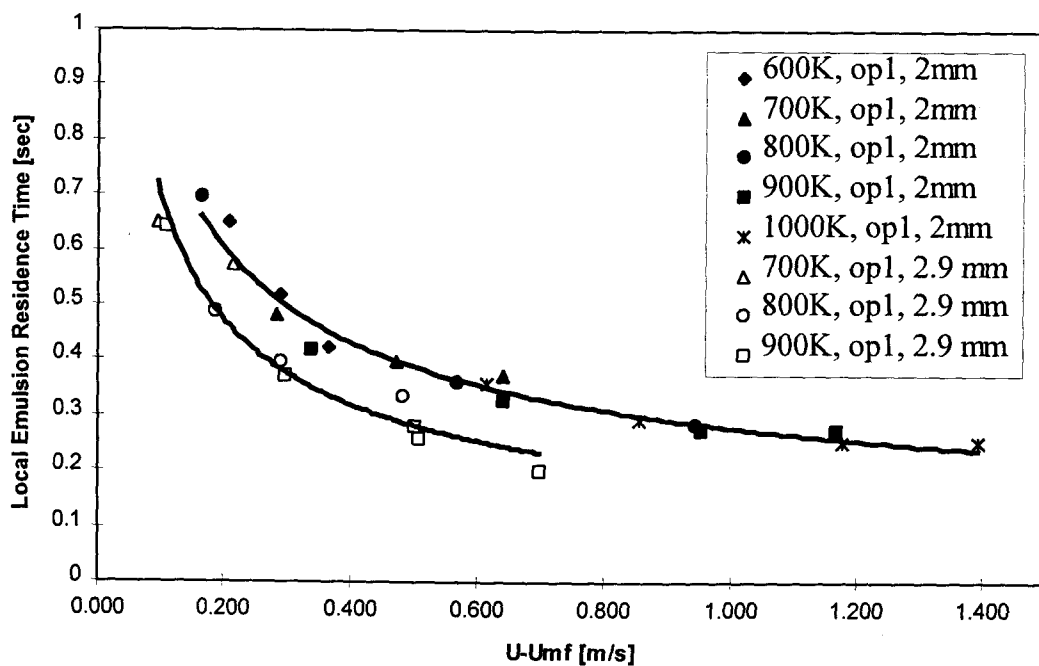


Figure 3.9 Local emulsion residence time versus excess velocity ($d_p=2$ mm and 2.9 mm, optical probe 1 (op1)).

bubble is more likely be detected than a smaller bubble. Thus, the characteristic diameter is smaller than the diameter that would be calculated based strictly on the average measured pierced length. Figure 3.10 shows a typical probability distribution of measured pierced lengths, the corresponding characteristic bubble diameter, the average pierced length and the bubble diameter calculated based on the average pierced length. The characteristic bubble diameter is the more accurate representation of bubbles in the bed since it accounts for the probability of detecting a bubble based on its size. To make the calculation as accurate as possible, a large number of measured pierced lengths was desired. For a given set of bed conditions, pierced lengths were measured as the heat transfer tube was rotated through all five of its circumferential orientations. The entire data set was then split in half to allow two calculations of the characteristic bubble diameter. This repetition, as well as repetition provided by repeating bed conditions entirely, provided a basis to analyze the bubble diameters. A plot of the (characteristic) bubble diameter versus fluidization velocity is shown in Figure 3.11. ANOVA reveals that the bubble diameter is not a primary function of temperature. Further ANOVA reveals that when the bubble diameter is plotted versus $U-U_{mf}$, the particle diameter dependence also falls out. This suggests that the bubble diameter variation can mostly be accounted for by variation in $U-U_{mf}$ only as shown in Figure 3.12.

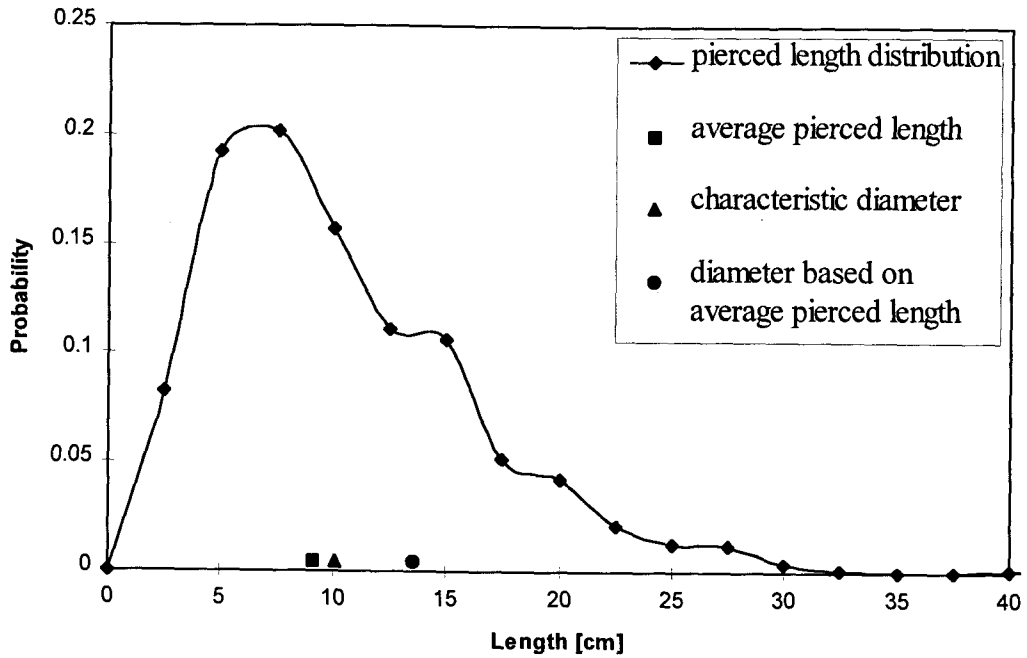


Figure 3.10 Pierced length distribution ($d_p = 2$ mm, $U/U_{mf} = 1.4$, $T_{bed} = 600$ K).

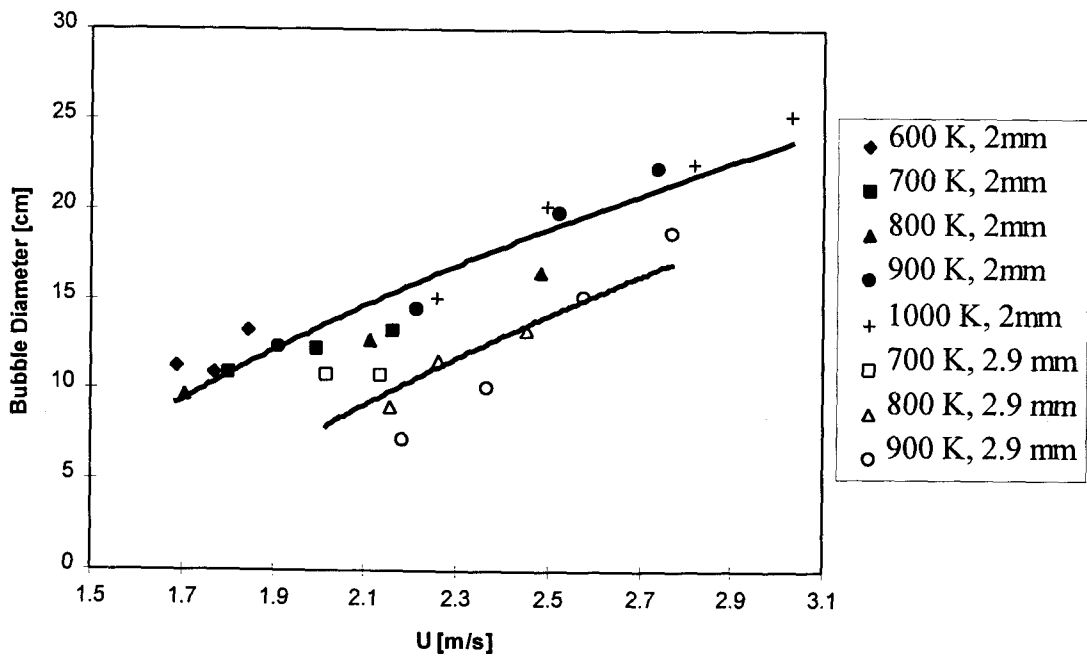


Figure 3.11 Bubble diameters versus fluidization velocity ($d_p = 2$ mm and 2.9 mm).

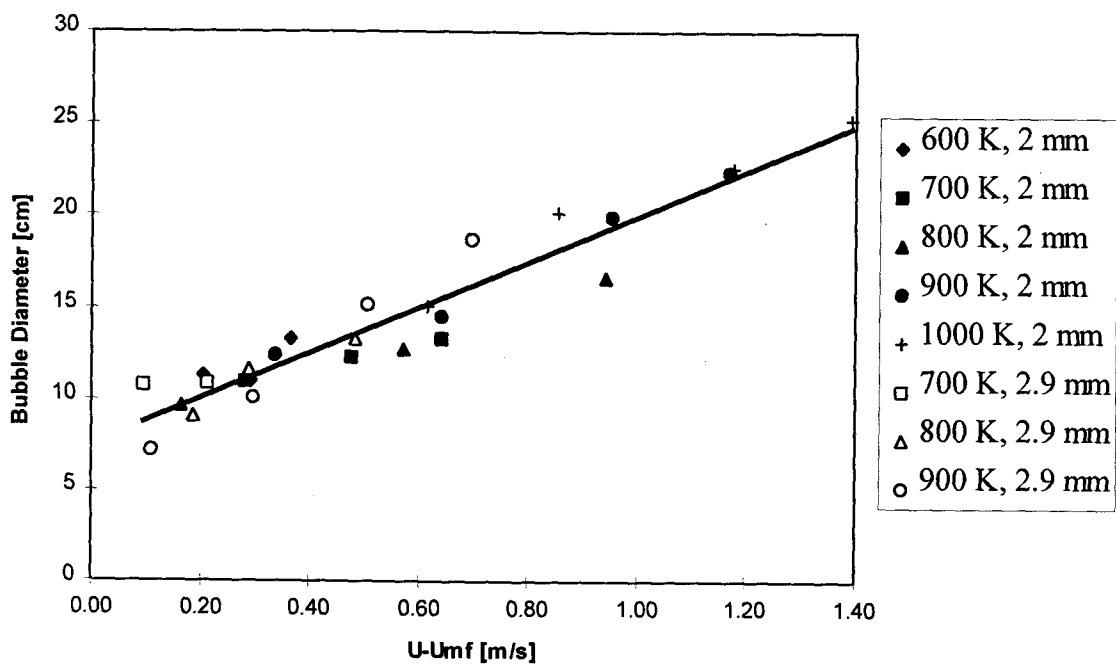


Figure 3.12 Bubble diameters versus excess velocity ($d_p = 2$ mm and 2.9 mm).

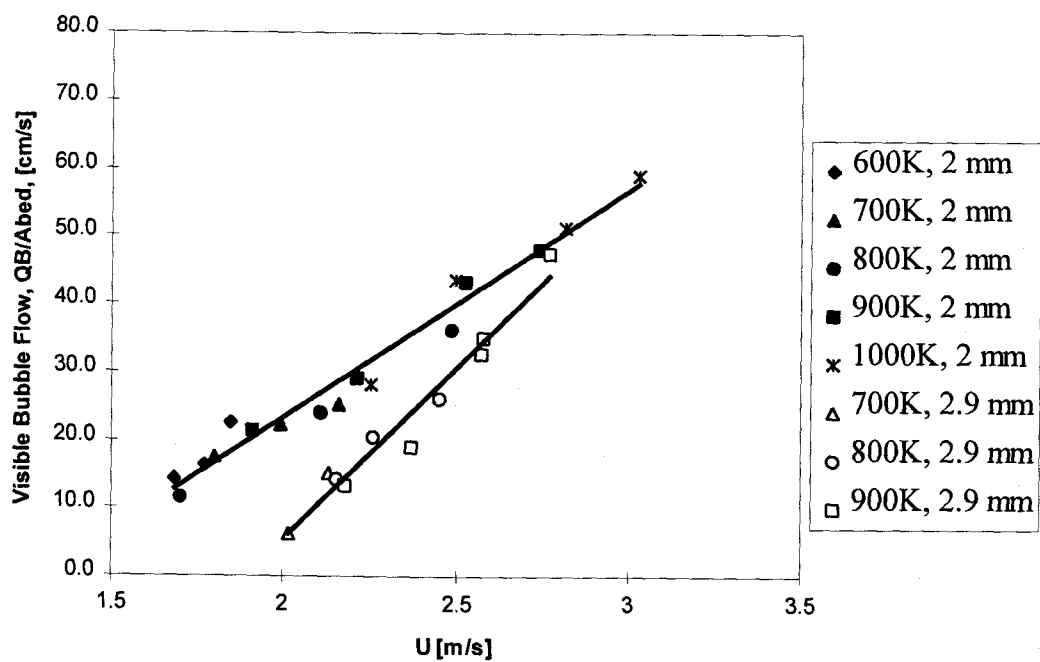


Figure 3.13 Visible bubble flow versus fluidization velocity ($d_p = 2$ mm and 2.9 mm).

3.1.6 Visible Bubble Flow

The visible bubble flow per unit of cross-sectional bed area was calculated for each bed condition and repeated at each bed condition (d_p , T and U) and each tube circumferential location. The average results at each bed condition are shown in Figure 3.13. ANOVA was performed to determine the major variables affecting the visible bubble flow. It was found that temperature was not a significant variable but that the particle diameter and the fluidization velocities (U , U/U_{mf} and $U-U_{mf}$) and their interactions are important.

3.1.7 Bubble Property Correlations

The bubble properties calculated in the present work were compared with correlations from other workers. Many efforts have been made to relate the rise velocity of a bubble to its diameter. Davies and Taylor (1950) derived a theoretical expression for the rate of rise of a single spherical cap bubble in a liquid which is described by the well-known expression

$$u_b = \frac{2}{3} \sqrt{gR_n} \quad (3.3)$$

where R_n is the radius of curvature of the nose of the bubble. Experimenters, as summarized by Clift and Grace (1985) have found that the following expression can be used in practice:

$$u_b = 0.711 \sqrt{gd_b} \quad (3.4)$$

where d_b is the diameter of a sphere having the same volume as the spherical cap bubble. A bubbling bed behaves similarly to a bubbling liquid of low viscosity, and Equation 3.4 has been shown to be valid in bubbling 3D beds for the rise velocity of an isolated bubble (Cranfield and Geldart, 1974). Some researchers have found that Equation 3.4 needs to be modified for bubbles rising in a swarm as found in an actively bubbling bed. Modifications have been of the following form (Werther, 1978):

$$u_b = 0.711\sqrt{gd_b} + \alpha(u - u_{mf}) \quad (3.5)$$

where α is a constant often assigned a value of $\alpha=1$. Equation 3.5 was originally suggested by analogy with swarms of gas bubbles in liquids. It has been shown applicable to a small particle system in which the bubbles travel upward much more quickly than the interstitial gas and are basically isolated from it and thus behave in a similar manner to a gas/liquid system. This is not, however, the case for large particle systems where there is considerable interchange between interstitial and bubble gas and thus Equation 3.5 is not expected to be valid for large particle systems. Figure 3.14 shows the relationship between bubble velocity and bubble diameter for the present work as well as the correlations of Equations 3.4 and 3.5. Equation 3.4 shows reasonable agreement with the present work while Equation 3.5 greatly over predicts the bubble velocity. The fact that Equation 3.4 underpredicts the data for higher bubble diameters can be accounted for by the fact that larger bubbles generally occur at higher excess velocities where increased bubble velocities are found due to coalescing. These results and comments agree with the results presented by other

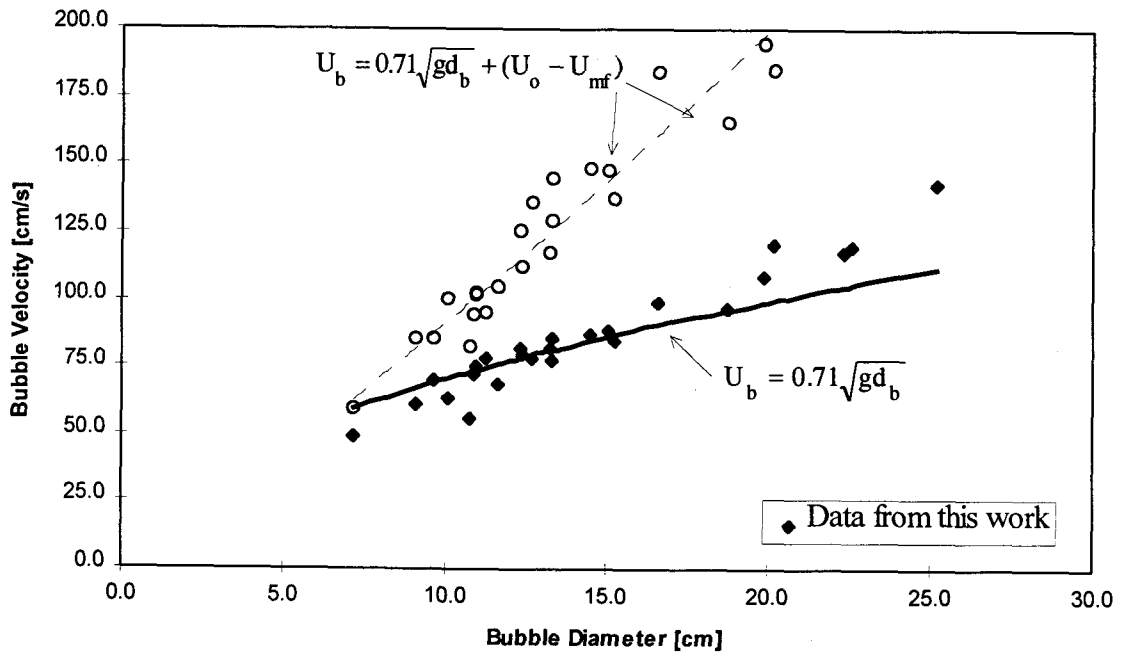


Figure 3.14 Bubble velocity versus bubble diameter correlations ($d_p = 2$ mm and 2.9 mm).

researchers of large particle systems (Geldart and Cranfield, 1971; Cranfield and Geldart, 1974; Glicksman et al., 1987; Werther, 1987).

3.2 Time-Average Heat Transfer Coefficients

3.2.1 Time- and Space-Average Heat Transfer Coefficients

Although local, time-averaged and local, instantaneous heat transfer coefficients are of primary interest for the present work, time- and space-average heat transfer coefficients can also be calculated. This can serve as a general check that the bed and equipment are operating as expected. Time- and space- average heat transfer coefficients for the present work are shown in Figure 3.15 for each particle size, bed temperature and fluidization velocity. These results are compared with data from Pidwerbecki (1994), Goshayeshi (1989) and Lei (1988) in Figure 3.16 for the 2.0 mm particles. The present work used the same particles as Pidwerbecki. Goshayeshi and Lei used particles with mean diameters of 2.14 mm and 3.23 mm. The particles used included particles from a range of screen opening sizes and the diameters were calculated using a mass averaging technique. Pidwerbecki used a deeper bed than the present work and located the tube at 71.1 cm above the distributor plate. The tube was located 43.7 cm above the distributor plate in the work by Goshayeshi and in the present work. Comparisons of the data in Figure 3.16 show good agreement. Some of the differences can be explained by different tube location, bed temperature and particle size. Also, in the present work, the optical probes, which were located directly

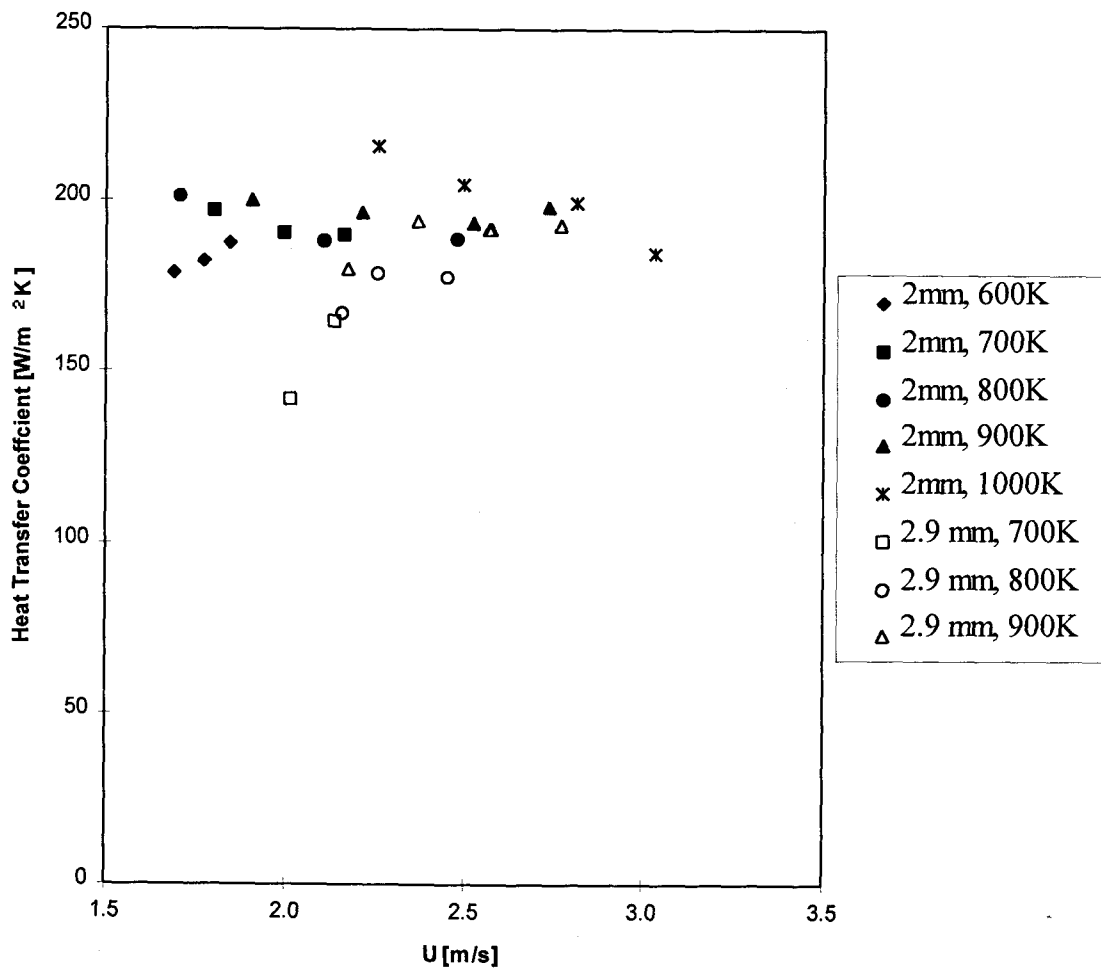
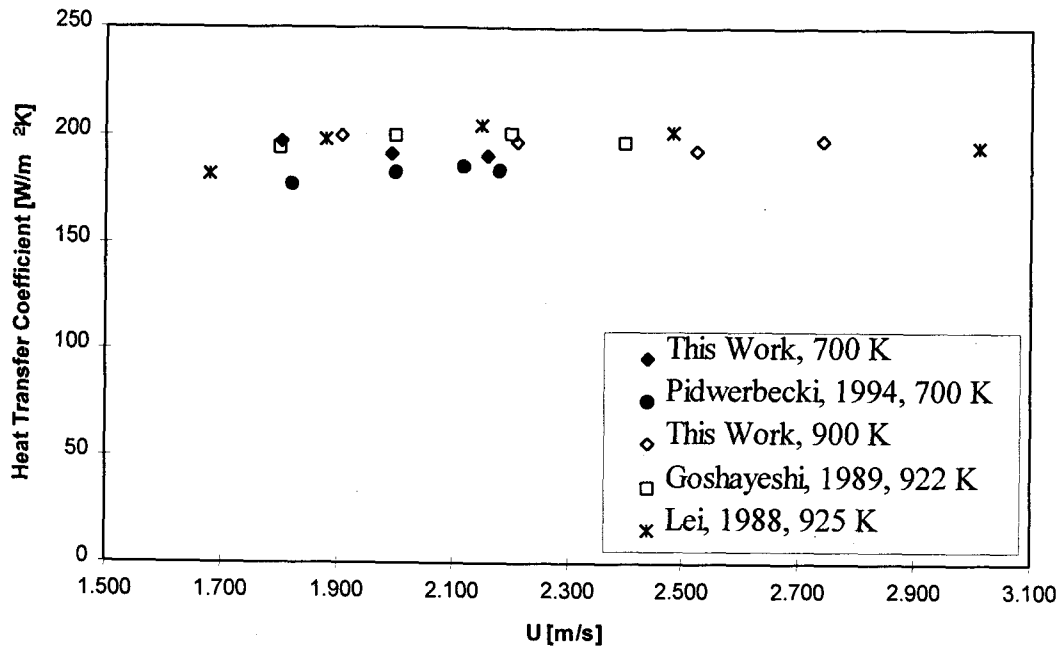
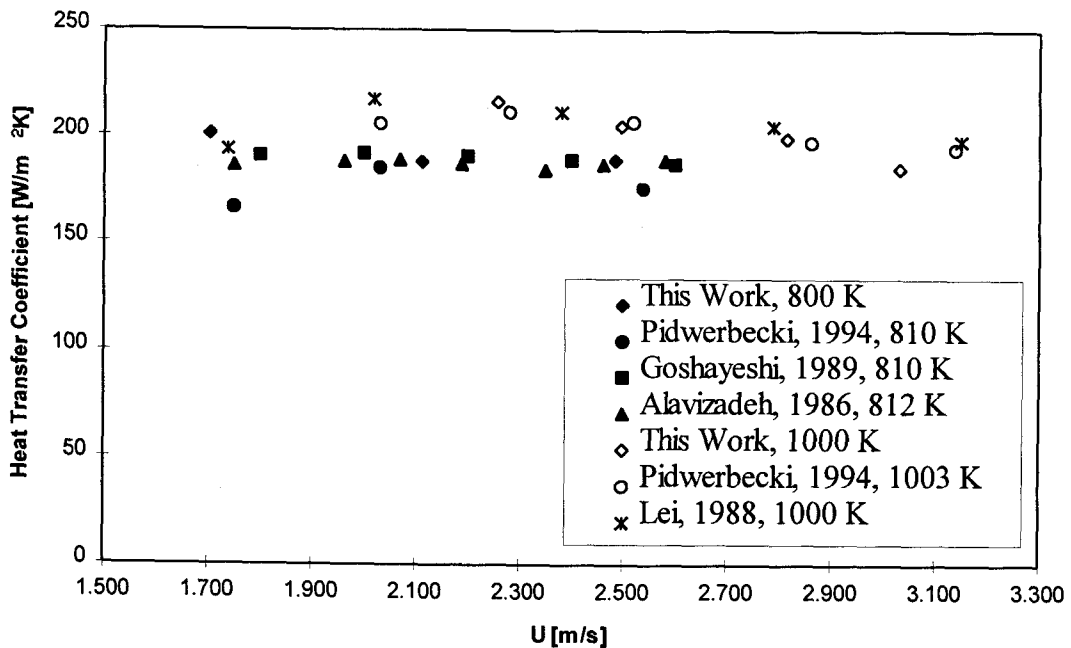


Figure 3.15 Time- and space- averaged heat transfer coefficients ($d_p = 2$ mm and 2.9 mm).



(a)



(b)

Figure 3.16 Time- and space- averaged heat transfer coefficients compared to other experimental data (a) $T_{\text{bed}} = 700 \text{ K}, 900 \text{ K}$; (b) $T_{\text{bed}} = 800 \text{ K}, 1000 \text{ K}$.

below the tube, could influence the heat transfer to the tube, although the probes were designed to minimize this intrusion. The spread in the data is expected to be large when the superficial velocity is near minimum fluidization. The bed does not always fluidize uniformly and local fluidization can occur randomly with parts of the bed in the bubbling regime and other parts of the bed behaving similar to a packed bed with thermal gradients. It has been observed in the 2D bed that once a rising bubble channel is created, bubbles tend to travel toward and join this channel. Random events then occur which cause this channel to suddenly shift to another location. These phenomena cause erratic heat transfer behavior at minimum and low fluidization velocities. For the present work at conditions near minimum fluidization, the optical probes and the tubes could cause local gas acceleration and particle fluidization even when the rest of the bed is quiescent. This could result in high heat transfer coefficients because of the vigorous particle and gas activity caused by the local fluidization as well as the low void fraction throughout the emulsion phase at these near-packed conditions. Hydrodynamic factors influencing the heat transfer coefficient will be studied in more detail in later sections. Overall, the agreement between the present work and previous researchers is good. Previous researchers have also compared these coefficients to other data and correlations and found good agreement. Goshayeshi (1989), for example, found that the correlations of Zabrodsky (1981), Mathur and Saxena (1986) and Decker and Glicksman (1983) were relatively successful in correlating the experimental results of his study and some other investigations.

Values for the average heat transfer coefficient for the cases of (1) 2.0 mm particles and 1003 K bed temperature and (2) 2.9 mm and 810 K from Pidwerbecki (1994) are shown in Figure 3.17. Actual radiation contribution (as opposed to blackbody radiation contribution) is at most 4.0 and 6.2 percent for cases (1) and (2), respectively. Similar results were obtained by Alavizadeh (1985), Lei (1988) and Goshayeshi (1989). The total heat transfer is therefore composed mostly of the convective/conductive modes. These results will be used later when the phenomenological models and correlations are investigated.

3.2.2 Radiative Heat Transfer Coefficient

Alavizadeh et al (1990) measured the radiation contribution for 2.14 mm particles in the OSU high-temperature fluidized bed facility. They found the radiation contribution to be about 8 and 13 percent for bed temperatures of 810 K and 1050 K, respectively. The radiative component can also be calculated using the following relation (Baskakov, 1985):

$$h_r = \sigma \epsilon_{bs} (T_b^2 + T_s^2) (T_b + T_s) \quad (3.6)$$

The bed-to-surface emissivity, ϵ_{bs} , is a generalized emissivity which depends on shape, disposition and emissivity of the radiating and receiving bodies. It can be estimated as follows:

$$\epsilon_{bs} = \left(\frac{1}{\epsilon_b} + \frac{1}{\epsilon_s} - 1 \right)^{-1} \quad (3.7)$$

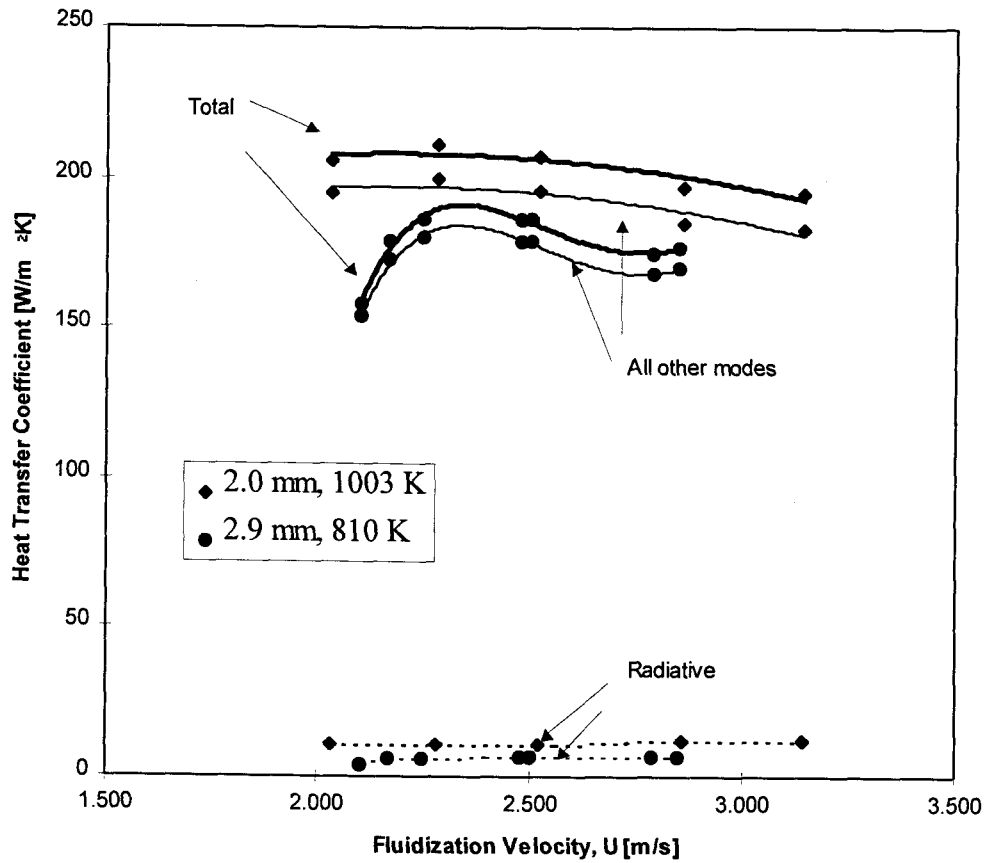


Figure 3.17 Radiative contribution to the heat transfer coefficient from Pidwerbecki (1994).

Because of the reentrant geometry of the emulsion phase, the effective emissivity of the bed is larger than the emissivity of the particle surface. The emissivity of the particles used in the present work was documented by Chung and Welty (1989) and is $\varepsilon_p=0.855-0.874$ (279K - 452K). The emissivity of the bed can then be approximated as ≈ 1 . The radiative contributions for the emulsion and bubbles phases are taken as identical for beds of large particles where the particle temperature remains approximately constant. Pidwerbecki (1994) experimentally measured a tube surface emissivity of 0.37 for the tube used in the present work. Using Equations 3.6 and 3.7, the radiative heat transfer coefficient was calculated and compared to the results of Alavizadeh (1985). The results agree very well with those of Alavizadeh et al. and therefore Equation 3.6 can be used as a correlation of the radiative heat transfer coefficient.

3.3 Time-Average Local Heat Transfer Coefficients

As with the time- and space-averaged coefficients, the time-averaged local heat transfer coefficients can be calculated, although they are not the main focus of the present work. They will be covered only briefly. The time-averaged local heat transfer coefficients for 2 mm particles for bed temperatures of 600K, 700K, 800K, 900K, and 1000K are shown on radial plots in Figures 3.18 (a)-(e), respectively. At 600K, the defluidized cap at $\theta = 180^\circ$ is noticeable. At this low temperature and velocity, the bed was most likely just entering the bubbling bed regime. All other plots reveal that the heat transfer coefficient generally decreased as the fluidization

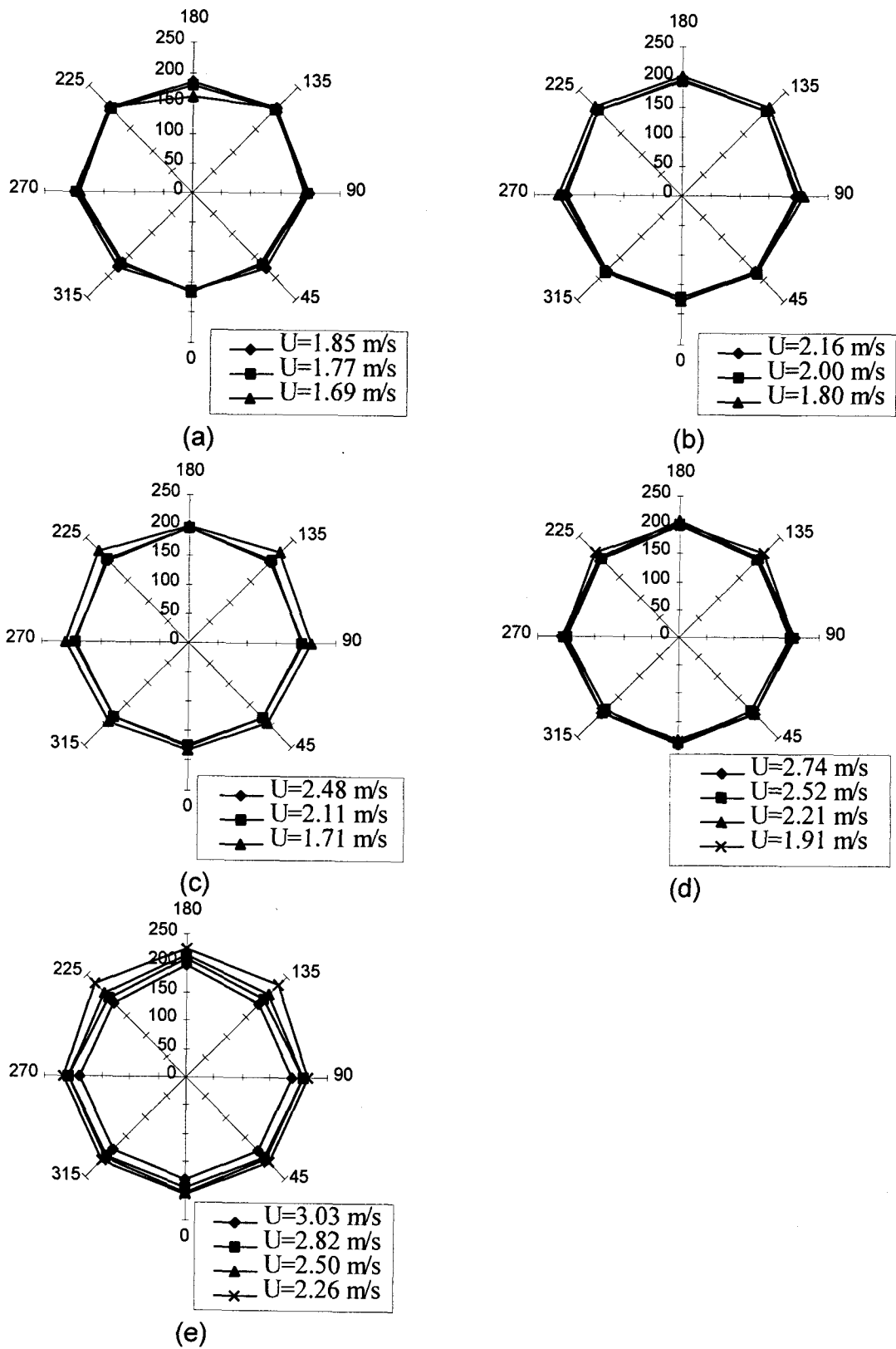


Figure 3.18 Time-averaged local heat transfer coefficients versus circumferential location (a) 600 K, (b) 700K, (c) 800 K, (d) 900 K and (e) 1000 K.

velocity increased. Due to the consistent shape, these conditions most likely corresponded to bubbling bed conditions. The maximum time-averaged local heat transfer coefficient occurred generally at $\theta = 135^\circ$, although some of the maxima occurred at $\theta = 180^\circ$ at higher temperatures.

3.4 Instantaneous Local Heat Transfer Coefficients

The instantaneous local heat transfer coefficient is an indication of the thermal and hydrodynamic activity at a point on the tube. Since the thermocouple transducer is not actually a single point, the instantaneous local heat transfer coefficient measured is actually an 'average' value for the surface area of the transducer on the tube surface. For these experiments, this area was at most 0.1 mm by 2.5 mm. Because the actual thermocouple junction was formed by burrs along the 2.5 mm length, the actual surface area was even less than the 0.25 mm². This area, then, can be taken to represent a "point" and the heat transfer coefficients measured represent local behavior. Because the sampling rate was 200 samples/sec and the response time of the transducer was greater than 100 Hz, the measured coefficients can be considered instantaneous for any activity having frequencies less than 100 Hz. Activity with frequencies greater than 100 Hz are not captured accurately in the power spectrum (they would be folded back on the frequency axis). Inspection of the power spectrum for the bed conditions investigated reveals that there is essentially no energy for frequencies from approximately 12 Hz to 100 Hz (all the energy is at lower frequencies). It is assumed, then, that there is no energy the power spectrum for

frequencies greater than 100 Hz for the bed conditions investigated. In other words, the data obtained can be considered 'instantaneous'. George (1993) found that the peak of the power spectrum occurred at less than 2 Hz and that a sampling rate of 100 Hz was sufficient for similar bed conditions.

The relative value of the heat transfer coefficient for given bed conditions and tube circumferential location can be used to infer the bubble and emulsion phase activity at the tube surface. Generally, it can be inferred that a relatively high heat transfer coefficient is produced when the tube surface is in contact with the emulsion phase while lower heat transfer coefficients are encountered when the bubble phase is in contact with the tube surface. When the emulsion phase is in contact with the tube surface, the degree of particle activity is represented by the frequency and magnitude of fluctuations as well as the magnitude of the average value of the heat transfer coefficient. Similar fluctuations are seen while the bubble phase is in contact with the tube surface. Fluctuations can also be the result of variations in the gas velocity, temperature and turbulence intensity.

Representative five second intervals for the instantaneous local heat transfer coefficients, for bed temperature $T = 600\text{K}$, for each of the fluidizing velocities investigated at this bed temperature are shown in Figures 3.19, 3.20 and 3.21. Each figure displays the instantaneous local heat transfer coefficients for circumferential locations $\theta = 0^\circ, 45^\circ, 90^\circ, 135^\circ, \text{ and } 180^\circ$. Similarly, the instantaneous local heat transfer coefficients are shown for bed temperatures of 700K (Figures 3.22, 3.23 and

3.24), 800K (Figures 3.25, 3.26 and 3.27), 900K (Figures 3.28, 3.29, 3.30 and 3.31), and 1000K (Figures 3.32, 3.33, 3.34 and 3.35).

It is also interesting to view the instantaneous local heat transfer coefficients when grouped by bed temperature and circumferential position. Five second intervals for the instantaneous local heat transfer coefficients for bed temperature $T = 600\text{K}$ for $\theta = 180^\circ, 135^\circ, 90^\circ, 45^\circ,$ and 0° are shown in Figures 3.36, 3.37, 3.38, 3.39 and 3.40, respectively. Each figure displays the instantaneous local heat transfer coefficients for the fluidization velocities investigated. Similarly, the instantaneous local heat transfer coefficients for bed temperatures of 700K (Figures 3.41, 3.42, 3.43, 3.44 and 3.45), 800K (Figures 3.46, 3.47, 3.48, 3.49 and 3.50), 900K (Figures 3.51, 3.52, 3.53, 3.54 and 3.55), and 1000K (Figures 3.56, 3.57, 3.58, 3.59 and 3.60).

Different heat transfer activity and trends can be inferred by observing the above graphs. In Figure 3.36 ($T = 600\text{K}, \theta = 180^\circ$), at low velocity, there are periods of approximately constant heat transfer coefficient. There is relatively little activity whether either the emulsion phase or the bubble phase is present. There is either a gas cushion or particles are sitting on the tube which are cooled. It is frequently observed that the heat transfer coefficient starts at a high value and then decreases (with relatively little fluctuation) as the nearby particles cool. At higher velocities, more activity is seen by the spikes in the heat transfer coefficient. There are still periods of relatively low activity. In Figure 3.37 ($T = 600\text{K}, \theta = 135^\circ$), the plots of heat transfer coefficient look similar to those for $\theta = 180^\circ$, but with more activity, although the activity is still somewhat limited. At both $\theta = 180^\circ$ and 135° , different types of bubble

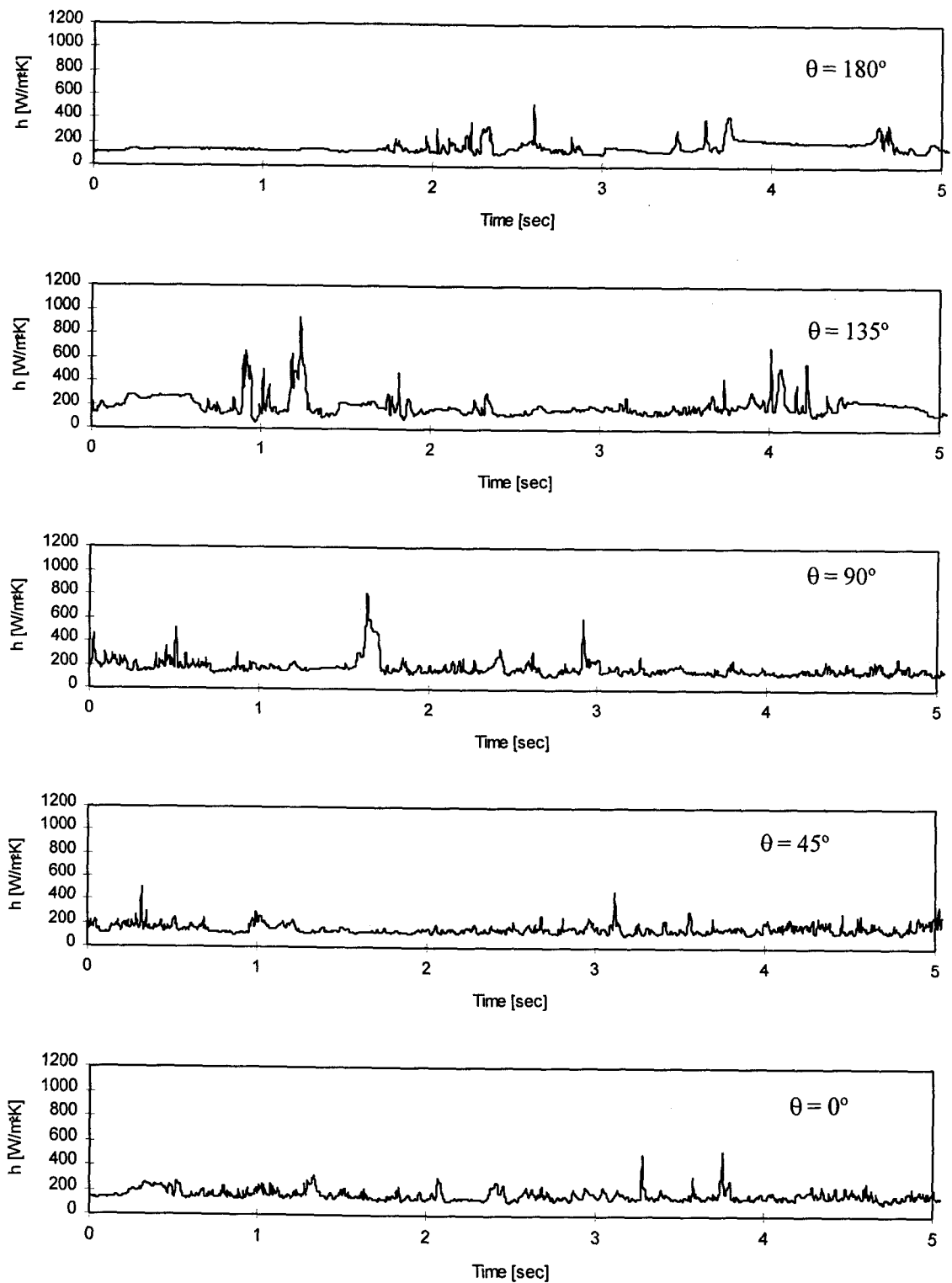


Figure 3.19 Instantaneous local heat transfer coefficients ($T_{bed} = 600$ K, $d_p = 2$ mm, $U = 1.69$ m/s).

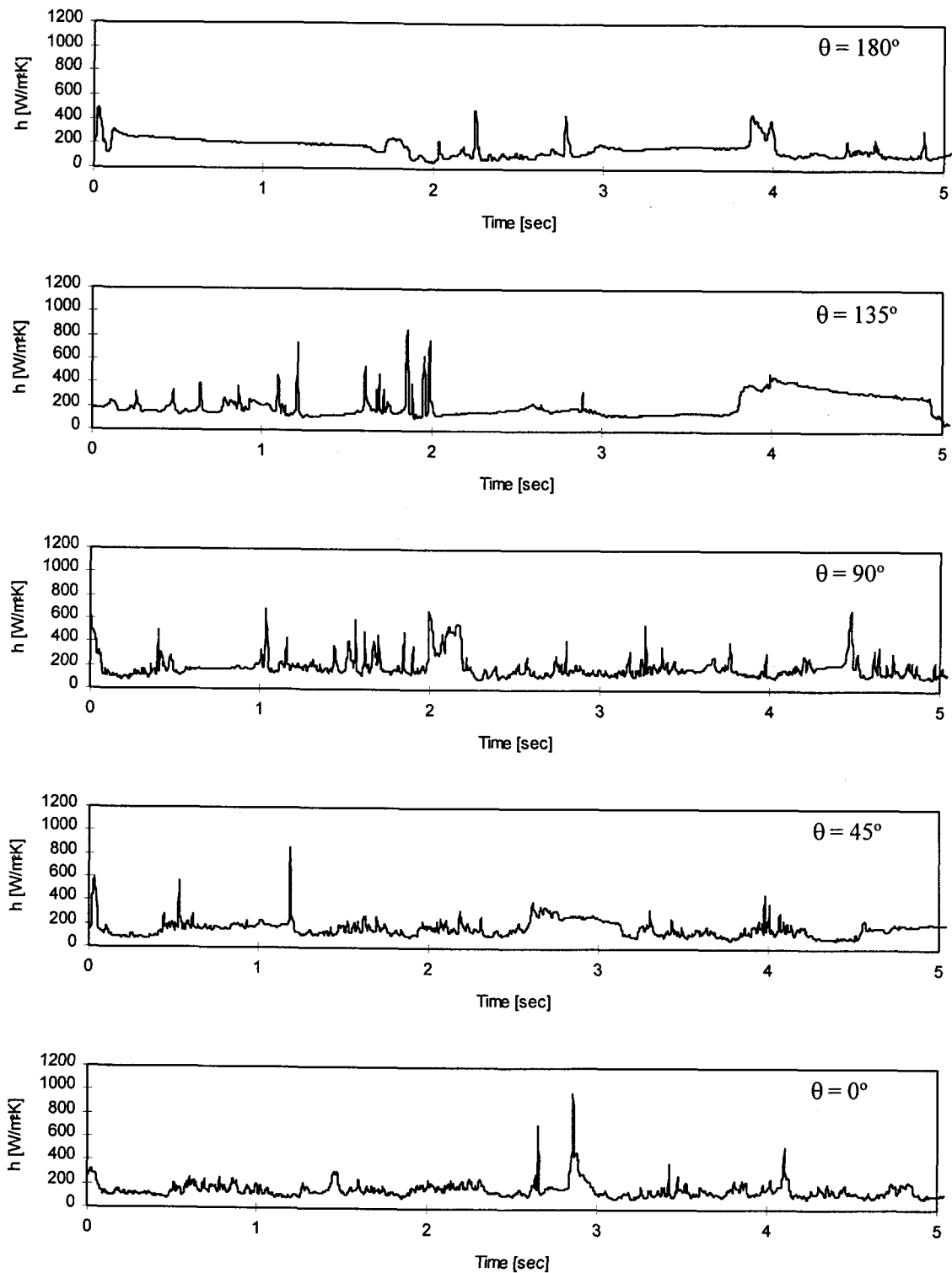


Figure 3.20 Instantaneous local heat transfer coefficients ($T_{\text{bed}} = 600$ K, $d_p = 2$ mm, $U = 1.77$ m/s).

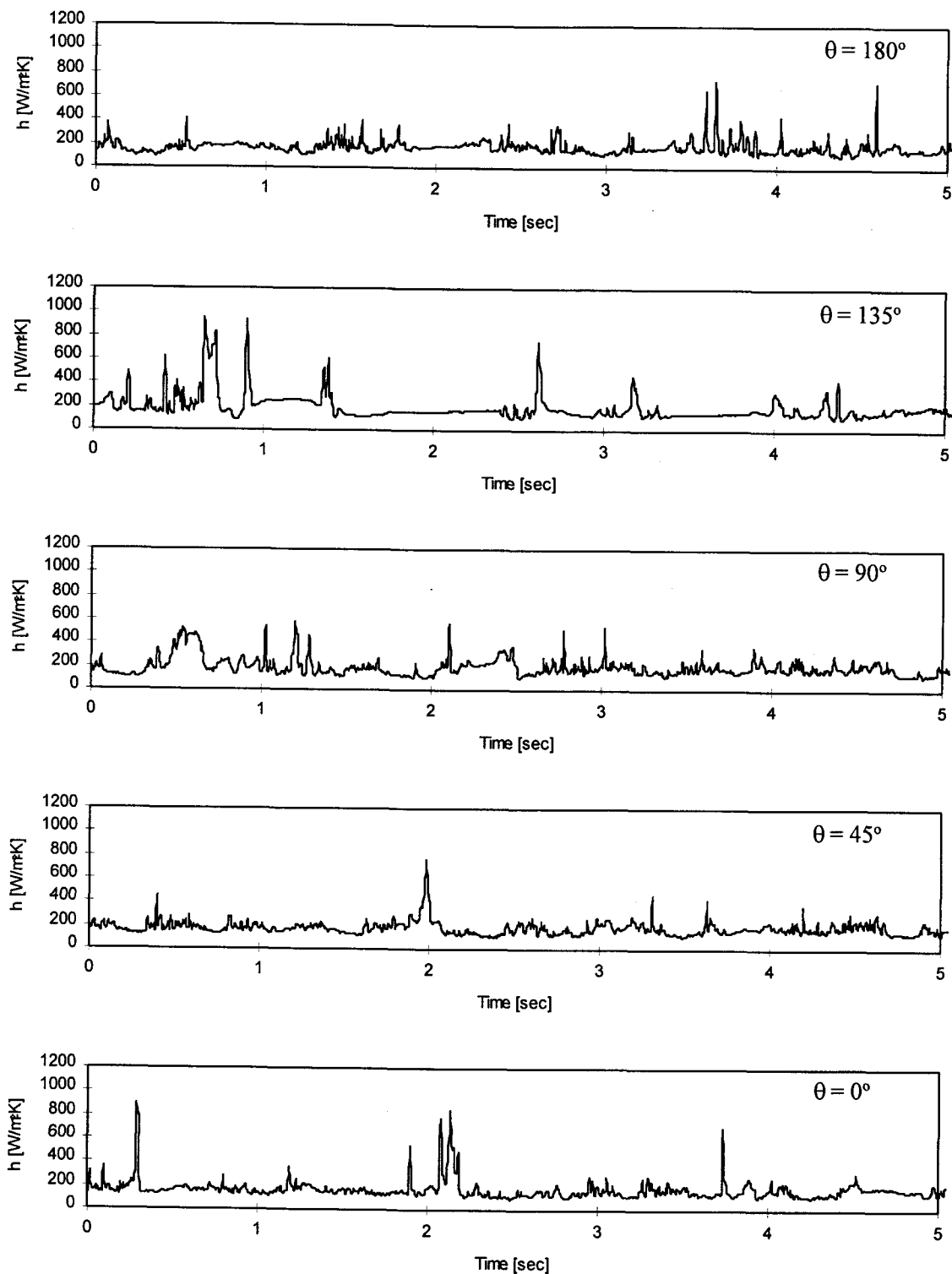


Figure 3.21 Instantaneous local heat transfer coefficients ($T_{\text{bed}} = 600$ K, $d_p = 2$ mm, $U = 1.85$ m/s).

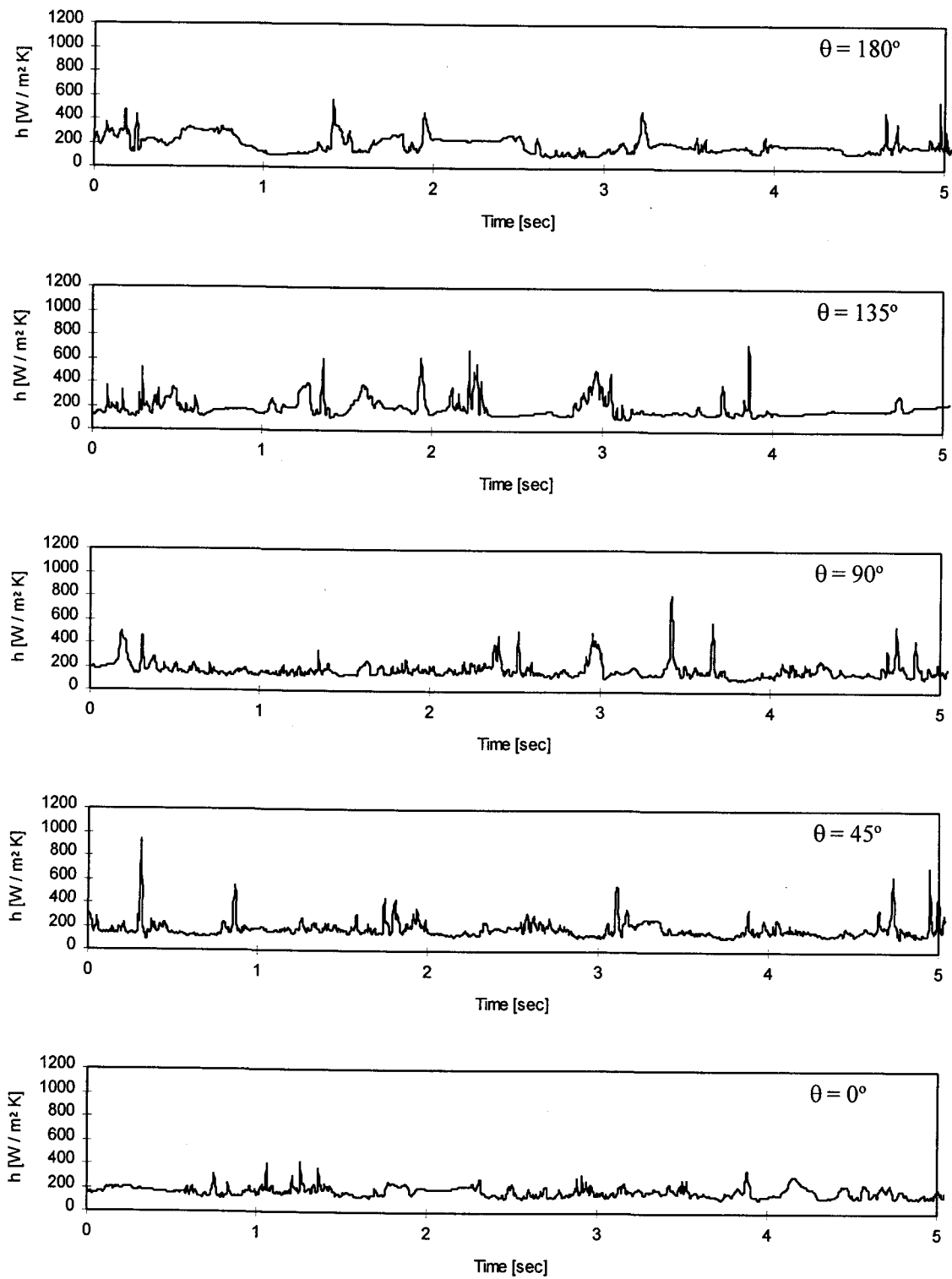


Figure 3.22 Instantaneous local heat transfer coefficients ($T_{\text{bed}} = 700 \text{ K}$, $d_p = 2 \text{ mm}$, $U = 1.80 \text{ m/s}$).

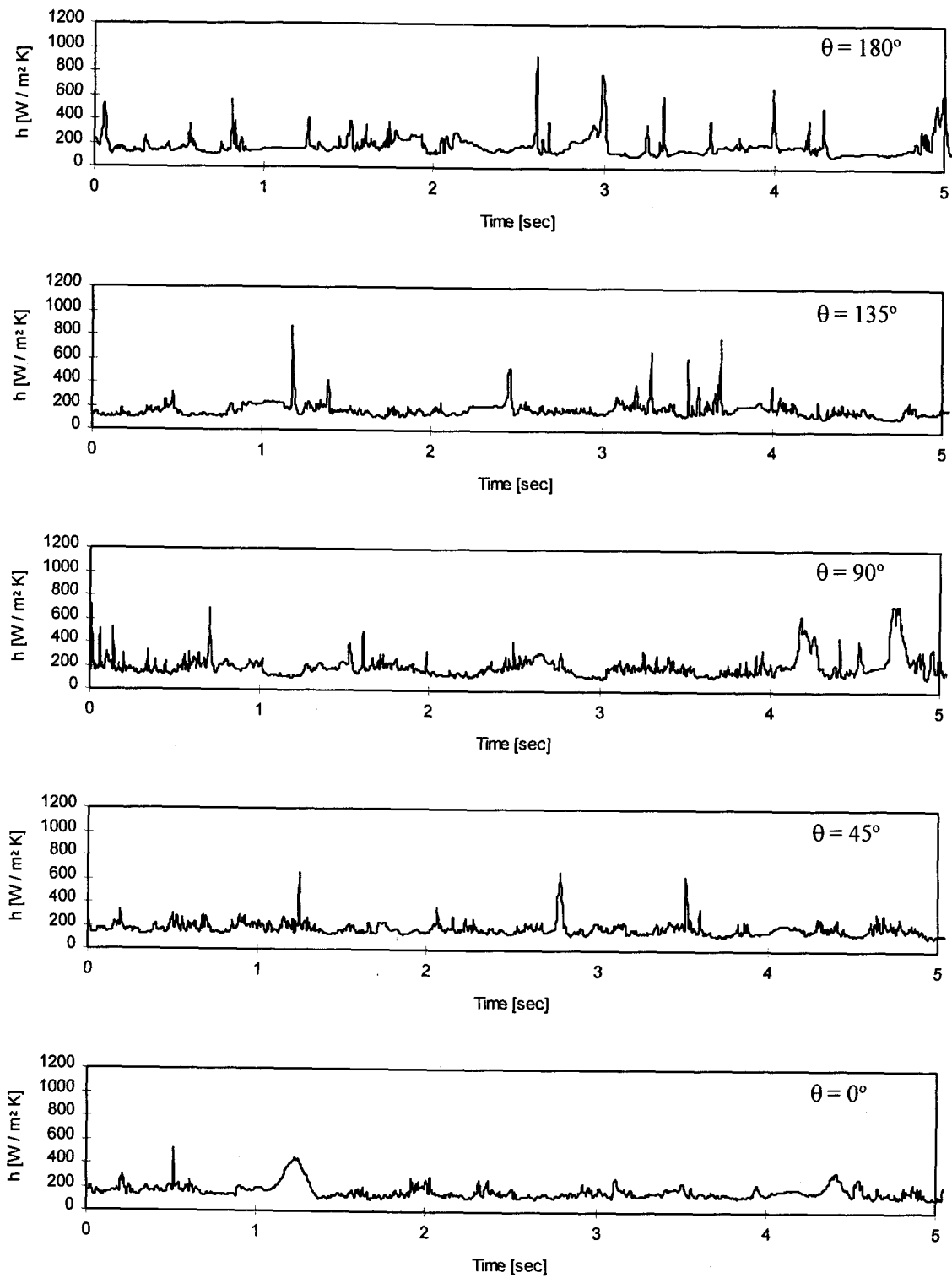


Figure 3.23 Instantaneous local heat transfer coefficients ($T_{\text{bed}} = 700 \text{ K}$, $d_p = 2 \text{ mm}$, $U = 2.00 \text{ m/s}$).

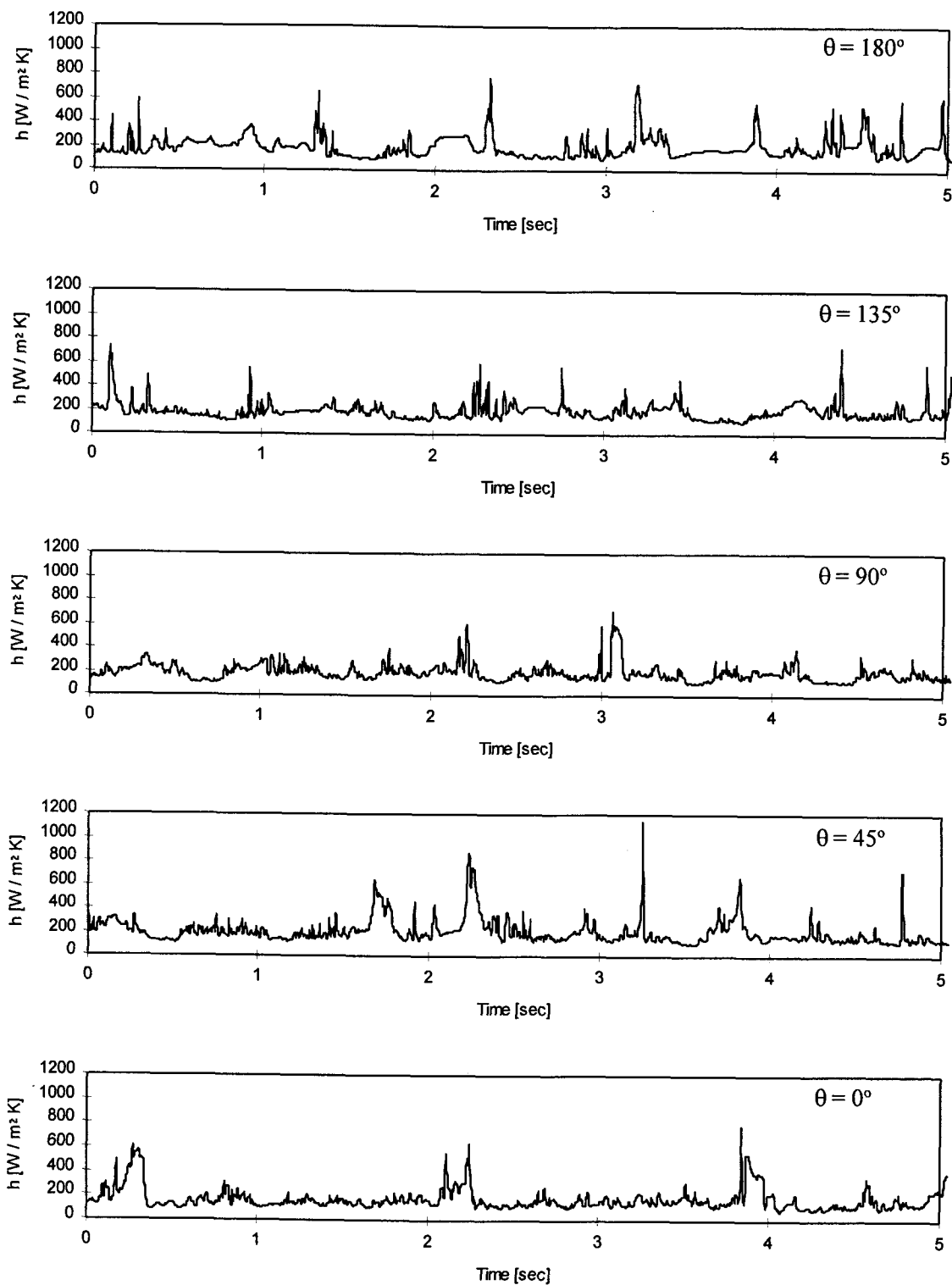


Figure 3.24 Instantaneous local heat transfer coefficients ($T_{\text{bed}} = 700 \text{ K}$, $d_p = 2 \text{ mm}$, $U = 2.16 \text{ m/s}$).

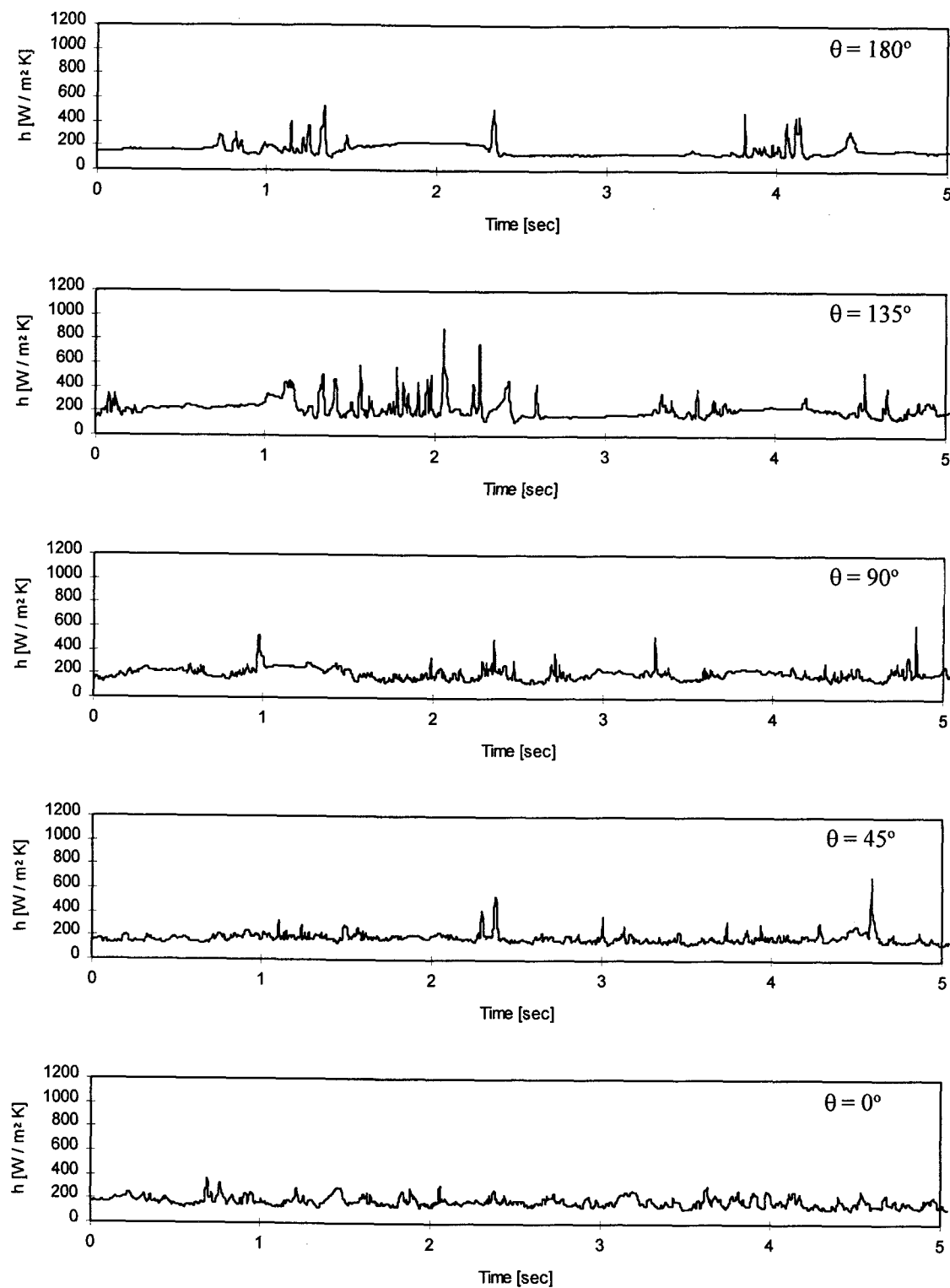


Figure 3.25 Instantaneous local heat transfer coefficients ($T_{\text{bed}} = 800$ K, $d_p = 2$ mm, $U = 1.71$ m/s).

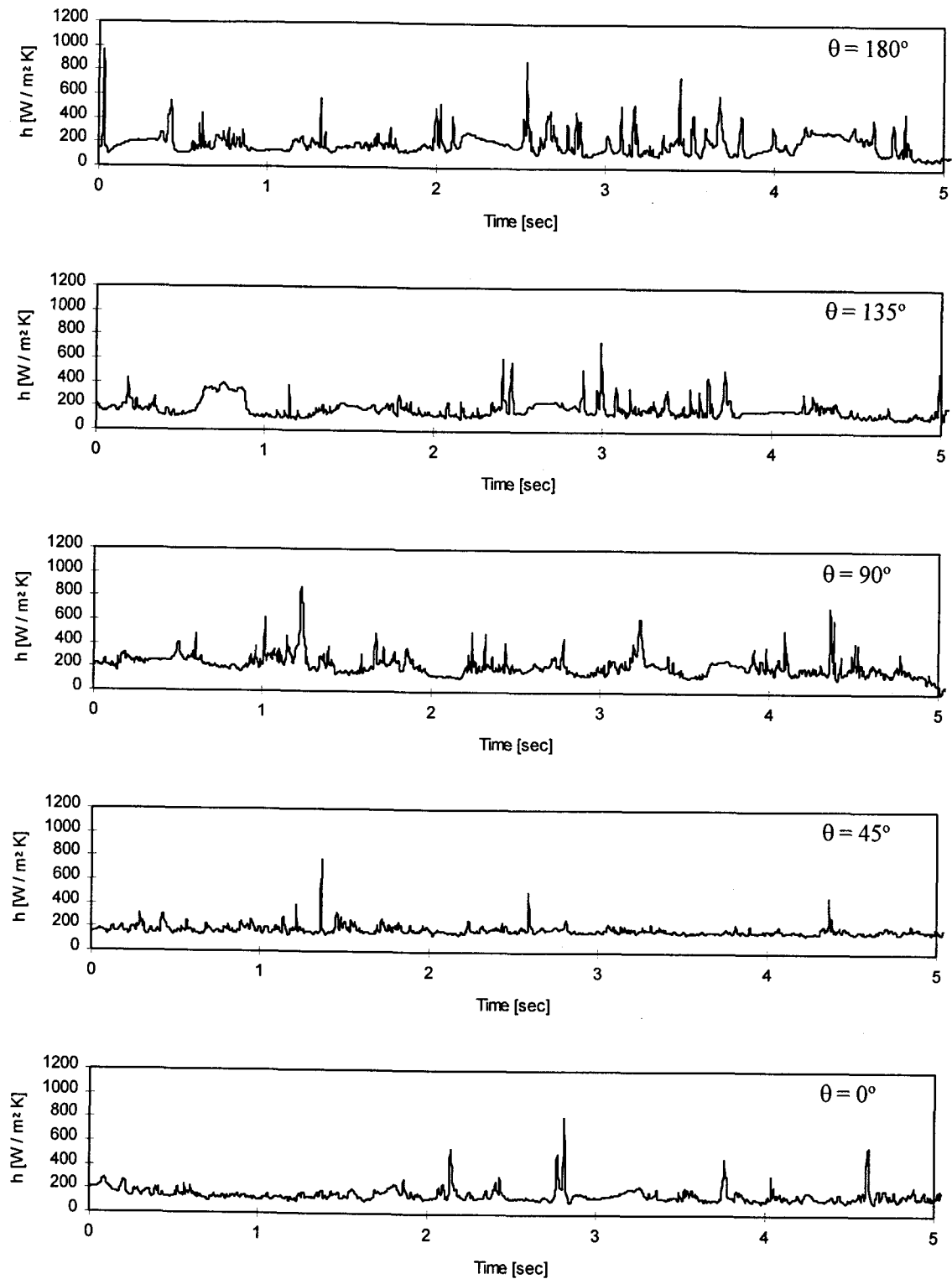


Figure 3.26 Instantaneous local heat transfer coefficients ($T_{\text{bed}} = 800 \text{ K}$, $d_p = 2 \text{ mm}$, $U = 2.11 \text{ m/s}$).

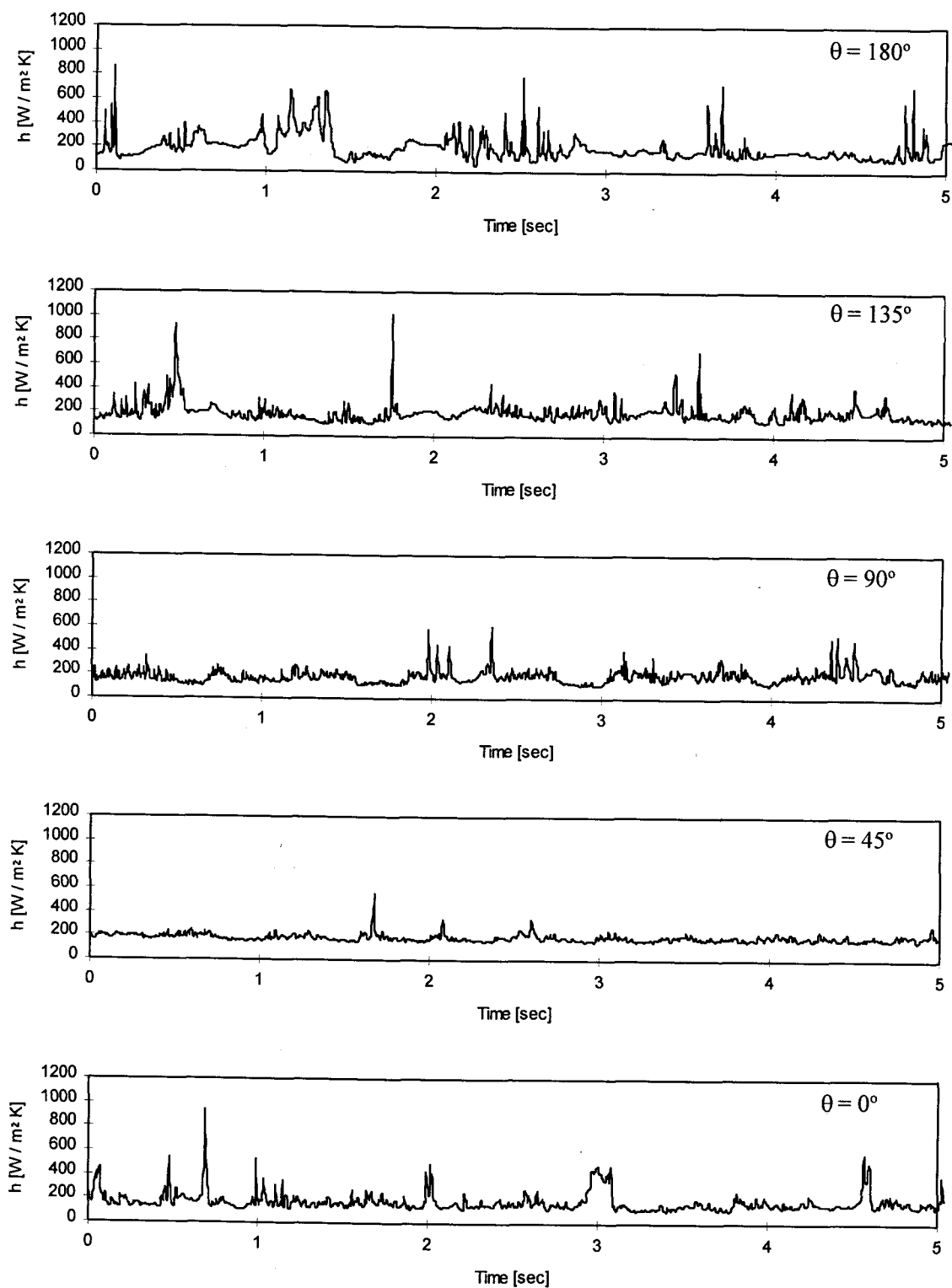


Figure 3.27 Instantaneous local heat transfer coefficients ($T_{\text{bed}} = 800$ K, $d_p = 2$ mm, $U = 2.48$ m/s).

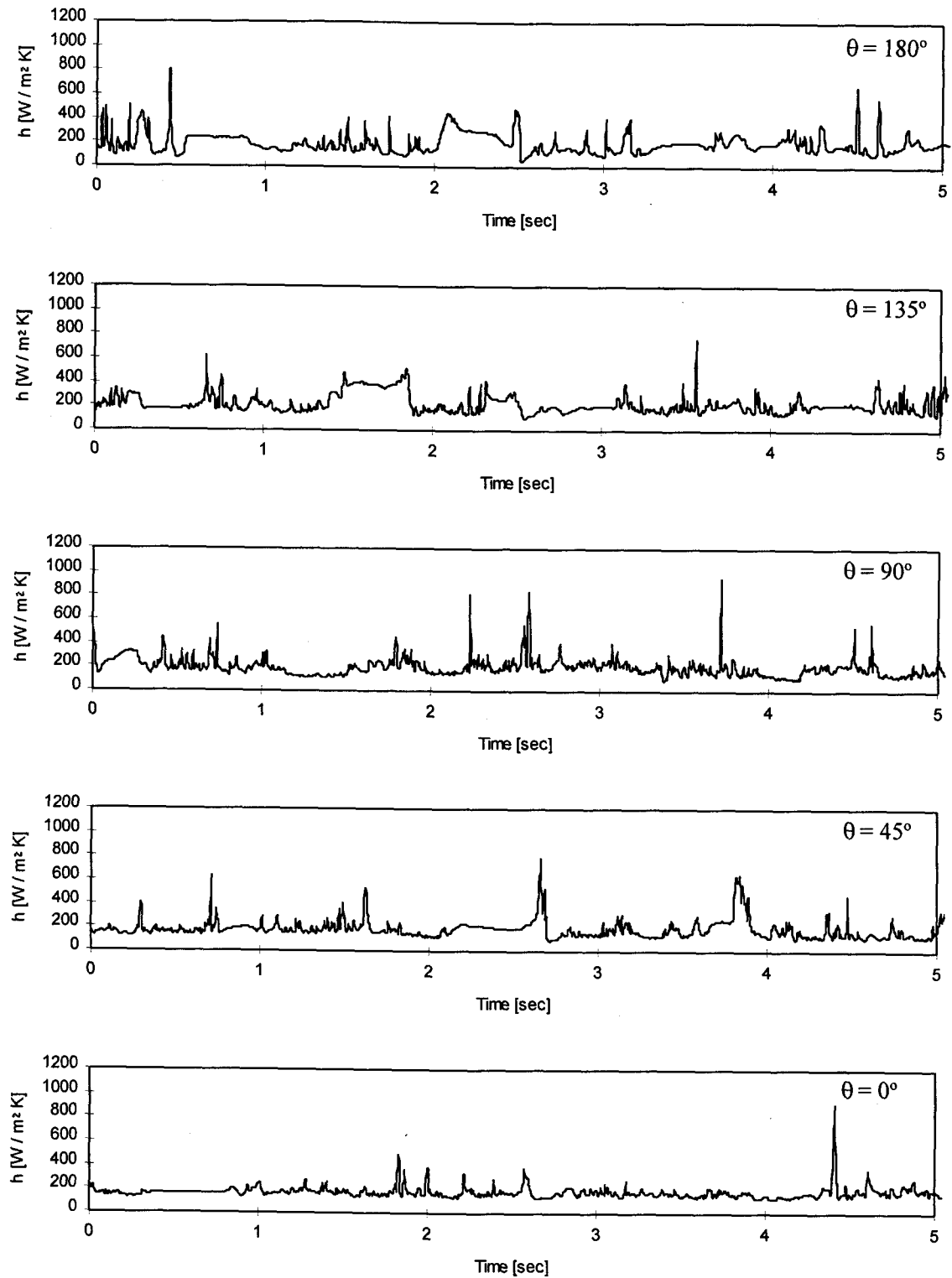


Figure 3.28 Instantaneous local heat transfer coefficients ($T_{\text{bed}} = 900 \text{ K}$, $d_p = 2 \text{ mm}$, $U = 1.91 \text{ m/s}$).

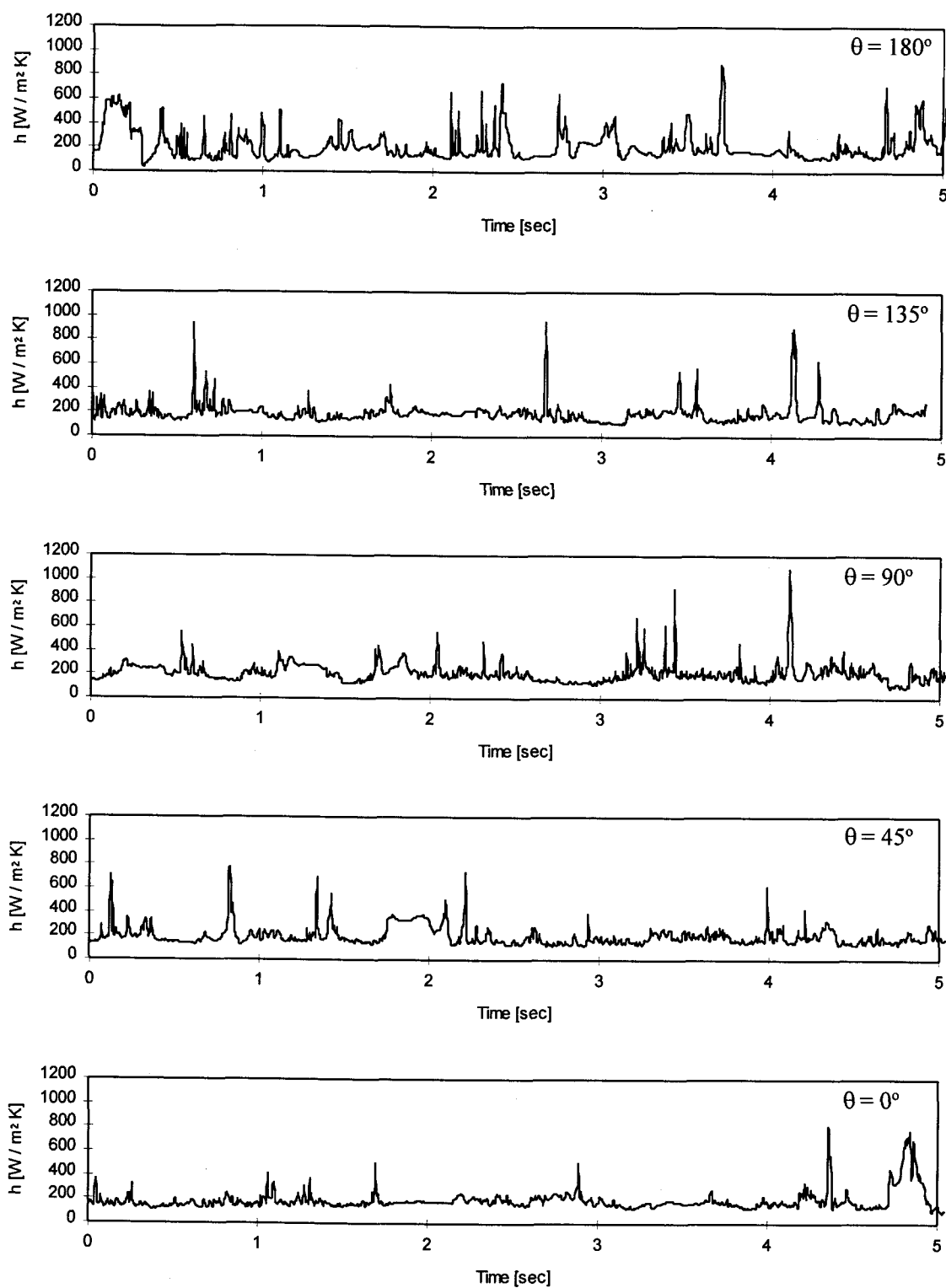


Figure 3.29 Instantaneous local heat transfer coefficients ($T_{\text{bed}} = 900$ K, $d_p = 2$ mm, $U = 2.21$ m/s).

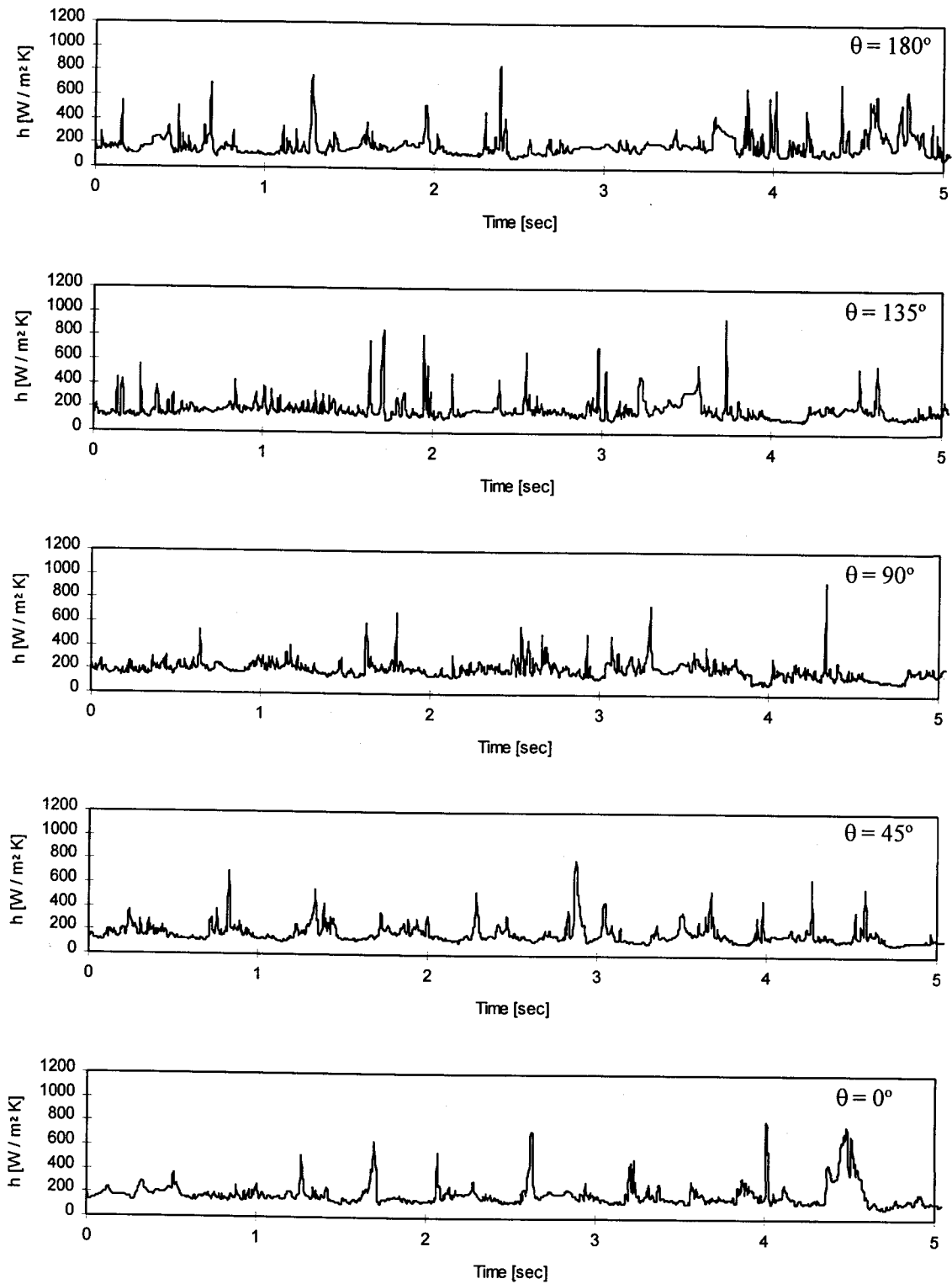


Figure 3.30 Instantaneous local heat transfer coefficients ($T_{\text{bed}} = 900 \text{ K}$, $d_p = 2 \text{ mm}$, $U = 2.52 \text{ m/s}$).

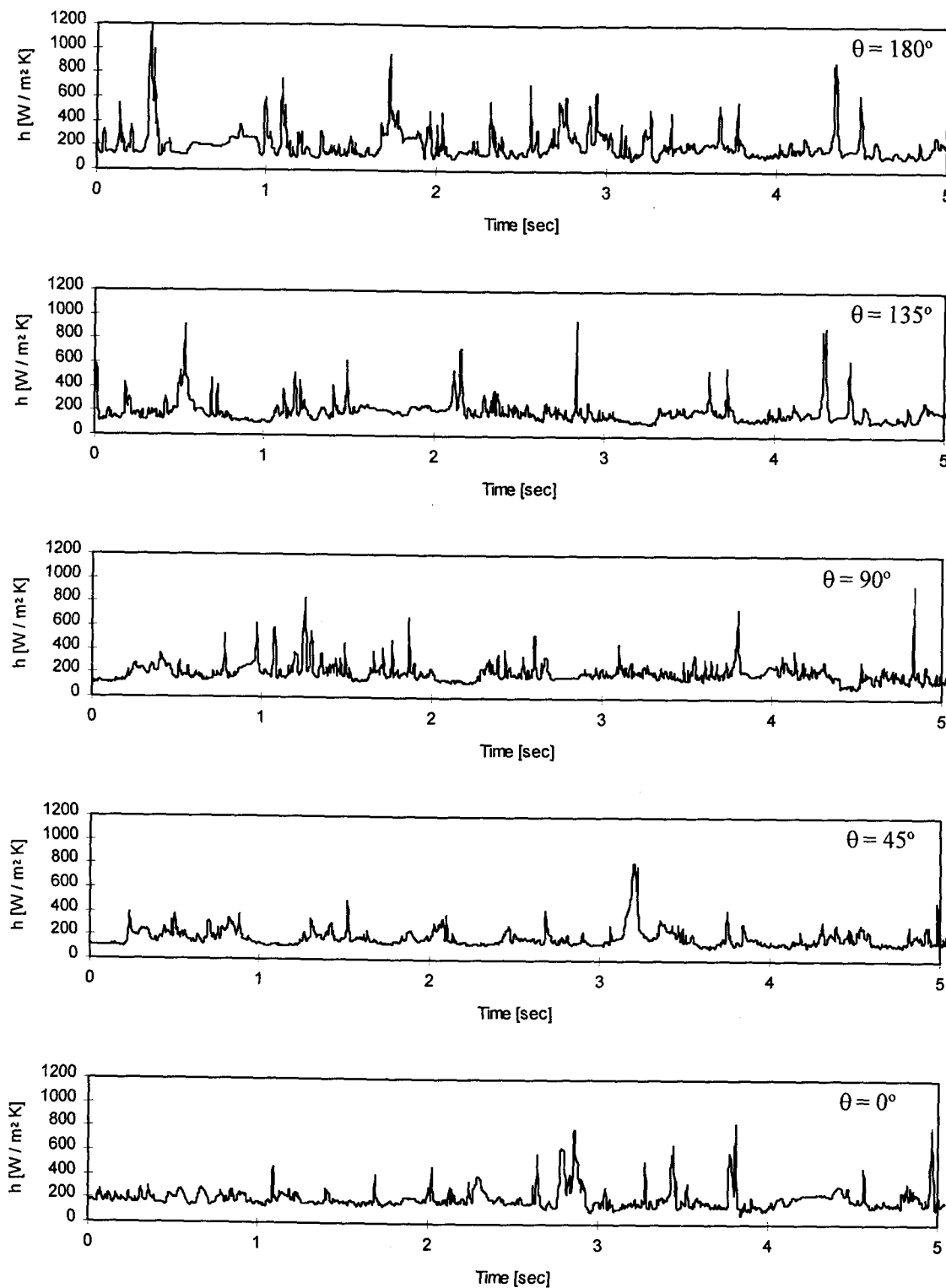


Figure 3.31 Instantaneous local heat transfer coefficients ($T_{\text{bed}} = 900 \text{ K}$, $d_p = 2 \text{ mm}$, $U = 2.74 \text{ m/s}$).

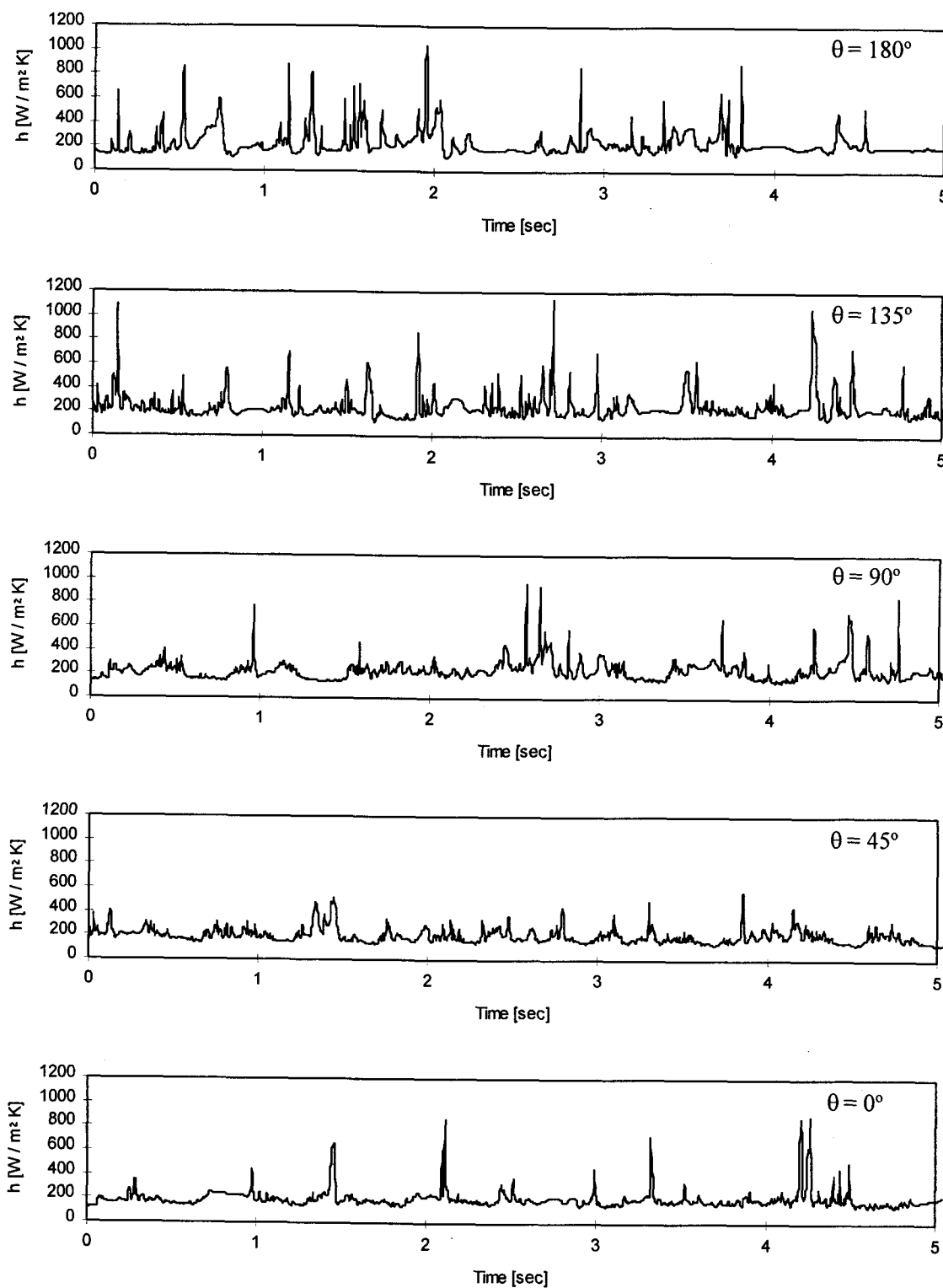


Figure 3.32 Instantaneous local heat transfer coefficients ($T_{\text{bed}} = 1000 \text{ K}$, $d_p = 2 \text{ mm}$, $U = 2.26 \text{ m/s}$).

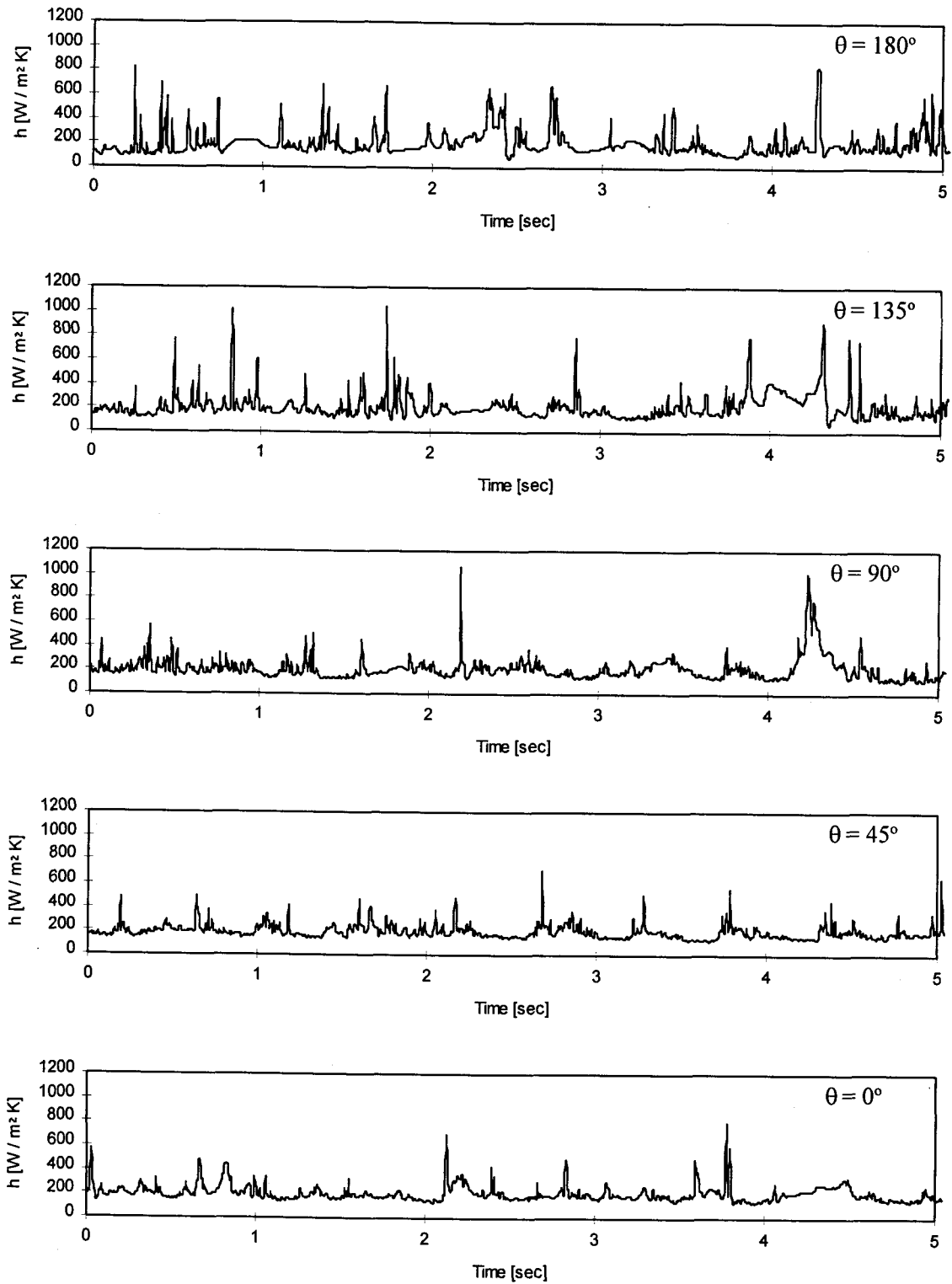


Figure 3.33 Instantaneous local heat transfer coefficients ($T_{\text{bed}} = 1000$ K, $d_p = 2$ mm, $U = 2.50$ m/s).

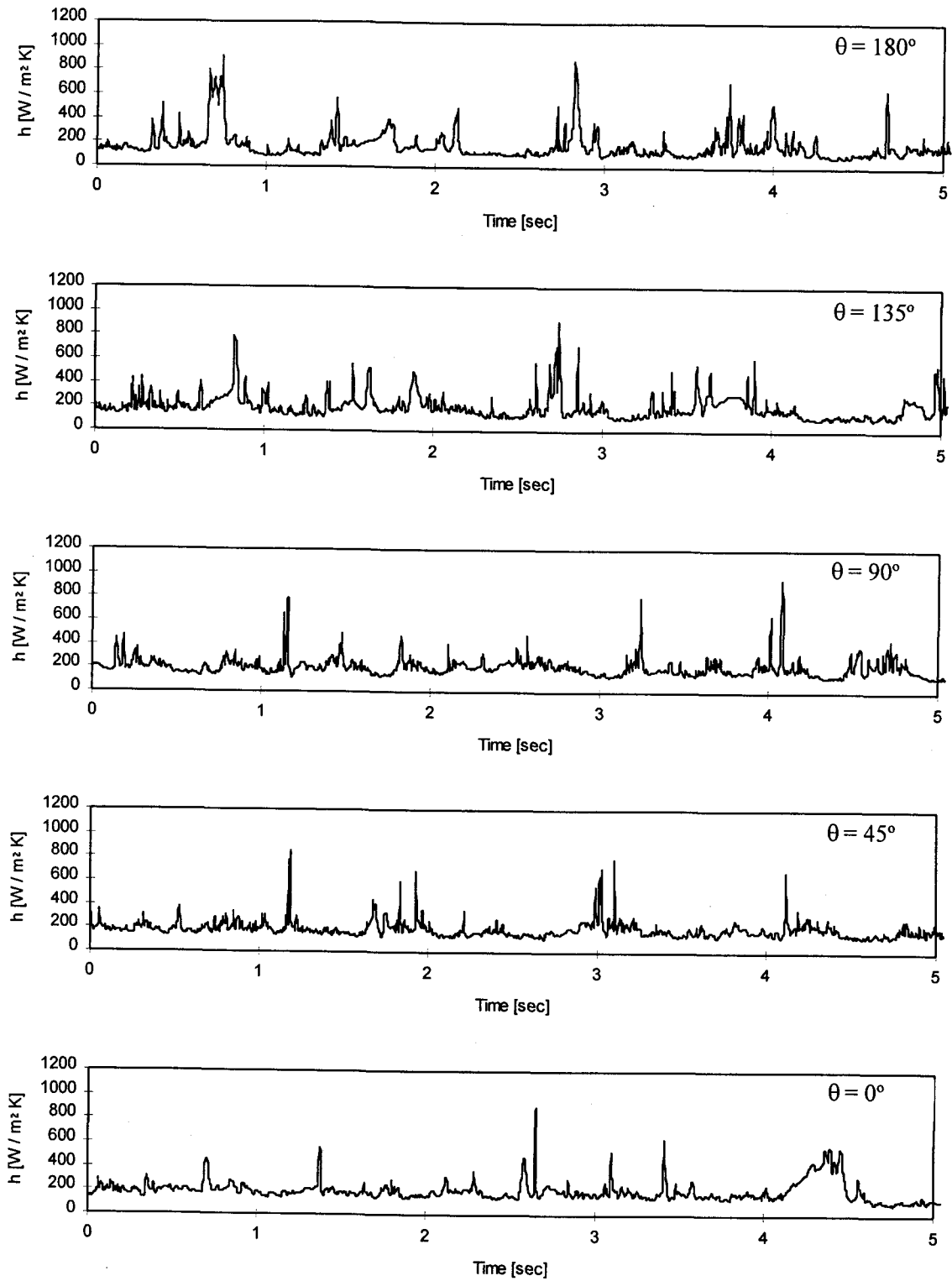


Figure 3.34 Instantaneous local heat transfer coefficients ($T_{\text{bed}} = 1000$ K, $d_p = 2$ mm, $U = 2.82$ m/s).

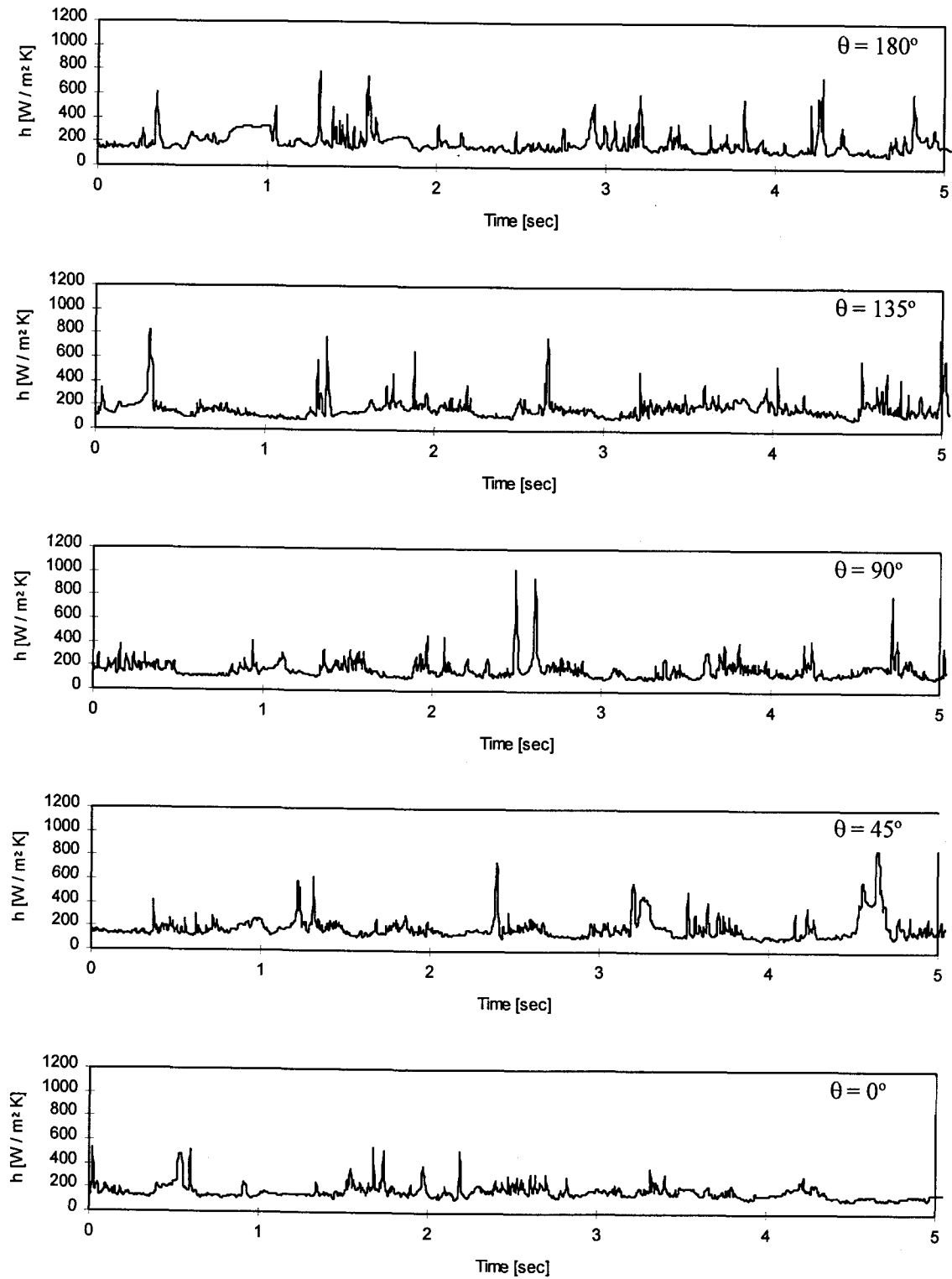


Figure 3.35 Instantaneous local heat transfer coefficients ($T_{\text{bed}} = 1000 \text{ K}$, $d_p = 2 \text{ mm}$, $U = 3.03 \text{ m/s}$).

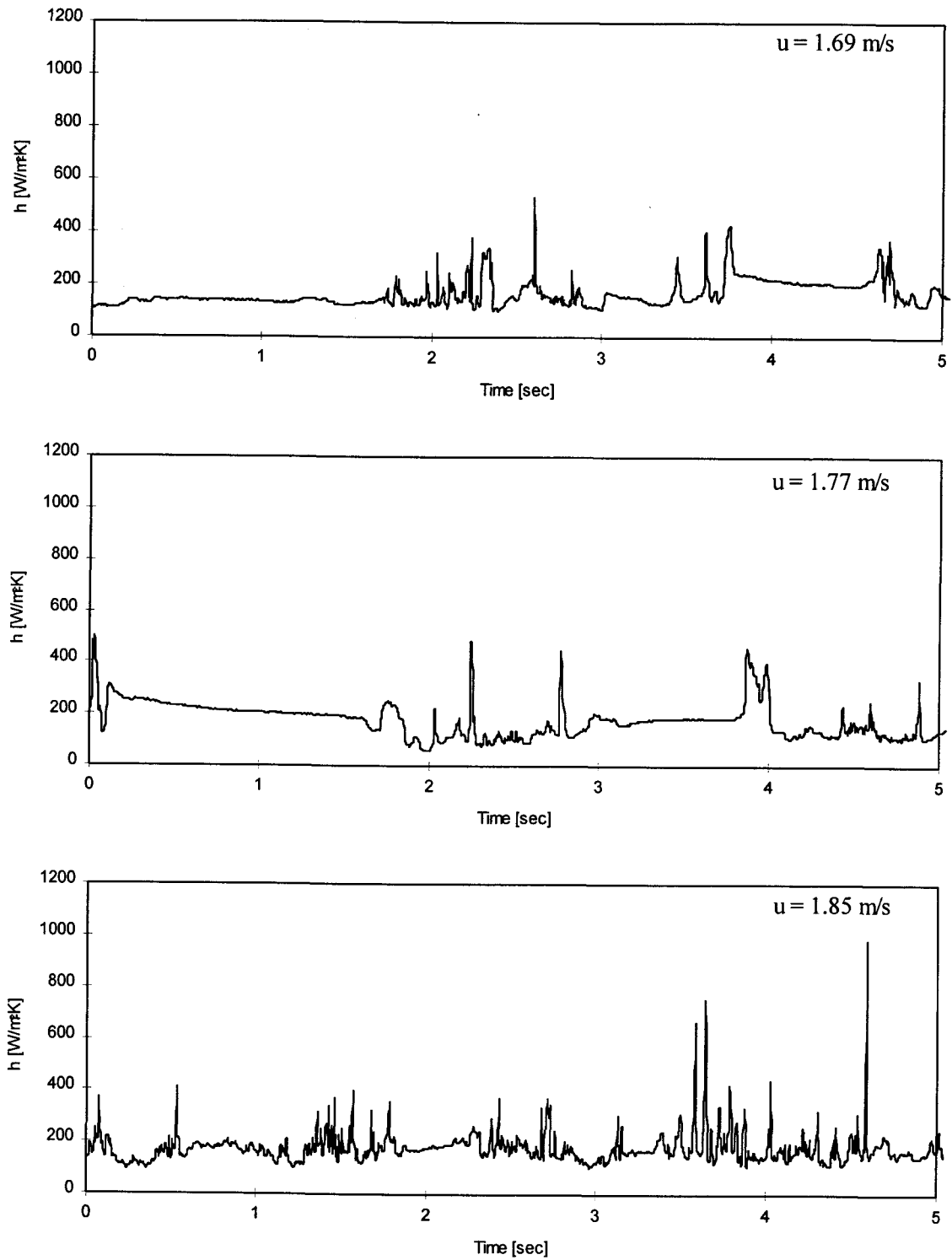


Figure 3.36 Instantaneous local heat transfer coefficients ($T_{\text{bed}} = 600 \text{ K}$, $d_p = 2 \text{ mm}$, $\theta = 180^\circ$).

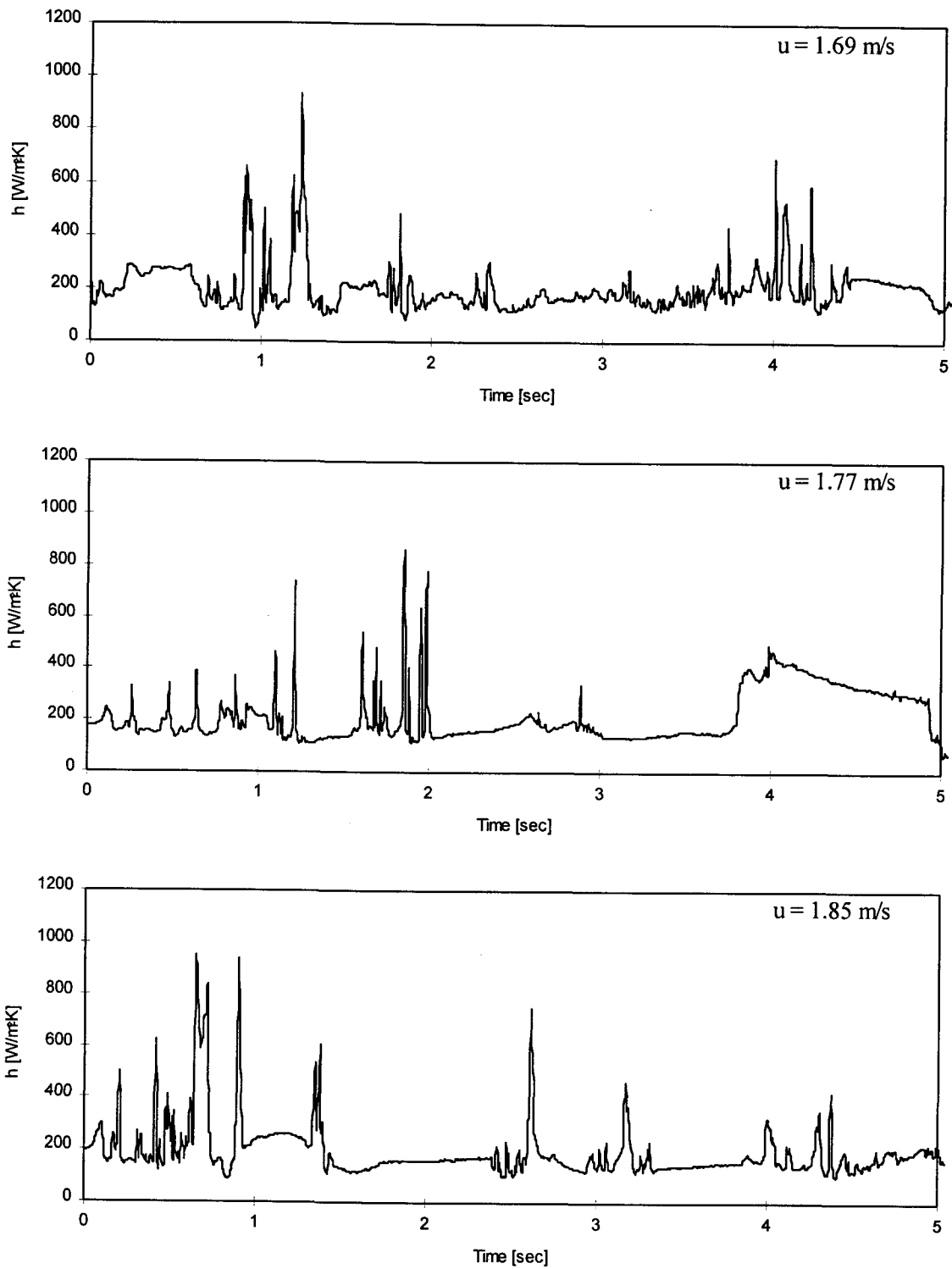


Figure 3.37 Instantaneous local heat transfer coefficients ($T_{\text{bed}} = 600 \text{ K}$, $d_p = 2 \text{ mm}$, $\theta = 135^\circ$).

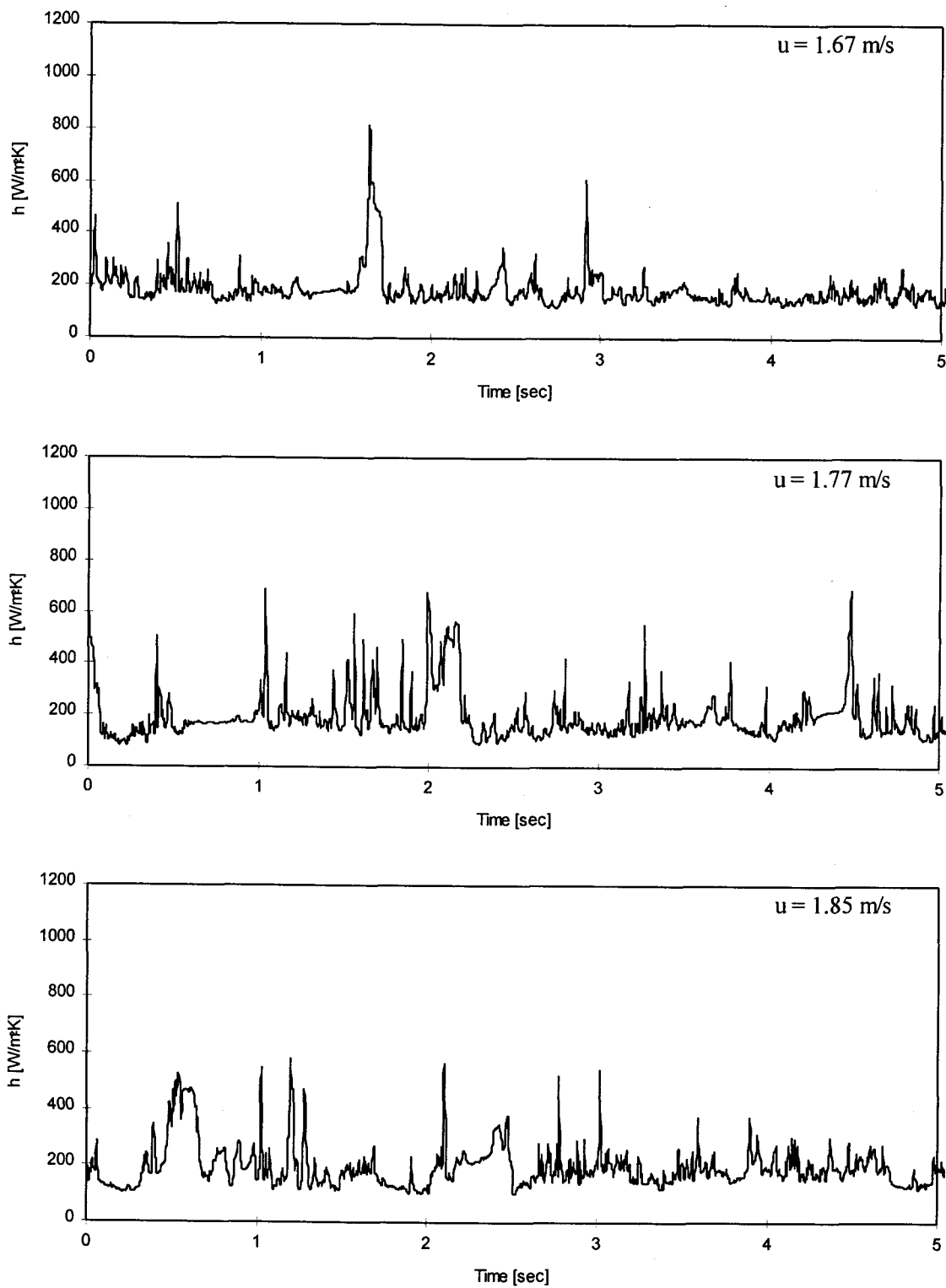


Figure 3.38 Instantaneous local heat transfer coefficients ($T_{\text{bed}} = 600 \text{ K}$, $d_p = 2 \text{ mm}$, $\theta = 90^\circ$).

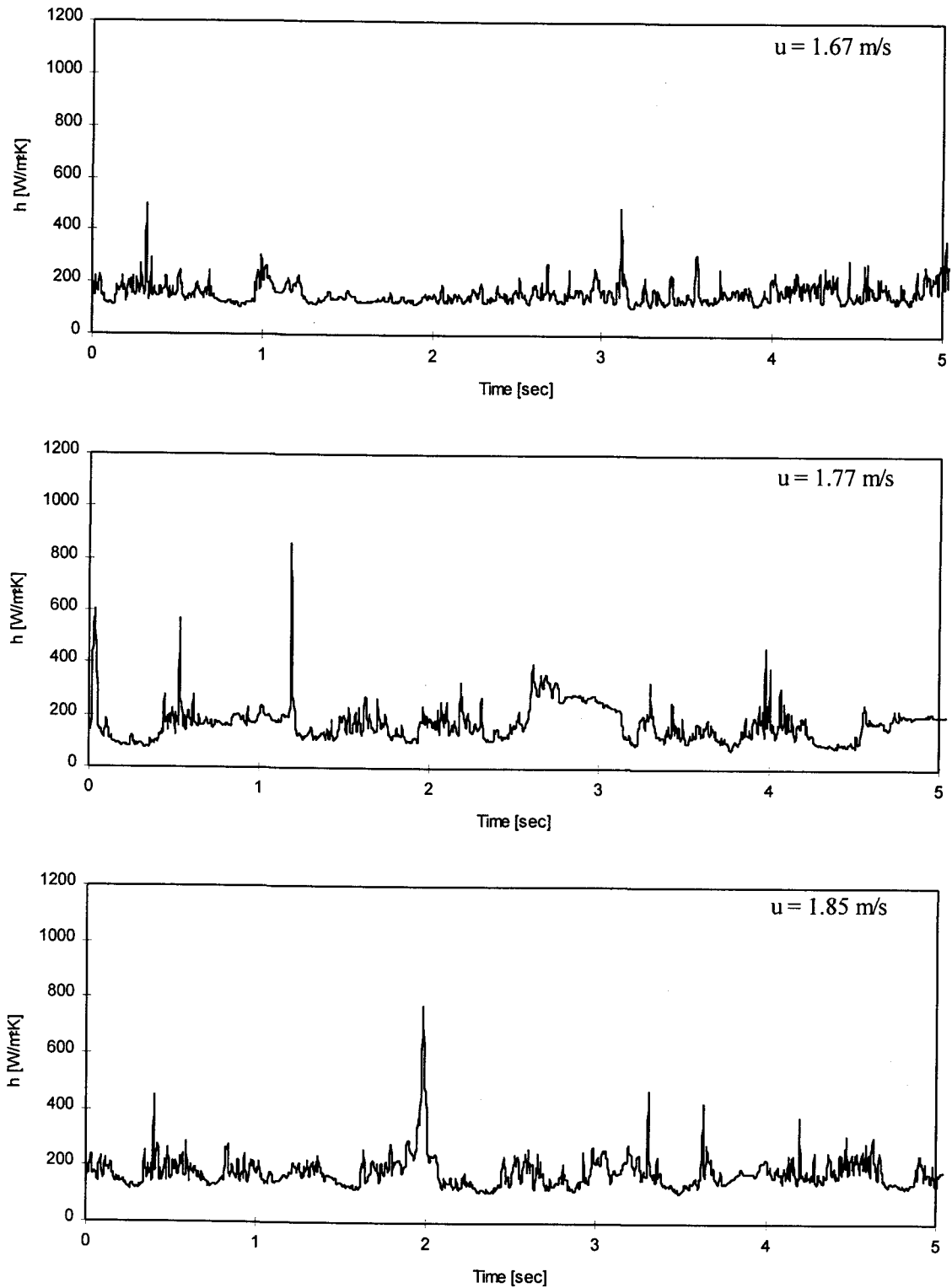


Figure 3.39 Instantaneous local heat transfer coefficients ($T_{\text{bed}} = 600 \text{ K}$, $d_p = 2 \text{ mm}$, $\theta = 45^\circ$).

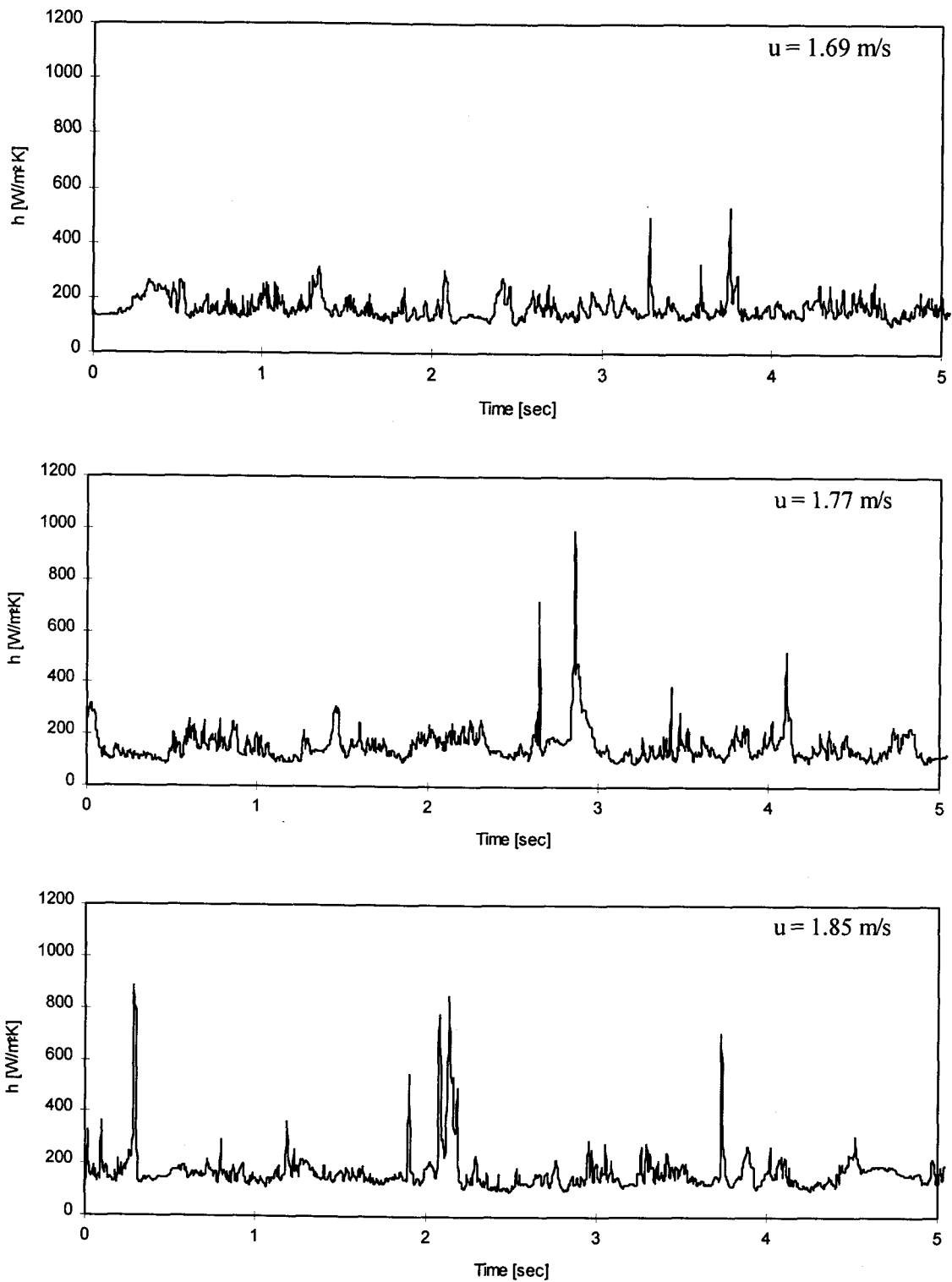


Figure 3.40 Instantaneous local heat transfer coefficients ($T_{\text{bed}} = 600 \text{ K}$, $d_p = 2 \text{ mm}$, $\theta = 0^\circ$).

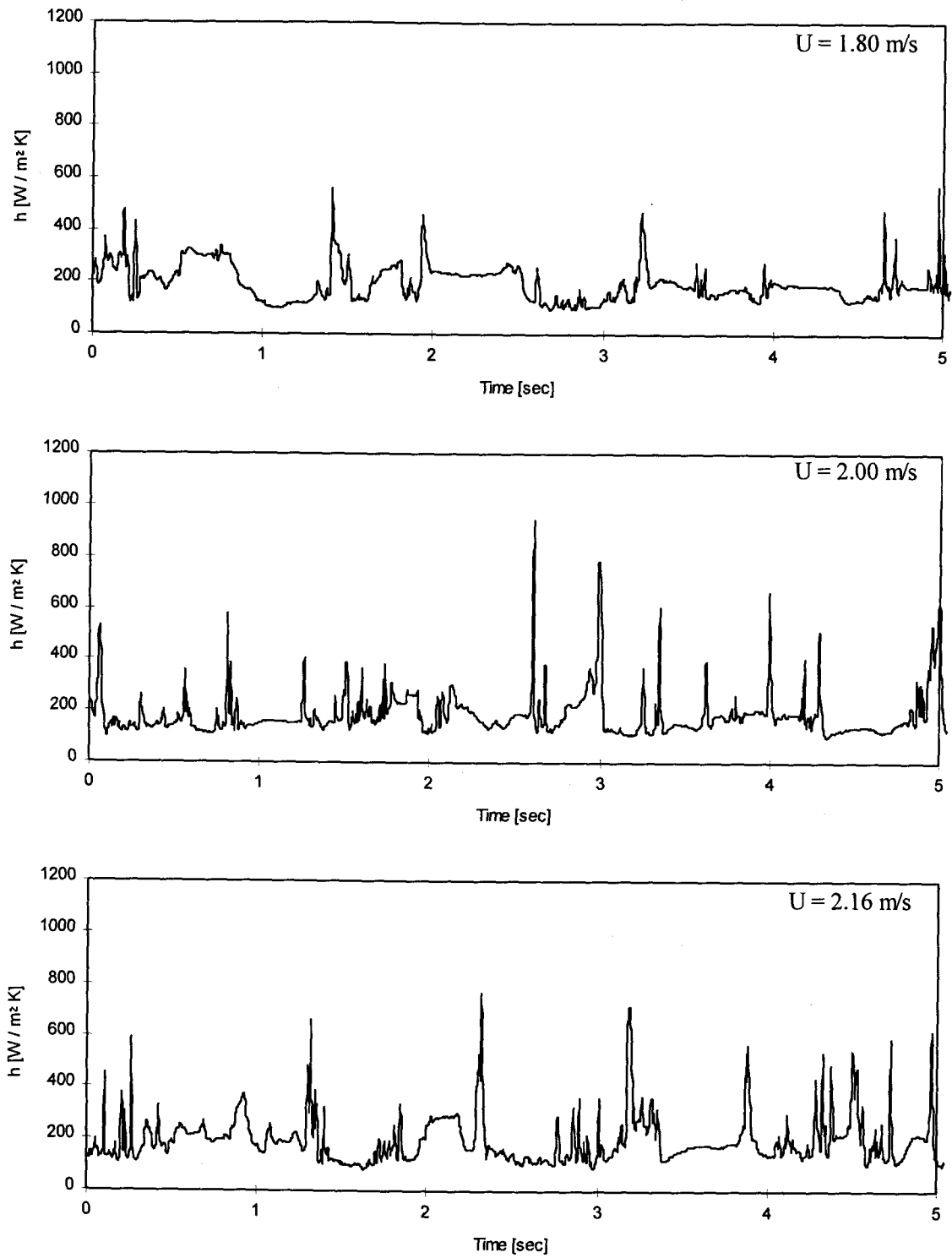


Figure 3.41 Instantaneous local heat transfer coefficients ($T_{\text{bed}} = 700 \text{ K}$, $d_p = 2 \text{ mm}$, $\theta = 180^\circ$).

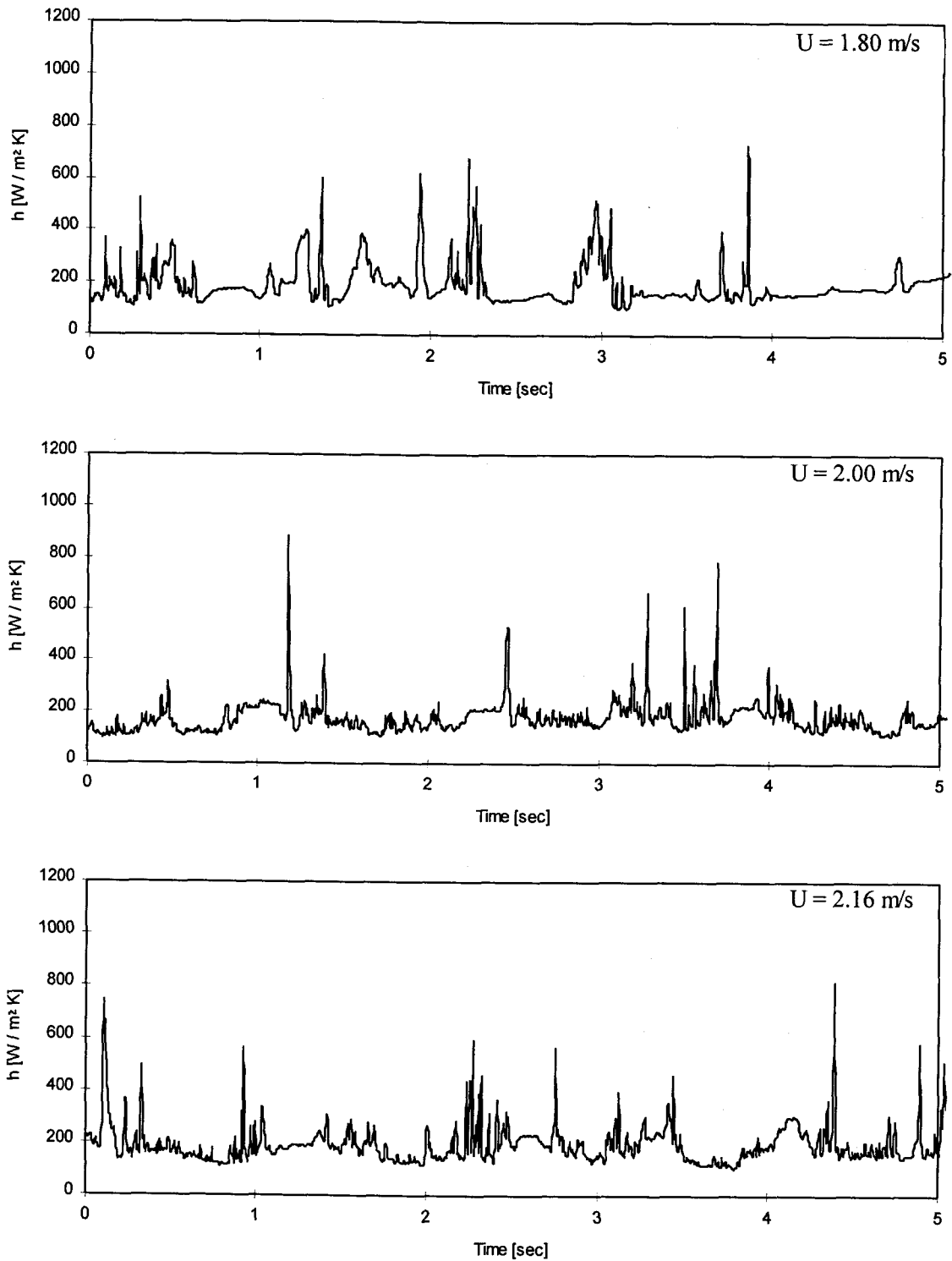


Figure 3.42 Instantaneous local heat transfer coefficients ($T_{\text{bed}} = 700 \text{ K}$, $d_p = 2 \text{ mm}$, $\theta = 135^\circ$).

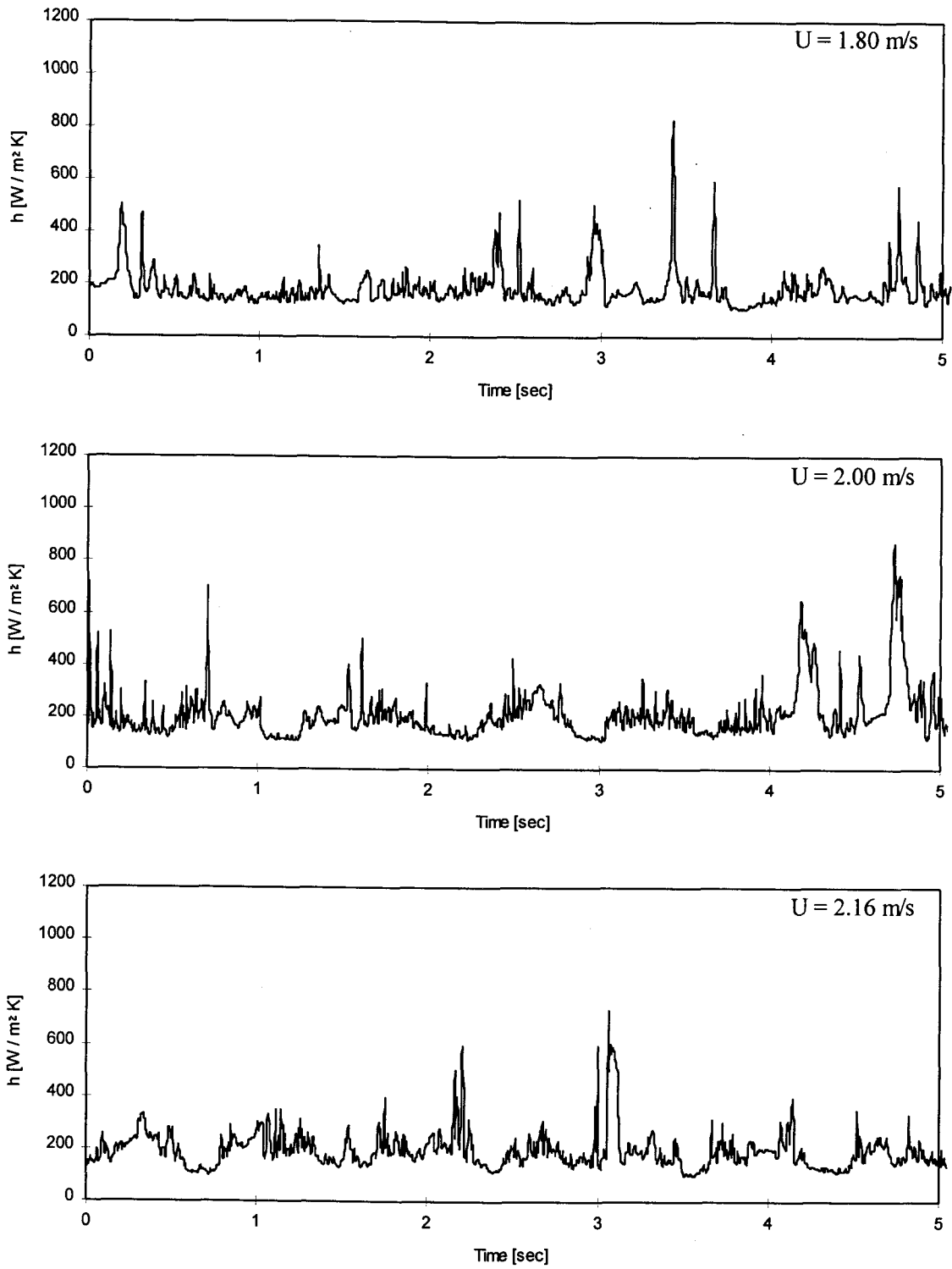


Figure 3.43 Instantaneous local heat transfer coefficients ($T_{\text{bed}} = 700 \text{ K}$, $d_p = 2 \text{ mm}$, $\theta = 90^\circ$).

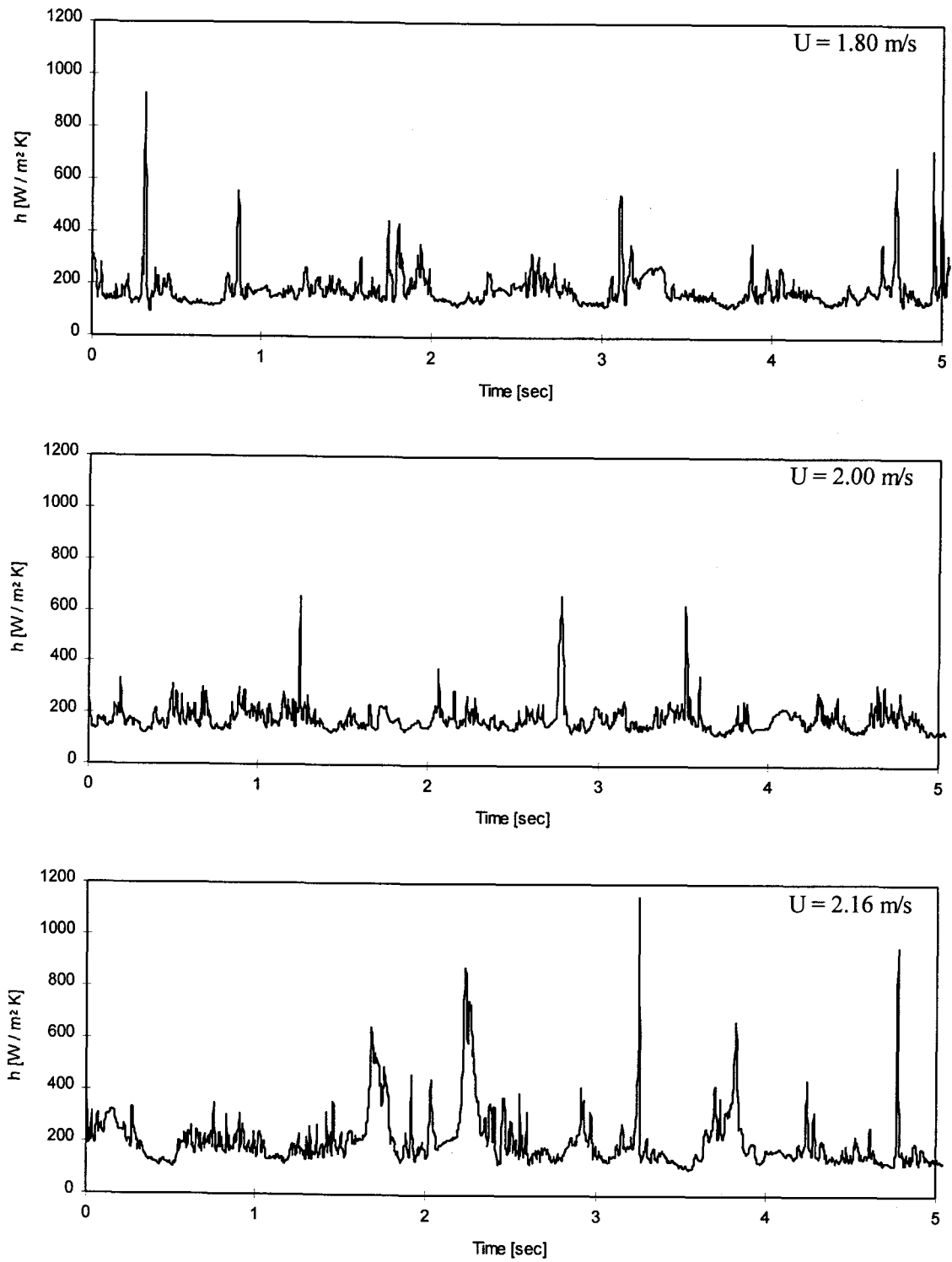


Figure 3.44 Instantaneous local heat transfer coefficients ($T_{\text{bed}} = 700 \text{ K}$, $d_p = 2 \text{ mm}$, $\theta = 45^\circ$).

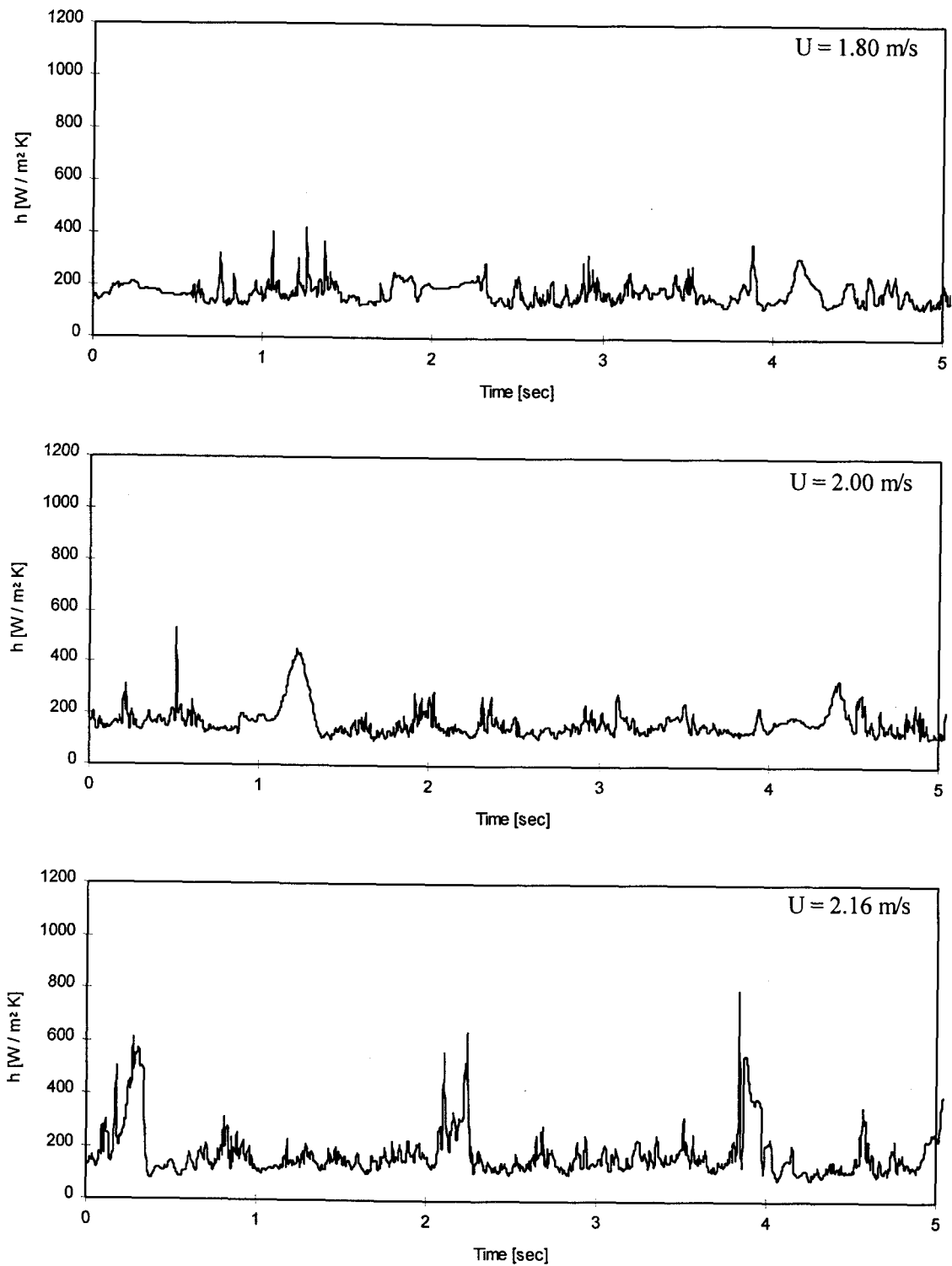


Figure 3.45 Instantaneous local heat transfer coefficients ($T_{\text{bed}} = 700 \text{ K}$, $d_p = 2 \text{ mm}$, $\theta = 0^\circ$).

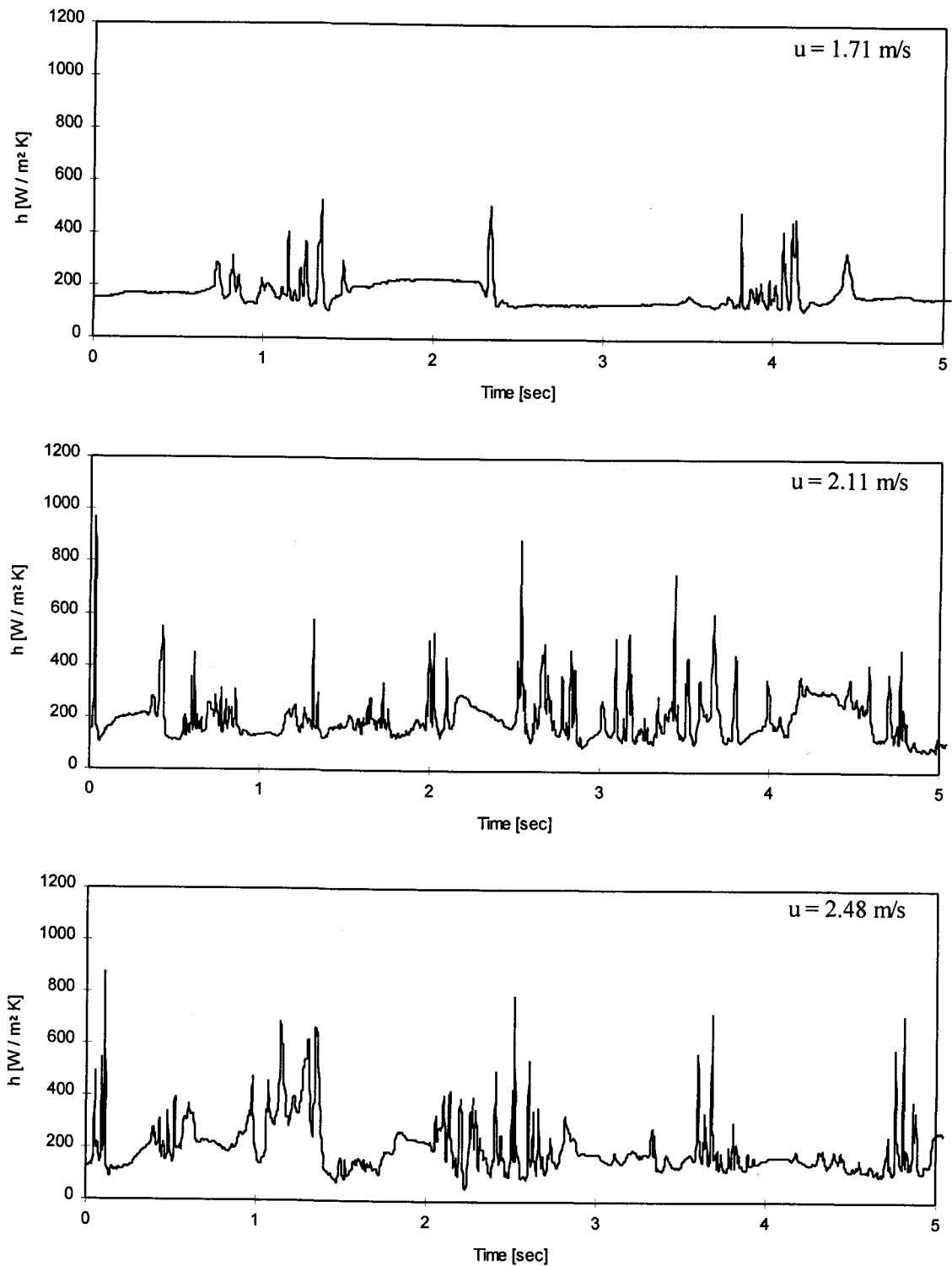


Figure 3.46 Instantaneous local heat transfer coefficients ($T_{\text{bed}} = 800 \text{ K}$, $d_p = 2 \text{ mm}$, $\theta = 180^\circ$).

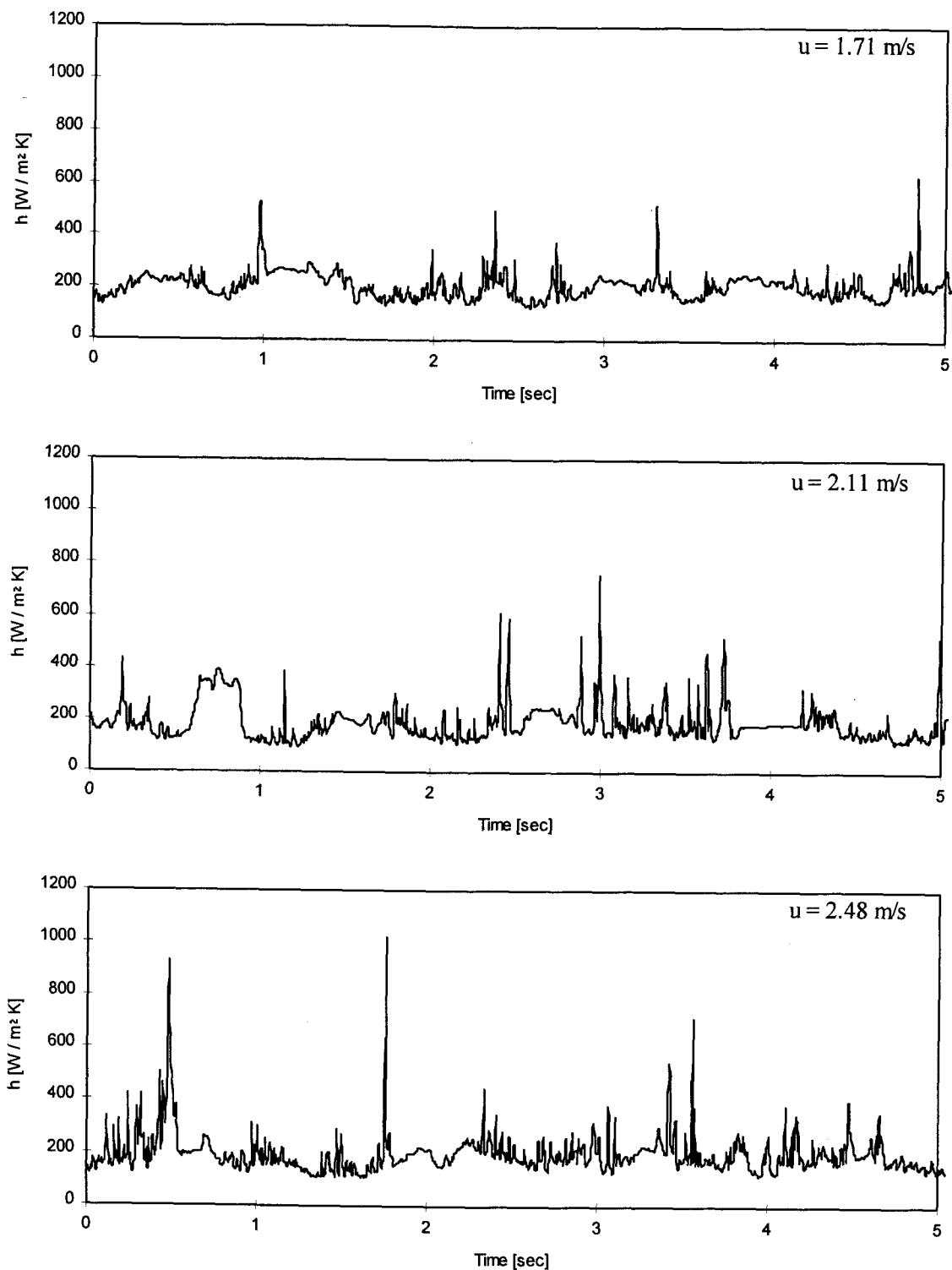


Figure 3.47 Instantaneous local heat transfer coefficients ($T_{\text{bed}} = 800 \text{ K}$, $d_p = 2 \text{ mm}$, $\theta = 135^\circ$).

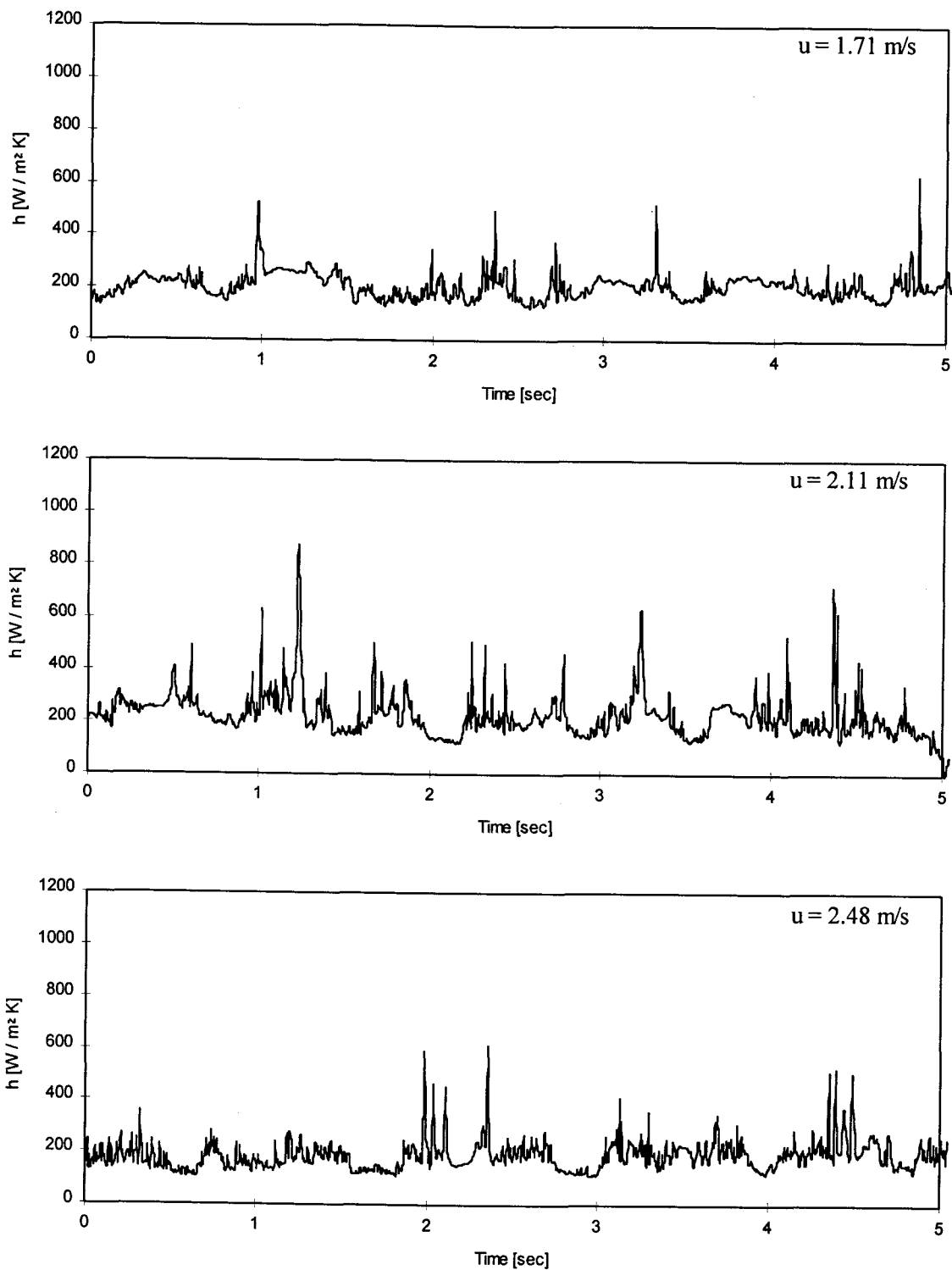


Figure 3.48 Instantaneous local heat transfer coefficients ($T_{\text{bed}} = 800 \text{ K}$, $d_p = 2 \text{ mm}$, $\theta = 90^\circ$).

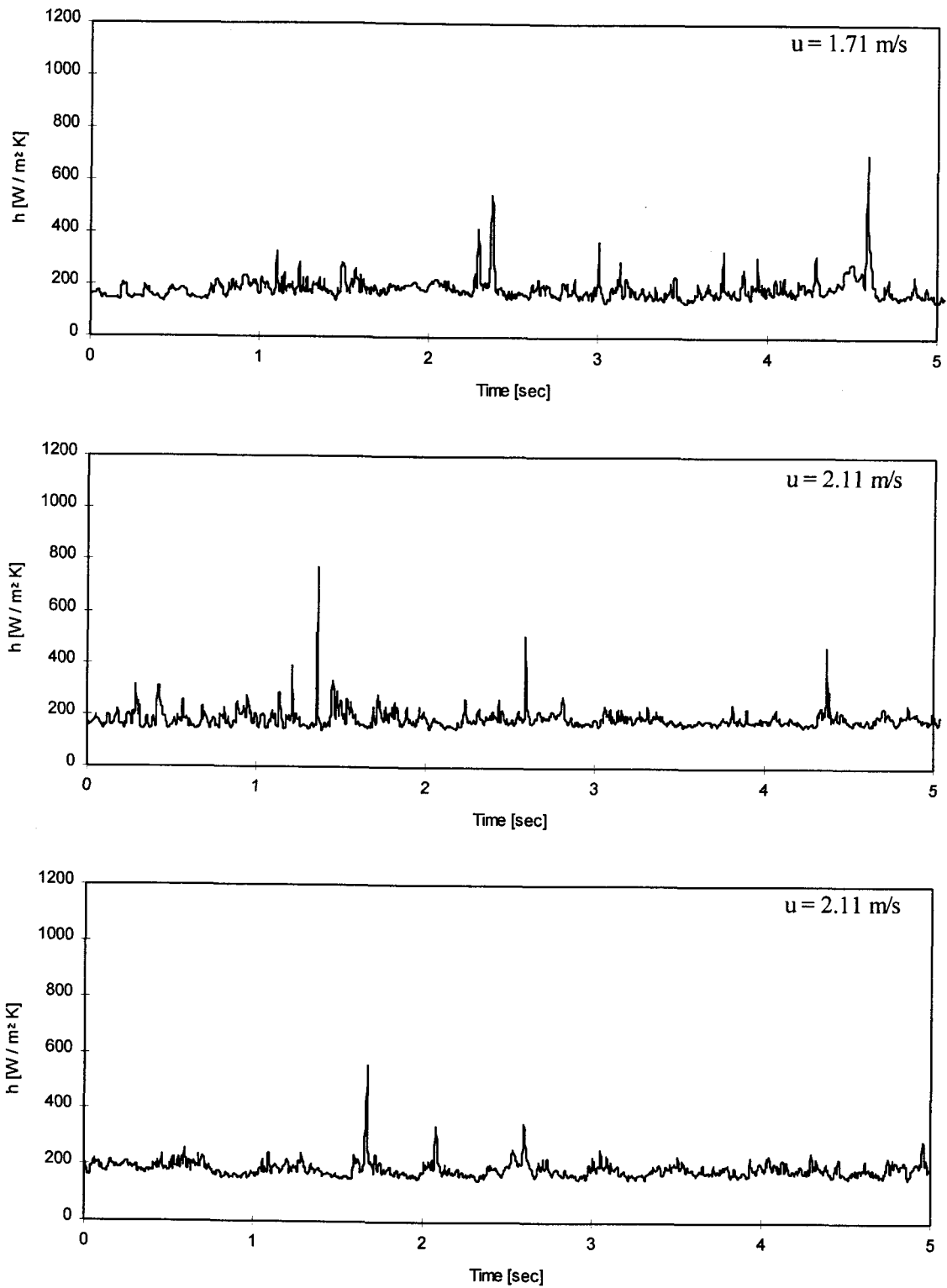


Figure 3.49 Instantaneous local heat transfer coefficients ($T_{\text{bed}} = 800 \text{ K}$, $d_p = 2 \text{ mm}$, $\theta = 45^\circ$).

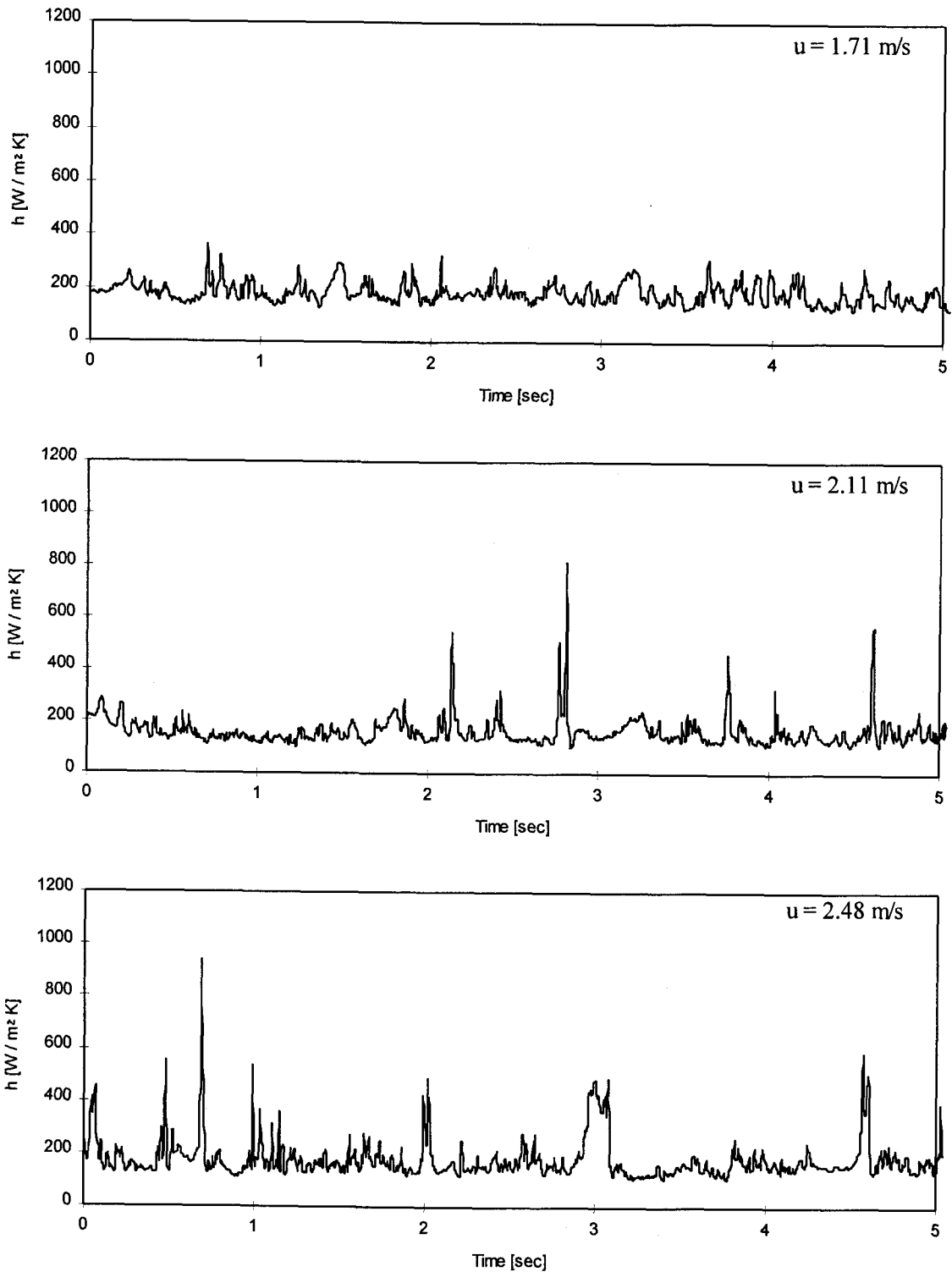


Figure 3.50 Instantaneous local heat transfer coefficients ($T_{\text{bed}} = 800 \text{ K}$, $d_p = 2 \text{ mm}$, $\theta = 0^\circ$).

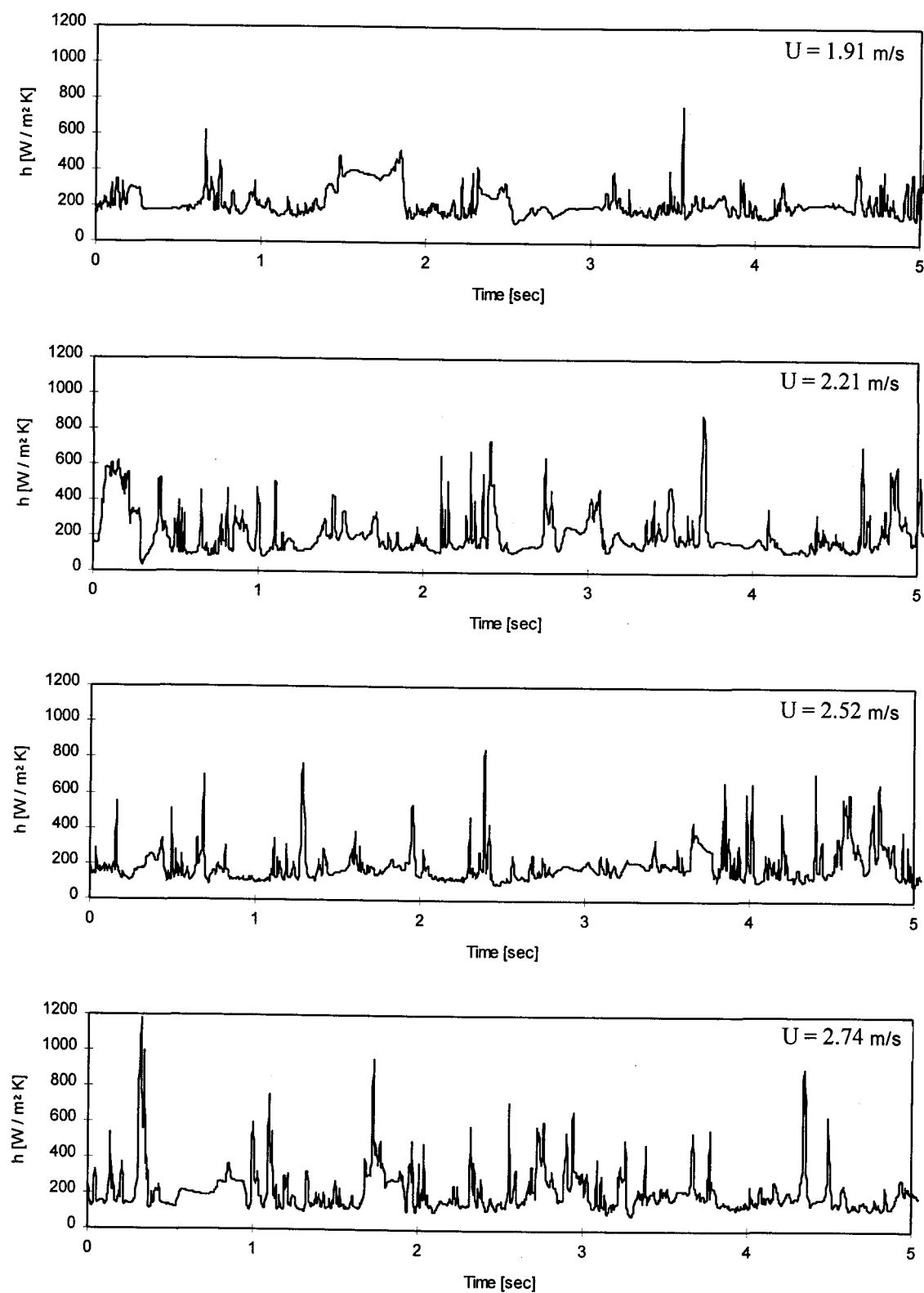


Figure 3.51 Instantaneous local heat transfer coefficients ($T_{\text{bed}} = 900 \text{ K}$, $d_p = 2 \text{ mm}$, $\theta = 180^\circ$).

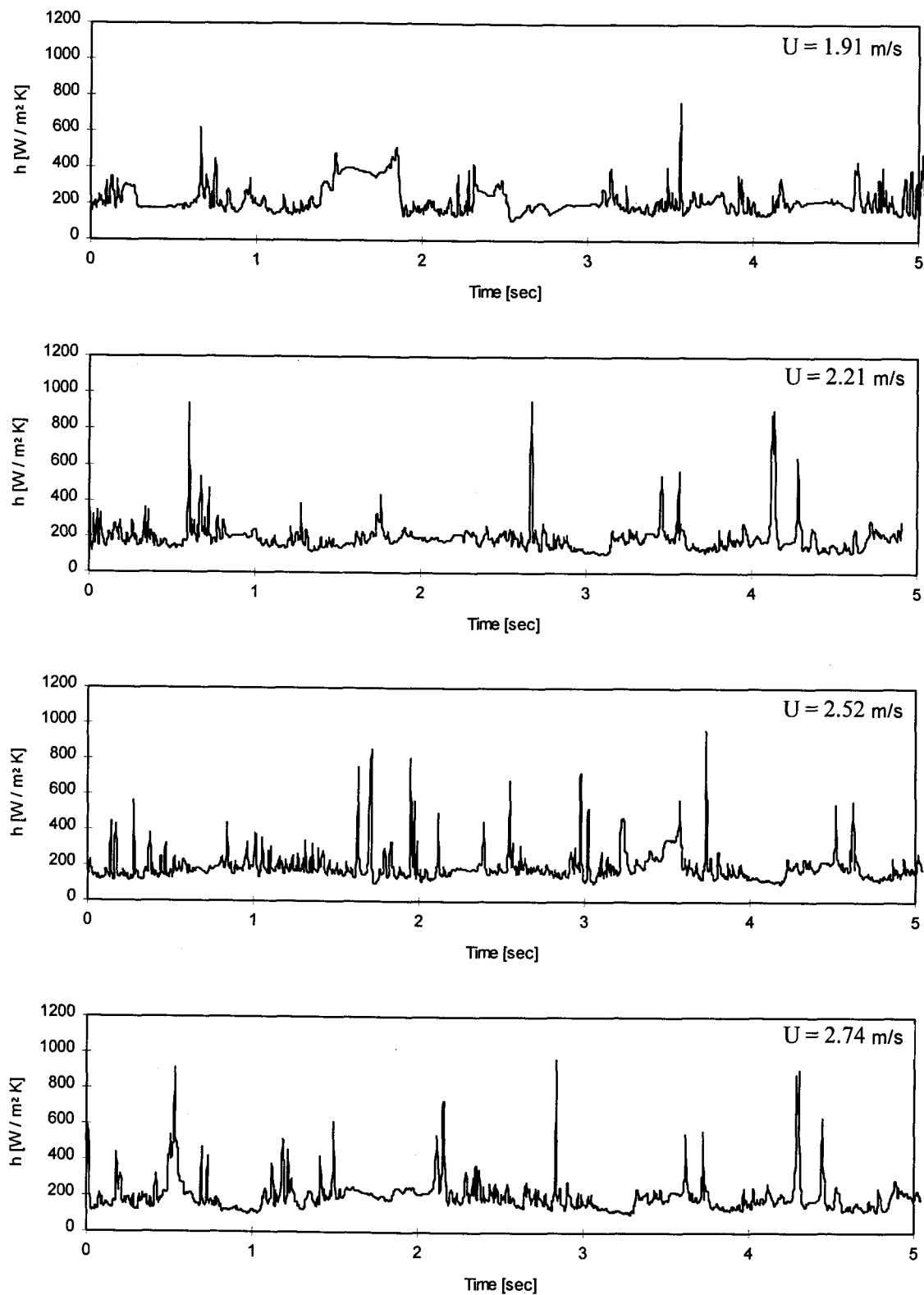


Figure 3.52 Instantaneous local heat transfer coefficients ($T_{\text{bed}} = 900 \text{ K}$, $d_p = 2 \text{ mm}$, $\theta = 135^\circ$).

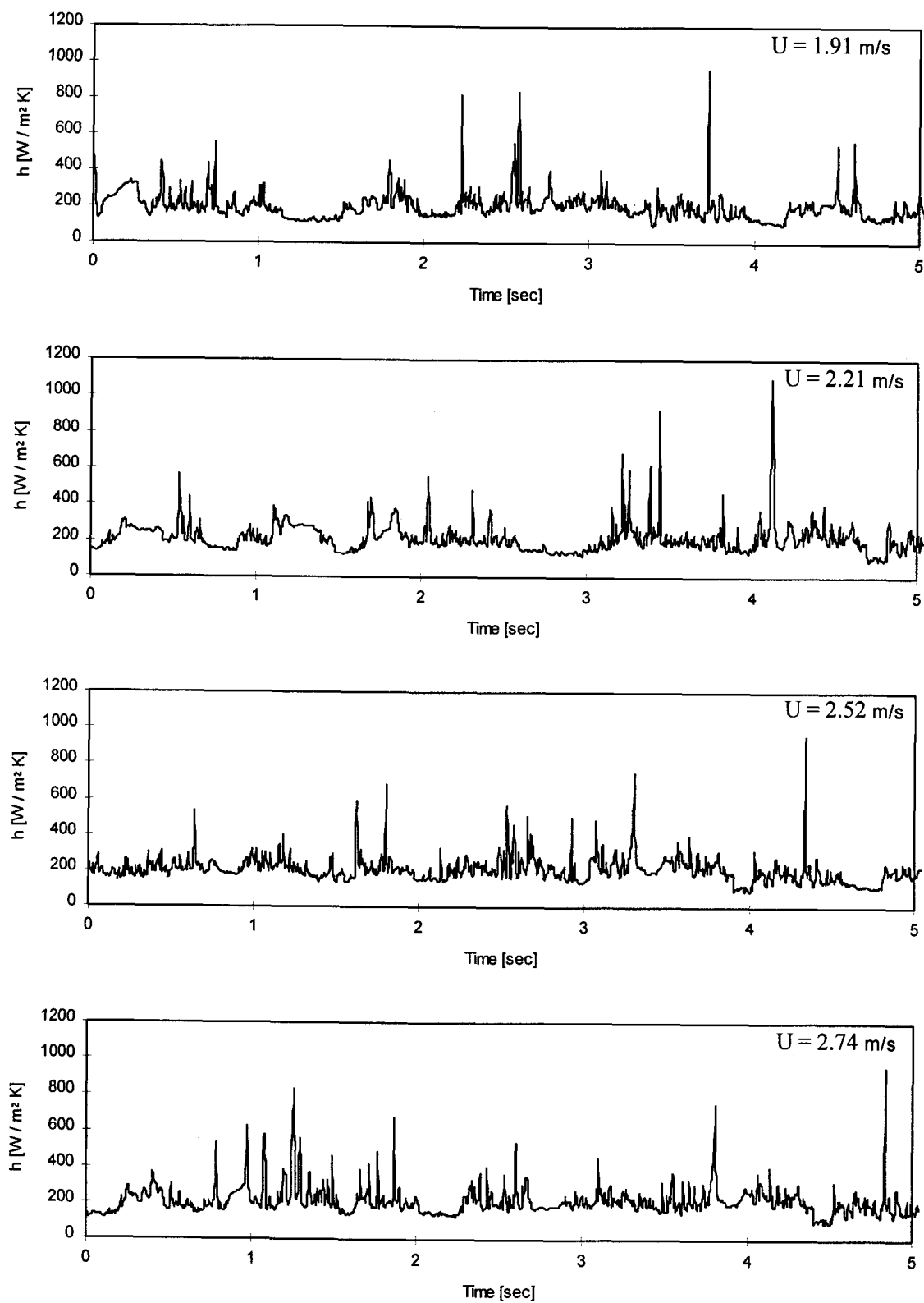


Figure 3.53 Instantaneous local heat transfer coefficients ($T_{\text{bed}} = 900 \text{ K}$, $d_p = 2 \text{ mm}$, $\theta = 90^\circ$).

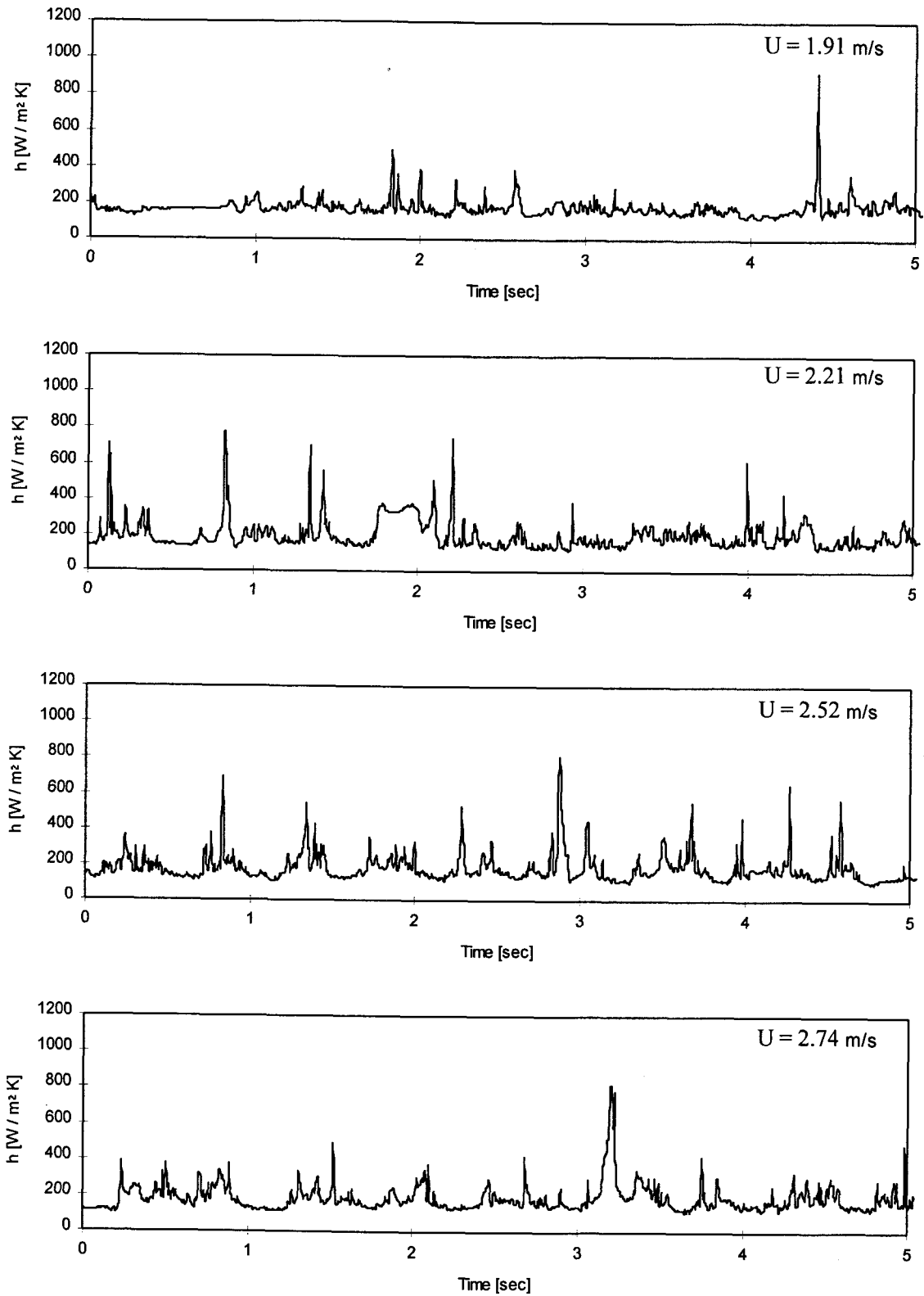


Figure 3.54 Instantaneous local heat transfer coefficients ($T_{\text{bed}} = 900 \text{ K}$, $d_p = 2 \text{ mm}$, $\theta = 45^\circ$).

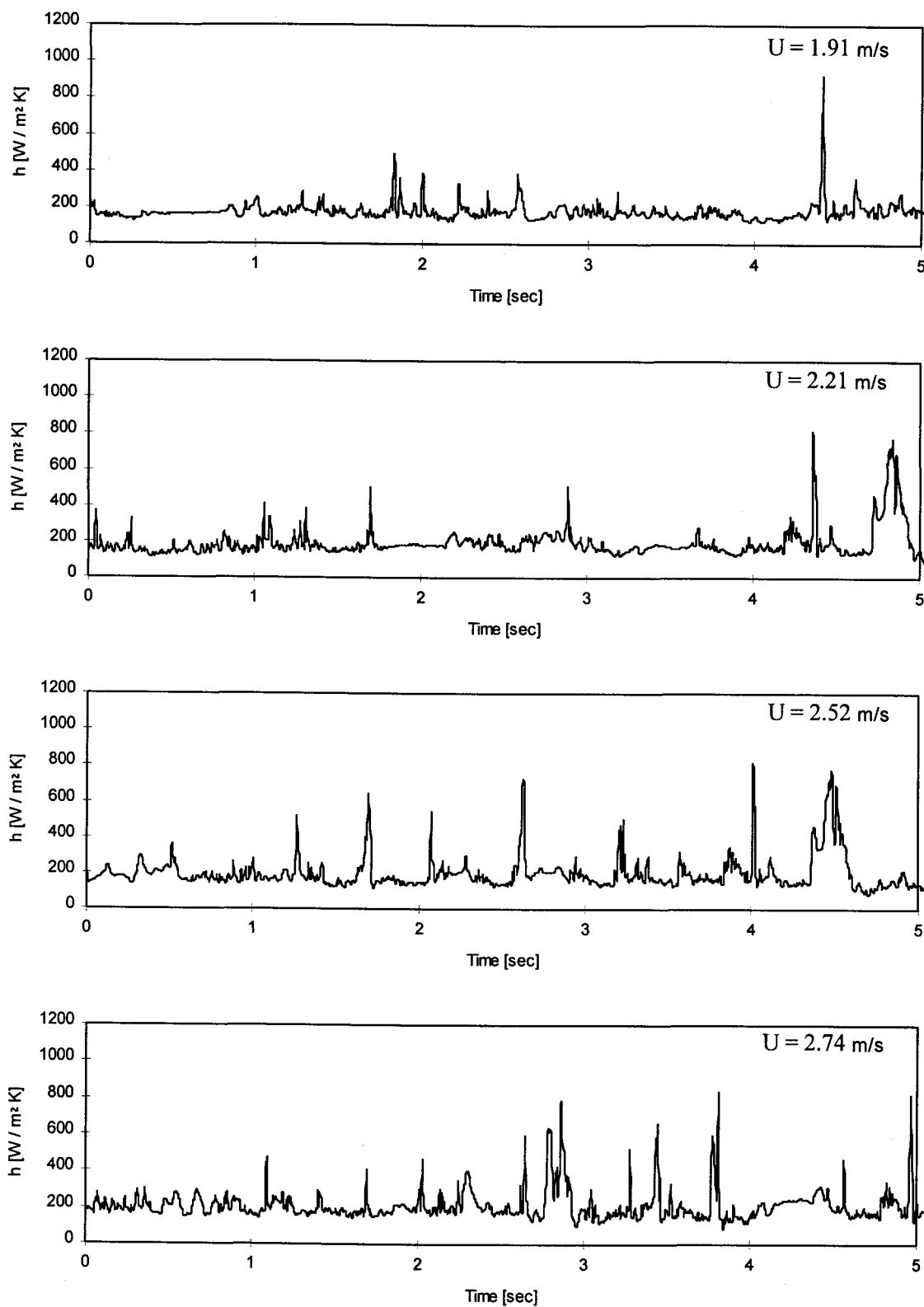


Figure 3.55 Instantaneous local heat transfer coefficients ($T_{\text{bed}} = 900 \text{ K}$, $d_p = 2 \text{ mm}$, $\theta = 0^\circ$).

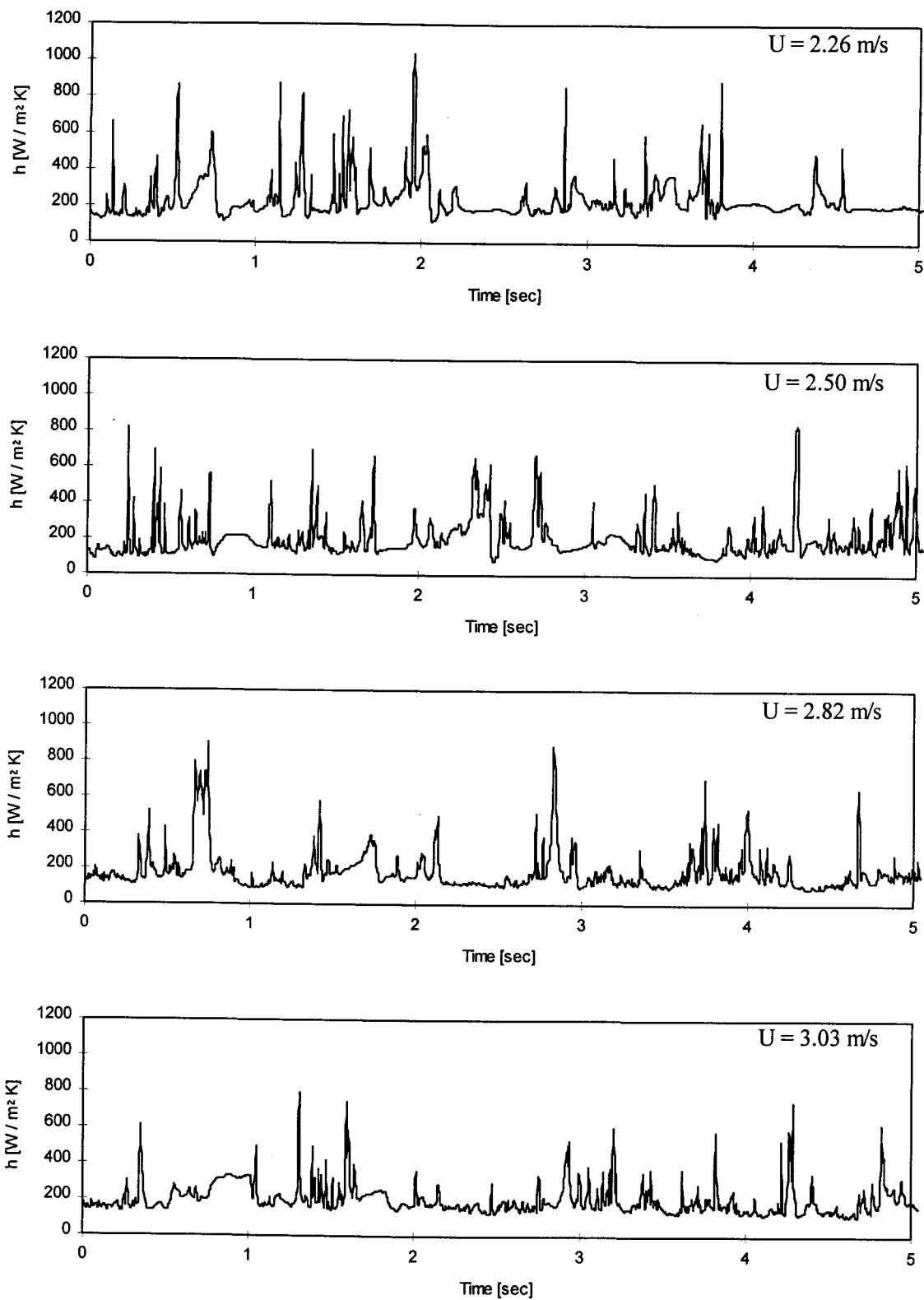


Figure 3.56 Instantaneous local heat transfer coefficients ($T_{\text{bed}} = 1000 \text{ K}$, $d_p = 2 \text{ mm}$, $\theta = 180^\circ$).

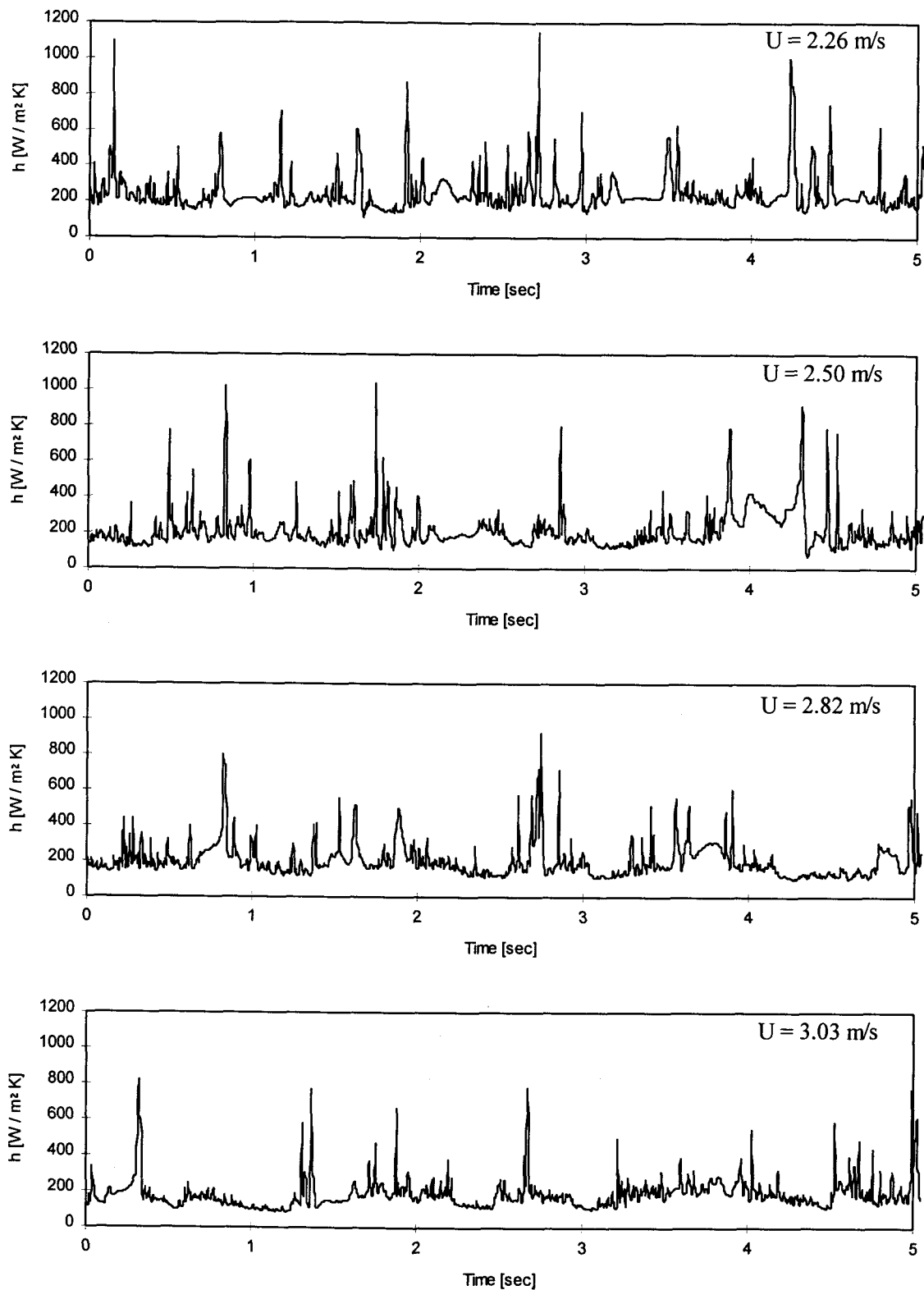


Figure 3.57 Instantaneous local heat transfer coefficients ($T_{\text{bed}} = 1000 \text{ K}$, $d_p = 2 \text{ mm}$, $\theta = 135^\circ$).

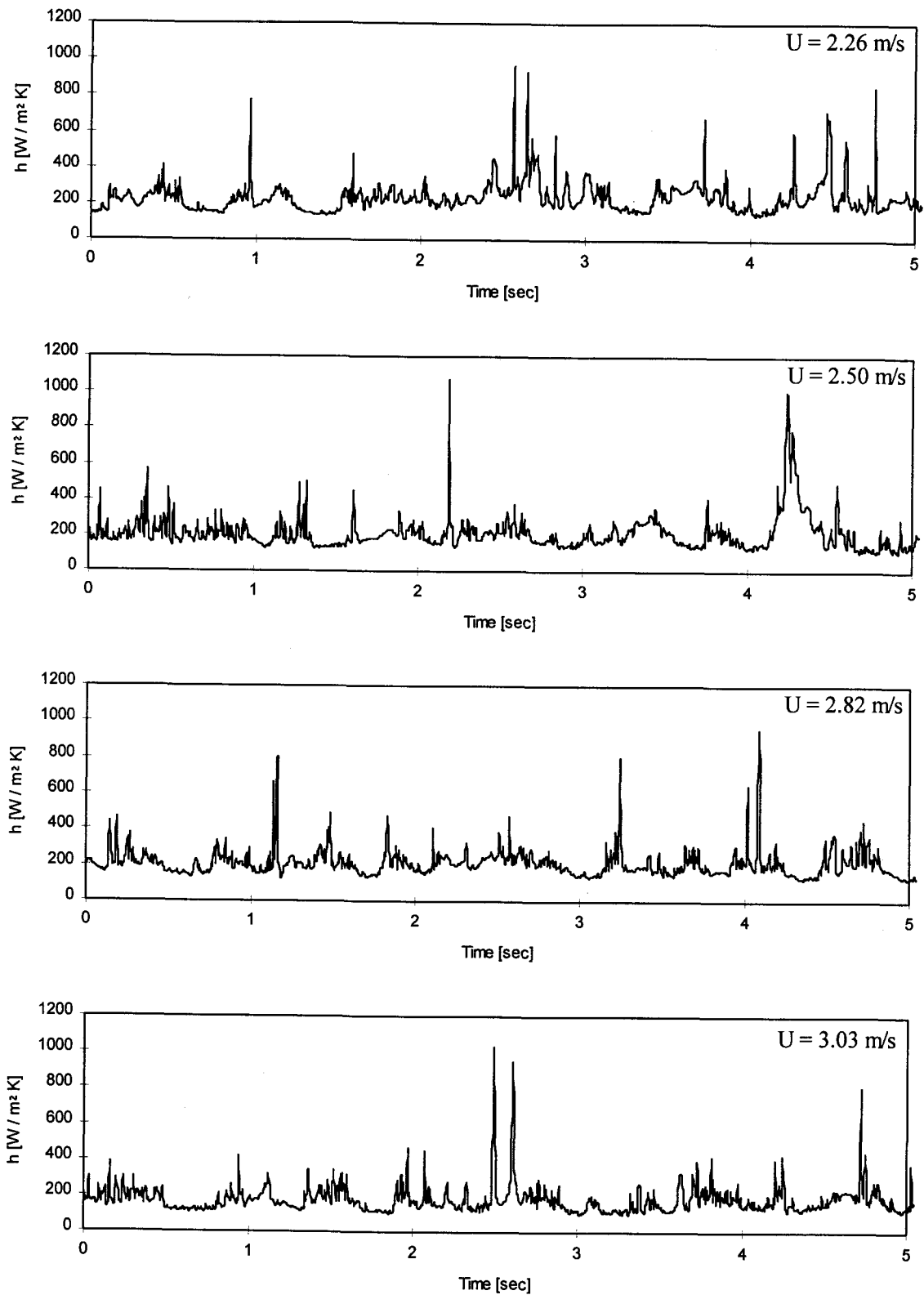


Figure 3.58 Instantaneous local heat transfer coefficients ($T_{\text{bed}} = 1000$ K, $d_p = 2$ mm, $\theta = 90^\circ$).

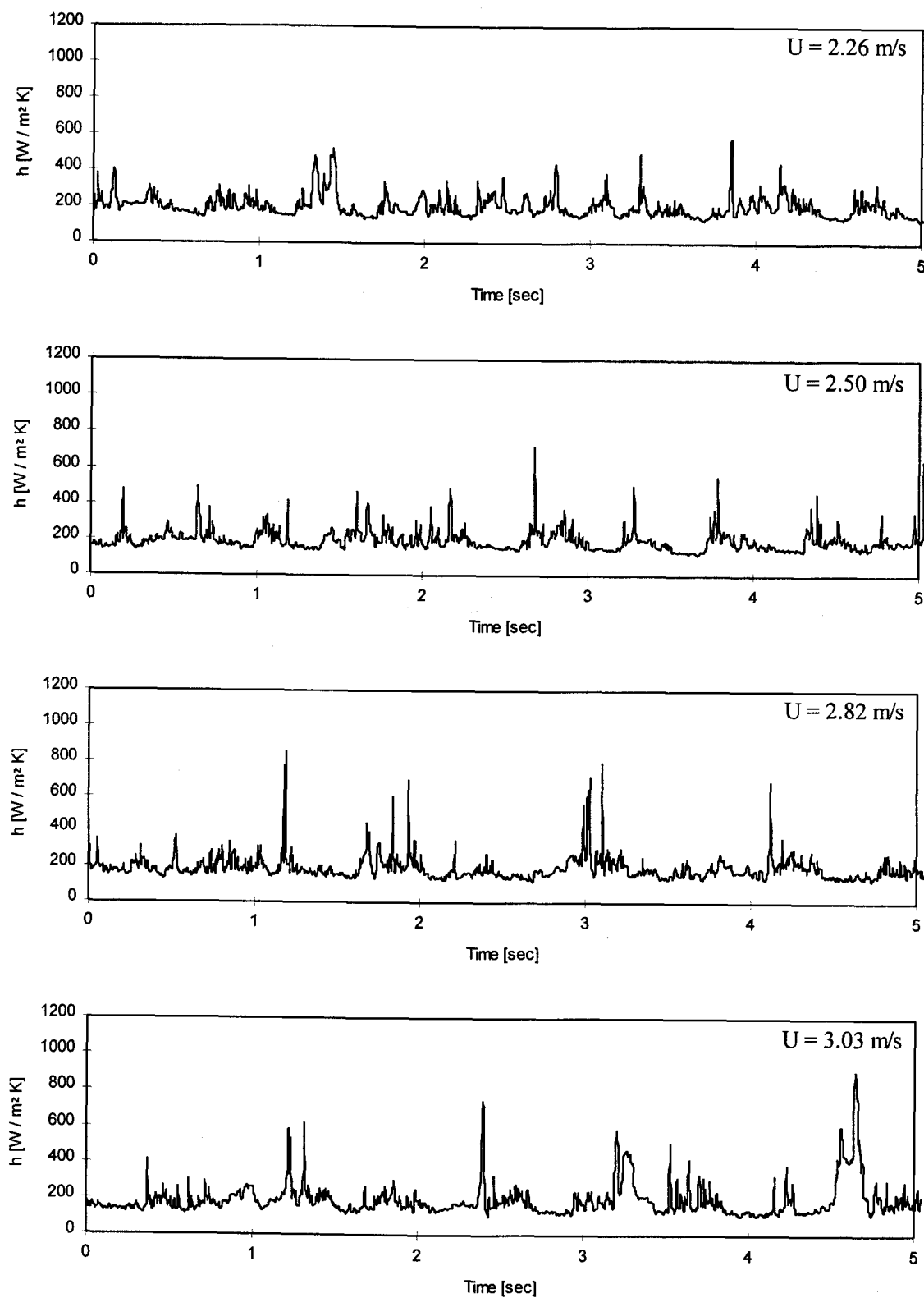


Figure 3.59 Instantaneous local heat transfer coefficients ($T_{\text{bed}} = 1000 \text{ K}$, $d_p = 2 \text{ mm}$, $\theta = 45^\circ$).

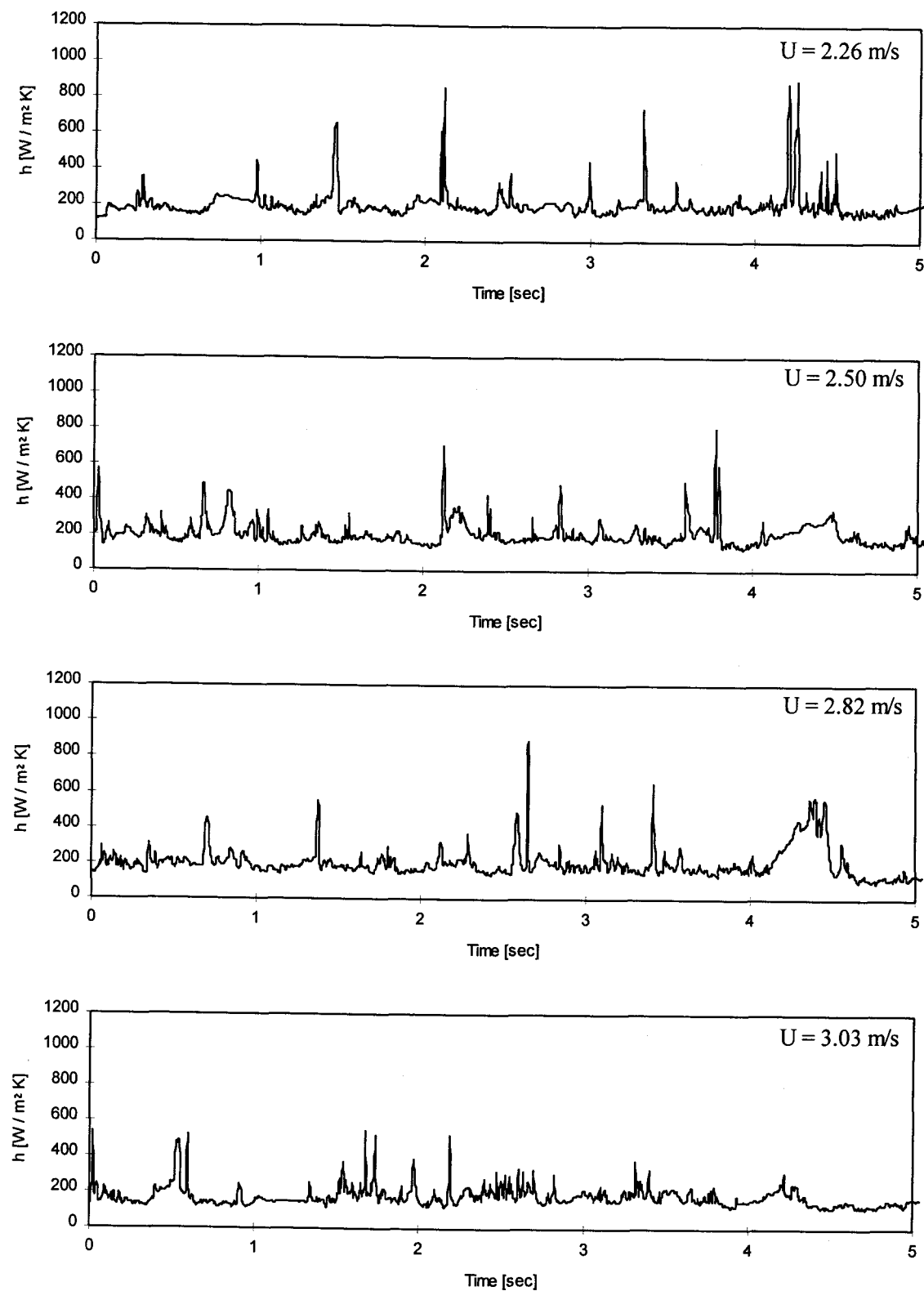


Figure 3.60 Instantaneous local heat transfer coefficients ($T_{\text{bed}} = 1000 \text{ K}$, $d_p = 2 \text{ mm}$, $\theta = 0^\circ$).

phase and emulsion phase activity can be distinctly observed at the tube surface as the emulsion phase and bubble phase replace each other.

In Figure 3.38 ($T=600\text{K}$, $\theta = 90^\circ$), it is seen that the activity at $\theta = 90^\circ$ is more consistent. While distinct bubble and emulsion phase activity can be observed, the signal looks more uniform than at $\theta = 135^\circ$ and $\theta = 180^\circ$. At higher velocities, the bubble and emulsion phases are more pronounced. The heat transfer coefficient in Figure 3.39 ($T=600\text{K}$, $\theta = 45^\circ$) is fairly constant at low velocity. At higher velocities, definite bubble and emulsion phase behavior can be seen. At $\theta = 0^\circ$ (Figure 3.40, $T=600\text{K}$, $\theta = 0^\circ$), at low velocities the signal suggests that a gas cushion is present. At higher velocities, distinct emulsion and bubble phases can be seen.

Similar trends can be seen for a bed temperature of $T=700\text{K}$. At $\theta = 180^\circ$ as shown in Figure 3.41, activity is relatively infrequent at low velocity while more violent at high velocity. At $\theta = 135^\circ$ (Figure 3.42), the lack of activity suggests either a gas cushion or cool particles are resident on the tube surface at lower velocities. At $\theta = 90^\circ$ (Figure 3.43), bubbles can be seen followed by an active emulsion phase (high particle activity in the emulsion phase). At $\theta = 45^\circ$ (Figure 3.44), a quiet, consistent gas cushion can be observed. Similarly, at $\theta = 0^\circ$ in Figure 3.45 a dominant gas cushion is present and is interrupted by brief emulsion packets.

At a bed temperature of $T=800\text{K}$, there is little activity at $\theta = 180^\circ$ at low velocity (Figure 3.46). This is either a gas layer or a cooled particle layer sitting on the tube. At higher velocity, the arrival of the emulsion phase is visible and the cooling of particle packets can be observed. At $\theta = 135^\circ$ (Figure 3.47), there is again

little activity at low velocity and more phase replacement at higher velocities. Figure 3.48 ($\theta = 90^\circ$) shows that the replacement of bubble and emulsion phases is periodic and there are few spikes. The instantaneous local heat transfer coefficient at $\theta = 45^\circ$ (Figure 3.49) is constant and shows little activity. There is more activity at $\theta = 0^\circ$ (Figure 3.50) than at $\theta = 45^\circ$, and distinct phases can be recognized as the velocity increases.

The instantaneous heat transfer coefficient for a bed temperature of $T=900\text{K}$ suggest that the bed was fully fluidized for the fluidization velocities investigated. At $\theta = 180^\circ$ in Figure 3.51, a stagnant cap is not observed as was found at low velocities for the lower temperatures. At both $\theta = 180^\circ$ (Figure 3.51) and $\theta = 135^\circ$ (Figure 3.52), there are larger spikes than at the lower bed temperatures. The emulsion phase, on the other hand, appears more distinct and discrete. At $\theta = 90^\circ$ (Figure 3.53), the particles are very active in the emulsion phase, but the spikes are not as large as that at $\theta = 135^\circ$ and $\theta = 180^\circ$. At $\theta = 45^\circ$ (Figure 3.54), the emulsion phase and bubble phase replacement is clearly periodic with similar residence times for the bubble and emulsion phases. At $\theta = 0^\circ$ (Figure 3.55), a gas cushion is present with spikes from particles which increase in frequency and magnitude with an increase in velocity.

For all of the velocities investigated at a bed temperature of $T=1000\text{K}$, the bed again appears to be fully fluidized. At $\theta = 180^\circ$ and $\theta = 135^\circ$ in Figures 3.56 and 3.57, respectively, the phase replacement is not as periodic and is more random than the activity seen at lower bed temperatures. The bubble and emulsion phase replacement activity at $\theta = 90^\circ$ (Figure 3.58) and $\theta = 45^\circ$ (Figure 3.59), is periodic with similar

residence times. At $\theta = 0^\circ$ (Figure 3.60), a gas cushion is again present but is replaced by the emulsion phase occasionally.

Several different types of activity can be characterized at the tube surface by the shape of the plots of the instantaneous local heat transfer coefficients versus time. In Figure 3.61, the instantaneous local heat transfer coefficient quickly steps up to a higher value, gradually increases from this point, and then returns to its initial low value. This could be explained as follows. At first the emulsion phase replaces the bubble phase which causes the sudden increase in magnitude. Next, the particles in the emulsion phase have increased activity and are replaced by or heated by warmer adjacent particles which results in the heat transfer coefficient continuing to increase. Another explanation for this phenomenon is that the emulsion phase comes in contact with the tube surface with little interparticle gas flow, then more gas is directed to this area resulting in increased heat transfer due to gas convection. After this period of gradually increasing heat transfer coefficient, the emulsion phase is replaced by the bubble phase and the instantaneous local heat transfer coefficient again drops off to the level it had before the emulsion phase came along. This type of activity was seen most frequently at $\theta = 0^\circ$ and $\theta = 180^\circ$ and at medium fluidization velocities. It was seen occasionally at $\theta = 90^\circ$, but not at $\theta = 45^\circ$ or $\theta = 135^\circ$.

A second type of activity is shown in Figure 3.62. Here, the instantaneous local heat transfer coefficient jumps from a low value to a relatively high value. Then, it decrease from the high value to an intermediate value. Finally, it jumps back from the intermediate value to the low value. This can be explained by the emulsion phase

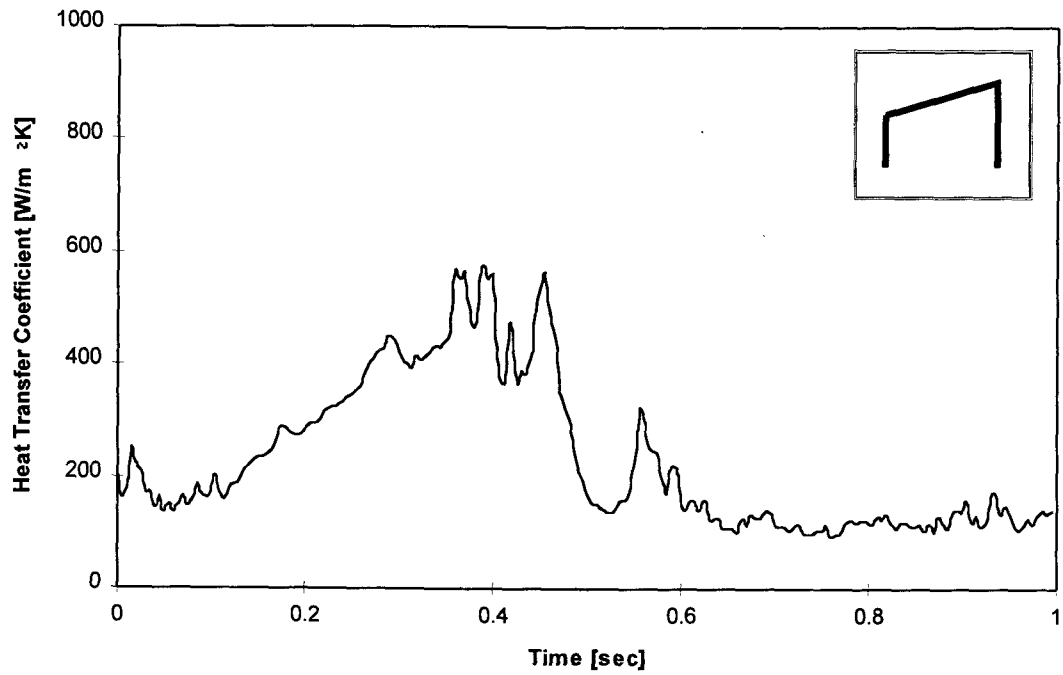


Figure 3.61 Instantaneous local heat transfer coefficient, Shape 1
 ($T_{\text{bed}}=1000\text{K}$, $d_p=2\text{ mm}$, $\theta = 0^\circ$, $U=2.82\text{ m/s}$).

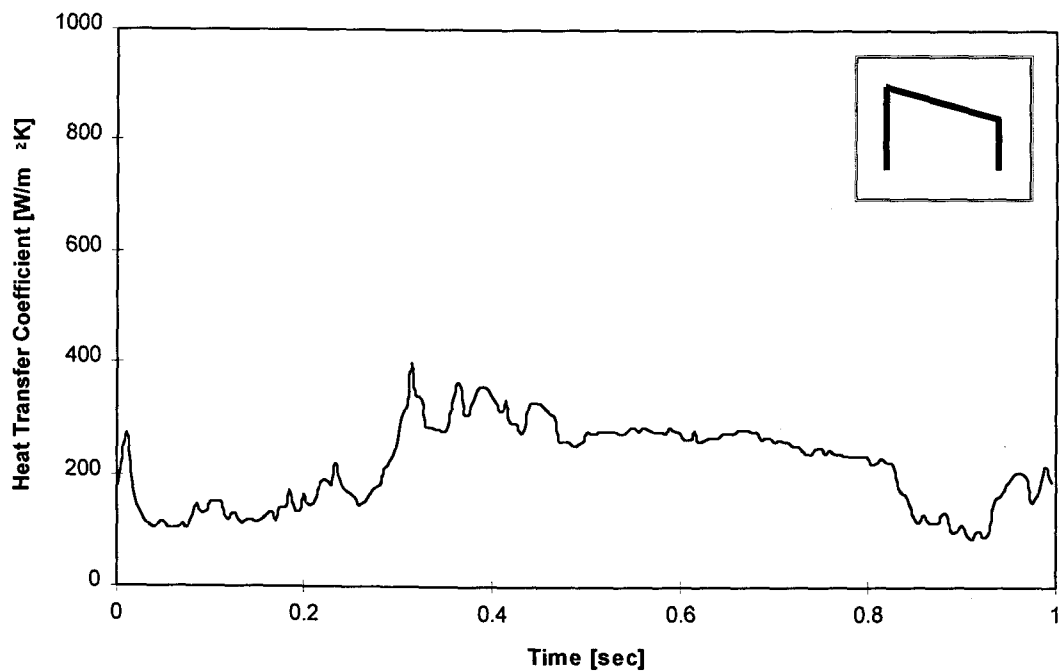


Figure 3.62 Instantaneous local heat transfer coefficient, Shape 2
 ($T_{\text{bed}}=800\text{K}$, $d_p=2\text{ mm}$, $\theta = 180^\circ$, $U=2.11\text{ m/s}$).

arriving at the tube surface, cooling off while it is in contact with the cooler tube surface, and then the emulsion phase being replaced by the bubble phase. This type of activity was seen mostly at $\theta = 135^\circ$ and $\theta = 180^\circ$, although it was seen at all circumferential locations. At these locations, the emulsion phase can behave as a stagnant cap where it sits on the tube and cools off. It was more commonly seen at medium and low velocities.

A third type of activity is shown in Figure 3.63. Here, the instantaneous local heat transfer coefficient jumps up from a low value to a relatively high value, then maintains an intermediate value until it drops back to the low value. An explanation for this behavior is that when the emulsion phase first impacts the tube surface, its momentum brings the hot particles very close to the tube surface (the gas layer is very thin). After the reaction of hitting the tube surface, while the emulsion phase is still resident, there is a thicker gas layer between the tube and the hot particles and thus the instantaneous local heat transfer coefficient drops to an intermediate emulsion phase value. Finally, the emulsion phase is replaced by the bubble phase and the instantaneous local heat transfer coefficient returns to the low value. This type of activity was seen at all circumferential locations, but more frequently at $\theta = 0^\circ$ and $\theta = 180^\circ$. It was also seen more frequently at lower fluidization velocities.

A fourth type of activity is shown in Figure 3.64. The instantaneous local heat transfer coefficient jumps from a low value to an intermediate value and maintains this intermediate value. Next, it rises to a high value and then drops to the low value. In this case, the emulsion phase arrives and causes an initial rise of the instantaneous

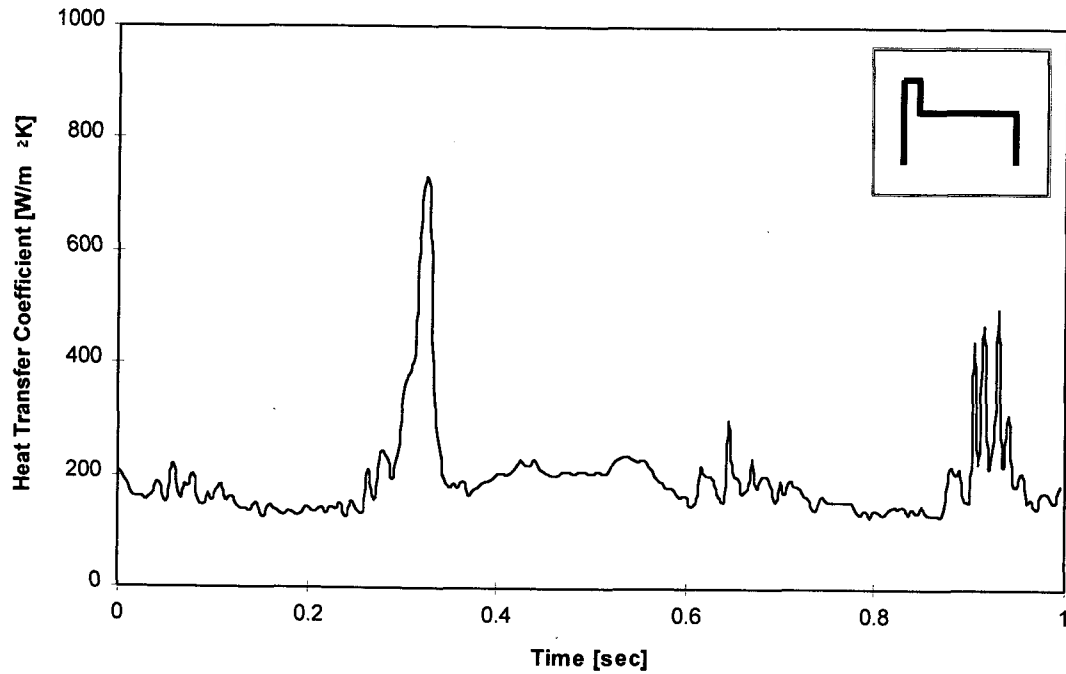


Figure 3.63 Instantaneous local heat transfer coefficient, Shape 3
 ($T_{\text{bed}}=900\text{K}$, $d_p=2\text{ mm}$, $\theta = 0^\circ$, $U=2.52\text{ m/s}$).

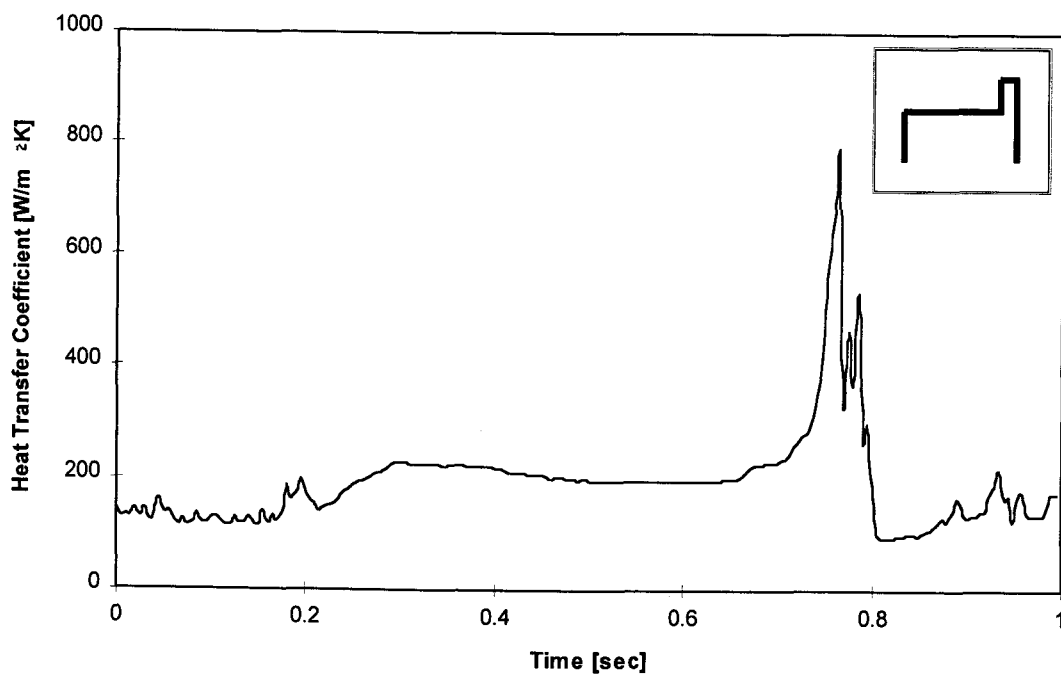


Figure 3.64 Instantaneous local heat transfer coefficient, Shape 4
 ($T_{\text{bed}}=900\text{K}$, $d_p=2\text{ mm}$, $\theta = 45^\circ$, $U=1.91\text{ m/s}$).

local heat transfer coefficient from a low value to an intermediate value. This intermediate value is maintained while the emulsion phase is resident. Finally, as the emulsion phase is being pushed away by an arriving bubble, the particles in the emulsion phase are pushed closer to the heat transfer surface. The thickness of the gas film between the tube and the particles which acts as a resistance to heat transfer is reduced and thus the instantaneous local heat transfer coefficient increases. Finally, the bubble arrives and the instantaneous local heat transfer coefficient returns to a low value. This phenomenon is similar to that found in Figure 3.63, only here it occurs at the end of the emulsion residence time instead of at the beginning. This type of behavior was seen at all circumferential locations and typically at intermediate fluidization velocities.

A fifth type of activity is shown in Figure 3.65. In this plot, the instantaneous local heat transfer coefficient jumps from a low value to a high value for a brief time. Next, it drops and maintains an intermediate value. The instantaneous local heat transfer coefficient then jumps up to a high value and then suddenly drops back to the low value. This type of activity is the superposition of the activity described for Figures 3.63 and 3.64. This shape was seen at all circumferential locations, but least frequently at $\theta = 90^\circ$. It was more commonly seen at lower fluidization velocities.

A sixth type of activity is shown in Figure 3.66. The instantaneous local heat transfer coefficient rises slowly from a low value to a high value and then declines slowly back to the low value. The transition from low to high and high to low values is gradual change as opposed to an instantaneous jump. This type of activity was

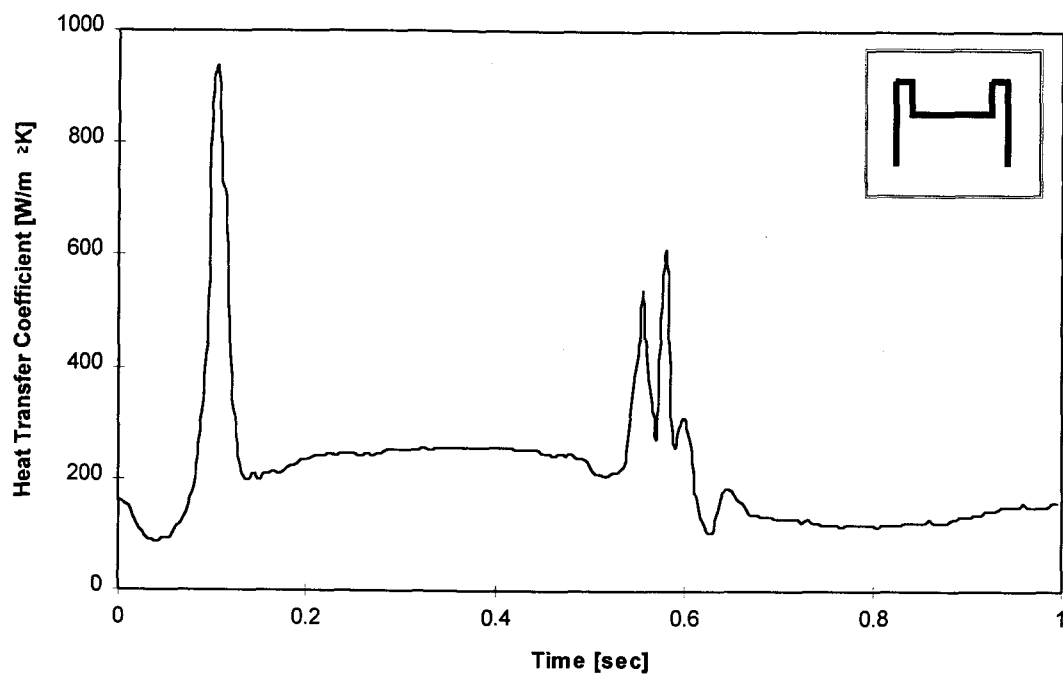


Figure 3.65 Instantaneous local heat transfer coefficient, Shape 5
 ($T_{\text{bed}}=600\text{K}$, $d_p=2$ mm, $\theta = 135^\circ$, $U=1.85$ m/s).

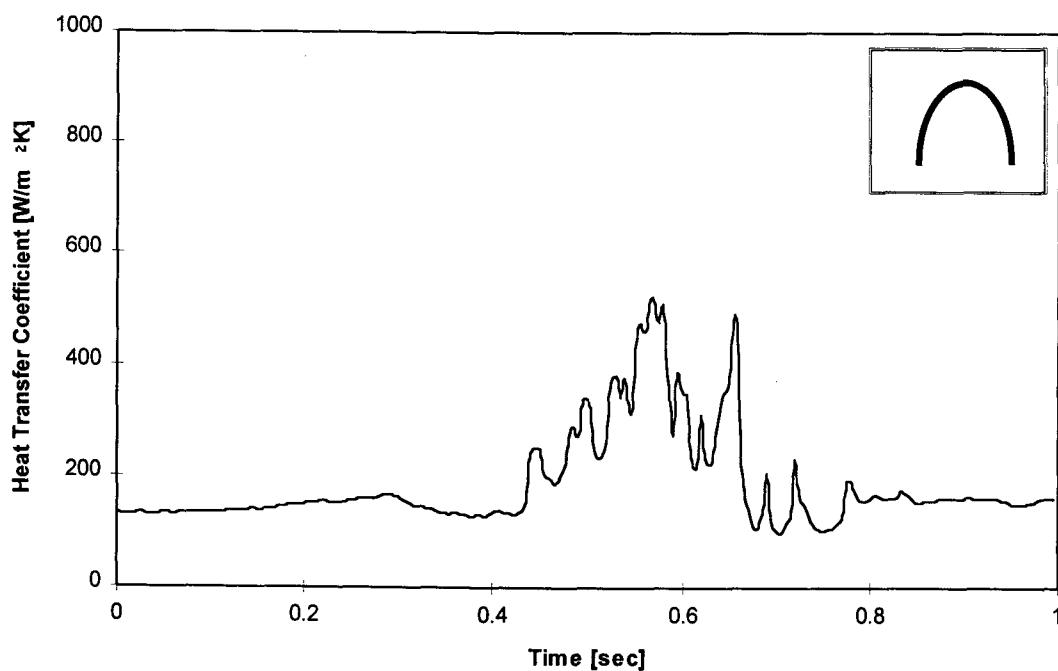


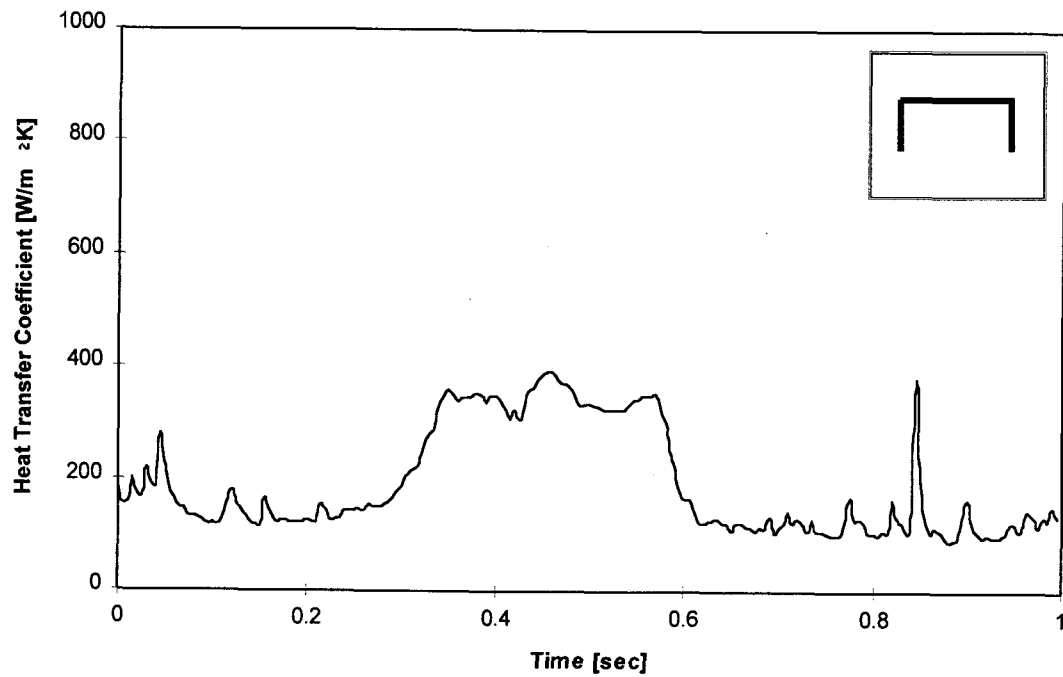
Figure 3.66 Instantaneous local heat transfer coefficient, Shape 6
 ($T_{\text{bed}}=700\text{K}$, $d_p=2$ mm, $\theta = 90^\circ$, $U=1.81$ m/s).

commonly seen at $\theta = 45^\circ$ and $\theta = 90^\circ$, although it could be seen occasionally at the other circumferential locations. It was seen uniformly at all fluidization velocities.

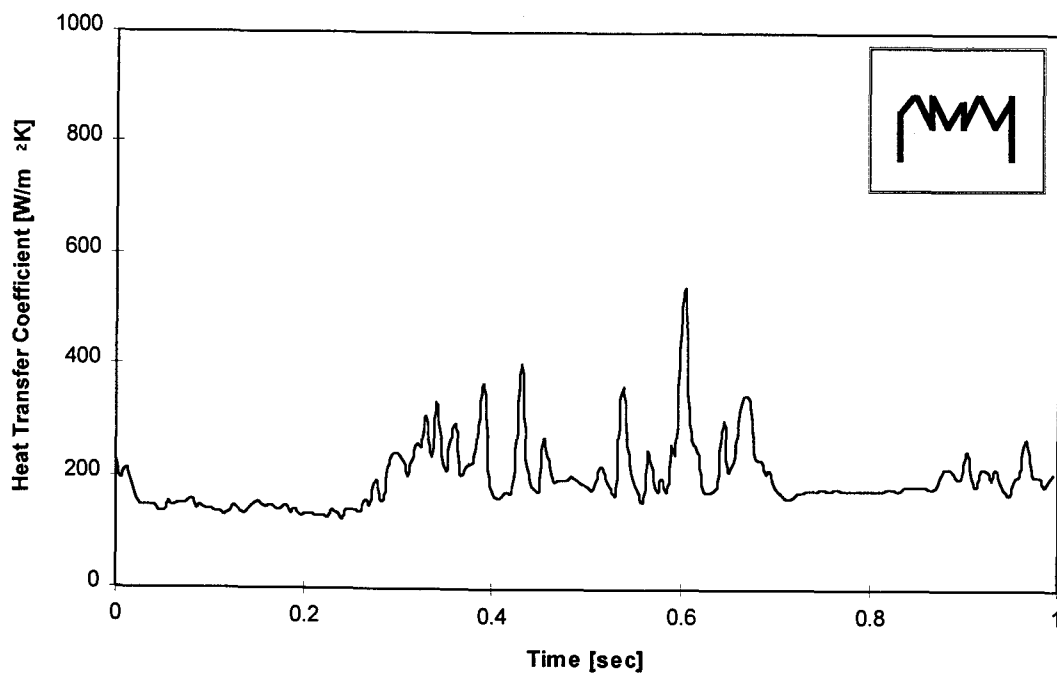
A seventh type of activity is shown in Figures 3.67(a) and 3.67(b). In these figures, the instantaneous local heat transfer coefficient rises quickly from a low value to a relatively high value, maintains this value and then drops back down to the low value. There are two distinct categories of this behavior. The first is shown in Figure 3.67(a) where the instantaneous local heat transfer coefficient maintains the high value with little activity or fluctuations. The second is shown in Figure 3.67(b) where the instantaneous local heat transfer coefficient fluctuates vigorously about the mean of the high value. The shape shown in Figure 3.67(a) was most often seen at $\theta = 0^\circ$ and $\theta = 180^\circ$ at low fluidization velocities. The shape shown in Figure 3.67(b) was seen frequently at all circumferential locations, fluidization velocities and bed temperatures.

An eighth type of activity is shown in Figures 3.68(a) and 3.68(b). In these cases, the instantaneous local heat transfer coefficient remains at its low value. As in Figures 3.67(a) and 3.67(b), there are two distinct categories. In one case there is little activity and the instantaneous local heat transfer coefficient is essentially constant and in the other there frequent fluctuations about the mean, as shown in Figures 3.68(a) and 3.68(b), respectively. These shapes seen mostly at $\theta = 135^\circ$ and $\theta = 180^\circ$ and at lower bed temperatures and low fluidization velocities.

Although there are no data available in the literature to directly compare the instantaneous heat transfer coefficients, the closest are the results of George (1993). In

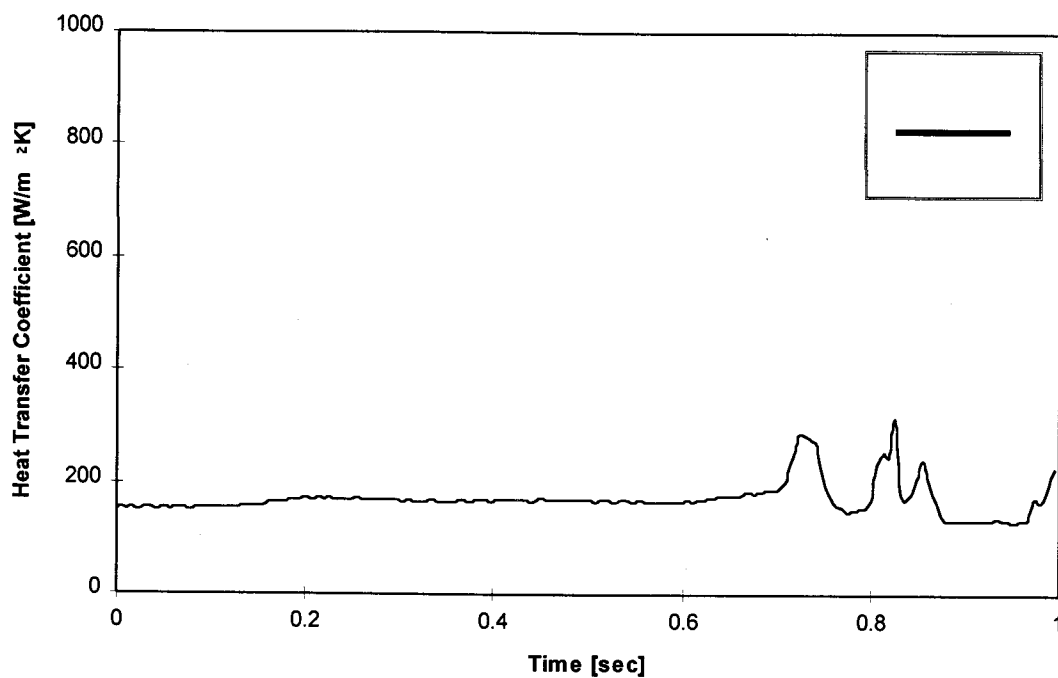


(a)

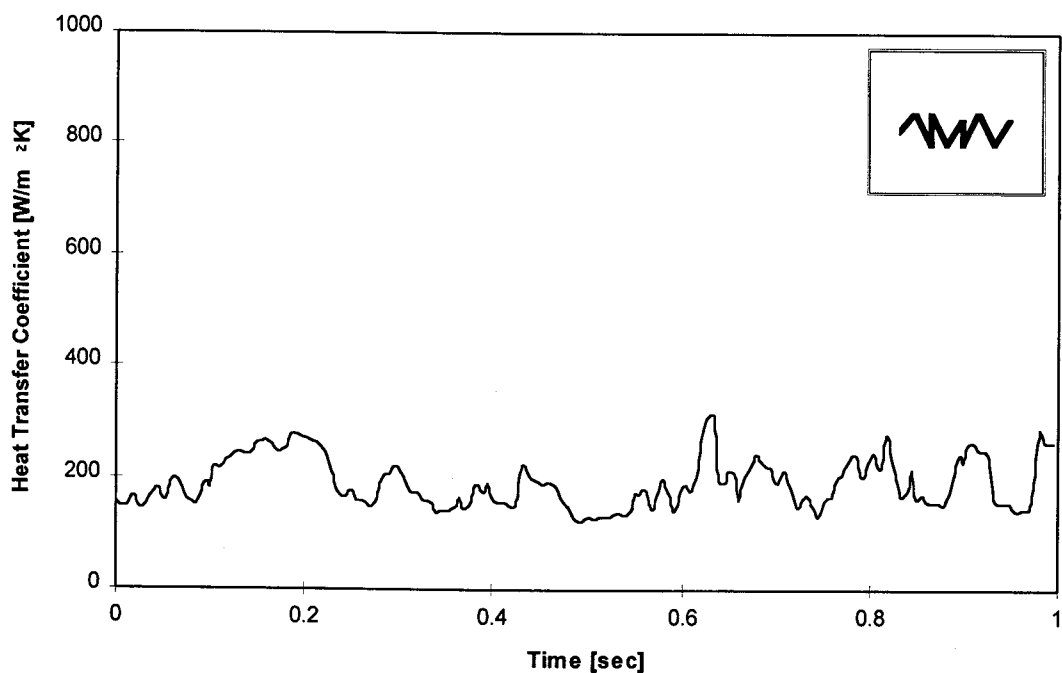


(b)

Figure 3.67 Instantaneous local heat transfer coefficient, Shape 7 (a) ($T_{bed}=800\text{K}$, $d_p=2$ mm, $\theta = 180^\circ$, $U=2.11$ m/s); (b) ($T_{bed}=900\text{K}$, $d_p=2$ mm, $\theta = 90^\circ$, $U=2.74$ m/s).



(a)



(b)

Figure 3.68 Instantaneous local heat transfer coefficient, Shape 8 (a) ($T_{bed}=800K$, $d_p=2$ mm, $\theta = 180^\circ$, $U=1.71$ m/s); (b) ($T_{bed}=900K$, $d_p=2$ mm, $\theta = 0^\circ$, $U=1.71$ m/s).

that work, instantaneous heat transfer coefficients for $d_p = 1.0$ mm at $T_{bed} = 835$ K are presented. His data displayed similar shapes and trends as those found in the present work.

3.4.1 Instantaneous Heat Transfer Coefficient Standard Deviation

The standard deviation of the instantaneous heat transfer coefficient is a measure of the time-weighted-average of the amount of fluctuation (activity) about the mean of the heat transfer coefficient. It can be used as an indication of the frequency and intensity of particle and bubble/emulsion phase activity. The activity causes changes in the magnitude of the instantaneous heat transfer coefficient. Fluctuations arise from bubble and emulsion phase replacement as well the degree of particle activity when each of these phases is in contact with the tube. Fluctuations can also be the result of variations in the gas velocity, temperature and turbulence intensity. Plots of the standard deviation versus θ are shown in Figures 3.69, 3.70, 3.71, 3.72 and 3.73 for $T_{bed} = 600\text{K}$, 700K , 800K , 900K and 1000K , respectively. In general, the standard deviation tends to increase from $\theta = 0^\circ$ to $\theta = 180^\circ$. For all of the data, the maximum standard deviation usually occurred at $\theta = 180^\circ$ while the minimum usually occurred at $\theta = 45^\circ$ and occasionally $\theta = 0^\circ$. Figures 3.74, 3.75, 3.76, 3.77 and 3.78 show the standard deviation plotted versus U/U_{mf} at $\theta = 0^\circ$, 45° , 90° , 135° , and 180° , respectively, for all five temperatures investigated. At $\theta = 0^\circ$, the standard deviation generally increased with U/U_{mf} . At $\theta = 0^\circ$ and 45° , the standard deviation generally increased and then leveled off as U/U_{mf} increased. At $\theta = 135^\circ$ and 180° , the standard

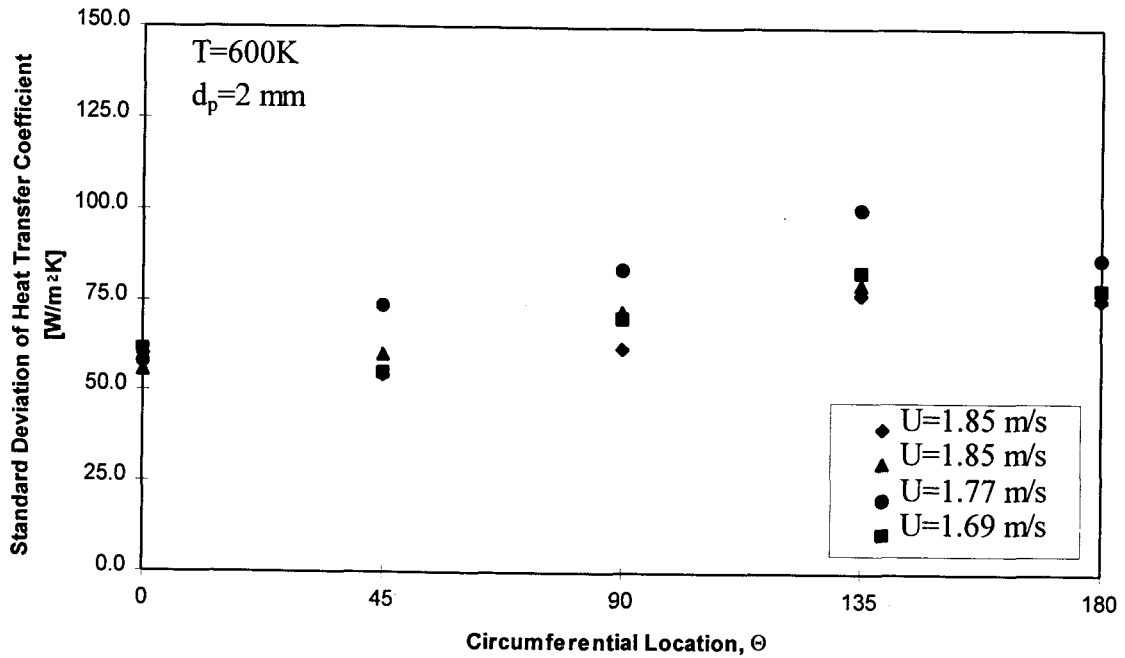


Figure 3.69 Standard deviation of instantaneous heat transfer coefficient versus θ ($T_{\text{bed}}=600\text{K}$, $d_p=2\text{ mm}$).

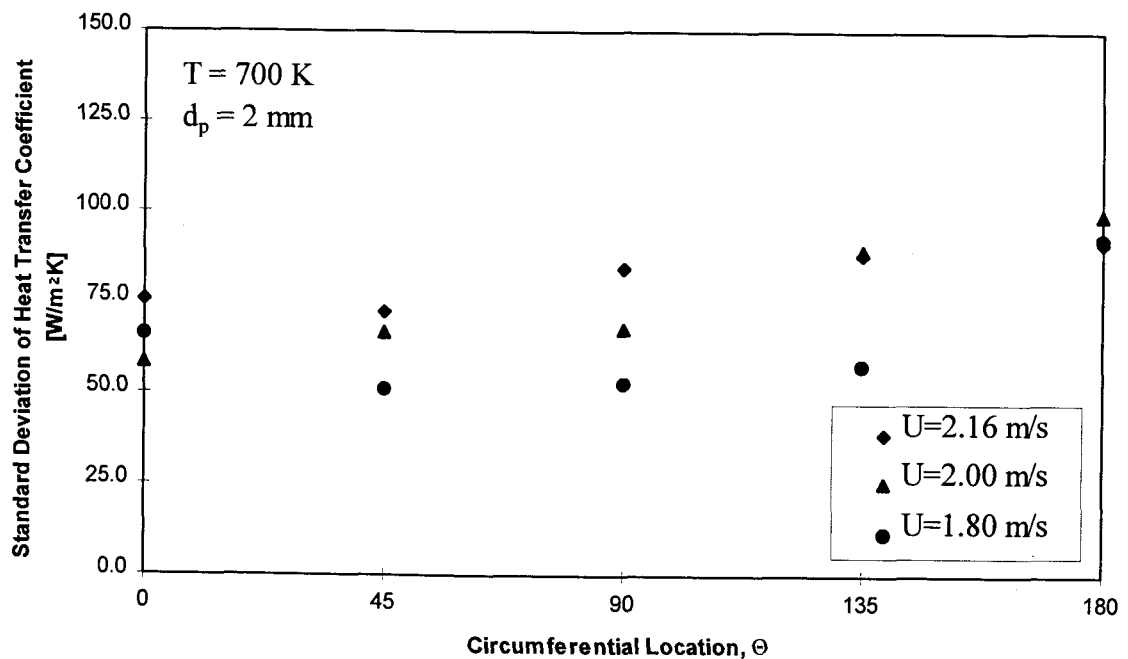


Figure 3.70 Standard deviation of instantaneous heat transfer coefficient versus θ ($T_{\text{bed}}=700\text{K}$, $d_p=2\text{ mm}$).

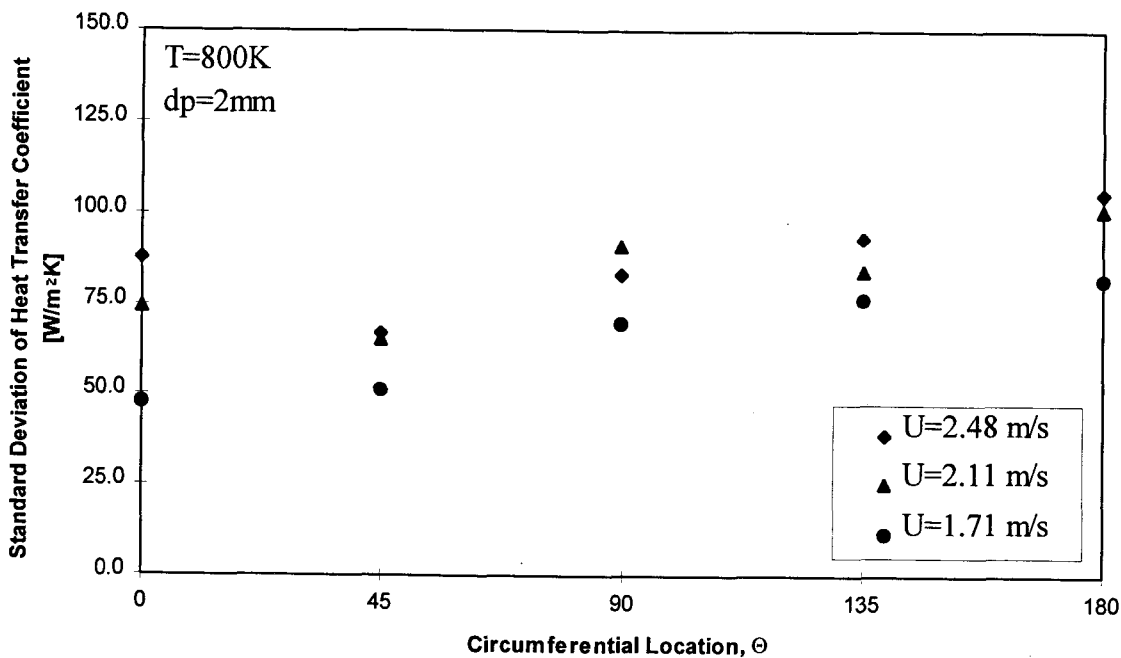


Figure 3.71 Standard deviation of instantaneous heat transfer coefficient versus θ ($T_{\text{bed}} = 800\text{K}$, $d_p = 2\text{ mm}$).

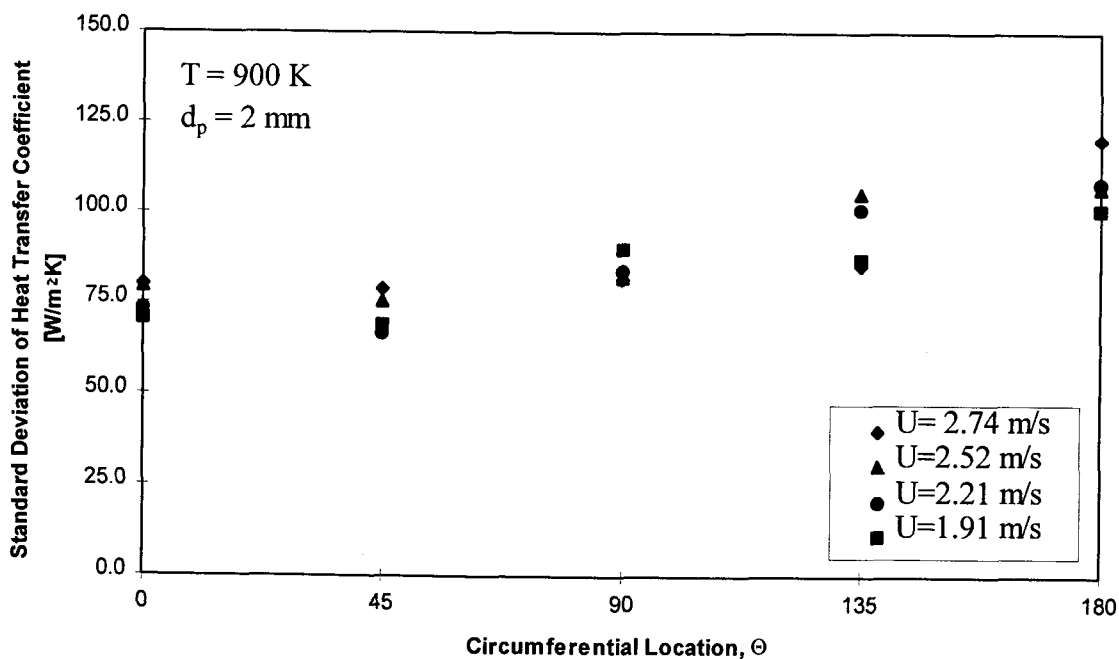


Figure 3.72 Standard deviation of instantaneous heat transfer coefficient versus θ ($T_{\text{bed}} = 900\text{K}$, $d_p = 2\text{ mm}$).

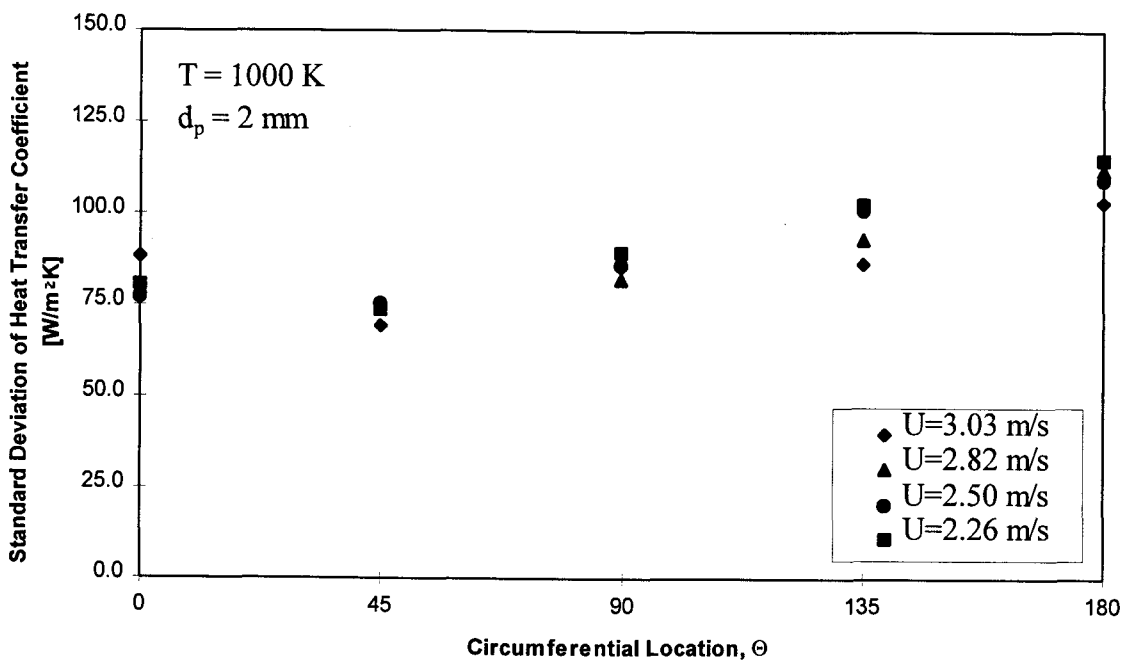


Figure 3.73 Standard deviation of instantaneous heat transfer coefficient versus θ ($T_{\text{bed}}=1000\text{K}$, $d_p=2 \text{ mm}$).

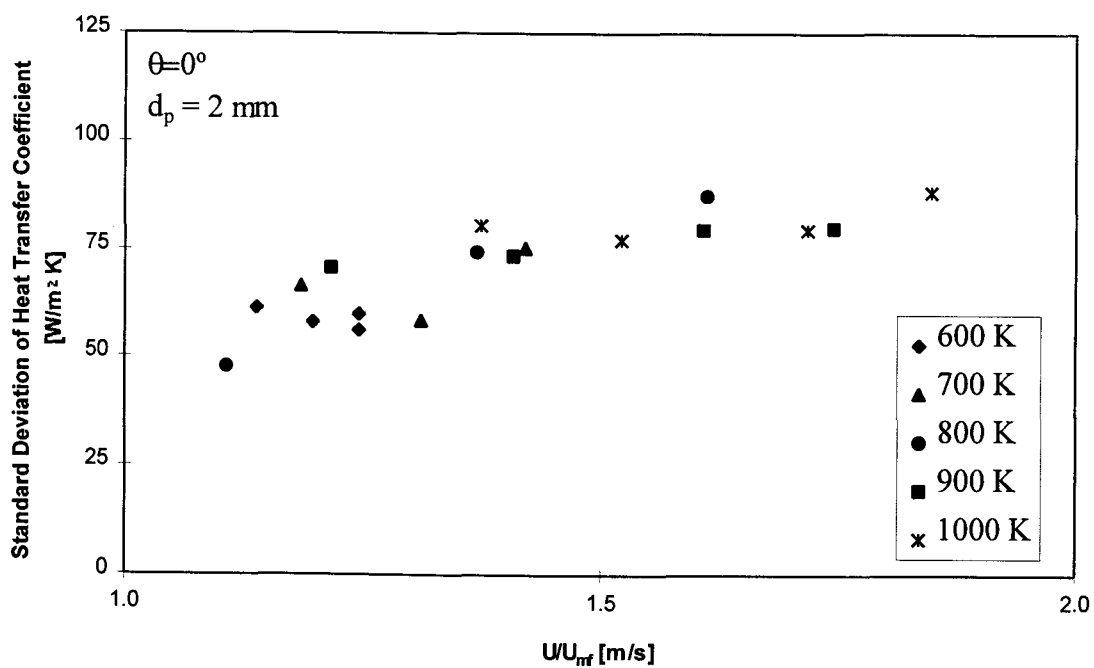


Figure 3.74 Standard deviation of instantaneous heat transfer coefficient versus U/U_{mf} ($\theta = 0^\circ$, $d_p=2 \text{ mm}$).

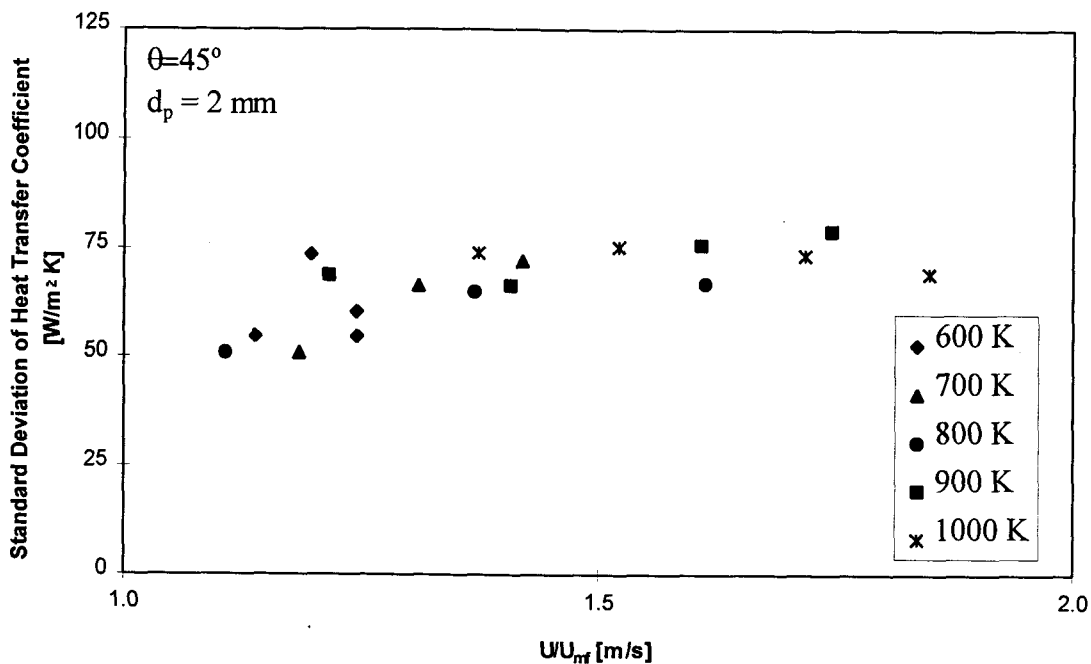


Figure 3.75 Standard deviation of instantaneous heat transfer coefficient versus U/U_{mf} ($\theta = 45^\circ$, $d_p = 2 \text{ mm}$).

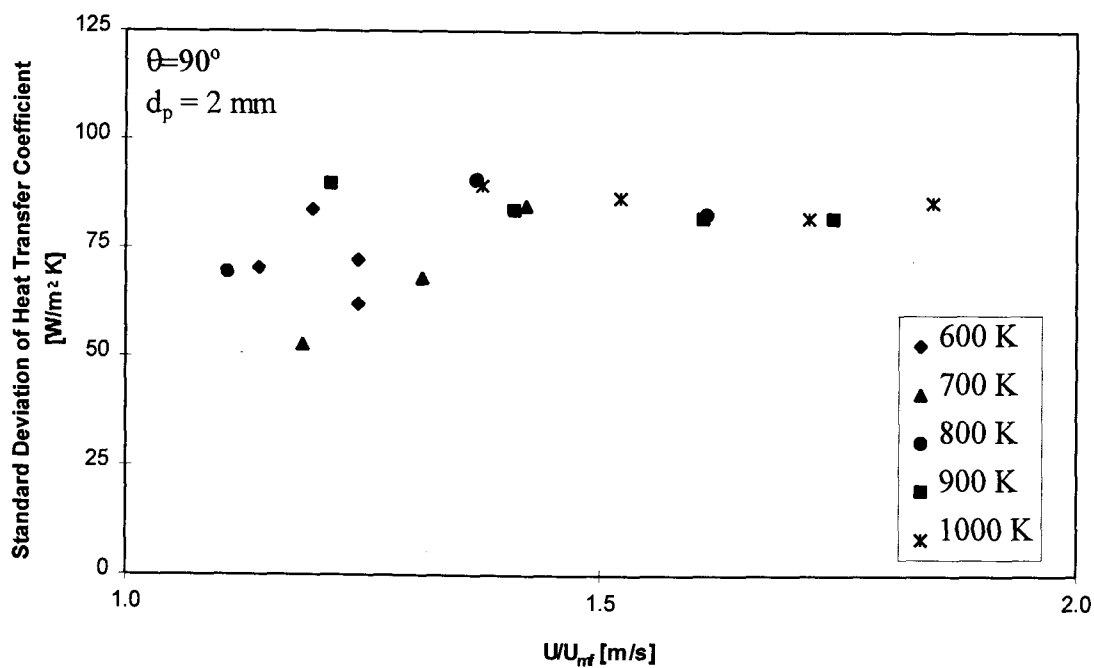


Figure 3.76 Standard deviation of instantaneous heat transfer coefficient versus U/U_{mf} ($\theta = 90^\circ$, $d_p = 2 \text{ mm}$).

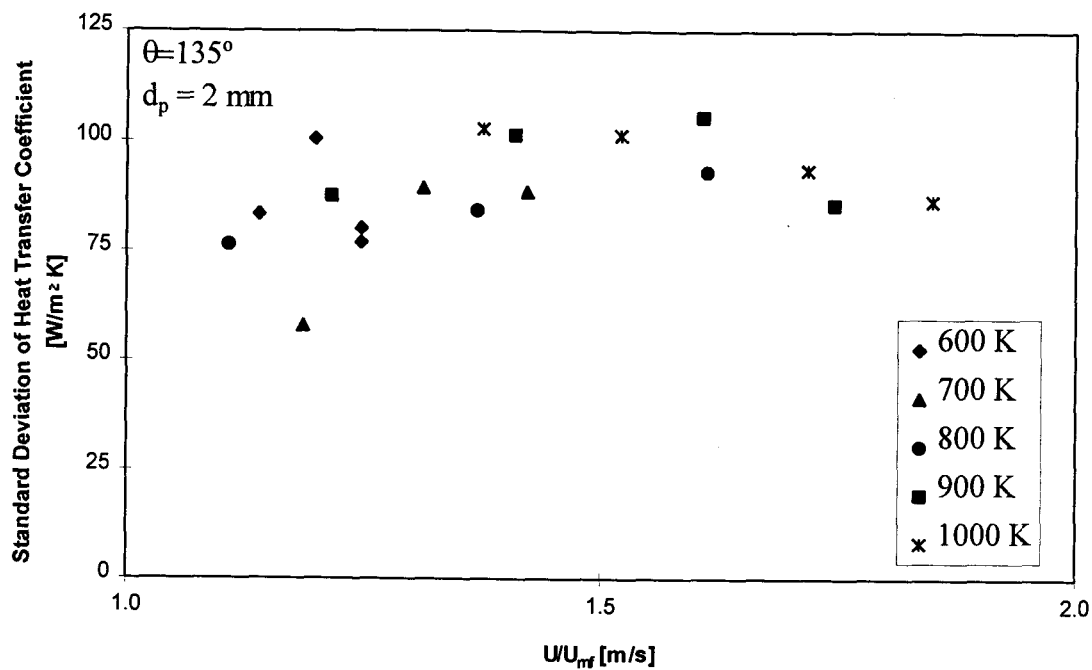


Figure 3.77 Standard deviation of instantaneous heat transfer coefficient versus U/U_{mf} ($\theta = 135^\circ$, $d_p = 2 \text{ mm}$).

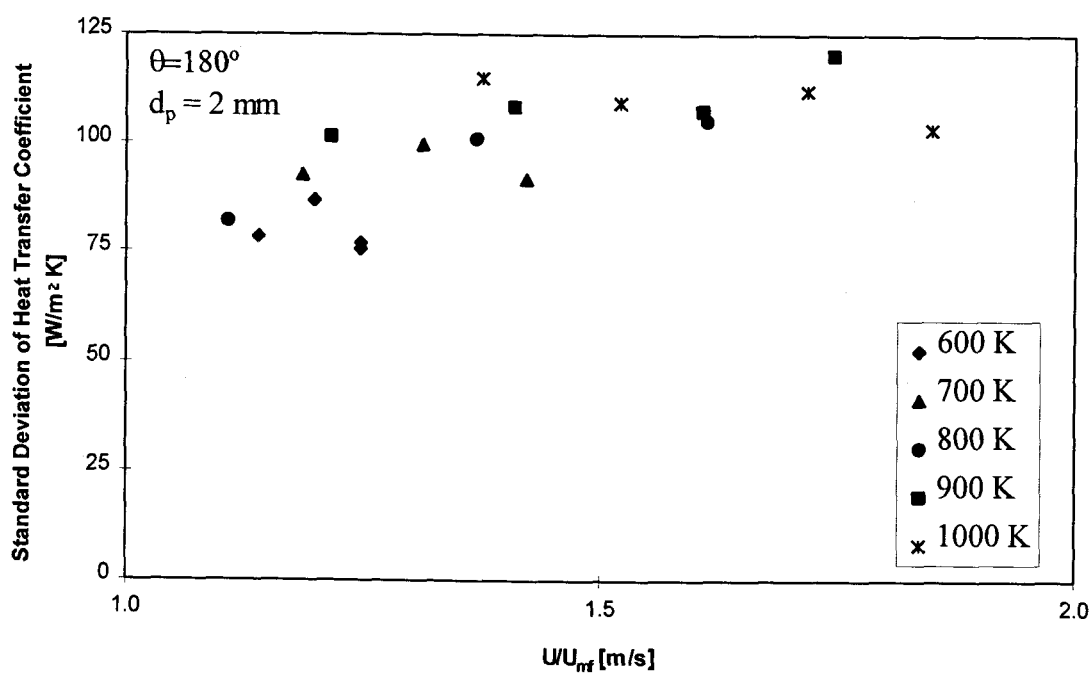


Figure 3.78 Standard deviation of instantaneous heat transfer coefficient versus U/U_{mf} ($\theta = 180^\circ$, $d_p = 2 \text{ mm}$).

deviation generally increased, leveled off, and then decreased as U/U_{mf} increased. Since the standard deviation does not show much variation with temperature when plotted versus U/U_{mf} , nondimensionalizing U with U_{mf} captures most of the dependence on temperature.

3.4.2 Maximum and Minimum Heat Transfer Coefficients

The heat transfer coefficient signal can be filtered in the same manner as the optical probe signal was filtered to separate bubble contact and emulsion phase contact heat transfer coefficients. It is assumed that the heat transfer coefficient is high during emulsion phase contact and low during bubble phase contact. The filtering is only effective if these two distinct phases alternate at the heat transfer surface. If the surface is exposed to a gas cushion or a mixed phase such as a continuous lower void fraction emulsion phase, then the filtering is not particularly meaningful. When the two distinct phases do exist, however, this technique can be used to calculate average minimum and maximum heat transfer coefficients. These coefficients can then be compared to models and correlations to check the accuracy of the models and correlations. Values for h_{max} , h_{min} , Δh_{max} , and Δh_{min} were calculated for the 2 mm case. Figures 3.79, 3.80, 3.81, 3.82 and 3.83 show h_{max} , h_{min} and h_{avg} plotted versus circumferential location for temperatures 600 K, 700 K, 800 K, 900 K and 1000 K, respectively. Figures 3.84, 3.85, 3.86, 3.87 and 3.88 show Δh_{max} and Δh_{min} plotted versus fluidization velocity for circumferential locations $\theta = 0^\circ, 45^\circ, 90^\circ, 135^\circ$ and

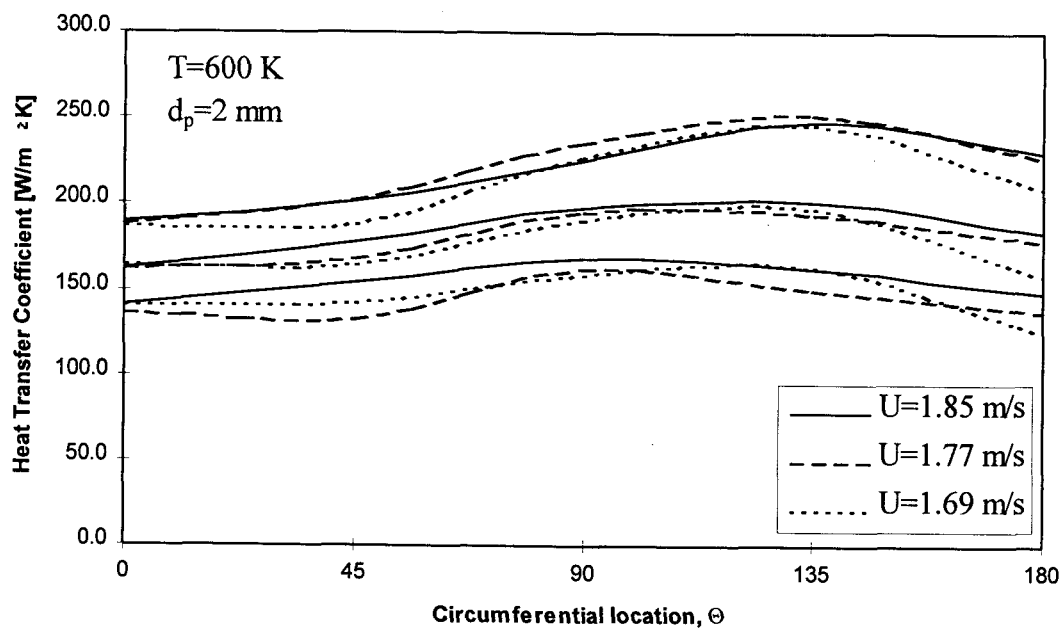


Figure 3.79 Average maximum, average, and average minimum heat transfer coefficient versus θ ($T_{\text{bed}} = 600\text{ K}$, $d_p = 2\text{ mm}$)

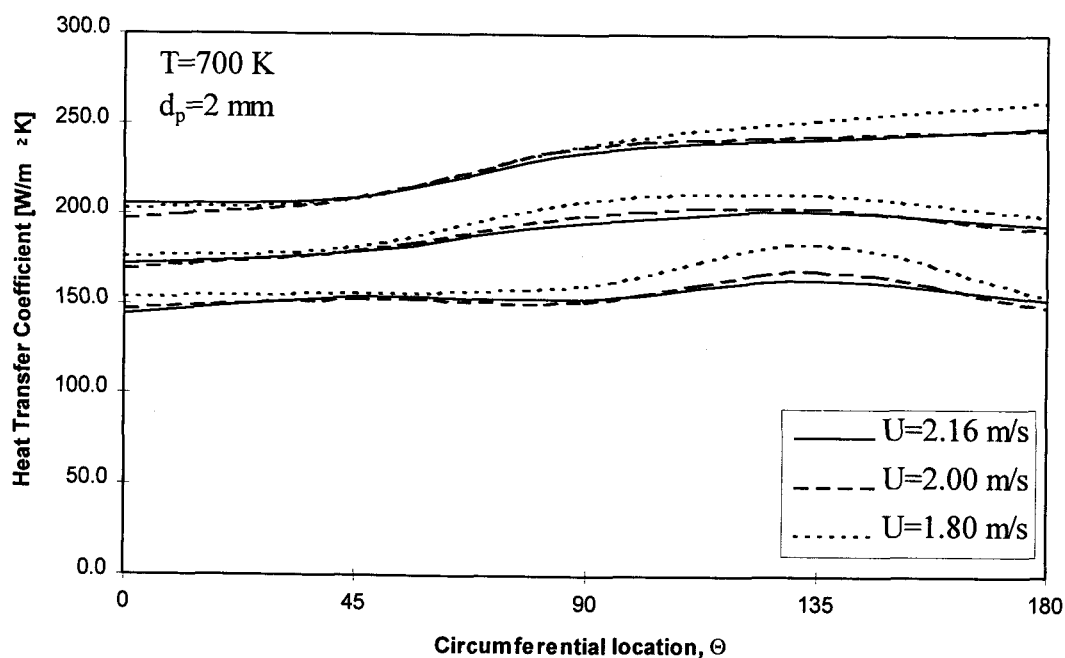


Figure 3.80 Average maximum, average, and average minimum heat transfer coefficient versus θ ($T_{\text{bed}} = 700\text{ K}$, $d_p = 2\text{ mm}$).

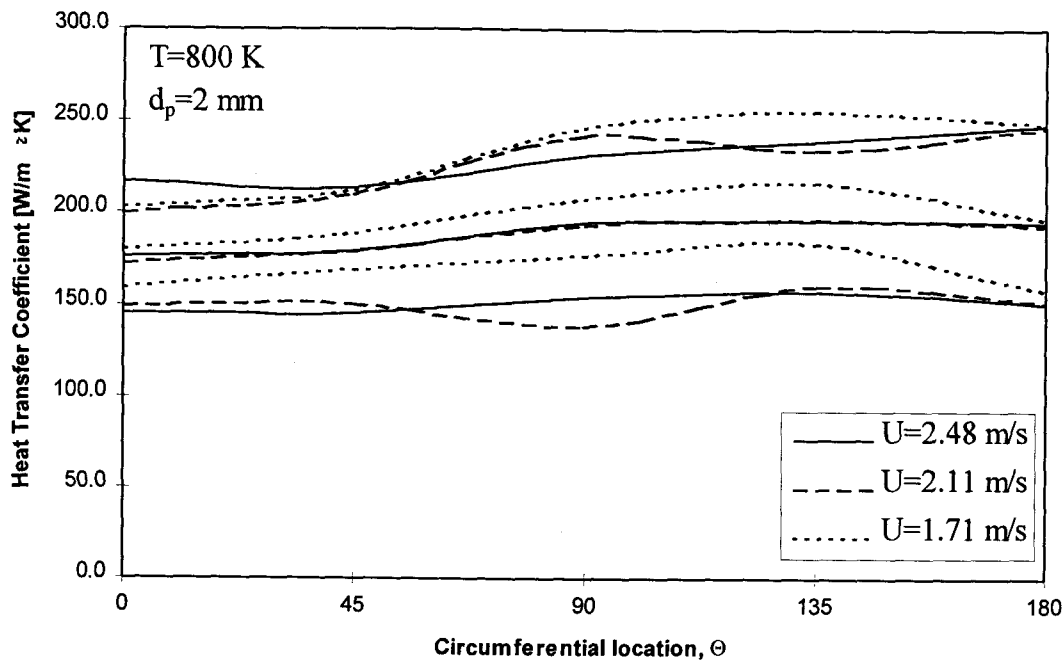


Figure 3.81 Average maximum, average, and average minimum heat transfer coefficient versus θ ($T_{\text{bed}}=800\text{K}$, $d_p=2\text{ mm}$).

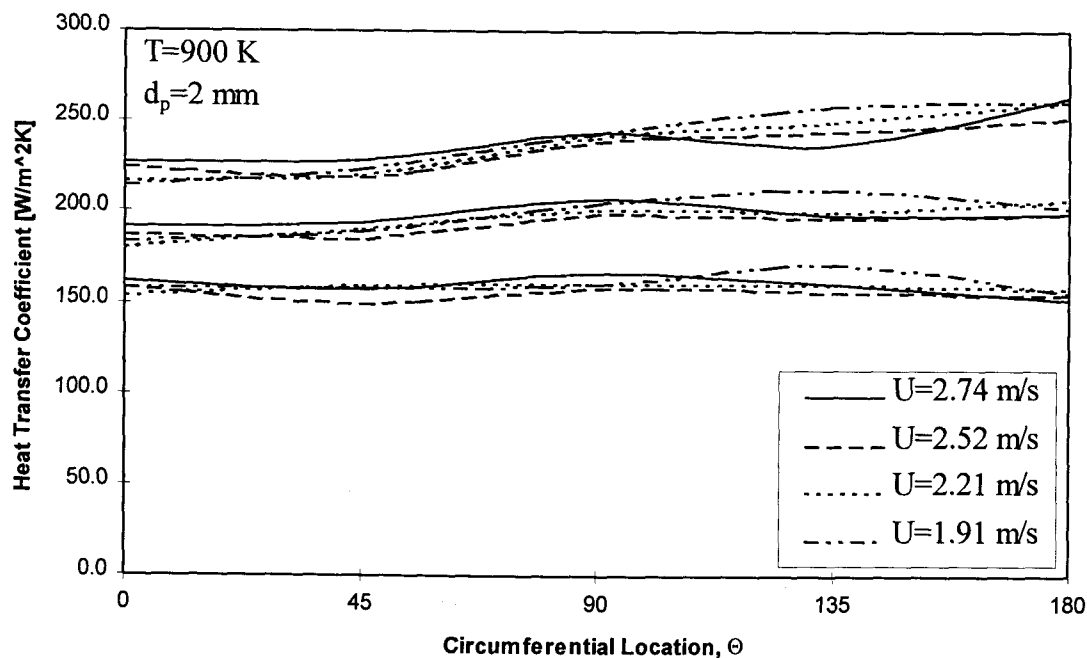


Figure 3.82 Average maximum, average, and average minimum heat transfer coefficient versus θ ($T_{\text{bed}}=900\text{K}$, $d_p=2\text{ mm}$).

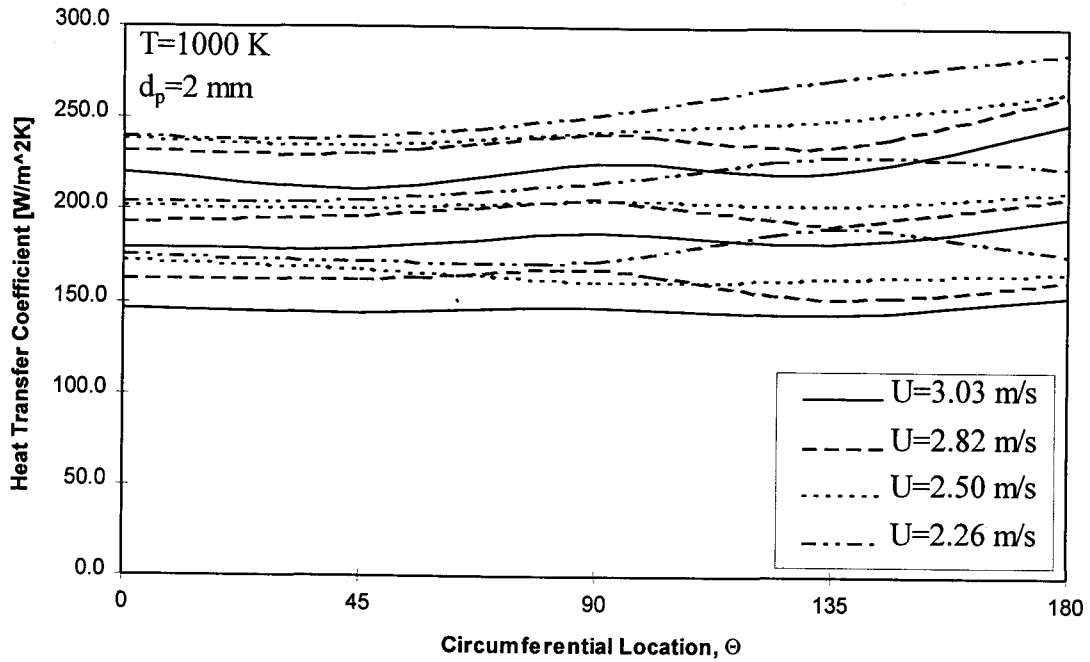


Figure 3.83 Average maximum, average, and average minimum heat transfer coefficient versus θ ($T_{bed}=1000K$, $d_p=2 mm$).

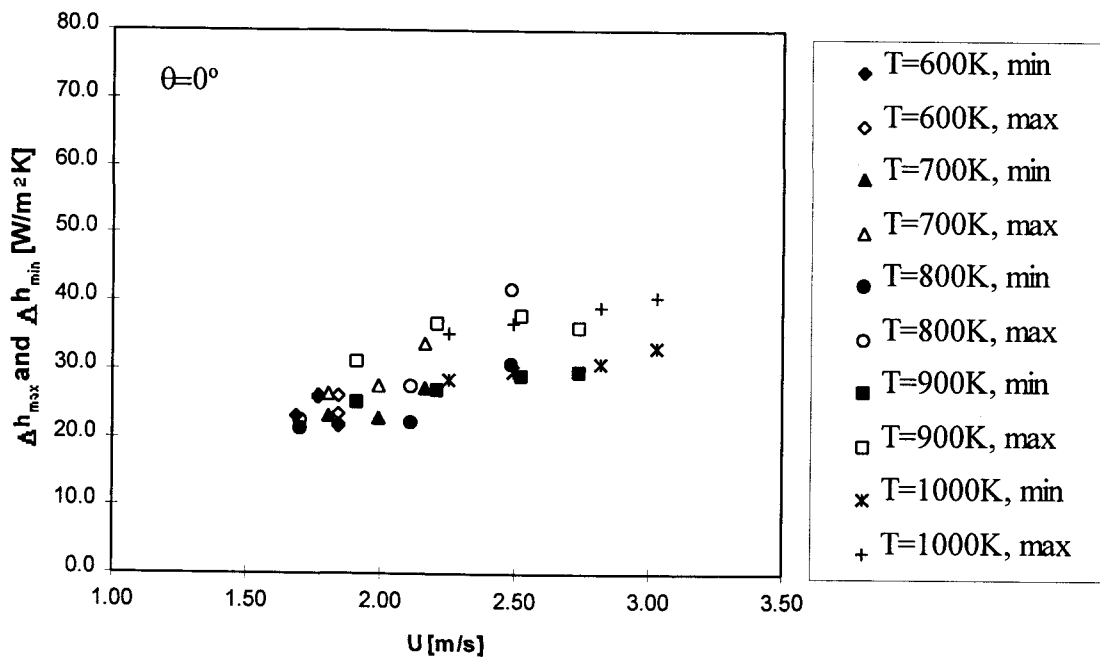


Figure 3.84 Δh_{max} and Δh_{min} versus U ($\theta = 0^\circ$ $d_p=2 mm$).

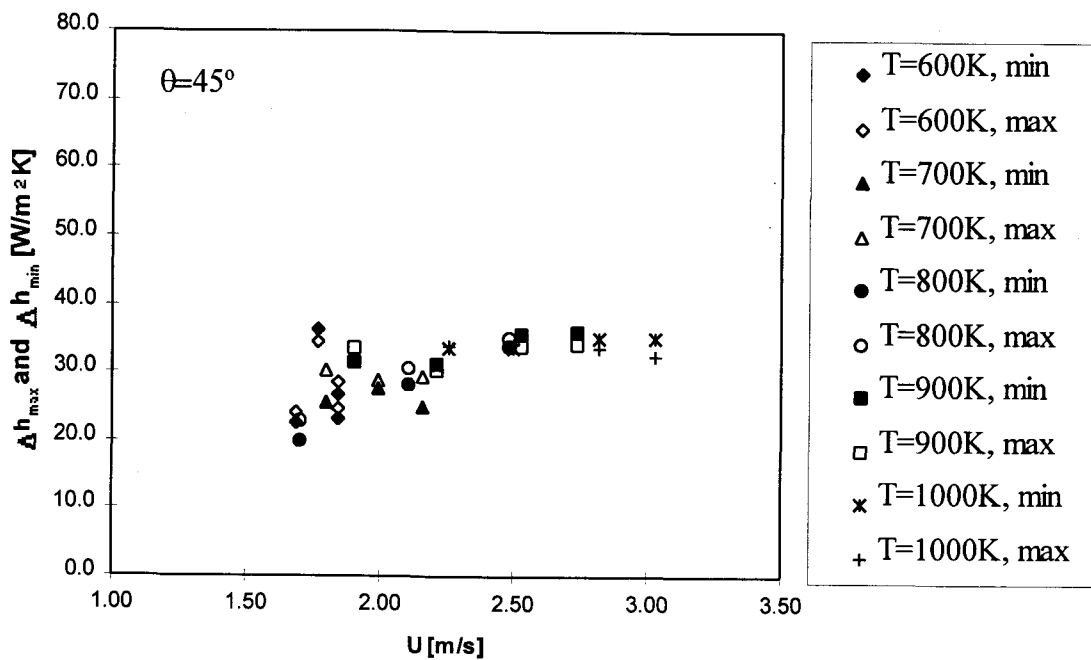


Figure 3.85 Δh_{\max} and Δh_{\min} versus U ($\theta = 45^\circ$ $d_p = 2$ mm).

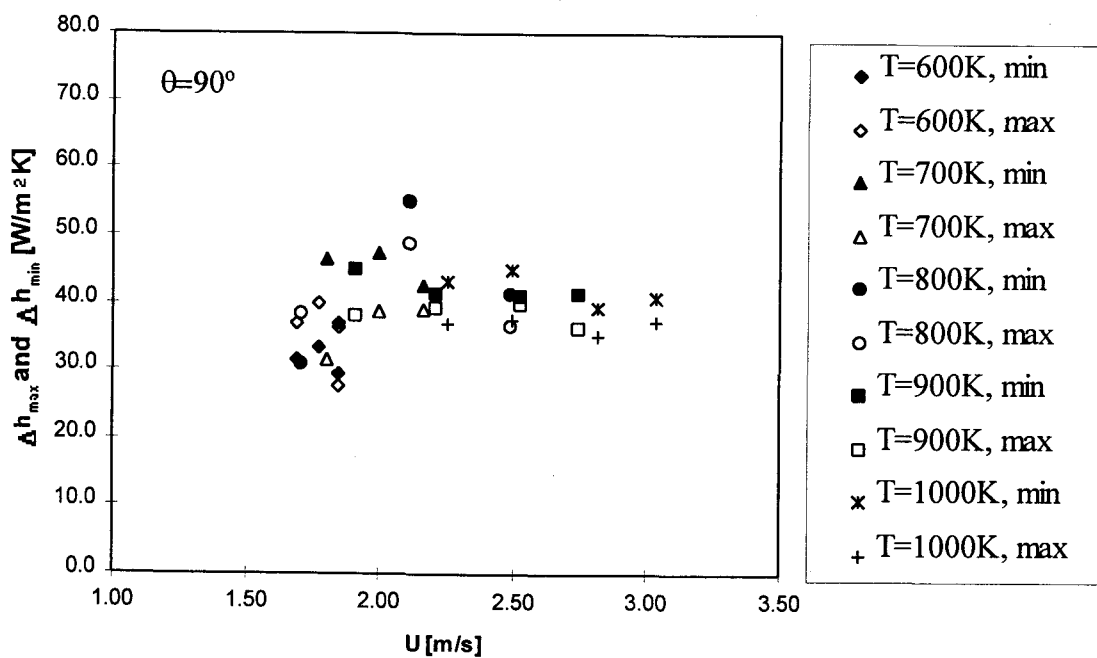


Figure 3.86 Δh_{\max} and Δh_{\min} versus U ($\theta = 90^\circ$ $d_p = 2$ mm).

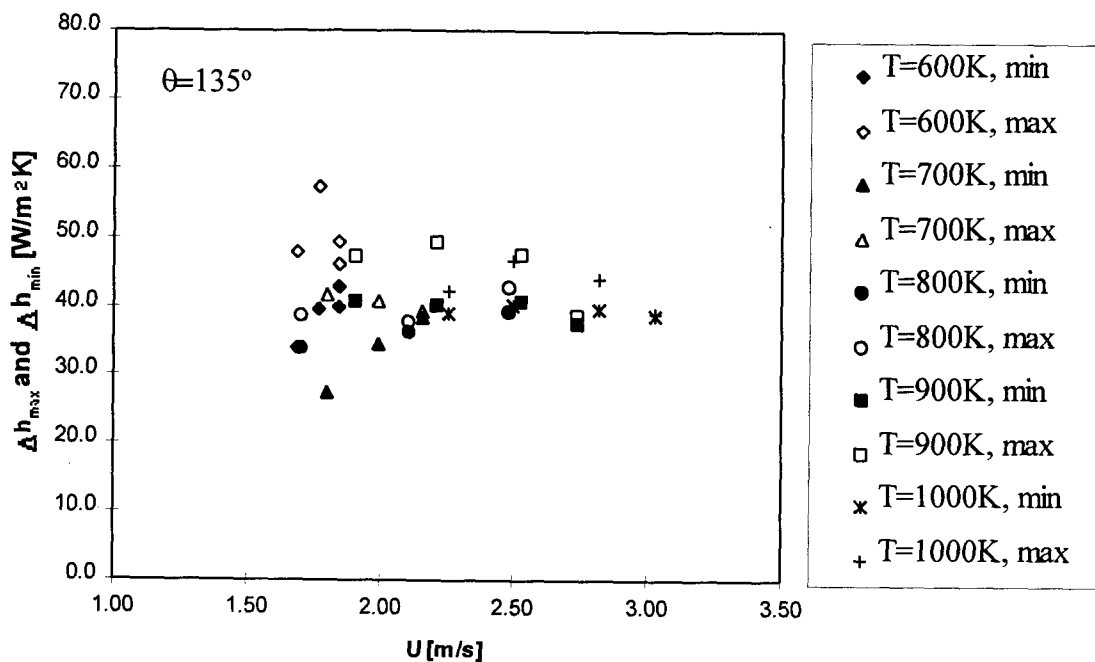


Figure 3.87 Δh_{\max} and Δh_{\min} versus U ($\theta = 135^\circ$ $d_p = 2$ mm).

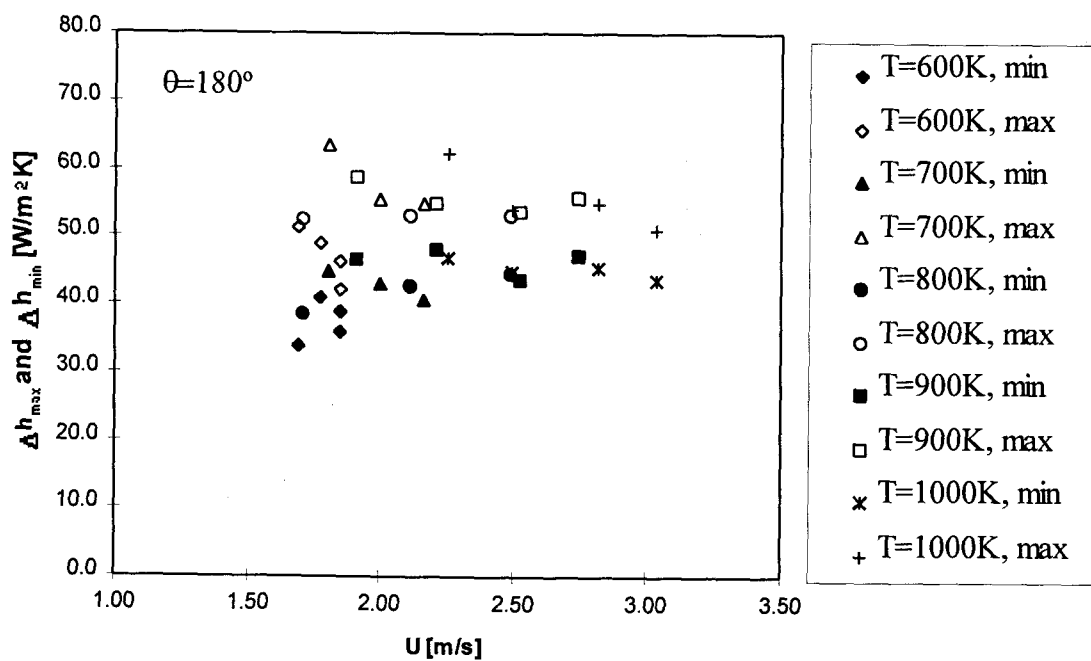


Figure 3.88 Δh_{\max} and Δh_{\min} versus U ($\theta = 180^\circ$ $d_p = 2$ mm).

180°, respectively. The trends are similar to those found for the standard deviation. These results will be discussed in detail when heat transfer coefficients are compared to models and correlations.

3.4.3 Bubble and Emulsion Phase Frequency on the Tube

Bubble frequency on the tube at each circumferential location was determined using the filtered heat transfer data. The appropriateness of the data is dependent on there being two distinct phases as mentioned above. Figures 3.89, 3.90, 3.91, 3.92 and 3.93 shows bubble frequency on the tube versus the nondimensional fluidization velocity for each bed temperature for circumferential locations $\theta = 0^\circ, 45^\circ, 90^\circ, 135^\circ$ and 180° , respectively. At $\theta = 0^\circ$, bubble frequency remained approximately constant as the fluidization velocity increased and was not a strong function of temperature. The average value was approximately 1.8 bubbles/sec. At $\theta = 45^\circ$, the bubble frequency again remain approximately constant. Some trends suggest an initial increase followed by a decrease. The average value was again approximately 1.8 bubbles/sec. At $\theta = 90^\circ$, bubble frequency initially increased and then remained constant at approximately 1.6 bubbles/sec. This trend is again seen at $\theta = 135^\circ$, where the bubble frequency approaches 1.5 bubbles/sec. The trend for initial increase followed by a constant value is very distinctly seen at $\theta = 180^\circ$. Here, the constant value is 1.7 bubbles/sec. For the fluidization velocities explored, the largest variations occur at $\theta = 180^\circ$ and 135° . Note that the emulsion frequency is equal to the bubble frequency, so these trends are also applicable to the emulsion phase. These

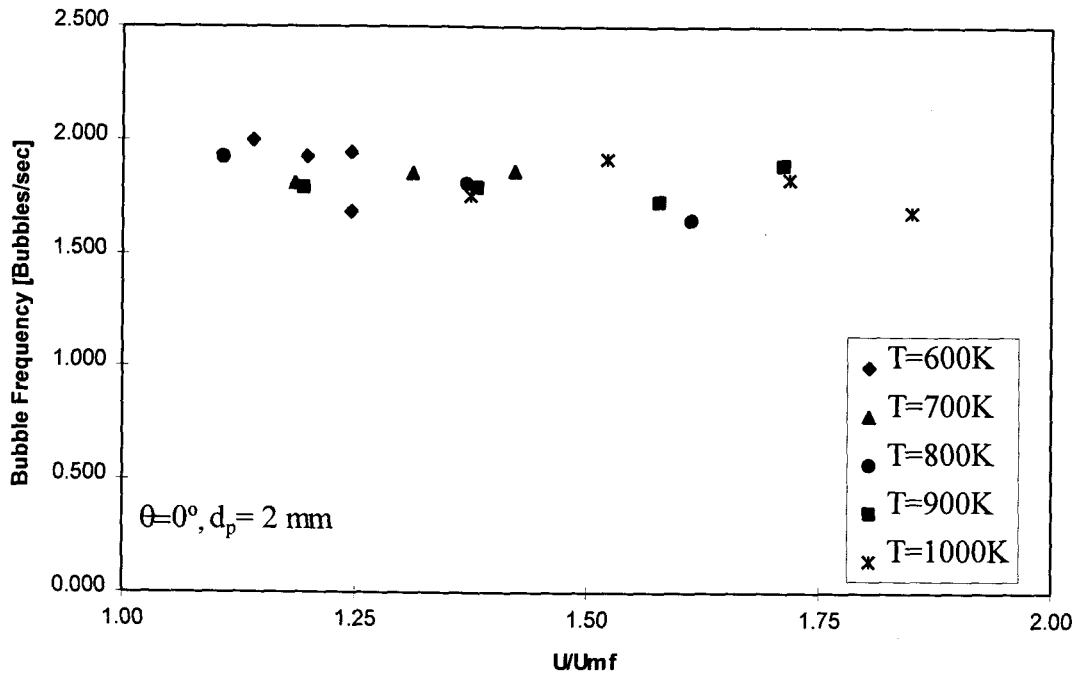


Figure 3.89 Bubble frequency on tube versus U/U_{mf} ($\theta = 0^\circ$, $d_p = 2$ mm).

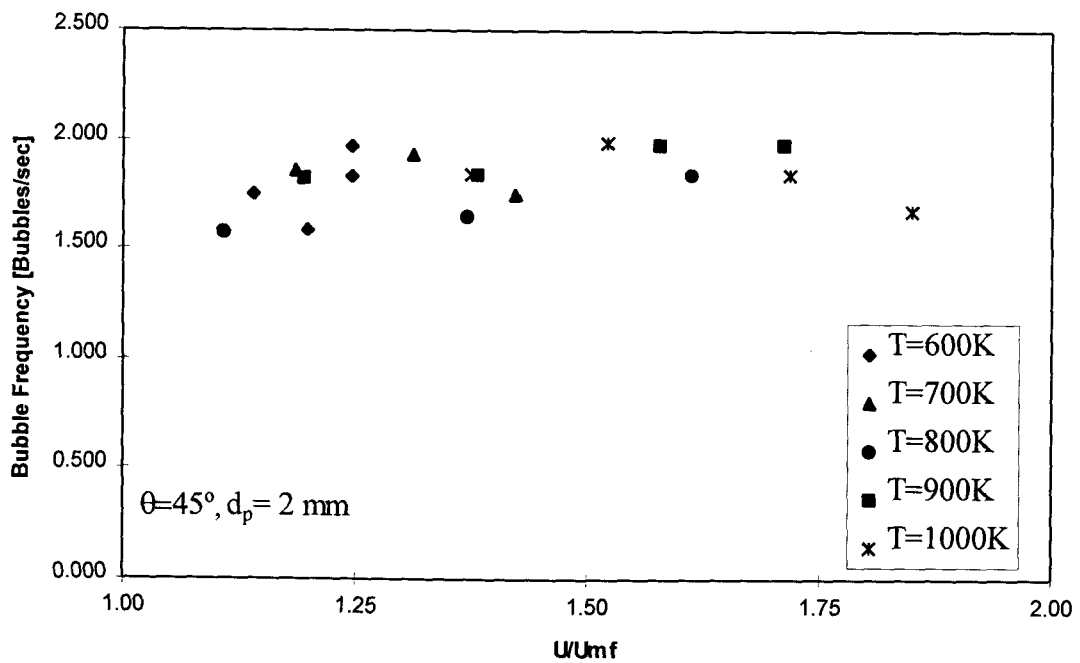


Figure 3.90 Bubble frequency on tube versus U/U_{mf} ($\theta = 45^\circ$, $d_p = 2$ mm).

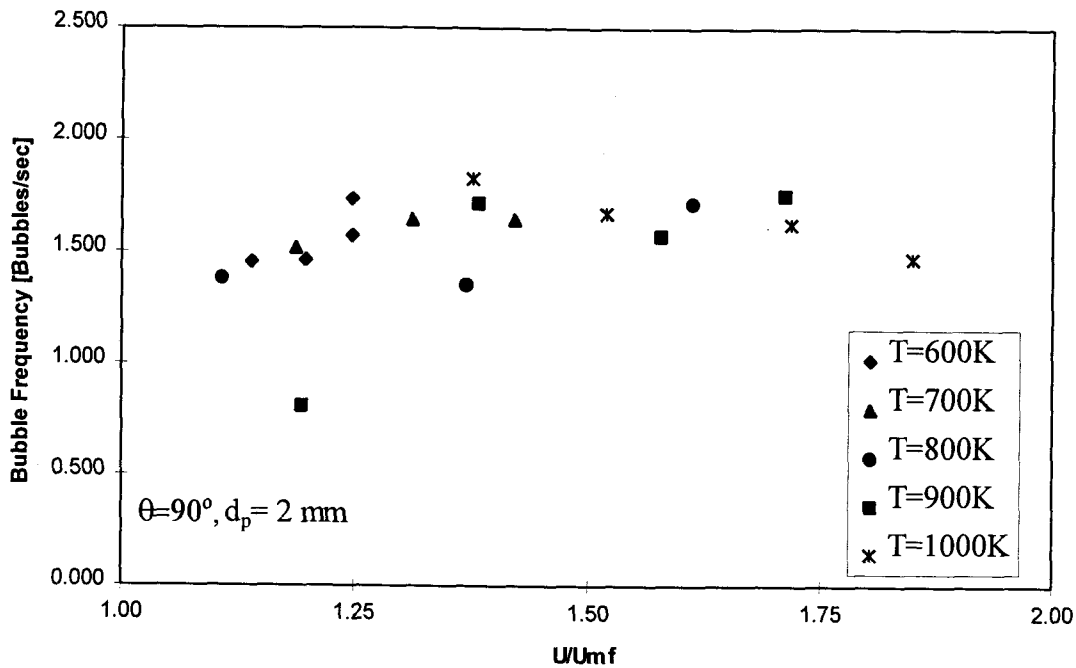


Figure 3.91 Bubble frequency on tube versus U/U_{mf} ($\theta = 90^\circ$, $d_p=2$ mm).

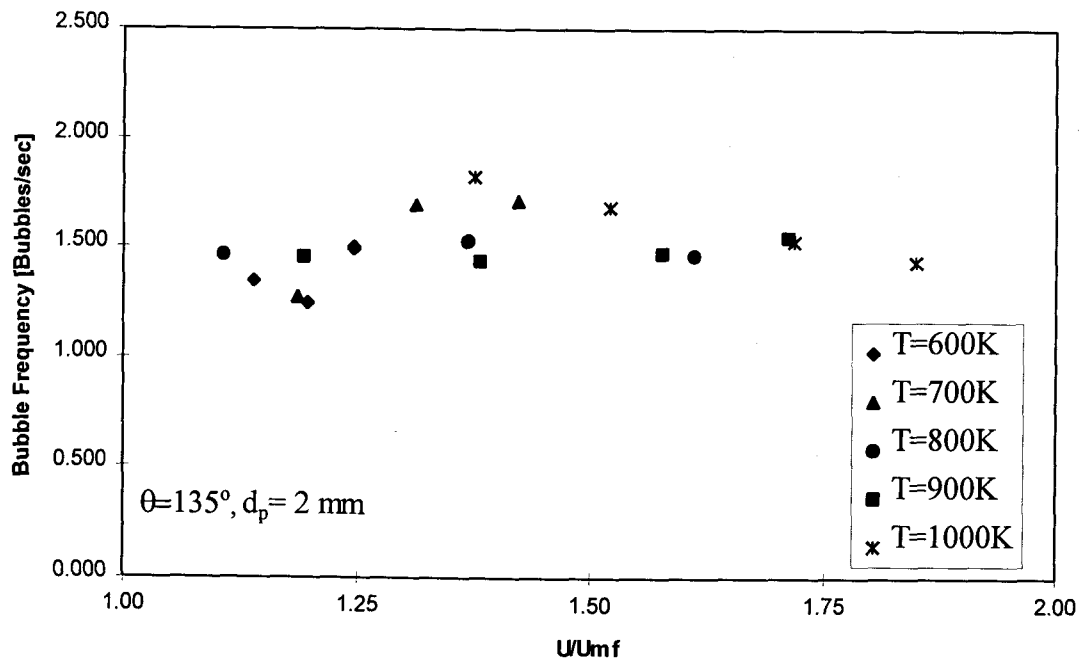


Figure 3.92 Bubble frequency on tube versus U/U_{mf} ($\theta = 135^\circ$, $d_p=2$ mm).

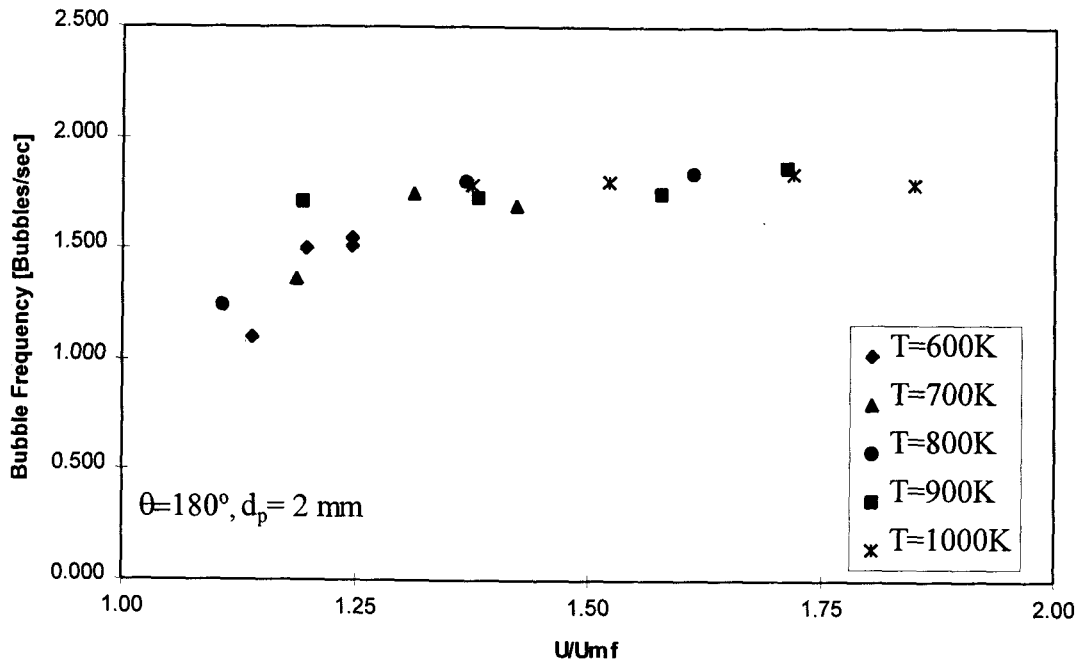


Figure 3.93 Bubble frequency on tube versus U/U_{mf} ($\theta = 180^\circ$, $d_p = 2$ mm).

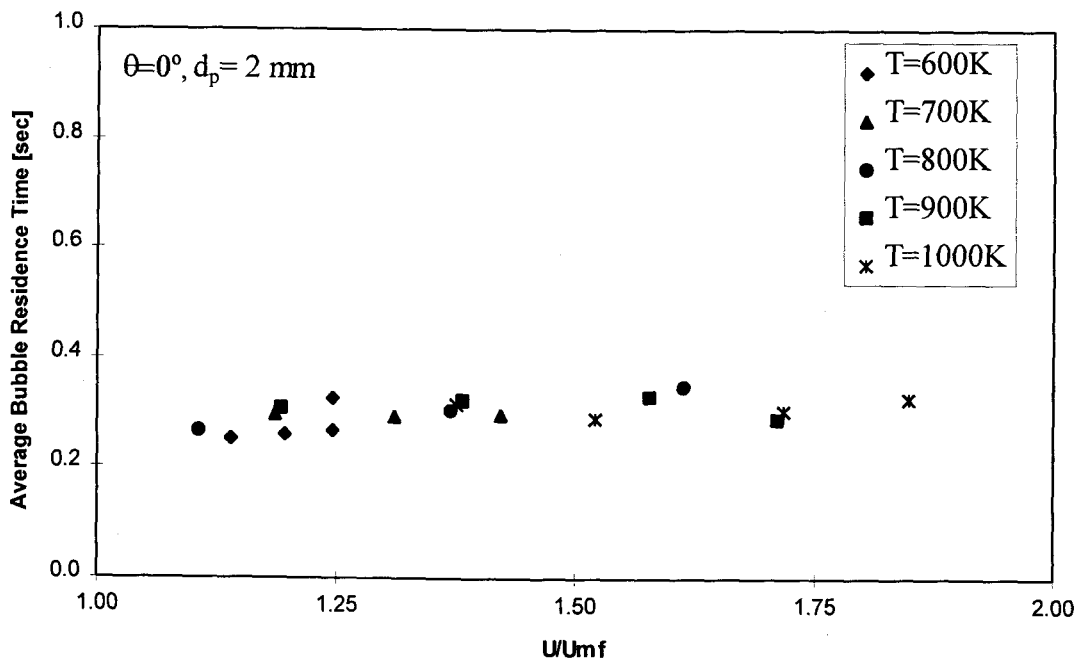


Figure 3.94 Average bubble residence time on tube versus U/U_{mf} ($\theta = 0^\circ$, $d_p = 2$ mm).

frequencies can be compared to the frequencies measured by the optical probe as shown in Figures 3.1 and 3.2. It is apparent that the two values are different. In general, however, the information from the optical probe could be used as a crude estimate of frequency on the tube, but it does not capture the detailed trends. Some of the discrepancies could be due to the error inherent in the filtering system for determining frequencies on the tube.

3.4.4 Average Bubble Residence Time on the Tube

The average bubble residence time was calculated using the filtered heat transfer data. The time for each bubble occurrence was averaged over the sample period. Figure 3.94, 3.95, 3.96, 3.97 and 3.98 show the average bubble residence times for circumferential locations $\theta = 0^\circ$, 45° , 90° , 135° and 180° , respectively. At the $\theta = 0^\circ$ location, the bubble residence time initially increased and then remained constant as the fluidization velocity increased. At $\theta = 45^\circ$, the bubble residence time remained essentially constant although there was a small initial decrease followed by an increase. This trend of an initial decrease followed by an increase is more distinct at $\theta = 90^\circ$. The behavior is more sporadic at $\theta = 135^\circ$, the variations at this location may be due to the stochastic influences on the location of high particle activity since the maximum heat transfer coefficient reaches its peak somewhere between $\theta = 90^\circ$ and $\theta = 180^\circ$, depending on the local fluidization behavior. At $\theta = 180^\circ$, the bubble residence time initially decreased and then remained constant. The same conclusions can be drawn about average bubble residence time measured by the optical probe

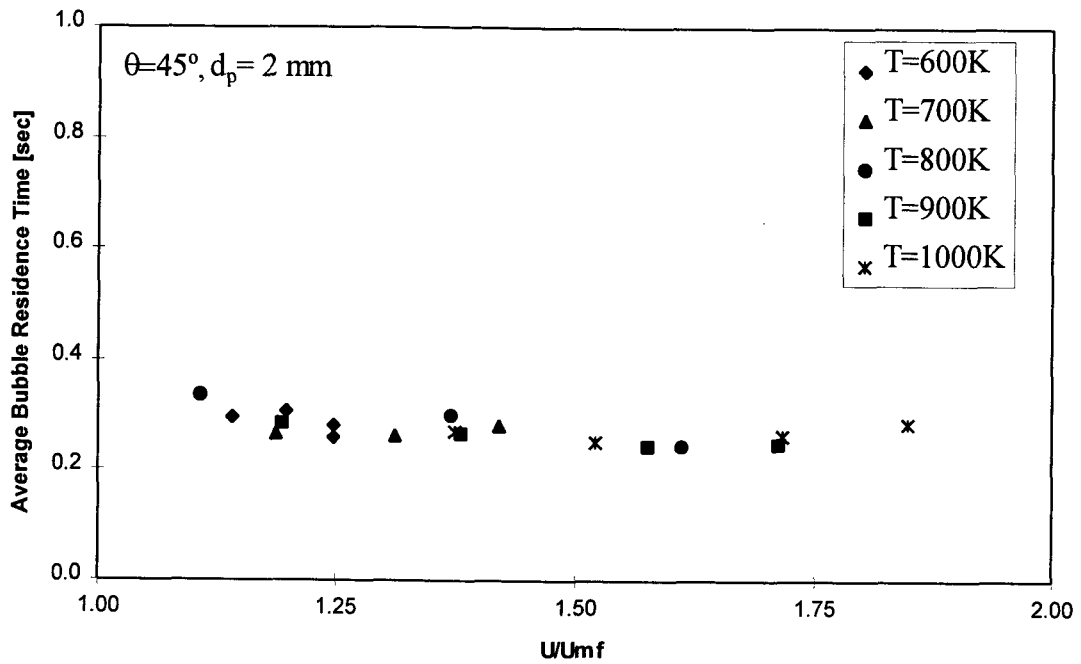


Figure 3.95 Average bubble residence time on tube versus U/U_{mf} ($\theta = 45^\circ$, $d_p = 2$ mm).

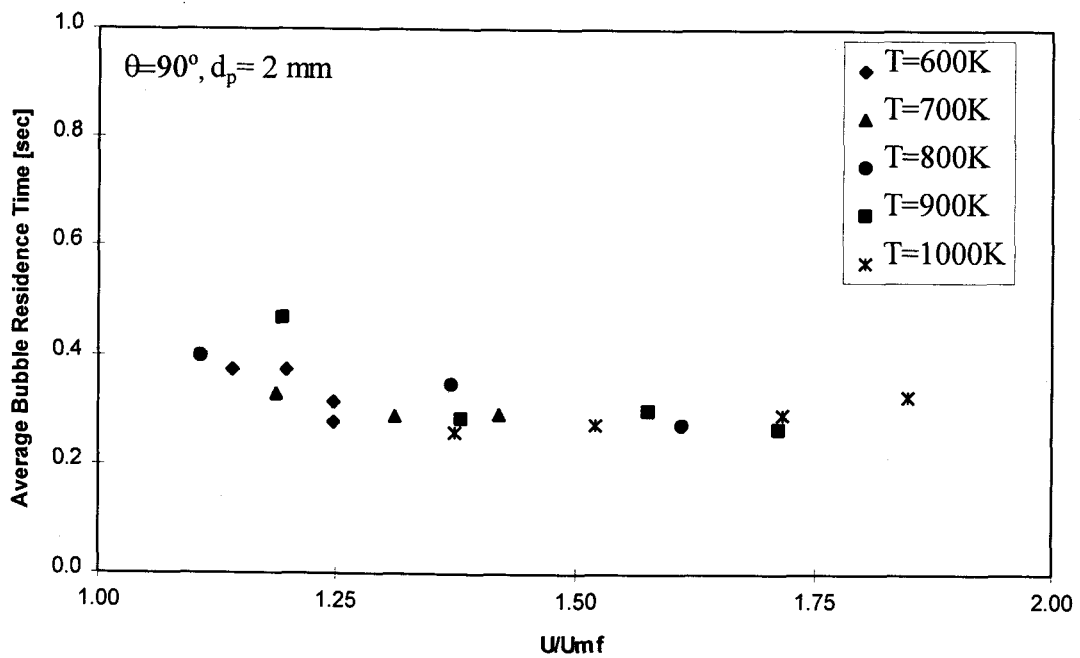


Figure 3.96 Average bubble residence time on tube versus U/U_{mf} ($\theta = 90^\circ$, $d_p = 2$ mm).

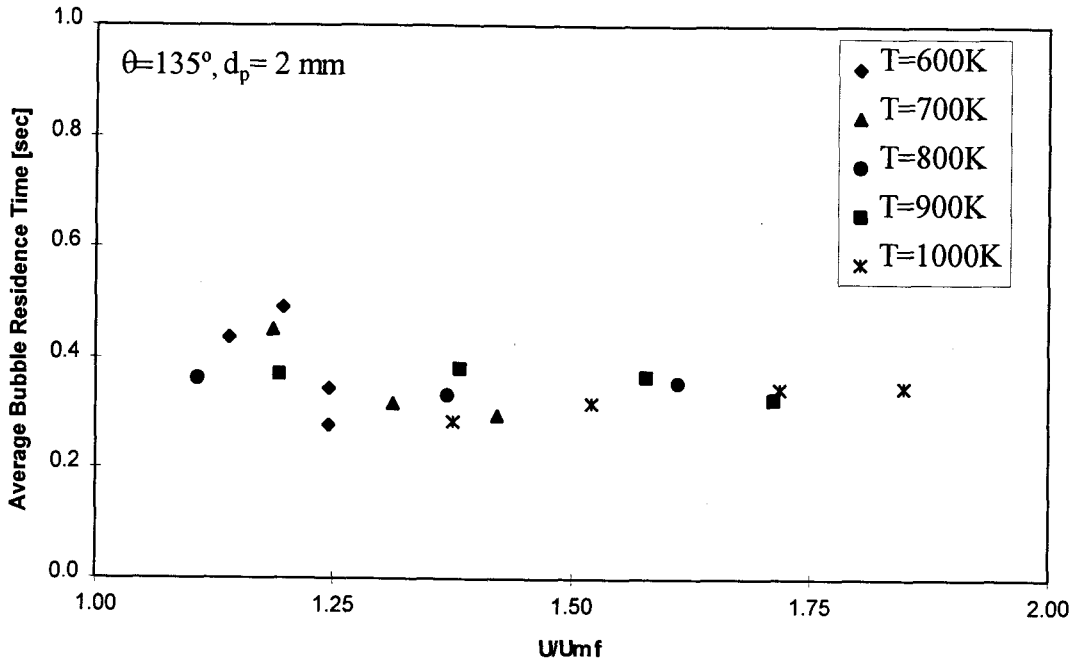


Figure 3.97 Average bubble residence time on tube versus U/U_{mf} ($\theta = 135^\circ, d_p=2 \text{ mm}$).

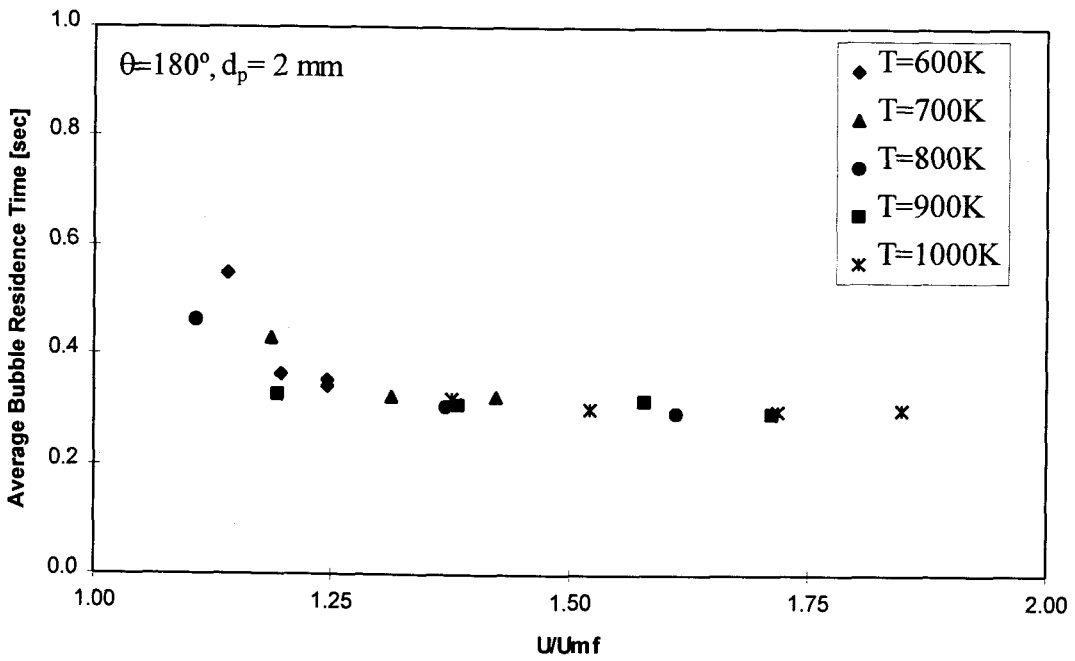


Figure 3.98 Average bubble residence time on tube versus U/U_{mf} ($\theta = 180^\circ, d_p=2 \text{ mm}$).

versus the values calculated on the tube as were mentioned above about bubble frequencies.

3.4.5 Bubble Time Fraction on the Tube

Figures 3.99, 3.100, 3.101, 3.102 and 3.103 show local bubble time fractions on the tube versus the nondimensional fluidization velocity for each bed temperature at circumferential locations $\theta = 0^\circ, 45^\circ, 90^\circ, 135^\circ$ and 180° , respectively. At $\theta = 0^\circ$, the bubble-time-fraction initially increased and then remained constant. At $\theta = 45^\circ$, the bubble time fraction showed a slight decrease. At $\theta = 90^\circ$, the bubble time fraction decreased at first and then remained constant. At $\theta = 135^\circ$, the bubble time fraction showed a slight decrease, although it remained essentially constant. This behavior is also seen at $\theta = 180^\circ$. By comparing these figures to the local bubble time fraction measured by the optical probes in Figures 3.6 and 3.7, is apparent that the probe information is not a good representation of the values on the tube.

3.5 Hydrodynamic and Heat Transfer Interaction

The optical probe signal and the instantaneous local heat transfer coefficient signal can be used to study the relationship between the arrival of the bubble or emulsion phase and the heat transfer coefficient. One relationship of interest is to see if the heat transfer coefficient increases more just before a bubble arrives or just after a bubble leaves the surface of the tube. The bubble velocity together with the travel

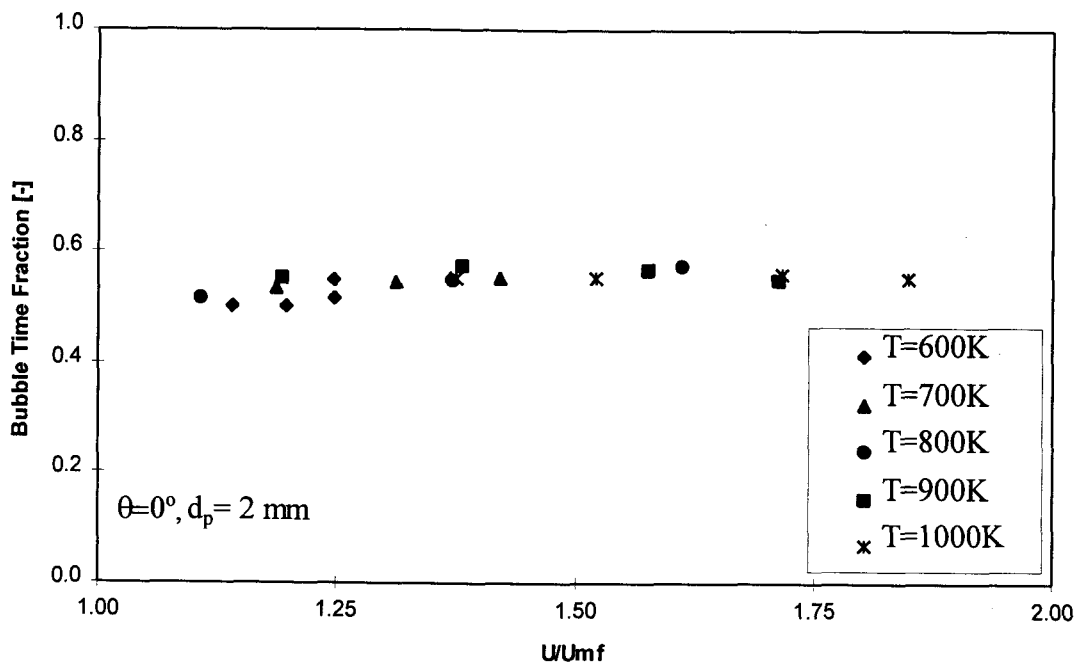


Figure 3.99 Bubble time fraction on tube versus U/U_{mf} ($\theta = 0^\circ$ $d_p = 2 \text{ mm}$).

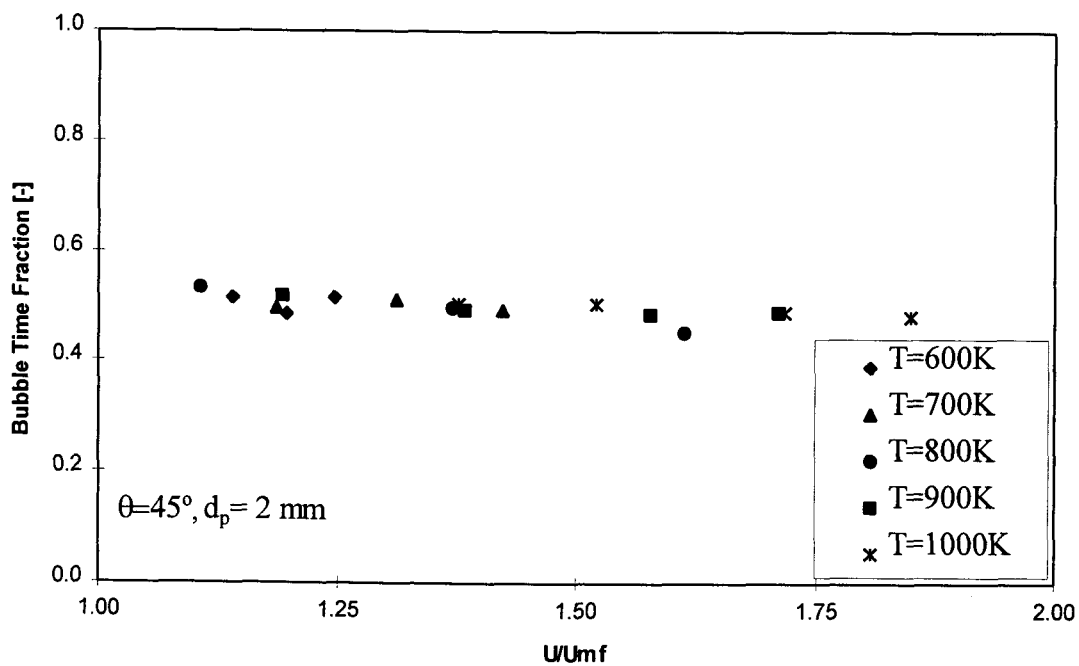


Figure 3.100 Bubble time fraction on tube versus U/U_{mf} ($\theta = 45^\circ$ $d_p = 2 \text{ mm}$).

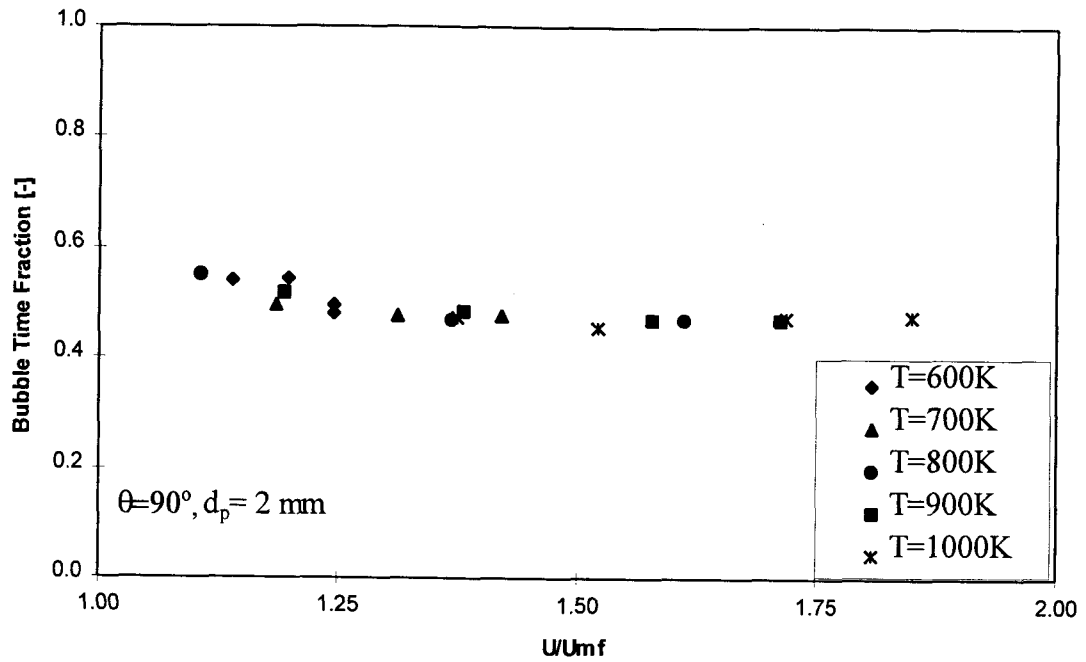


Figure 3.101 Bubble time fraction on tube versus U/U_{mf} ($\theta = 90^\circ$ $d_p = 2$ mm).

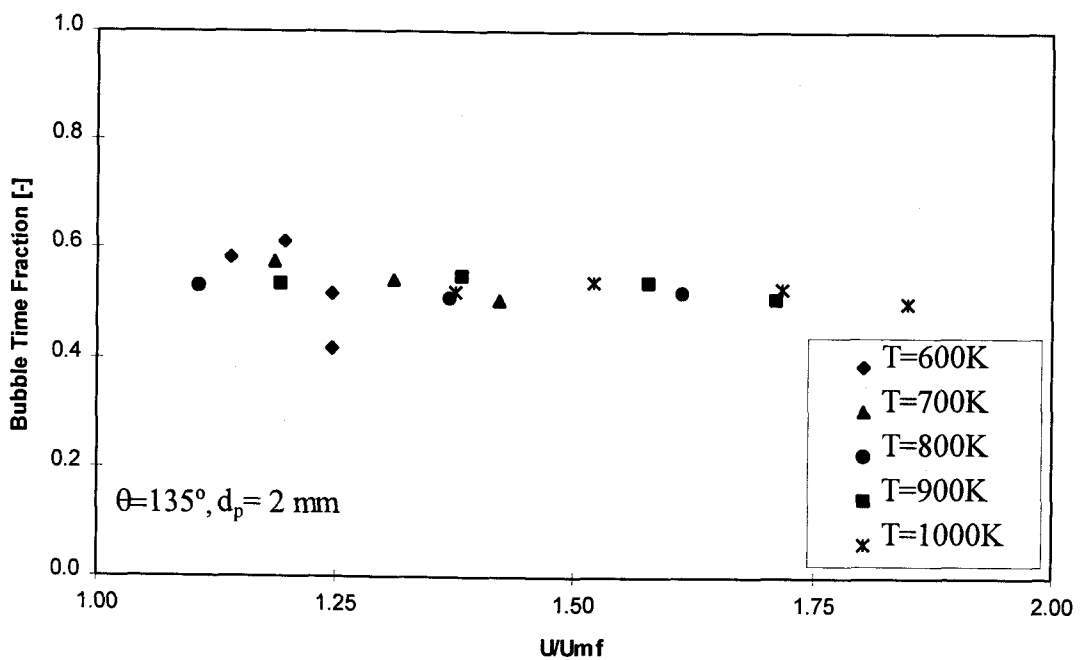


Figure 3.102 Bubble time fraction on tube versus U/U_{mf} ($\theta = 135^\circ$ $d_p = 2$ mm).

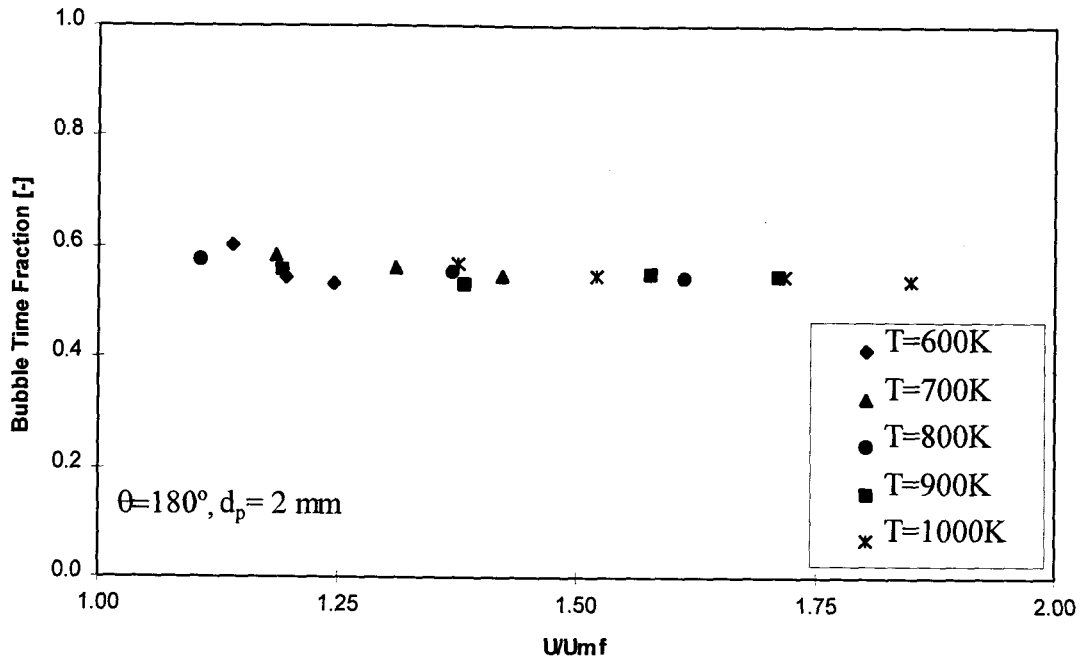


Figure 3.103 Bubble time fraction on tube versus U/U_{mf} ($\theta = 180^\circ$, $d_p = 2$ mm).

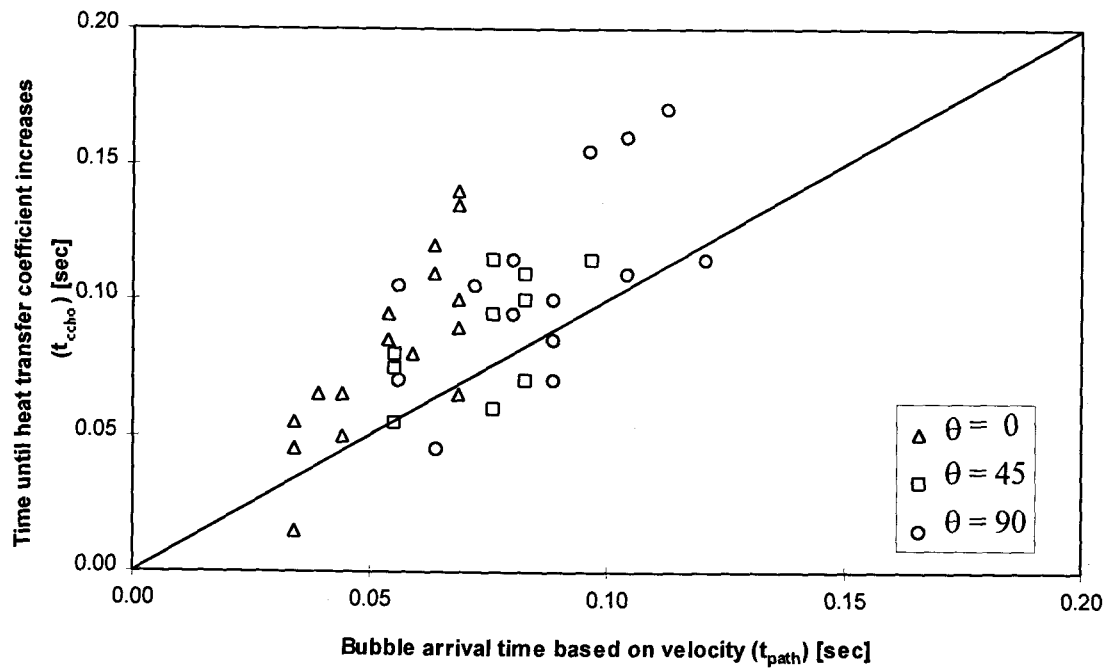


Figure 3.104 Relationship between bubble arrival and magnitude of heat transfer coefficient on tube.

path distance from the (upper) optical probe to the tube surface can be used to determine the expected arrival time of the bubble at the tube surface, t_{path} . Alternately, the instantaneous local heat transfer coefficient can be cross-correlated with the optical probe signal to determine the lag time, t_{ccho} . If t_{ccho} is less than t_{path} , then the heat transfer coefficient increases before the bubble arrives. If t_{ccho} is greater than t_{path} , then the heat transfer coefficient increases after the bubble arrives. Using the assumption that the heat transfer coefficient does not peak while the bubble is in contact with the tube surface, then it can be interpreted that for this case, the heat transfer coefficient increases the most after the bubble departs.

Although there can be heat transfer coefficient fluctuations at the surface of the tube due to bubbles that do not pass through the optical probes below the tube or that even come in actual contact with the tube surface, these calculations can be used to examine general tendencies. Note also that while the calculation of t_{path} is reasonable at circumferential locations of $\theta = 0^\circ$ and 45° , and possibly 90° , it is not as reasonable for $\theta = 135^\circ$, and 180° . A plot of t_{ccho} versus t_{path} is shown for $\theta = 0^\circ$, 45° , and 90° in Figure 3.104. In general, t_{ccho} is greater than t_{path} , which means that the heat transfer coefficient increases after the bubble arrives (i.e. when the bubble is leaving). This agrees with the findings of Tuot and Clift (1973).

3.6 Heat Transfer Correlations

The minimum and maximum local heat transfer coefficients calculated above by filtering the instantaneous local heat transfer coefficient can be used to examine

existing correlations of the heat transfer coefficient. Most of the existing models were developed for calculation of time-averaged heat transfer coefficients. Those that were developed on a mechanistic basis can be broken apart by component (heat transfer mode) and compared to the minimum and maximum local heat transfer coefficients. Although each of these models could be assumed to apply on a local basis, very few have a θ -dependence, so it is questionable if they can be considered truly local. A few of the more fundamental models (e.g. Adams and Welty, 1981; Adams (1982b)) can be applied to calculate local, instantaneous values, but generally require input that cannot be measured and must be assumed. This, along with their cumbersome nature, makes them less attractive and not qualitatively better than more simple correlations.

The correlations investigated in the present work include those that have been tested in the literature for large particle systems and include the following:

Mathur and Saxena (1986):

$$\text{Nu}_p = 5.95 (1 - \varepsilon)^{2/3} + 0.055 \text{Ar}^{0.3} \text{Re}_p^{0.2} \text{Pr}^{1/3} \quad (3.8)$$

Ganzha et al. (1982):

$$\text{Nu}_p = 8.95 (1 - \varepsilon)^{2/3} + 0.12 \text{Re}_p^{0.8} \text{Pr}^{0.43} \frac{(1 - \varepsilon)^{0.133}}{\varepsilon^{0.8}} \quad (3.9)$$

Borodulya et al.(1980):

$$\text{Nu}_p = 0.37 \text{Re}_p^{0.71} \text{Pr}^{0.31} \quad (3.10)$$

Zabrodsky et al. (1981):

$$h_w = 7.2 \frac{k_g}{d_p} (1 - \varepsilon)^{2/3} + 26.6 U^{0.2} \rho_g c_{p_g} d_p \quad (3.11)$$

Glicksman and Decker #1 (1980):

$$\text{Nu} = (1 - \delta_B)(9.3 + 0.042 \text{Re Pr}) \quad (3.12)$$

Glicksman and Decker #2 (1979):

$$\text{Nu} = (1 - \delta_B)(6 + 0.5 \text{Re}_p \text{Pr}) \quad (3.13)$$

Catipovic (1979):

$$\begin{aligned} \text{Nu}_p = & 6(1 - \beta) + (0.0175 * \text{Ar}^{0.46} \text{Pr}^{0.33}(1 - \beta) \\ & + \frac{d_p}{D_T}(0.88 \text{Re}_{p,mf}^{0.5} + 0.0042 \text{Re}_{p,mf}) \text{Pr}^{0.33} \beta \end{aligned} \quad (3.14)$$

The above correlations can be seen to take the following form:

$$\text{Nu}_p = (1 - f_b)\text{Nu}_{p,e,pc} + (1 - f_b)\text{Nu}_{p,e,gc} + f_b\text{Nu}_{p,b} \quad (3.15)$$

With the exception of Catipovic, the above correlations either neglect the bubble phase contribution or lump the bubble contribution through the use of an effective ε . Note that void fractions are related as follows:

$$\begin{array}{ccccc} L_m(1 - \varepsilon_m) & = & L_{mf}(1 - \varepsilon_{mf}) & = & L_f(1 - \varepsilon_f) \\ \text{fixed bed} & & \text{at } u_{mf} & & \text{bubbling bed} \end{array} \quad (3.16)$$

The emulsion phase components of the above correlations can be compared to the average maximum local heat transfer coefficient by using an appropriate ε for the emulsion phase.

The bubble phase component can be estimated using the bubble component in the correlation of Catipovic or using that suggested by Decker and Glicksman (1983) for the bubble phase:

$$\text{Nu}_{p,b} = 0.664 \left[\frac{(U_b + 3U_{mf})d_p}{\nu} \right]^{0.5} \text{Pr}^{0.33} \left(\frac{d_p}{L} \right)^{0.5} \quad (3.17)$$

To investigate the above correlations, the contribution due to radiative heat transfer had to be subtracted out of the data obtained in the experiments. The correlation in Equation 3.6 was used to calculate the radiative contribution which was subtracted from the experimentally measured heat transfer coefficients.

To use the listed correlations with the experimental data, an appropriate void fraction ϵ was calculated following the analysis of Ganzha et al. (1982). Because the bed voidage near the heat transfer surface is larger than the bulk bed voidage, they followed the analysis of Kimura and Kaneda (1955) and calculated a bed voidage near the surface, ϵ_w , based on the voidage in the bulk of the bed, $\bar{\epsilon}$, such that

$$\epsilon_w = 1 - \frac{(1 - \bar{\epsilon}) \left[0.7293 + 0.5139 \left(d_p / D_T \right) \right]}{\left[1 + \left(d_p / D_T \right) \right]} \quad (3.18)$$

This equation was used to calculate ϵ_w at minimum fluidization conditions. Based on their investigations, they then noted that as the fluidization velocity was increased beyond minimum fluidization, the bed voidage near the surface changed more rapidly than in the bulk of the bed at first. At higher gas flows, the rate of voidage change became slower. To account for this, they propose the following:

$$\epsilon = \epsilon_w + 1.65 A(1 - \bar{\epsilon}) \left[1 - \exp(-a / A^2) \right] \quad (3.19)$$

where $\bar{\epsilon}$ is the bed voidage at minimum fluidization and

$$a = \left| 0.367 \ln \left[\left(\epsilon_w - \bar{\epsilon} \right) / \left(1 - \bar{\epsilon} \right) \right] \right| \quad (3.20)$$

and

$$A = \left(\text{Re} - \text{Re}_{mf} \right) / \text{Ar}^{0.5} \quad (3.21)$$

The above relations were used to compute emulsion phase voidage near the heat transfer surface at any fluidization velocity. Except for Catipovic, the forms of the correlations above are based on the emulsion phase characteristics and only account for the bubble phase through an effective voidage. This is because only time-averaged data were available to check the correlation. In the present work, the bubble phase and emulsion phase heat transfer coefficients were calculated separately. In comparing these correlations to the experiment results, emulsion phase voidage was required and the bubble phase was be accounted for separately.

3.6.1 Emulsion Phase (Average Maximum Heat Transfer Coefficient)

The average maximum local heat transfer coefficient was used to check the emulsion phase (the sum of particle convective and gas convective) components of the above available correlations. The comparison of the difference between the measured and predicted values of the Nusselt number is shown in Figure 3.105 for all circumferential locations. The correlation by Ganzha is the best fit. When comparing the correlation by Ganzha to the correlation by Mathur, it is apparent that the correction for variation in the void fraction, ϵ , is beneficial. In the Ganzha model, the particle convection term appears to do an adequate job but the gas convection term does not correctly account for variation with Re. The correlations listed above have

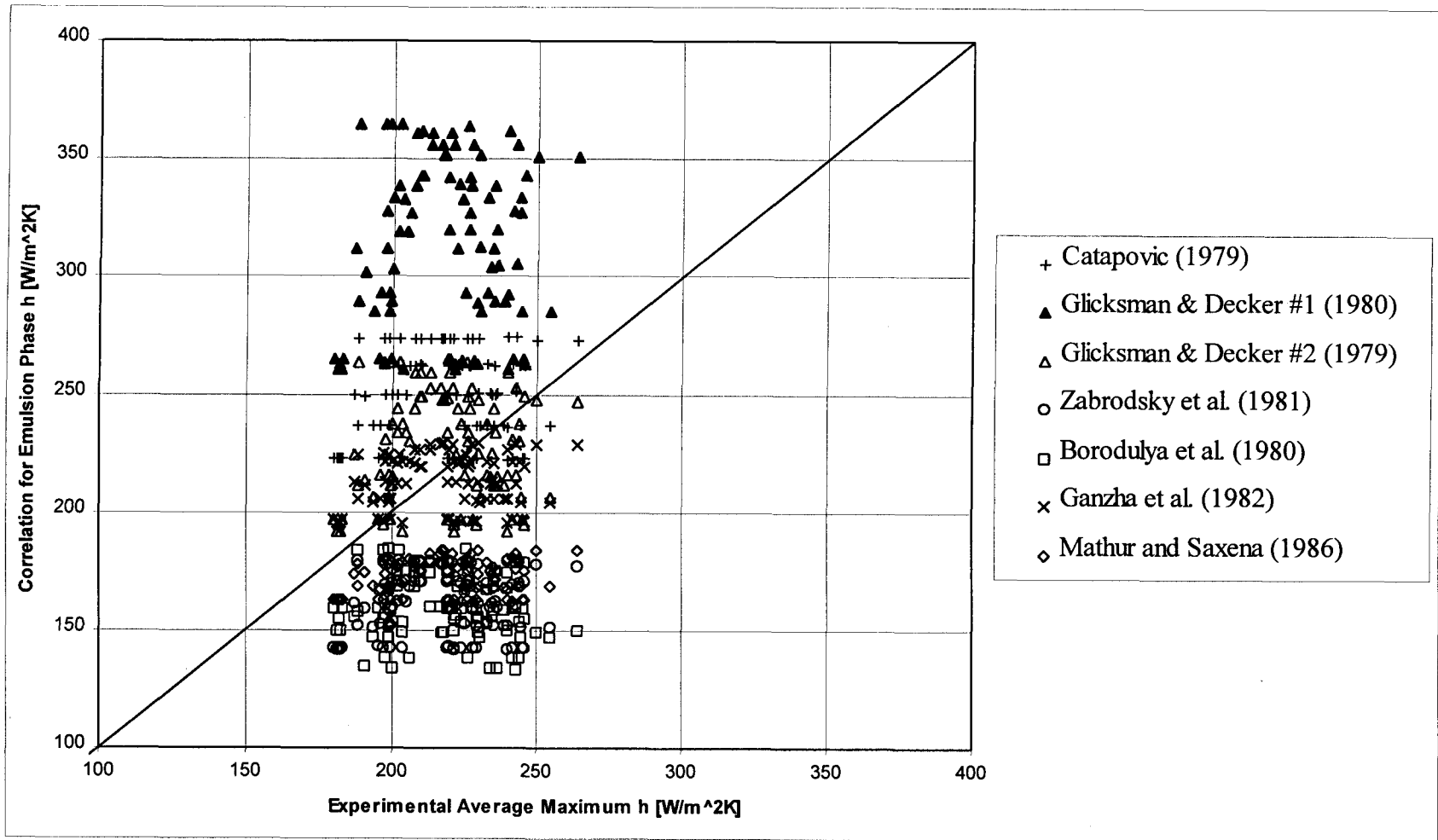


Figure 3.105 Comparison of measured emulsion phase (average maximum) heat transfer coefficients to values predicted by various correlations.

Reynolds number dependence varying from powers of 0.2 to 1.0. Regression analysis on the current data yields a dependence of the Nusselt with $Re^{0.5}$. It was also found that the dependence on Prandtl number is $Pr^{1/3}$ as proposed by the correlations of Mathur, Catipovic and Borodulya. Finally, regression analysis also suggests a dependence of the gas convection term on $Ar^{0.3}$ as suggested by Mathur (Catipovic also has an Ar dependence).

The correlations were next checked for at each circumferential location. All of the correlations showed trends with respect to the circumferential location, θ . This is not surprising since these correlations were developed for space-averaged heat transfer coefficients. There is a dearth of information available in the literature for the dependence of the heat transfer coefficient correlations on θ . The dependence on θ can be accounted for with the void fraction, ε . Adams (1984) suggested a time-averaged variation as shown in Figure 3.106. For the present work, the void fraction was calculated using Equation 3.19 and the bulk bed emulsion voidage near the cylinder was modified to account for variation in θ . Instead of the time-averaged variation suggested by Adams above, an instantaneous linear variation as shown in Figure 3.106 is proposed. The minimum fluidization value of 0.58 was selected for $\theta = 0^\circ$ where the emulsion phase was modeled as being at minimum fluidization conditions as it approached the tube. The packed-bed value of 0.44 was selected for $\theta = 180^\circ$ where the emulsion phase was modeled as a lee-stack sitting packed on top of the tube.

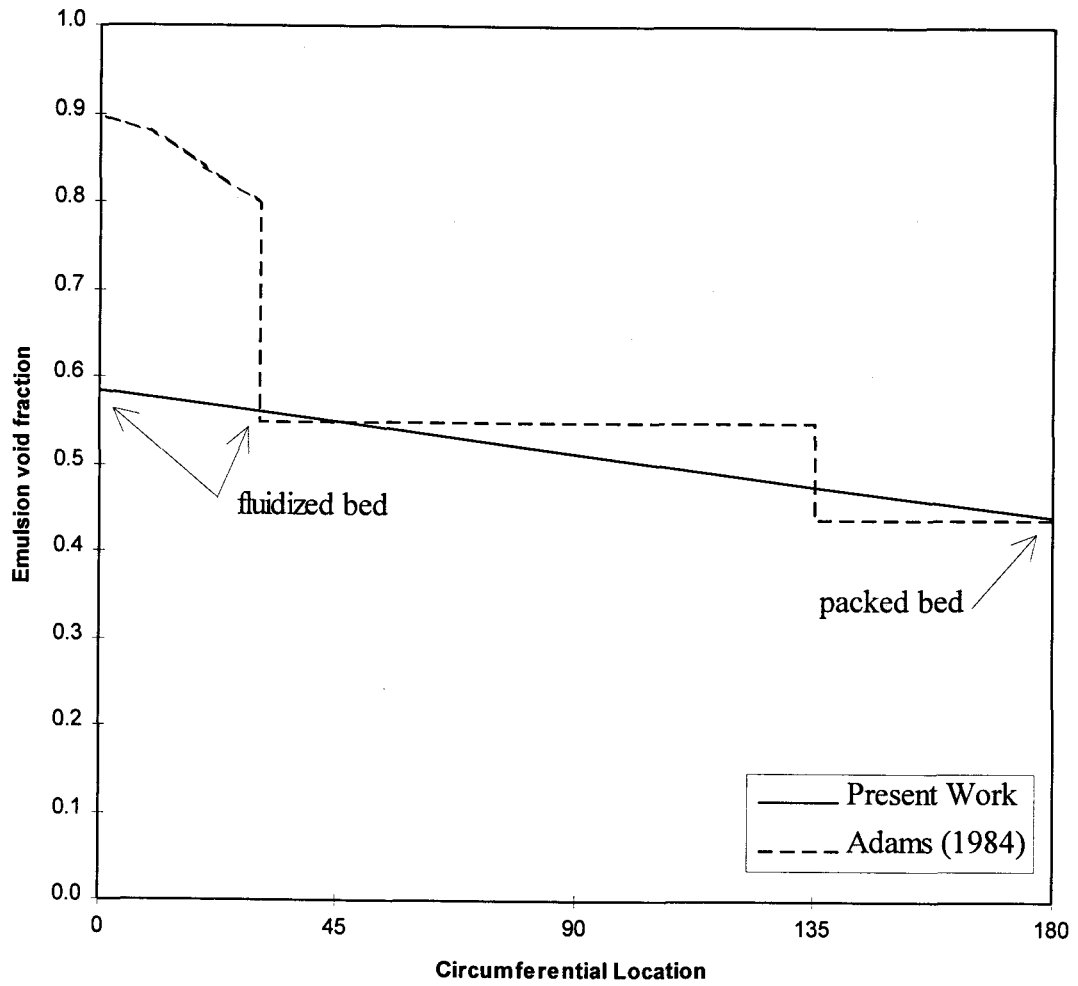


Figure 3.106 Void fraction dependence on θ .

The final modified correlation of Ganzha for the emulsion phase local heat transfer coefficient, then, is

$$\text{Nu}_{p,e} = 8.95(1-\varepsilon)^{2/3} + 0.016\text{Ar}^{0.3}\text{Re}_p^{0.5}\text{Pr}^{1/3} \frac{(1-\varepsilon)^{0.133}}{\varepsilon^{0.8}}. \quad (3.22)$$

Comparisons between this correlation and the experimentally obtained values are shown for each circumferential location in Figures 3.107, 3.108, 3.109, 3.110 and 3.111 for $\theta = 0^\circ, 45^\circ, 90^\circ, 135^\circ$ and 180° , respectively. The comparison is also shown for all θ in Figure 3.112. This correlation predicted heat transfer coefficients for the conditions in the present work within ± 15 percent. It applies to the range of conditions investigated in the present work: $44,000 < \text{Ar} < 136,000$; $27 < \text{Re}_{mf} < 57$; $39 < \text{Re} < 72$; and $6.8 < \text{Pr} < 7.0$.

3.6.2 Bubble Phase (Average Minimum Heat Transfer Coefficient)

There is little information available in the literature about heat transfer coefficient correlations for the bubble phase in large particle fluidized systems. Because the correlations available are based on time-averaged data, the bubble phase is accounted for through an effective voidage as mentioned above. The correlations above are based on models and dimensionless groups appropriate for the emulsion phase (particle convective and gas convective) and are not based on parameters governing the bubble phase contribution to heat transfer. The bubble phase is only accounted for through the use of an effective voidage. Perhaps for this reason, the bubble phase correlation of Catipovic greatly underpredicts the experimental data in

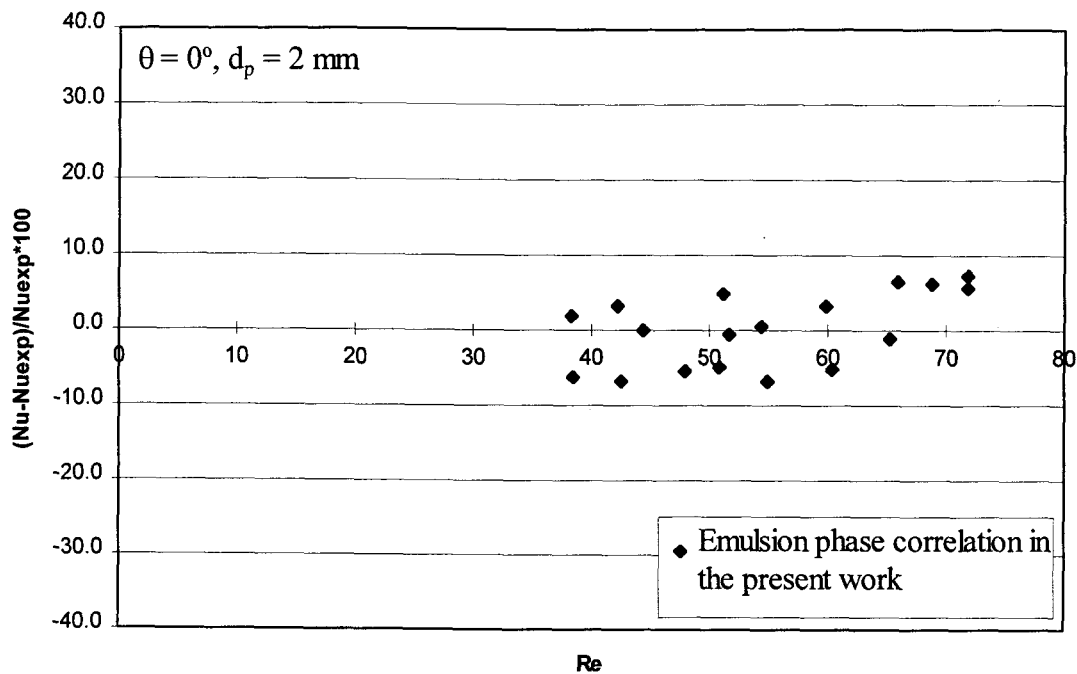


Figure 3.107 Comparison of measured emulsion phase (average maximum) heat transfer coefficients to correlation developed in the present work ($\theta = 0^\circ$).

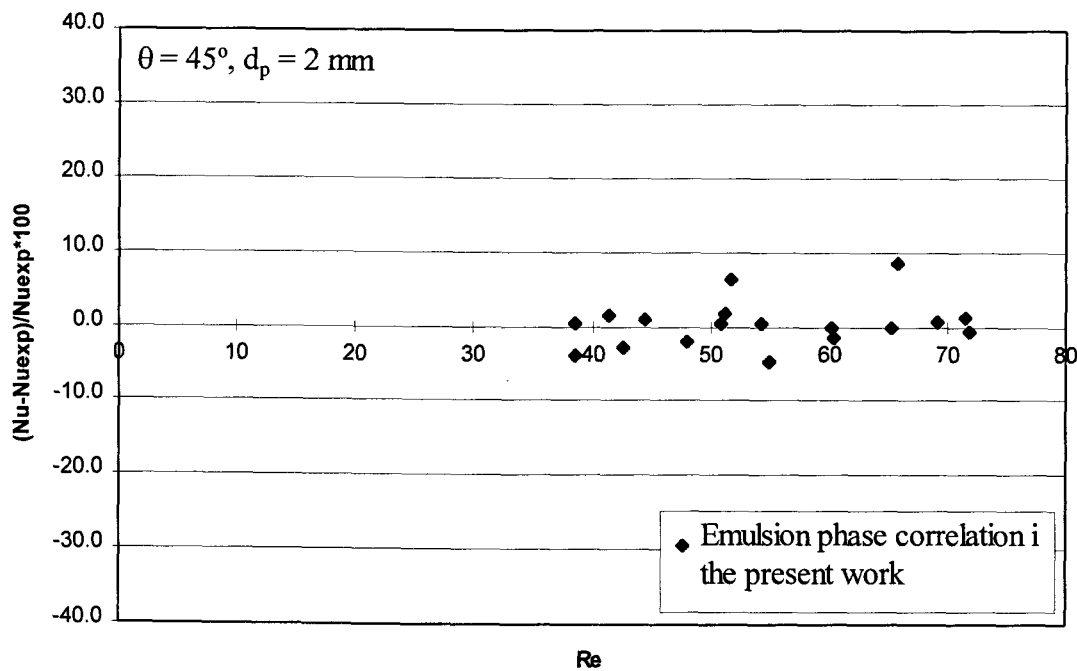


Figure 3.108 Comparison of measured emulsion phase (average maximum) heat transfer coefficients to correlation developed in the present work ($\theta = 45^\circ$).

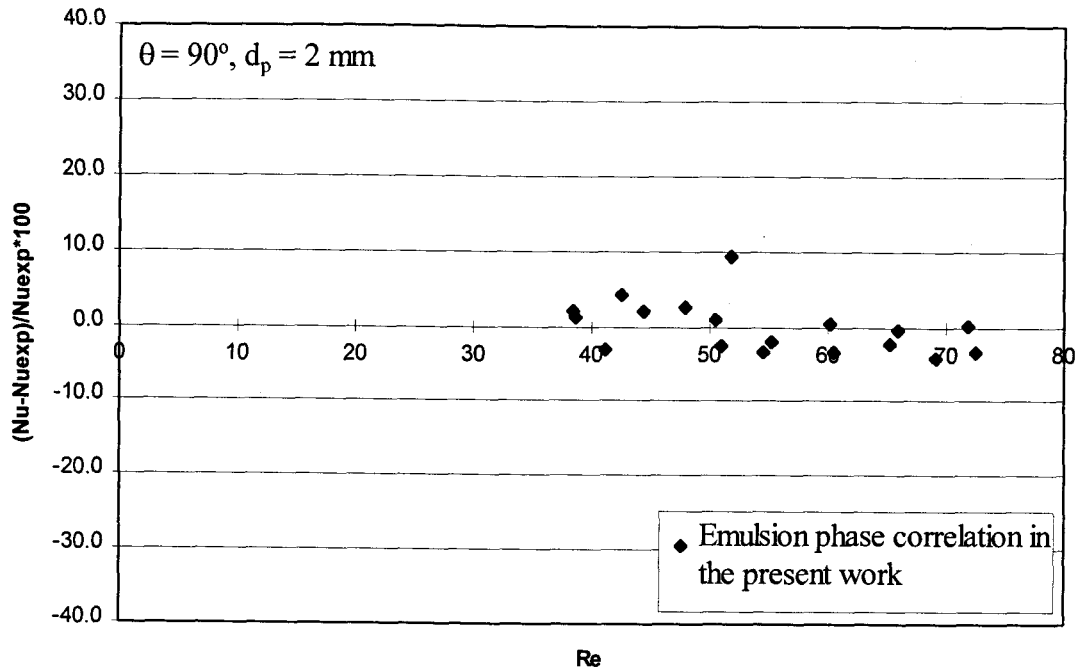


Figure 3.109 Comparison of measured emulsion phase (average maximum) heat transfer coefficients to correlation developed in the present work ($\theta = 90^\circ$).

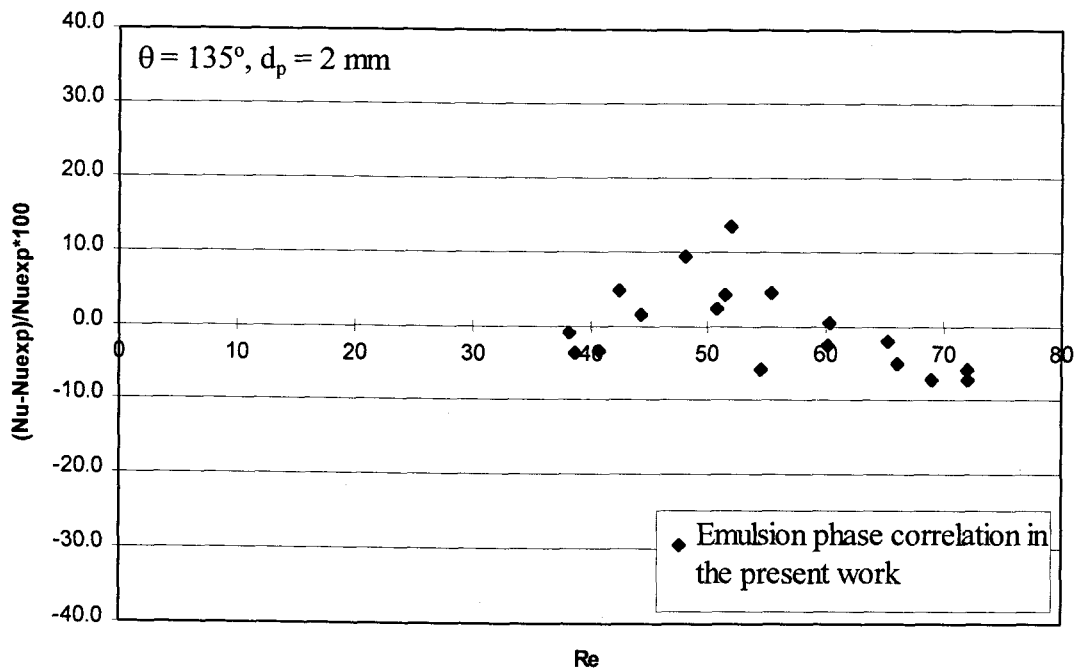


Figure 3.110 Comparison of measured emulsion phase (average maximum) heat transfer coefficients to correlation developed in the present work ($\theta = 135^\circ$).

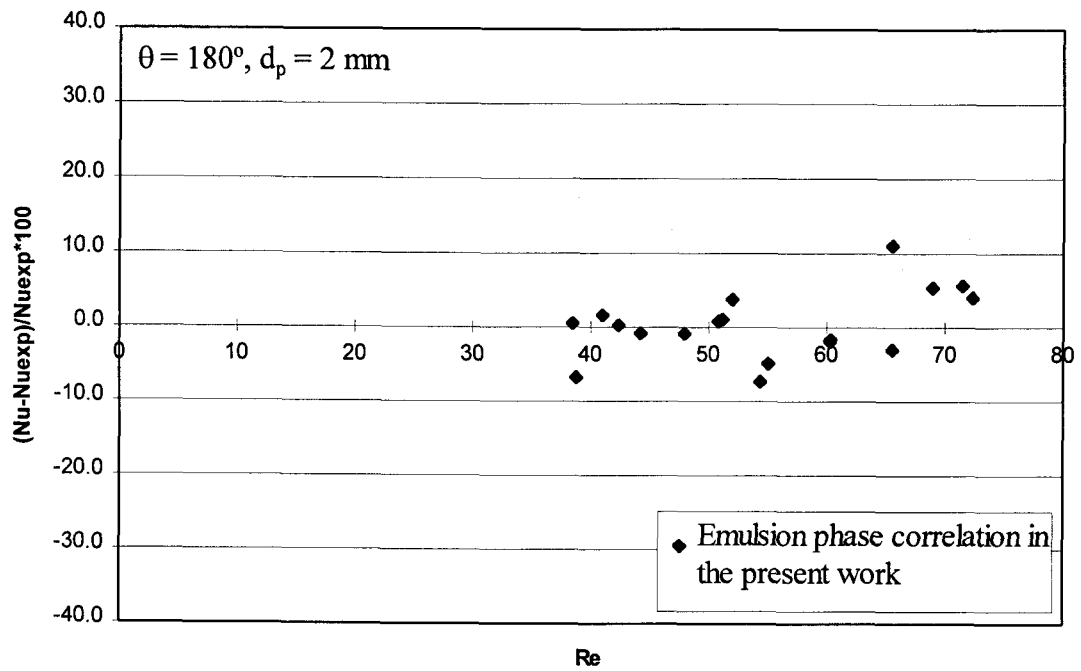


Figure 3.111 Comparison of measured emulsion phase (average maximum) heat transfer coefficients to correlation developed in the present work ($\theta = 180^\circ$).

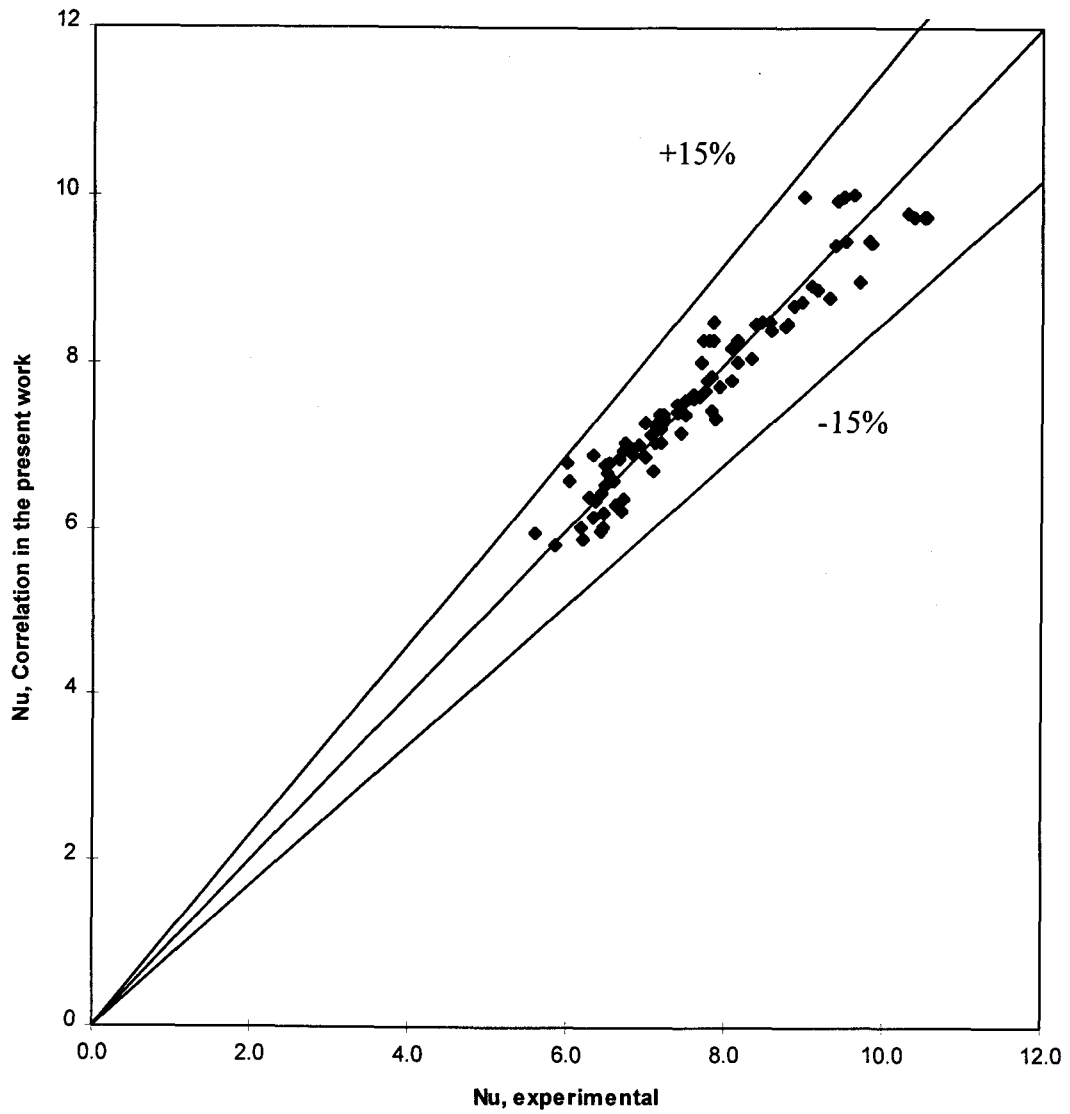


Figure 3.112 Comparison of measured emulsion phase (average maximum) heat transfer coefficients to correlation developed in the present work.

the present work. The correlations of Decker and Glicksman also underpredict the present data. This is not unexpected, however, since this model relies on a velocity, $U_b + 3U_{mf}$, which is the value of gas velocity through a bubble predicted by the potential flow model of Davidson (Kunii and Levenspiel, 1991). This has generally been found to be inaccurate, especially for large particle systems. The gas throughflow has been found to be significantly different than that predicted by two-phase theory (Geldart and Cranfield, 1972). George (1991) also found the bubble phase contribution to be significantly larger than predicted by available correlations.

To propose a new bubble phase correlation, the approach of Catipovic was followed whereby the bubble phase contribution was found to depend primarily on the minimum fluidization Reynolds number. In correlating the present data with Re_{mf} , however, it was found that there was a trend with respect to Re that was not accounted for. Regression analysis yielded the following best fit:

$$Nu_{p,b} = 1.13 \frac{Re_{mf}^{0.73}}{Re^{0.3}} \quad (3.23)$$

Although it is surprising to find that Nu_b actually decreases weakly with increasing Re , this can be explained based on observations made in the two-dimensional bed facility. At higher Re , there are generally fewer particles in the bubble resulting in lower heat transfer coefficient.

The above correlation is compared to the experimental data in Figure 3.113. This correlation predicted heat transfer coefficients for the conditions in the present work within ± 15 percent. It applies to the range of conditions investigated in the

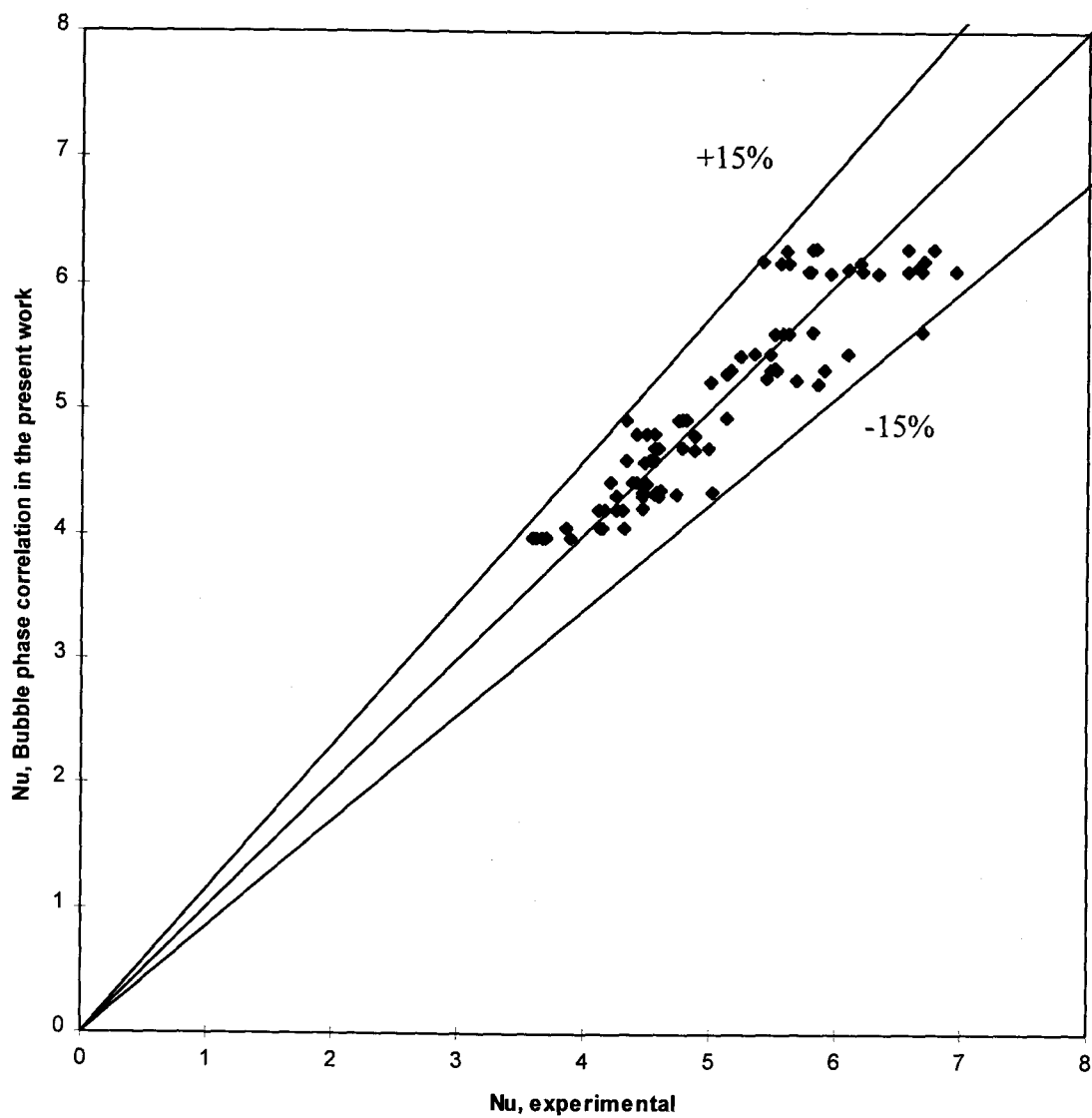


Figure 3.113 Comparison of measured bubble phase (average minimum) heat transfer coefficients to correlation developed in the present work.

present work: $44,000 < Ar < 136,000$; $27 < Re_{mf} < 57$; $39 < Re < 72$; and $6.8 < Pr < 7.0$.

4. CONCLUSIONS AND RECOMMENDATIONS

4.1 Conclusions

The purpose of this research was to study fluidized bed hydrodynamics and heat transfer. Two optical probes were used in a 2D bed to validate the interpretation of the probe signals. Probe signal processing methodology was developed and bubbles properties were calculated. To study heat transfer simultaneously, a tube instrumented with an instantaneous heat flux sensor was built to measure instantaneous local heat transfer coefficients.

Experiments were performed in a high-temperature fluidized bed over a range of temperatures and fluidization velocities. The experiments were run for cases that corresponded to a bubbling fluidized bed. The instantaneous local heat transfer coefficients were measured at circumferential increments of 45° around the tube. Bubble properties were also measured for two different particles sizes. Heat transfer and hydrodynamic information were measured and studied over a range in conditions. The measured average maximum and minimum local heat transfer coefficients were compared with time- and space-averaged correlations available in the literature.

The following are conclusions drawn from the gathering and examination of these data and are applicable only to the range of conditions investigated:

1. The optical probe signal processing methodology developed in Chapter 2 provides an accurate method for determining bubble properties such as bubble (or emulsion) frequency, bubble velocity, pierced length, characteristic bubble size, bubble (or

emulsion) residence time, and bubble (or emulsion) time fraction. The methodology was validated by comparing the processed signal information to values obtained using video-tape of the same events.

2. The instantaneous heat transfer coefficient was measured accurately. The key to this was calibrating the instantaneous sensor built for the tube. The accuracy of the calibration constant obtained was validated by thorough and repeated calibration checks throughout the experimental program.
3. The following is a summary of the conclusions about the dependence of bubble properties on the variables of fluidization velocity, bed temperature and particle size:
 - Bubble frequency increases with fluidization velocity, decreases with particle size, and is not a function of temperature. Bubble frequency is dependent on particle size. Measured bubble frequencies compared favorably with other similar data in the literature (no data were available for the same conditions).
 - Bubble velocity increases with fluidization velocity and decreases with particle size. Bubble velocity is not a function of temperature. For the variables investigated, it was found that $U-U_{mf}$ is the only important variable for predicting bubble velocity.
 - Local bubble time fraction increases with fluidization velocity and particle size and is not a function of temperature. Note that this implies that local emulsion time fraction decreases with fluidization velocity.

- Local bubble residence time increases only slightly with fluidization velocity and particle size and is independent of temperature. Local emulsion residence time decreases with velocity and particle size.
 - Bubble diameter increases with fluidization velocity, decreases with particle size, and is independent of temperature. Bubble diameter variation can be accounted for by variation in $U-U_{mf}$ only.
 - Visible bubble flow increases with fluidization velocity, decreases with particle size, and is not dependent on temperature.
4. The decrease in bubble velocity with particle size can be explained on the basis that bubble diameter also decreases with particle size. The smaller diameter bubbles rise slower by a force-balance analogy with gas bubbles rising in a liquid. Bubble diameters get smaller as particle size increases because the excess velocity, $U-U_{mf}$, decreases. Bubble diameter is determined by the excess velocity and bubble velocity is determined by the bubble diameter.
5. The following correlation from Clift and Grace (1985):

$$U_b = 0.71\sqrt{gd_b}$$

(3.4)

was found to give the best fit relationship between bubble velocity and bubble diameter.

5. The following are conclusions about the instantaneous heat transfer coefficient:
- At $\theta = 180^\circ$, a gas cushion or a stagnant lee stack of cooled off particles is present at low velocities. At higher velocities, more activity is seen at this

location. Distinct bubble and emulsion phase activity can be seen as the emulsion and bubble phases replace each other. Also at higher velocities, the arrival of the emulsion phase is visible and the cooling-off of the particles packets can be observed. Some of these activities are not present at the higher temperature where the fluidization velocities investigated corresponded to a more vigorously bubbling bed.

- At $\theta = 135^\circ$, the behavior is similar to that at $\theta = 180^\circ$, but with more activity. Distinct emulsion and bubble phases can be seen. At both $\theta = 135^\circ$ and $\theta = 180^\circ$, there are larger spikes in the magnitude of the instantaneous heat transfer coefficient at higher bed temperatures as compared to lower temperatures.
- At $\theta = 90^\circ$, the activity does not vary much with fluidization velocity. Distinct bubble and emulsion phases can be seen, but not as clearly as at $\theta = 180^\circ$ and 135° . The activity is uniformly periodic with similar residence times for each phase compared to other locations.
- At $\theta = 45^\circ$, the heat transfer coefficient is fairly constant at low velocities which suggests that this area might be covered by a gas cushion. At higher velocities, definite bubble and emulsion phase behavior can be observed and is often periodic as was observed at $\theta = 90^\circ$.
- At $\theta = 0^\circ$, the signal suggests that a gas cushion is present at low velocities. At higher velocities, distinct bubble and emulsion phases can be seen.

There are spikes from particles which increase in frequency and magnitude with an increase in fluidization velocity.

- Eight types of emulsion and bubble phase contact dynamics at the tube surface were identified. Each type has different implications for heat transfer which helps to explain the degree of difficulty in modeling heat transfer from first principles.
- The standard deviation of the instantaneous heat transfer coefficient is a measure of the time-weighted-average of the amount of fluctuation (activity) about the mean of the heat transfer coefficient. It can be used as an indication of the frequency and intensity of particle and bubble/emulsion phase activity. The activity causes changes in the magnitude of the instantaneous heat transfer coefficient. Fluctuations arise from bubble and emulsion phase replacement as well the degree of particle activity when each of these phases is in contact with the tube. Fluctuations can also be the result of variations in the gas velocity, temperature and turbulence intensity.
- The standard deviation of the heat transfer coefficient was used to quantify the extent of fluctuations in the instantaneous heat transfer about the mean. It tends to increase from $\theta = 0^\circ$ to $\theta = 180^\circ$ with the maximum generally occurring at $\theta = 180^\circ$ and the minimum usually occurring at $\theta = 45^\circ$ and occasionally $\theta = 0^\circ$. The standard deviation does not vary much with temperature and increases, levels off, and then decreases with fluidization

velocity. This helps to explain why the time-average heat transfer coefficient often exhibits similar behavior.

- The instantaneous heat transfer coefficient signal can be processed to calculate average maximum and average minimum heat transfer coefficients which correspond to average emulsion and average bubble phase coefficients, respectively.
- Δh_{\max} and Δh_{\min} at first increase with fluidization velocity and then decrease. The behavior captured in the current experiments depended on what fluidization velocities were investigated.
- Bubble and emulsion phase frequencies on the tube can be calculated using the filtered heat transfer data. The appropriateness of these data is dependent on the presence of two distinct phases. The frequency generally increases at low fluidization velocities and then remains at a constant value, with the value depending on the circumferential location.
- The bubble residence time next to the tube initially decreases and then remains constant, although the behavior varies somewhat at different circumferential locations. The behavior is more sporadic at $\theta = 135^\circ$, due to the stochastic influences of high particle activity since the heat transfer reaches its peak between $\theta = 90^\circ$ and $\theta = 180^\circ$.
- The bubble time fraction on the tube decreases slightly with increasing fluidization velocity.

- For $\theta = 0^\circ$ and $\theta = 45^\circ$, the heat transfer coefficient increases more significantly as a bubble departs relative to when a bubble is just arriving.
- Bubble frequency measured in the bed below the heat transfer surface (tube) provides a reasonable approximation to bubble frequency on the tube. Bubble (and emulsion) time fraction measured in the bed below the tube, however, is not a good indication of the values on the tube.
- Correlations available in the literature, although developed for time- and space- averaged heat transfer coefficients can be used as a basis to correlate the average maximum (emulsion phase) and average minimum (bubble phase) local heat transfer coefficients. In order to do this, the void fraction must be interpreted correctly and a variation with θ must be considered.
- The correlation by Ganzha et al. (1982) showed the best fit for the emulsion phase heat transfer coefficient. This correlation was modified in the present work to include dependence on the Archimedes number as well as the form of the dependence on the Prandtl number as proposed by Mathur and Saxena (1986). The correlation was also modified to include dependence on the tube circumferential location. The modified correlation is:

$$\text{Nu}_{p,e} = 8.95(1 - \varepsilon)^{2/3} + 0.016 \text{Ar}^{0.3} \text{Re}_p^{0.5} \text{Pr}^{1/3} \frac{(1 - \varepsilon)^{0.133}}{\varepsilon^{0.8}} \quad (3.22)$$

where ε is calculated based on the results of Kimura and Kaneda (1955) but modified in the present work to account for variation with θ . This

correlation predicted heat transfer coefficients for the conditions in the present work within ± 15 percent. It applies to the range of conditions investigated in the present work: $44,000 < Ar < 136,000$; $27 < Re_{mf} < 57$; $39 < Re < 72$; and $6.8 < Pr < 7.0$.

- There is a dearth of information in the literature for predicting local bubble phase heat transfer coefficients. The only correlation that showed promise for fitting the present data is that by Catipovic (1979) where a dependence on Re_{mf} was suggested. A regression analysis revealed that the following form was the best fit:

$$Nu_{p,b} = 1.13 \frac{Re_{p,mf}^{0.73}}{Re_p^{0.3}} \quad (3.23)$$

This correlation predicted heat transfer coefficients for the conditions in the present work within ± 15 percent. It applies to the range of conditions investigated in the present work: $44,000 < Ar < 136,000$; $27 < Re_{mf} < 57$; $39 < Re < 72$; and $6.8 < Pr < 7.0$.

4.2 Recommendations

1. A commercial heat flux sensor could be attached to the surface of the cylinder next to the instantaneous heat flux sensor. There are sensors commercially available which could be used, although they would have a relatively slow time response since they would need to be covered with shim stock to protect them from the harsh fluidized bed environment. This sensor could be used in the calibration of

k/L or in place of the instantaneous heat flux sensor for the time-averaged portion of the heat transfer coefficient. The instantaneous sensor could then be used just to measure the instantaneous contribution about the mean.

2. Multiple sensors could be mounted around the cylinder. If these were located at the same axial tube position, but at different circumferential locations, they could be used to examine heat transfer around the tube on an instantaneous as well as a time-sequence basis. If there were not room for this and the sensors were mounted at different axial locations, it would still be useful to measure data at more than one circumferential location to reduce the time required to obtain data (more than one data set could be taken at a time).
3. A capacitance probe could be mounted next to the instantaneous heat flux sensor to provide information on the instantaneous and time average residence time, frequency and time fraction for the bubble and emulsion phases. This would be better than inferring these properties from the instantaneous heat transfer signal. The capacitance probe could also be used to determine emulsion phase (and bubble phase) void fractions.
4. A radiative heat transfer sensor could be mounted next to the instantaneous heat flux sensor. A time-average or, even better, an instantaneous sensor could be used to provide information about the radiative contribution so that the remaining contributions from convection and conduction could be studied. In the present work, the radiative contribution was estimated using the work of previous

researchers who measured time-averaged radiative heat transfer coefficients in the same bed.

5. The present work could be extended to cover a wider array of particles sizes, bed temperatures, bed materials, tube arrays, fluidization velocities, etc.
6. The optical probes could be constructed out of fiber optic or some other alternative material instead of the fused quartz rods. The rods are fragile and on several occasions, they broke during a run. When this happened, the bed had to be cooled-off, drained of bed material and the test section opened up. The optical probes had to be removed and new quartz rods had to be fabricated, inserted and aligned in the probes. The probes then had to be inserted in the bed with their positions carefully aligned and measured. Finally, the bed was warmed up and brought back to the conditions where testing was terminated. This is a very time consuming effort. A light-transmitting material more durable than the fused quartz would be convenient.
7. The fluidized bed facility could be improved to expand its function. Blower capacity could be increased. Viewports could be installed on the sides of the test section for observation during experiments.
8. Deterministic chaos could be applied to the optical probe and instantaneous heat transfer signals to determine flow and heat transfer regime delineation.

BIBLIOGRAPHY

Adams R.L., "An Approximate Formula for Gas Convection Dominant Heat Transfer in Large-Particle Fluidized Beds," *ASME J. Heat Transfer*, **103**, 395-397 (1981a).

Adams R.L., "Extension of the Adams-Welty Fluid Bed Heat Transfer Model to the Packed Bed Case," *ASME J. Heat Transfer*, **103**, 602-604, (1981b).

Adams R.L., "An Approximate Model of Bubble Phase Convective Heat Transfer to a Horizontal Tube in a Large Particle Fluid Bed," *ASME J. Heat Transfer*, **104**, 565-567 (1982a).

Adams R.L., "Coupled Gas Convection and Unsteady Conduction Effects in Fluid Bed Heat Transfer Based on a Single Particle Model," *Int. J. Heat Mass Transfer*, **25**, 1819-1828 (1982b).

Adams R.L., "Heat Transfer in Large Particle Bubbling Fluidized Beds," *ASME J. Heat Transfer*, **106**, 85-90, (1984).

Adams R.L., and J.R. Welty, "A Gas Convection Model of Heat Transfer in Large Particle Fluidized Beds," *AIChE*, **25**, 395-405, (1979).

Adams R.L., and J.R. Welty, "An Analytical Study of Bubble and Adjacent Tube Influence on Heat Transfer to a Horizontal Tube in a Gas Fluidized Bed," *ASME Journal of Heat Transfer*, **104**, 202-209 (1982).

Adams R.L., J.R. Welty, N. Alavizadeh, and B. Mahbod, "The Radiative Contribution to Heat Transfer Between a High-Temperature Fluidized Bed and an Immersed Tube," (1984).

Alavizadeh, N., "An Experimental Investigation of Radiative and Total Heat Transfer around a Horizontal Tube Immersed in a High-Temperature Gas-Solid Fluidized Bed," Ph.D. Thesis, Dept. of Mech. Eng., Oregon State Univ. (1985).

Alavizadeh, N., R.L. Adams, J.R. Welty and A. Goshayeshi, "An Instrument for Local Radiative Heat Transfer Measurement around a Horizontal Tube Immersed in a Fluidized Bed," *ASME J. Heat Transfer*, **112**, 486-491, (1990).

Allahwala, S.A., B. Singh and O.E. Potter, "Bubble Frequency and Distribution in Fluidized Beds," *Chem. Eng. Commun.*, **11**, 255-280, (1981).

Andeen, B.R., L.R. Glicksman and R. Bowman, "Heat Transfer from Flattened Horizontal Tubes," *Fluidization*, Cambridge Univeristy Press, 345-350, (1978).

Baskakov, A.P. and O.K. Vitt, "Investigation of Heat Transfer Coefficient Pulsations and of the Mechanism of Heat Transfer from a Surface Immersed into a Fluidized Bed, (1973).

Baskakov, A.P. and V.M. Suprun, "Determination of the Convective Component of the Heat-Transfer Coefficient to a Gas in a Fluidized Bed," *Intl. Chem. Engr.*, **12**, 324-326, (1972).

Baskakov, A.P., "The Mechanism of Heat Transfer Between a Fluidized Bed and a Surface," *Intl. Chem. Engr.*, **4**, 320-324, (1964).

Baskakov, A.P., B.V. Berg, O.K. Vitt, and N.F. Filippovsky, "Heat Transfer to Objects Immersed in Fluidized Beds," *Powder Technology*, **8**, 273-282, (1973).

Baskakov, A.P., "Ch. 13B, Heat Transfer in Fluidized Beds: Radiative Heat Transfer in Fluidized Beds," *Fluidization, 2nd Edition*, ed. by Davidson, J.F., R. Clift, and D. Harrison, Academic Press, London, (1985).

Basu, P., "Bed to Wall Heat Transfer in a Fluidized Bed Coal Combustor," *AIChE Sym. Series*, **74**, 187-193, (1978).

Berg, B.V. and A.P. Baskakov, "Investigation of Local Heat Transfer Between a Fixed Horizontal Cylinder and a Fluidized Bed," *Intl. Chem. Engrg.*, **14**, 440-443, (1974).

Bernis, A., F.Vergnes, P. LeGoff, and J.P. Mihe, *Powder Technology*, **17**, 229-234, (1977).

Bock, H.J., and O. Molerus, "Influence of Hydrodynamics on Heat Transfer in Fluidized Beds," In *Fluidization*, ed. by Grace, J.R. and J.M. Matsen, 217, Plenum, New York (1980).

Bordoulya, V.A. and V.I. Kovensky, "Radiative Heat Transfer Between a Fluidized Bed and a Surface," *Int. J. Heat Mass Transfer*, **26**, 277-287, (1983).

Borodulya, V.A., V.L. Ganzha, A.I. Podberezsky, S.N. Upadhyay, and S.C. Saxena, "High Pressure Heat Transfer Investigations for Fluidized Beds of Large Particles and Immersed Vertical Tube Bundles," *Int. J. Heat Mass Transfer*, **26**, 1577-1584, (1983).

Borodulya, V.A., V.L. Ganzha, A.I. Zheltov, S.N. Upadhyay, and S.C. Saxena, "Heat Transfer between Gas-Solid Fluidized Beds and Horizontal Tube Bundles," *Letters in Heat and Mass Transfer*, **7**, 83-95, (1980).

Borodulya, V.A., Y.S. Teplitsky, I.I. Markevich, A.F. Hassan, and T.P. Yeryomenko, "Heat Transfer Between a Surface and a Fluidized Bed: Consideration of Pressure and Temperature Effects," *Int. J. Heat Mass Transfer*, **34**, 47-53, (1991).

Botterill, .S.M., and A.O.O. Denloye, "Gas Convective Heat Transfer to Packed and Fluidized Beds," *AIChE Symp. Ser., Fluidization: Appl. to Coal Conv. Proc.*, **74**, 194-202, (1978).

Botterill, .S.M., and A.O.O. Denloye, "A Theoretical Model of Heat Transfer to a Packed or Quiescent Fluidized Bed," *Chem. Eng. Sci.*, **33**, 509-515, (1978).

Botterill, J.S.M. and A.O.O. Denloye, "Gas Convective Heat Transfer to Packed and Fluidized Beds," *AIChE Symp. Ser.*, **74**, 71, 194-202 (1978).

Botterill, J.S.M., and J.R. Williams, "The Mechanism of Heat Transfer to Gas-Fluidised Beds," *Trans. Instn. Chem. Engrs.*, **41**, 217-230, (1963).

Botterill, J.S.M., *Fluidized-Bed Heat Transfer*, Academic Press, NY (1975).

Botterill, J.S.M., Y. Teoman, K.R. Yuregir, "Temperature Effects on the Heat Transfer Behavior of Gas Fluidized Beds," *AIChE Symposium Series*, **77**, 30-340, (1981).

Brewster, M.Q., and C.L. Tien, "Radiative Transfer in Packed Fluidized Beds: Dependent Versus Independent Scattering," *ASME J. Heat Transfer*, **104**, 573-579, (1982).

Broomhead, D.S. and G.P. King, "Extracting Qualitative Dynamics from Experimental Data," *Physica*, **9D**, 217-236, (1986).

Cai, P. G., De Michele, and A.T. Gradassi, "A Generalized Method for Predicting Gas Flow Distributin Between the Phases in FBC," *ASME Fluidized Bed Combustion*, **2**, 991-1002, (1993).

CanadaG.S., and M.H. McLaughlin, "Large Particle Fluidization and Heat Transfer at High Pressures," *AIChE Symp. Ser., Fluidization: Appl. to Coal Conv. Proc.*, **74**, 27-37, (1978).

Carson R., P. Hansen, J. Wheeldon, and A. Manaker, "Heat Tranfer Rates to Tubing in Utility-Type Bubbling Fluidized Bed Coal Combustors," *ASME/JSME Thermal Engr. Proc.*, 507-511, (1991).

Catipovic, N.M., "Heat Transfer to Horizontal Tubes in Fluidized Beds: Experimental and Theory," Ph.D. Thesis, Dept. of Chem. Eng., Oregon State University (1979).

Catipovic, N.M., G.N. Jovanovic, and T.J. Fitzgerald, "Regimes of Fluidization for Large Particles," *AIChE J.*, **2**, 543-547, (1978).

Catipovic, N.M., T.J. Fitzgerald, A.H. George, and J.R. Welty, "Experimental Validation of the Adams-Welty Model for Heat Transfer in Large-Particle Fluidized Beds," *AIChE Journal*, **2**, 714-72, (1982).

Chandran, R., and J.C. Chen, "Bed-Surface Contact Dynamics For Horizontal Tubes in Fluidized Beds," *AIChE 20th Natl. Heat Transfer Conf.*, (1981).

Chandran, R., J.C. Chen, and F.W. Staub, "Local Heat Transfer Coefficients around Horizontal Tubes in Fluidized Beds," *ASME J. Heat Transfer*, **10**, 152-157, (1980).

Chandran, R., J.C. Chen, and F.W. Staub, "Local Heat Transfer Coefficients Around Horizontal Tubes in Fluidized Beds," (1980).

Chen, J.C., "Heat Transfer to Tubes in Fluidized Beds, *ASME Paper 76-HT-7*, (1976).

Chen, J.C., and K.L. Chen, "Analysis of Simultaneous Radiative and Conductive Heat Transfer in Fluidized Beds," *Chem. Eng. Commun.*, , 255-271, (1981).

Cheremisinoff, N.P., "Review of Experimental Methods for Studying the Hydrodynamics of Gas-Solid Fluidized Beds," *Ind. Eng. Chem. Process*, **2**, 329-351, (1986).

Cherrington, D.C., L.P. Golan, and F.G. Hammitt, "Industrial Application of Fluidized Bed Combustion - Single Tube Heat Transfer Studies," *Proc. 5th Intl. Conf. on Fluidized Bed Combustion*, 184-209, (1977).

Chiba, T., K. Terashima, and H. Kobayashi, "Lateral Distribution of Bubble Sizes in Two-Dimensional Gas-Fluidized Beds," *J. Chem. Engr. Japan*, , 167-169, (1975).

Chiba, T., K. Terashima, H. Kobayashi, "Behavior of Bubbles in Gas-Solid Fluidized Beds: Initial Formation of Bubbles," *Chem. Engrg. Science*, **2**, 965-972, (1972).

Chung, B.T., L.T. Fan, and C.L. Hwang, "A Model of Heat Transfer in Fluidized Beds," *J. Heat Transfe*, 105-110, (1972).

Chung T.Y., and J.R. Welty, "Heat Transfer Characteristics for Tubular Arrays in a High-Temperature Fluidized Bed: An Experimental Study of Bed Temperature Effects," *Experimental Thermal and Fluid Science*, , 388-394, (1990).

Chung, T.Y., and J.R. Welty, "Tube Array Heat Transfer in Fluidized Beds - A Study of Particle Size Effects," *AIChE J.*, **35**, 1170-1176, (1989).

Clift, R. and J.R. Grace, in *Fluidization*, 2nd ed., J.F. Davidson et al., eds., p.73, Academic Press, New York, (1985).

Clough D.E., and A.W. Welmer, "Time-Dependent Behavior of Bubble Volume in Fluidized Beds," *Ind. Chem. Fundam.*, **2**, 235-241, (1985).

Cranfield, .R., and D. Geldart, "Large Particle Fluidisation," *Chem. Engrg. Science*, **2**, 935-947, (1974).

Cranfield, R.R., "A Probe for Bubble Detection and Measurement in Large Particle Fluidised Beds," *Chem. Eng. Sci.*, **27**, 239, (1972).

Crescitelli, S., G. Donsi, L. Massimilla, and G. Volpicelli, "Instantaneous Heat Transfer Coefficient at the Wall of Fluidization," *Heat Transfer - Soviet Research*, **1**, 114-120, (1981).

Davidson, J.F. and Harrison, D., *Fluidized Particles*, Cambridge University Press (1963).

Davies, R.M. and G.I. Taylor, *Proc. Roy Soc.*, **A200**, 375 (1950).

Daw, C.S. and J.S. Halow, "Characterization of Voidage and Pressure Signals from Fluidized Beds Using Deterministic Chaos Theory," *ASME Fluidized Bed Combustion*, 777 (1991).

Daw, C.S. and J.S. Halow, "Evaluation and Control of Fluidization Quality Through Chaotic Time Series Analysis of Pressure-Drop Measurements," *AIChE Symposium Series*, **89**(296), 103, (1993).

Daw, C.S. and J.S. Halow, "Modeling Deterministic Chaos in Gas-Fluidized Beds," *AIChE Symposium Series*, **88**(289), 61, (1992).

Daw, C.S., W.F. Lawkins, D.J. Downing and N.E. Clapp, Jr., "Chaotic Characteristics of a Complex Gas-Solids Flow," *Physical Review A*, **41**(2), 1179, (1990).

De Lasa, H., S.L.P. Lee, and Bergougnou, "Bubble Measurement in Three-Phase Fluidized Beds Using a U-Shaped Optical Fiber," *Can. J. Chem. Eng.*, **62**, 165, (1984).

Decker N., and L.R. Glicksman, "Heat Transfer in Large Particle Fluidized Beds," *Int. J. Heat Mass Transfer*, **26**, 1307-1320, (1983).

- Decker, N.A., and L.R. Glicksman, "Conduction Heat Transfer at the Surface of Bodies Immersed in Gas Fluidized Beds of Spherical Particles," *AIChE Symp. Series*, **7**, 341-349, (1981).
- Denloye, A.O.O., and J.S.M. Botterill, "Bed to Surface Heat Transfer in a Fluidized Bed of Large Particles," *Powder Technology*, **1**, 197-203, (1978).
- Doebelin, E.O., *Measurement Systems: Application and Design*, 4th ed., 157, (1990).
- Doss, H.S., J. Pietruszkiewicz, G.O. Thomas, J.R. Hamm, and W.A. Bezella, "A Characterization of Pressurized Fluidized Beds and Pulverized Coal Fired Power Plants," *ASME preprint 84-AES-1*, (1984).
- Dutta, S., and Wen, C.Y., "A Simple Probe for Fluidized Bed Measurement," *Can. J. Chem. Eng.*, **57**, 115, (1979).
- Ergun, S., *Chem. Eng. Progr.*, **48**, 93, (1952).
- Fatani, A.A., "An Analytical Model of Radiative and Convective Heat Transfer in Small and Large Particle Gas Fluidized Beds," Ph.D. Thesis, Dept. of Mech. Eng., Oregon State Univ. (1983).
- Figliola, R.S., D.E. Beasley, and C. Subramaniam, "Instantaneous Heat Transfer Between an Immersed Horizontal Tube and a Gas Fluidized Bed," *ASME J. Heat Transfer*, **84-HT-111**, (1984).
- Fraser, A.M. and H.L. Swinney, "Independent Coordinates for Strange Attractors from Mutual Information," *Physical Review A*, **33**(2), 1134, (1986).
- Fuller, T.A., T.J. Flynn, C.S. Daw, and J.S. Halow, "Interpretation of Pilot-Scale, Fluidized Bed Behavior Using Chaotic Time Series Analysis," *ASME Fluidized Bed Combustion*, **1**, 141, (1993).
- Gabor J.D., "Wall-to-Bed Heat Transfer in Fluidized Beds," *AIChE J.*, **1**, 249-250, (1972).
- Gabor, J.D., "Heat Transfer to Particle Beds with Gas Flow Less Than or Equal to that Required for Incipient Fluidization," *Chem. Eng. Sci.*, **25**, 985-996 (1970).
- Ganzha, V.L., S.N. Upadhyay, and S.C. Saxena, "A Mechanistic Theory for Heat Transfer Between Fluidized Beds of Large Particles and Immersed Surfaces," *Int. J. Heat Mass Transfer*, **25**, 1531-1540, (1982).

Gardon, R., "A Transducer for the Measurement of Heat-Flow Rate," *J. Heat Transfer*, 396-398, (1960).

Geldart, D., "Types of Gas Fluidization," *Powder Technology*, 7, 285-291 (1973).

Geldart, D., "The Effect of Particle Size and Size Distribution on the Behavior of Gas-Fluidized Beds," *Powder Technology*, , 201-215, (1972).

Geldart, D., "The Size and Frequency of Bubbles in Two- and Three-dimensional Gas-Fluidised Beds," *Powder Technology*, 4, 41-55, (1970).

Geldart, D., and J.R. Kelsey, "The Use of Capacitance Probes in Gas Fluidised Beds," *Powder Technology*, 6, 45, (1972).

Geldart, D., and R.R. Cranfield, "The Gas Fluidisation of Large Particles," *Chem. Engrg. J.*, 3, 211, (1972).

Gelperin, N.I. and V.G. Ainshtein, "Heat Transfer in Fluidized Beds," in *Fluidization*, edited by J.F. Davidson and D. Harrison, Academic Press (1971).

Gelperin, N.I., V.G. Ainshtein, and L.A. Korotyanskaya, "Heat Transfer between a Fluidized Bed and Staggered Bundles of Horizontal Tubes," *Intl. Chem. Engrg.*, , 137-142, (1969).

Gelperin, N.I., V.G. Ainshtein, and N.A. Romanova, "On the Effect of the Height of the Heat-Exchange Surface on the Heat-Transfer Coefficient in a Fluidized Bed," *Intl. Chemical Engrg.*, 1, 502-505, (1974).

George, A.H., and J.L. Smalley, "An Instrumented Cylinder for the Measurement of Instantaneous Local Heat Flux in High Temperature Fluidized Beds," *Int. J. Heat Mass Transfer*, 34, 3025-3036, (1991).

George, A.H., "A Transducer for the Measurement of Instantaneous Local Heat Flux to Surfaces Immersed in High-Temperature Fluidized Beds," *Int. J. Heat Mass Transfer*, 3, 763-769, (1987).

George, A.H., "Instantaneous Local Heat Transfer Coefficients and Related Frequency Spectra for a Horizontal Cylinder in a High Temperature Fluidized Bed," *Int. J. Heat Mass Transfer*, 36(2), 337-345, (1993).

George, A.H., "An Experimental Study of Heat Transfer in a Large Particle Fluidized Bed at Elevated Temperature," Ph.D. Thesis, Dept. of Mech. Eng., Oregon State Univ. (1981).

George, A.H., "Documentation for the OSU High Temperature Fluidized Bed Facility", unpublished, Oregon State University Department of Mechanical Engineering (1981).

Glicksman, L., W. Lord, J. Valenzuela, A. Bar-Cohen, and R. Hughes, "A Model of the Fluid Mechanics in Fluidized Bed Combustors," *AIChE Symp. Ser.*, **7**, 139-147, (1981).

Glicksman, L.R., and N. Decker, "Heat Transfer in Fluidized Beds with Large Particles," Dept. of Mech. Eng., MIT (1979).

Glicksman, L.R., "Heat Transfer in Fluidized Bed Combustors," in *Fluidized Bed Boilers, Design and Application*, edited by P. Basu, Pergamon Press, NY, 1152-1157, (1984).

Glicksman, L.R., and G. McAndrews, "The Effect of Bed Width on the Hydrodynamics of Large Particle Fluidized Beds," *Powder Technology.*, **4**, 159-167, (1985).

Glicksman, L.R., and N. Decker, "Heat Transfer from an Immersed Surface to Adjacent Particles in a Fluidized Bed: The Role of Radiation and Particle Packing," *Proce. of the Seventh Int. Heat Transfer Conf.*, Munich, **6**, 45-50 (1982).

Glicksman, L.R., and N.A. Decker, "Heat Transfer from an Immersed Surface to Adjacent Particles in a Fluidized Bed: The Role of Radiation and Particle Packing," *Proc. of the Seventh Int. Heat Transfer Conf.*, Munich, **6**, 45-50 (1982).

Glicksman, L.R., N.A. Decker, "Design Relationships for Predicting Heat Transfer to Tube Bundles in Fluidized Bed Combustors," *Proc. of the Sixth Int. Conf. on Fluidized Bed Combustion*, Atlanta, GA, **3**, 1152-1157 (1980).

Glicksman, L.R., W.K. Lord, and M. Sakagami, "Bubble Properties in Large-Particle Fluidized Beds," *Chem. Engr. Sci.*, **4**, 479-491, (1987).

Glicksman, L., R. Peloux, N. Decker, and T. Shen, in *Proceedings of the Fifth International Conference on Fluidized Bed Combustion*, Dec 12-14, 1977, **III**, 700, MITRE Corp., McLean, VA (1978).

Glicksman, L.R., and T. Yule, "Gas Throughflow in a Bubbling Fluidized Bed," *Fluidization V*, Proc. of the 5th Engrg Found. Conf. on Fluidization, Ostergaard, K. and A. Sorensen, ed. 103-110 (1986).

Gloski, D., L. Glicksman, and N. Decker, "Thermal Resistance at a Surface in Contact with Fluidized Bed Particles," *Int. J. Heat Mass Transfer*, **2**, 599-610, (1984).

Goblirsch, G., R.H. Vander Molen, K. Wilson, and D. Hajicek, "Atmospheric Fluidized Bed Combustion Testing of North Dakota Lignite," *6th Intl. Fluidized Bed Conference* (1980).

Godard, K., J.F. Richardson, "Bubble Velocities and Bed Expansions in Freely Bubbling Fluidised Beds, 663-670, (1968).

Golan, L.P., and D.C. Cherrington, "Heat Transfer and Unit Response of a Large Fluidized Bed Combustor," *AICHE Symp. Ser.*, **7**, 374-383, (1981).

Gosmeyer, C.D. "An Experimental Study of Heat Transfer in a Large Particle Heated Fluidized Bed," Master's Thesis, Dept. of Chem. Eng., Oregon State Univ. (1979).

Goshayeshi, A., "Experimental Studies of Heat Transfer with an Array of Horizontal Tubes Immersed in a High-Temperature Fluidized Bed," Ph.D. Thesis, Dept. of Mech. Eng., Oregon State Univ. (1989).

Goshayeshi, A., J.R. Welty, R.L. Adams, and N. Alavizadeh, "Local Heat Transfer Coefficients for Horizontal Tube Arrays in High Temperature Large Particle Fluidized Beds - An Experimental Study," *23rd ASME/AICHE National Heat Transfer Conference Denver Aug 4-7*, (1985).

Goshayeshi, A., J.R. Welty, R.L. Adams, and N. Alavizadeh, "Local Heat Transfer Coefficients for Horizontal Tube Arrays in High Temperature Large Particle Fluidized Beds - An Experimental Study," *ASME Journal of Heat Transfer*, **10**, 907-912, (1986).

Grace and Harrison, "The Behavior of Freely Bubbling Fluidised Beds," *Chem. Eng. Sci.*, **24**, 497, (1969).

Grace, J.R., and D. Harrison, "The Behavior of Freely Bubbling Fluidised Beds," *Chem. Engrg. Science*, **2**, 497-508, (1969).

Grassberger, P. and I. Procaccia, "Measuring the Strangeness of Strange Attractors," *Physica*, **9D**, 189, (1983).

Grewal, N.S., "A Generalized Correlation for Heat Transfer Between a Gas-Solid Fluidized Bed of Small Particles and an Immersed Staggered Array of Horizontal Tubes," *Powder Technology*, **3**, 145-154, (1981).

Grewal, N.S., "Maximum Heat Transfer Coefficient Between a Horizontal Tube and a Gas-Solid Fluidized Bed," *Ind. Eng. Chem. Proc. Des. Dev.*, **2**, 108-116, (1981).

Grewal, N.S., and S.C. Saxena, "Heat Transfer Between a Horizontal Tube and a Gas-Solid Fluidized Bed," *Int. J. Heat Mass Transfer*, **23**,1505-1519, (1980).

Grewal, N.S., S.C. Saxena, "Experimental Studies of Heat Transfer between a Bundle of Horizontal Tubes and a Gas-Solid Fluidized Bed of Small Particles," *Ind. Eng. Chem. Process Des. Dev.*, **2**, 367-376, (1983).

Gunn, D.J., and H.H. Al-Doori, "The Measurement of Bubble Flows in Fluidized Beds by Electrical Probe," *Int. J. Multiphase Flow*, **11**, 535, (1985).

Gutfinger, C., and N. Abuaf, "Heat Transfer in Fluidized Beds,"

Hager, W.R. and W.J. Thomson, "Bubble Behavior Around Immersed Tubes in a Fluidized Bed," *AIChE Symposium Series*, **69**, 68, (1973).

Hager, W.R., and W.J. Thomson, "Bubble Behavior Around Immersed Tubes in a Fluidized Bed," *Fluidization, AIChE Symposium Series*, **6**, 68-77, (1973).

Henwood, G.A., U.K. Atomic Energy Authority, Report AERE-R6027 (1969).

Ho, T.C., N. Yutani, L.T. Fan, and W.P. Walawender, "Stochastic Modeling of Bubble Formation on the Grid in a Gas-Solid Fluidized Bed," *Canadian J. Chem. Engrg.*, **6**, 654-659, (1983).

Holman, J.P., *Heat Transfer*, 4th edn, p. 102, McGraw-Hill, New York (1976).

Horio, M., and A. Nonaka, "A Generalized Bubble Diameter Correlation for Gas-Solid Fluidized Beds," *AIChE J.*, **33**, 1865-1872, (1987).

Horio, M., and J. Koike, "A Simple Algorithm of Bubble Size Prediction for Three Dimensional Fluidized Beds," *ASME Intl. Conf. Fluidized Bed Combustion*, , 495-500, (1993).

Ishiguro, H., K. Ichikawa, and H. Nariai, "Unsteady Fluidization Structure and Heat Transfer Around a Horizontal Heated Circular Cylinder in a Gas Fluidized Bed," *ASME/JSME Thermal Engr. Conf.*, , 513-520, (1991).

Jackson, R., "The Mechanics of Fluidized Beds," *Trans. Inst. Chem. Eng.*, **41**, 13-28 (1963).

Jin, Y., Q. Yu, L. Zhang, and Z. Wang, "Study of the Effect of Bubbles on the motion of Solid Particles in a Fluidized Bed by a Laser-Tracer Method," *Intl. Chemical Engrg.*, **2**, 454-461, (1982).

Johnson, D.E., *Introduction to Filter Theory*, Prentice-Hall Inc., 43, (1976).

Jovanovic, G. and N. Catipovic, "A New Approach in Classifying Solids in Bubbling Gas-Fluidized Bed," *Fluidization IV: Proc. of the Intl. Conf on Fluidization*, Kashikojima, Japan, Kunni, D. and R. Toei, R. (eds), (1983).

Junge, D.C., "Design and Operation of High Temperature Fluidized Bed Facility," unpublished report, Dept. of Mech. Engrg, Oregon State Univ. (1978).

Katoh, Y., M. Miyamoto, T. Chimura, and Y. Idei, "The Study of Partical Behavior in the Expansion of Fluidized Bed Using a Simple Optical Probe," *ASME/JSME Thermal Engr. Proc.*, , 493-497, (1991).

Khan, T., and R. Turton, "The Measurement of Instantaneous Heat Transfer Coefficients around the Circumference of a Tube Immersed in a High Temperature Fluidized Bed," *Int. J. Heat Mass Transfer*, **35**, 3397-3406, (1992).

Kimura, M., K. Nono, and T. Kaneda, "Distribution of void in Packed Tube," *Chem. Eng. Japan*, **19**, 397-900 (1955).

Kolar, A.K., N.S. Grewal, and S.C. Saxena, "Investigation of Radiative Contribution in a High Temperature Fluidized-Bed Using the Alternate-Slab Model," *Int. J. Heat Mass Transfer*, **22**, 1695-1703, (1979).

Ku, A.C., M. Kuwata, and F.W. Staub, "Heat Transfer to Horizontal Tube Banks in a Turbulent Fluidized Bed of Large Particles," *AIChE Symposium Series*, **7**, 359-367, (1981).

Kubie, J., "Bubble Induced Heat Transfer in Gas Fluidized Beds," *Int. J. Heat Mass Transfer*, **19**, 1441-1453, (1976).

Kubie, J., and J. Broughton, "A Model of Heat Transfer in Gas-Fluidized Beds," *Int. J. Heat Mass Transfer*, **1**, 289-299, (1975).

Kunii, D., and O. Levenspiel, *Fluidization Engineering*, Butterworth-Heinemann, (1991).

Kunii, D., K. Yoshida, and I. Hiraki, "The Behavior of Freely Bubbling Fluidized Beds," *Proc. Intl. Symp. on Fluidization* (Ed. A.A.H Drinkenburg), Netherlands Univ. Press, 243, (1967).

Kurosaki, Y., T. Ishize, and I. Satoh, "Mechanism of Heat Transfer Enhancement of Fluidized Beds: Estimation of Direct Contact Heat Exchange from Heat Transfer

Surface to Fluidized Particles by using an Optical Visualization Technique," *ASME/JSME Thermal Engr. Proc.*, 465-472, (1991).

Leckner, D. and Hogberg, D, "Material Loss from the Heat Exchange Surface of a Fluidized Bed Combustor," *Proc. from the 1st Intl. Fluidized-Bed Combustion and Applied Technology Symposium*, Beijing, Hemisphere Publishing, V67-V76, (1984).

Lei, D.H., "An Experimental Study of Radiative and Total Heat Transfer between a High Temperature Fluidized Bed and an Array of Immersed Tubes," Ph.D. Thesis, Dept. of Mech. Eng., Oregon State Univ. (1988).

Leon, A.M., P.J. Choksey, and S.A. Bunk, "Design, Construction, Operation, and Evaluation of a Prototype Culm Combustion Boiler/Heater Unit," *DOE Report FE-3269-9A*, (1979).

Levenspiel, O., and J.S. Walton, "Bed-Wall Heat Transfer in Fluidized Systems," *Heat Transfer Symposium Series No.9*, **50**, 1-13, (1952).

Levy, E.K., and J.W. Stallings, "Tube Erosion in Bubbling Fluidized Beds," *Fluidized Bed Combustion*, 1139-1144, (1991).

Lockett, M.J., J.F. Davidson, and D. Harrison, "On the Two-Phase Theory of Fluidisation," *Chem. Eng. Sci.*, **22**, 1059, (1967).

Loew, O., B. Shmutter, and W. Resnick, "Particle and Bubble Behavior and Velocities in a Large-Particle Fluidized Bed with Immersed Obstacles," *Powder Technology*, **2**, 45-57, (1979).

Lord, W.K., G. McAndrews, M. Sakagami, J.A. Valenzuela, and L.R. Glicksman, "Measurement of Bubble Properties in Fluidized Beds," *Proc. 7th Intl. Fluidized Bed Comb. Conf.*, **1**, 76, (1982).

Mahbod, B., "A Theoretical Study of the Radiative Contribution to Heat Transfer between a High-Temperature, Large-Particle Gas-Fluidized Bed and an Immersed Tube," Ph.D. Thesis, Dept. of Mech. Eng., Oregon State University (1984).

Maskaev, V.K., and A.P. Baskakov, "Features of a External Heat Transfer in a Fluidized Bed of Coarse Particles," *Intl. Chemical Engrg.*, **1**, 80-83, (1974).

Masson, H., and R. Jottrand, " Measurement of Local Bubble Properties in a Fluidized Bed," *Fluidization* (Eds. J.F. Davidson and D.L. Keairns), Cambridge Univ. Press, **1**, (1978).

Mathur, A., and S.C. Saxena, "A Correlation for Heat Transfer Between Immersed Surfaces and Gas-Fluidized Beds of Large Particles," *Energy*, **1**, 843-852, (1986).

Matsen, J.M., "Evidence of Maximum Stable Bubble Size in Fluidized Bed," *AIChE Symp. Ser.*, **6**, 30-33, (1973).

Matsuura, A., and L. Fan, "Distribution of Bubble Properties in a Gas-Solid-Liquid Fluidized Bed," *AIChE J.*, **30**, 894, (1984).

McGaw, D.R., "The Development of a Mechanism for Gas-Particle Heat Transfer in Shallow Fluidised Beds of Large Particles," *Chem. Eng. Sci.*, **3**, 11-18, (1977).

McKain, D.L., N.N. Clar, A.I. Karamavruc, and R. Turton, "Local, Time-Varying Bed-To-Tube Heat Transfer in Bubbling Fluidized Beds," *ASME Gas-Solids Flows*, **166**, (1993).

Mei, J.S., J.M. Rockery, W.F. Lawson, and E.H. Robey, "Flow Regime Transitions in Fluidized Beds of Coarse Particles," *Fluidized Bed Combustion*, 1225-1232, (1991).

Mickley, H.S., and D.F. Fairbanks, "Mechanism of Heat Transfer to Fluidized Beds," *AIChE Journal*, , 374-384, (1955).

Mickley, H.S., D.F. Fairbanks, and R.D. Hawthorn, *Chem. Eng. Prog. Symp. Ser.*, **57**(32), 51 (1961).

Mudde, R.F., H.B.M. Schulte, and H.E.A. VanDen Akker, "Analysis of a Bubbling 2-D Gas-Fluidized Bed Using Image Processing," *Powder Technology*, **8**, 149-159, (1994).

Mueller, B.T., D.V. Pence, and D.E. Beasley, "Emulsion Phase Contact Dynamics and Heat Transfer in Large and Small Particle Gas-Fluidized Beds," *ASME/JSME Thermal Engineering Conference*, , 499-508, (1995).

Ni, L., and D. Moslemian, "Pressure Fluctuation with in a Large Particle Gas Fluidized Bed in the Presence of Horizontal Tube Banks," *ASME Gas-Solid Flows*, **166**, 3-16, (1993).

O'Brien, J.E., M.L. Wade, and A.M. Terpolilli, "The Contribution of Gas Convection to Total Heat Transfer for a Horizontal Cylinder Submerged in a Fluidized Bed," *AIChE Symp. Ser.*, **8**, 48-55, (1985).

O'Brien, T.J., M. Syamial, P. Nicoletti, and I. Celik, "Time-Averaged Hydrodynamic Equations of Fluidization," *AIChE Symposium Series*, **8**, 192-197, (1993).

- Ozkaynak, T.F., and J.C. Chen, "Emulsion Phase Residence Time and Its Use in Heat Transfer Models in Fluidized Beds," *AIChE J.*, **2**, 544-550, (1980).
- Ozkaynak, T.F., J.C. Chen, and T.R. Frankenfield, "An Experimental Investigation of Radiation Heat Transfer in a High Temperature Fluidized Bed," *Intl. Conf. on FBC* (1983).
- Park, W.H., W.K. Kang, C.E. Capes, and G.L. Osberg, "The Properties of Bubbles in Fluidized Beds of Conducting Particles as Measured by an Electroresistivity Probe," *Chem. Eng. Sci.*, **24**, 851, (1969).
- Partridge, B.A., and P.N. Rowe, "Analysis of Gas Flow in a Bubbling Fluidised Bed When Cloud Formation Occurs," *Trans. Inst. Chem. Engrs.*, **44**, 349, (1966).
- Peeler, J.P.K., and A.B. Whitehead, "Solids Motion at Horizontal Tube Surfaces in a Large Gas-Solid Fluidized Bed," *Chem. Engr. Sci.*, **37**, 77-82, (1982).
- Pence, D.V., D.E. Beasley, and R.S. Figliola, "Heat Transfer and Surface Renewal Dynamics in Gas Fluidized Beds," *J. Heat Transfer*, **116** (1994).
- Pidwebecki, D., "Heat Transfer in the Splash-Zone of a High Temperature Fluidized Bed," Ph.D. Thesis, Dept. of Mech. Eng., Oregon State Univ. (1994).
- Press, W.H., B.P. Flannery, S.A. Teukolsky, and W.T. Vetterling, *Numerical Recipes: The Art of Scientific Computing (Fortran Version)*, Cambridge University Press, 415, (1989).
- Qian, R.Z., H.S. Li, W.D. Hunag, and D.C. Liu, "Measurement and Analysis of Instantaneous Local Heat Transfer Coefficients for a Horizontal Tube in a High Temperature Fluidized Bed," *ASME Intl. Conf. on Fluidized Bed Combustion*, **2**, 1201-1207, (1993).
- Ramayya, A. V., S.P. Venkateshan, and A.K. Kolar, "Large Particle Fluidization Studies with a Differential Pressure Fluctuation Record," *ASME Intl. Conf. Fluidized Bed Combustion*, , 877-885, (1993).
- Reid, W.P., "Distribution of Sizes of Spheres in a Solid from a Study of Slices of the Solid," *J. of Math. and Physics*, **XXXIV**, 95, (1955).
- Richardson, J.F., and K.J. Shakiri, "Heat Transfer Between a Gas-Solid Fluidized Bed and a Small Immersed Surface," *Chem. Eng. Sci.*, **34**, 1019-1029, (1979).
- Rooney, N.M. and D. Harrison, in *Fluidization Technology*, ed. by D.L. Keairns, Hemisphere Pub. Corp., **2**, 3 (1976).

Rowe, P.N. and B.A. Partridge, "An X-Ray Study of Bubbles in Fluidised Beds," *Trans. Instn. Chem. Engrs.*, **43**, 157, (1965).

Rowe, P.N. and H. Masson, "Interaction of Bubbles with Probes in Gas Fluidised Beds," *Trans. Instn. Chem. Engrs.*, **59**, 177, (1981).

Rowe, P.N., "Prediction of Bubble Size in a Gas Fluidised Bed," *Chem. Eng. Sci.*, **3**, 258-288, (1976).

Samson, T., "Heat Transfer to Objects in Fluidized Beds," *Fluidization and its Applications*, **1**, (1973).

Saxena, S.C. and V.L. Ganzh, "Heat Transfer to Immersed Surfaces in Gas-Fluidized Beds of Large Particles and Powder Classification," *Powder Technology*, **39**, 199 (1984).

Saxena, S.C., "Heat Transfer Between Immersed Surfaces and Gas-Fluidized Beds," *Advances in Heat Transfer*, Academic Press, **19**, 97-189, (1989).

Saxena, S.C., "Heat Transfer from a Bank of Immersed Horizontal Smooth Tubes in a Fluidized Bed," *Letters in Heat and Mass Transfer*, , 225-229, (1979).

Saxena, S.C., and R. Vadivel, "Heat Transfer and Hydrodynamic Studies in Gas-Fluidized Beds," *Energy*, **1**, 353-362, (1989).

Saxena, S.C., N.S. Rao, V.N. Tanjore, "Diagnostic Procedures for Establishing the Quality of Fluidization of Gas-Solid Systems," *Experimental Thermal and Fluid Science*, 56-73, (1993).

Schouten, J.C. and C.M. van den Bleek, "Chaotic Hydrodynamics of Fluidization: Consequences for Scaling and Modeling of Fluid Bed Reactors," *AIChE Symposium Series*, **88**(289), 70, (1992).

Schouten, J.C. and C.M. van den Bleek, "Chaotic Behavior in a Hydrodynamic Model of a Fluidized Bed Reactor," *ASME Fluidized Bed Combustion*, 459, (1991).

Sellakumar, K.M., and V. Zakkay, "Bubble Characterization in Pressurized Fluidized-Bed Combustors with Bed Internals," *Combust. Sci. and Tech.*, **6**, 359-374, (1988).

Shah, P.J., S.N. Upadhyay, and S.C. Saxena, "Heat Transfer from Large Diameter Smooth Horizontal Tubes Immersed in Gas Fluidized Beds," *20th National Heat Transfer Conf. AIChE*, (1981).

- Sitnai, O., "Solids Mixing in a Fluidized Beds with Horizontal Tubes," *Ind. Eng. Chem. Process*, **2**, 533-538, (1981).
- Sitnai, O., "Utilization of the Pressure Differential Records from Gas Fluidized Beds with Internals for Bubble Parameters Determination," *Chem. Engr. Sci.*, **37**, 1059-1066, (1982).
- Sitnai, O., S.C. Dent, and A.B. Whitehead, "Asymptotic Bubble Size in Tubed Fluidized Beds," *Chem. Engr. Science*, **37**, 1429-1430, (1982).
- Skinner, D.G., "The Fluidised Combustion of Coal," *M&B Monograph CE/3*, ed. by J.C. Cook, Mills & Boon Limited, London (1971).
- Skinner, G.T., "Analog Network to Convert Surface Temperature to Heat Flux," *ARS J.* **3485**, 569-570, (1960).
- Skrzycke, D.P., K. Nguyen, and C.S. Daw, "Characterization of the Fluidization Behavior of Different Solid Types Based on Chaotic Time Series Analysis of Pressure Signals," *ASME Fluidized Bed Combustion*, **1**, 155, (1993).
- Smalley, J.L., "Development of a Transducer to measure Instantaneous Local Heat Flux to a Surface Immersed in a High Temperature Fluidized Bed," M.S. Thesis, Montana State Univ, Bozeman, Montana, U.S.A. (1990).
- Stringer, J. "Is a Fluidized Bed a Chaotic Dynamic System?," *Proc. of the ASME International Conf. on Fluidized Bed Combustion*, San Francisco, CA, **1**, ed. by A.M. Manaker, (1989).
- Stringer, J. "High Temperature Corrosion of Metals and Alloys in Fluidized Bed Combustion Systems," *Proc. of the Fifth Int. Conf. on Fluidized Bed Combustion* (12-14 Dec. 1977), MITRE Corp., McLean, VA, **3**, 682 (1978).
- Syromyatnikov, N.I., "The Theory of External Heat Transfer in a Fluidized Bed," *Intl. Chemical Engrg.*, **1**, 483-485, (1974).
- Syromyatnikov, N.I., V.M. Kulikov, V.S. Nosov, and V.N. Korolev, "The Instantaneous Local Rate of External Heat Transfer in an Inhomogenous Fluidized Bed," *Heat Transfer - Soviet Research*, **4**, 42-50, (1976).
- Szekely, J., R.J. Fisher, "Bed to Wall Radiation Heat Transfer in a Gas-Solid Fluidized Bed," *Chem. Eng. Sci.*, **2**, 833-849, (1969).

Takens, F. "Detecting Strange Attractors in Turbulence," *Lecture Notes in Mathematics Dynamic Systems and Turbulence*, ed. by Dold, A. and B. Eckmann, **898**, Springer-Verlag, New York, (1980).

Tam, S.W., and M.K.Devine, "A Study of Fluidized Bed Dynamical Behavior: A Chaos Perspective," *Applied Chaos*

Tamarin, A.I., S.S. Zabrodskiy, and Y.G. Yepanov, "Heat Transfer between a Horizontal Staggered Tube Bundle and a Fluidized Bed," *Heat Transfer - Soviet Research*, , 51-55, (1976).

Tang, J.T., and W. Howe, "Heat Transfer for the 6'x6' Atmospheric Fluidized Bed Development Facility," *ASME Paper 80-HT-128* (1980).

Toomey, R.D. and H.F. Johnstone, *Chemical Engineering Progress*, **48**(220), (1952).

Toomey, R.D., and Johnstone, H.P., "Gaseous Fluidisation of Solid Particles," *Chem. Eng. Sci.*, **48**, 220, (1952).

Tsutsui, T., and T. Miyauchi, "Fluidity of a Fluidized Catalyst Bed and Its Effect on the Behavior of the Bubbles," *Intl. Chem. Engrg.*, **20**, 386, (1980).

Tsutsui, T., and T. Miyauchi, "Fluidity of a Fluidized Catalyst Bed and Its Effect on the Behavior of the Bubbles," *Intl. Chem. Engrg.*, **2**, 386-393, (1980).

Tuot, J., and R. Clift, "Heat Transfer Around Single Bubbles in a Two-Dimensional Fluidized Bed," *AIChE Symposium Series*, **6**, 78-84, (1973).

Tuot, J., and R. Clift, *AIChE Symp. Ser.*, **69**, 128, p.78 (1973).

Vadivel, R., and V.N. Vedamurthy, "An Investigation of the Influence of Bed Paramters on the Variation of the Local Radiative and Total Heat Transfer Coefficients around an Embedded Horizontal Tube,"

Van Den Bleek, C.M. and J.C. Schouten, "Can Deterministic Chaos Create Order in Fluidized-Bed Scale-Up?," *Chemical Eng. Science*, **48**(13), 2367-2373, (1993).

van der Stappen, M.L.M., J.C. Schouten and C.M. van den Bleek, "Application of Determinisitic Chaos Theory in Understanding the Fluid Dynamic Behavior of Gas-Solids Fluidization," *AIChE Symposium Series*, **89**(296), 91, (1993).

van der Stappen, M.L.M., J.C. Schouten and C.M. van den Bleek, "Determinisitic Chaos Analysis of the Dynamical Behavior of Slugging and Bubbling Fluidized Beds," *ASME Fluidized Bed Combustion*, **1**, 129, (1993).

Vreedenberg, H.A., "Heat Transfer Between a Fluidized Bed and a Horizontal Tube," *Chem. Eng. Sci.*, 52-66, (1958).

Walker, S.W., *Fast Fourier Transforms*, CRC Press Inc., 14, (1991).

Weihong, L, B. Guangxiang, Z. Zengrong, Y. Jianhua, and C. Kefa, "Measurements of Bubble and Particle Motion in a Two-Dimensional FB," *9th Intl. Conf. Fluidized Bed Comb.*, 2, 1198, (1987).

Werther, J., *German Chem. Eng.*, 1, 166 (1978).

Werther, J., "Bubbles in Gas Fluidised Beds - Part I," *Trans. Instn. Chem. Engrs.*, 5, 149-159, (1974).

Werther, J., "Bubbles in Gas Fluidised Beds - Part II," *Trans. Instn. Chem. Engrs.*, 5, 160-169, (1974).

Werther, J., and O. Molerus, "The Local Structure of Gas Fluidized Beds - I. A Statistically Base Measuring System," *Int. J. Multiphase Flow*, 1, 103, (1973).

Werther, J., and O. Molerus, "The Local Structure of Gas Fluidized Beds - II. The Spatial Distribution of Bubbles," *Int. J. Multiphase Flow*, , 123-138, (1973).

Werther, J., and O. Molerus, "The Local Structure of Gas Fluidized Beds - I. A Statistically Based Measuring System," *Int. J. Multiphase Flow*, , 103-122, (1973).

Werther, J., D.Bellgardt, H. Groenewald, and K. Hilligardt, "Influence of Immersed Heat Exchange Surfaces on Fluid Mechanics and Solids Mixing in Fluidized Beds," *Proc. 9th Intl. Conf. on Fluidized-Bed Combustion*, , 515-522, (1987).

Wright, S.J., R. Hickman, and H.C. Ketley, "Heat Transfer in Fluidised Beds of Wide Size Spectrum at Elevated Temperature," *British Chem. Eng.*, 15, 1551-1554, (1970).

Xavier, A.M., and J.F.Davidson, "Heat Transfer to Surfaces Immersed in Fluidised Beds in the Freeboard Region," *AIChE Symposium Series*, 7, 368-373, (1981).

Xavier, A.M., and J.F.Davidson, "Heat Transfer to Surfaces Immersed in Fluidised Beds, Particularly Tube Arrays," *Fluidization*, Cambridge University Press, 333-338, (1978).

Yasui, G., and L.N. Johanson, "Characteristics of Gas Pockets in Fluidized Beds," *AIChE J.*, 4, 445, (1958).

Yoshida, K., J. Sakane, and F. Shimizu, "A New Probe for Measuring Fluidization Bed Characteristics at High Temperatures," *Ind. Eng. Chem. Fundam.*, **21**, 85, (1982).

Yoshida, K., T. Ueno, and D. Kunii, "Mechanism of Bed-Wall heat Transfer in a Fluidized Bed at High Temperatures," *Chem. Eng. Sci.*, **2**, 77-82, (1974).

Zabrodsky, S.S., *Hydrodynamics and Heat Transfer in Fluidized Beds*, MIT Press, Cambridge (1966).

Zabrodsky, S.S., Y.G. Epanov, D.M. Galershtein, S.C. Saxena, and A.K. Kolar, "Heat Transfer in a Large-Particle Fluidized Bed with Immersed in-Line and Staggered Bundles of Horizontal Smooth Tubes," *Int. J. Heat Mass Transfer*, **2**, 571-579, (1981).

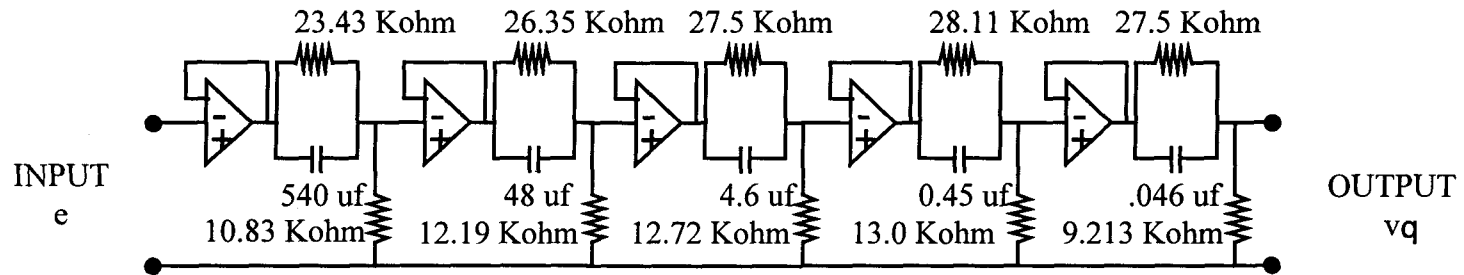
Zhang, X.R., G.M. Homsy, and W.T. Ropchan, "Bubble Formation in a Single-Jet Gas-Solid Fluidized Bed," *Int. J. Multiphase Flow*, **1**, 649-660, (1987).

Ziegler, E.N., L.B. Koppel, and W.T. Brazelton, "Effects of Solid Thermal Properties on Heat Transfer to Gas Fluidized Beds," *I&EC Fund.*, , 324-328, (1964).

APPENDIX

LAPLACE TRANSFORM OF TIME-VARYING TERM:

$$\frac{\overline{\delta q(s)}}{\delta T_s(s)} = \sqrt{k\rho c} \sqrt{s} \quad \Rightarrow \quad \frac{v(s)}{e(s)} = A\sqrt{k\rho c} \sqrt{s} \quad \leftarrow \begin{array}{l} \text{Transfer} \\ \text{Function} \\ (s=j\omega) \end{array}$$



$$\Rightarrow q_w(t) = \frac{k}{L} [\langle T_s \rangle - T_i] + \frac{1}{\beta} [v_q(t) - \langle v_q \rangle]$$

Constants to calibrate

Figure A.1 Analog conditioning circuit representing transfer function.

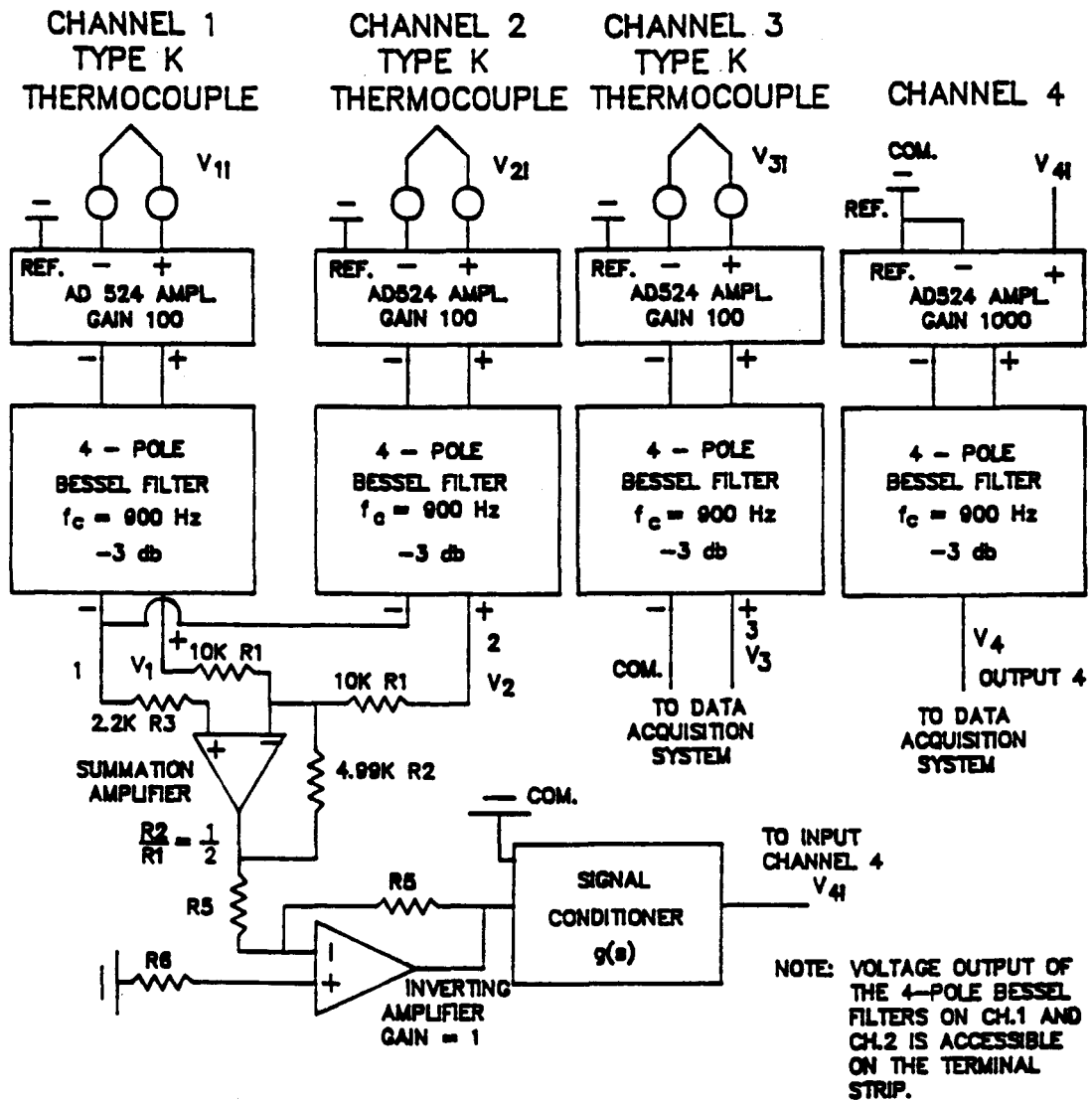


Figure A.2 Signal conditioning circuit associated with the heat flux sensor
(Smalley, 1990).

Table A.1 Summary of test conditions for 3D High-Temperature Experiments.^{1,2} $d_p = 2.0 \text{ mm}$

T_{bed} [K]		600		700		800		900		1000	
U_{mf} [m/s]		1.48		1.52		1.54		1.60		1.64	
U [m/s]	U/U_{mf}	1.68	1.14	1.80	1.19	1.71	1.11	1.91	1.19	2.26	1.38
		1.77	1.20	2.00	1.31	2.11	1.37	2.12	1.38	2.50	1.52
		1.85	1.25	2.16	1.42	2.48	1.61	2.52	1.58	2.82	1.72
								2.74	1.71	3.03	1.85

 $d_p = 2.9 \text{ mm}$

T_{bed} [K]		700		800		900	
U_{mf} [m/s]		1.92		1.97		2.07	
U [m/s]	U/U_{mf}	2.01	1.05	2.16	1.09	2.18	1.05
		2.13	1.11	2.26	1.15	2.37	1.14
				2.45	1.24	2.57	1.24

¹ Heat transfer coefficients were measured for 2.0 mm particles only. Bubble properties were measured for 2.0 and 2.9 mm particles.

² Heat transfer coefficients were measured at tube circumferential locations of $\theta = 0^\circ, 45^\circ, 90^\circ, 135^\circ,$ and 180° .